Polarimetric Observations at Low Radio Frequencies

Jamie Stephen Farnes

This Dissertation is Submitted for the
Degree of Doctor of Philosophy
1 June 2012

UNIVERSITY OF CAMBRIDGE

Cavendish Astrophysics Group
And
Trinity Hall
University of Cambridge

For mum and dad…

Contents

List of Figures

List of Tables

Declaration

I hereby declare that this thesis, entitled "*Polarimetric Observations at Low Radio Frequencies*", is not substantially the same as any that I have submitted, or will be submitting, for a degree, diploma, or other qualification at this, or any other, University.

This dissertation is the result of my own work and includes nothing which is the outcome of work done in collaboration except where specifically indicated in the text.

Various figures in this thesis are reproduced from the work of other authors, for illustrative purposes or discussion. Such figures are always credited in the associated caption. This thesis contains less than sixty thousand words.

Jamie Farnes

Summary

Polarimetric Observations at Low Radio Frequencies

Jamie Stephen Farnes

Magnetic fields play a fundamental role in the evolution of astrophysical systems. These fields can be studied through wide-field spectropolarimetry, which allows for faint polarised signals to be detected at relatively low radio frequencies. An interferometric polarisation mode has recently become available at the Giant Metrewave Radio Telescope (GMRT). A detailed analysis of the GMRT's instrumental response is presented. The findings are used to create a polarisation pipeline, which in combination with rotation measure (RM) Synthesis is used for the detection of extended linearly polarised emission at 610 MHz. A number of compact sources are detected and their Faraday depth and polarisation fraction are reported for the first time.

New holography observations of the GMRT's primary beam are presented. Instantaneous off-axis polarisation is substantial and scales with the Stokes I beam. The developed beam models are used to reduce direction-dependent instrumental polarisation, and the Stokes I beam is shown to deviate from circular symmetry. A new technique for electric vector polarisation angle calibration is developed that removes the need for known sources on the sky, eliminates ionospheric effects, and avoids a flaw in current methods which could erroneously yield multiple Faraday components for sources that are well-parameterised by a single RM.

A sample of nine galaxies from two Southern Compact Groups are then presented, with constraints being placed on the polarised fraction, RM, spectral index, star formation rate, companion sources, and hydrodynamical state. One galaxy has a displaced peak of radio emission that is extended beyond the disk in comparison to the near-IR disk – suggesting the radio disturbance may be a consequence of ram pressure stripping. Linear polarisation is detected from the core of NGC 7552 at 610 MHz, while another three galaxies ESO 0353–G036, NGC 7590, and NGC 7599 are found to be unpolarised. An analysis of additional extended sources allows for an FR-I and an FR-II radio source to be morphologically classified.

Finally, spatial spectral variations are identified in the youngest known Galactic supernova remnant G1.9+0.3, with flatter spectra in the NW and SE. Models of cosmic ray acceleration at oblique shocks suggest the variation is most consistent with an ambient B field perpendicular to the axis of bilateral symmetry. For the first time, the presence of polarised emission is detected. There is increased ordering of the B field in the NW and strong Faraday depolarisation must also be present. An intrinsically radially-oriented field could be provided by a systematic gradient in RM of ≈ 140 rad m^{-2} from N to S and can also explain the depolarisation. Such a gradient may be caused by an anisotropic regular magnetic field within the remnant or in an intervening Faraday screen. The lack of strong constraints on the RM, and the remnant's current evolutionary stage, leave open the possibility that Rayleigh–Taylor instability formation has not yet fully taken place.

ACKNOWLEDGEMENTS

- First and foremost I offer my deepest gratitude to my supervisor, Dave Green, who has always been available to answer my stupid, really stupid, and completely stupid questions. He has been extremely supportive, offering patience and knowledge while also allowing me to work in my own way. Without him, this thesis would certainly not have been completed. I simply could not have asked for a better or more friendly supervisor. If you haven't yet, google 'Dave Green facts', I'm convinced they're all essentially true – except number one, which is only true in winter.

- I am also exceptionally grateful to Julia Riley, for being such a consistently happy face whenever I have visited the astrophysics coffee room, for a multitude of useful conversations, for all of her very constructive comments on various manuscripts, and for convincing me to be an undergraduate demonstrator – an experience I have thoroughly enjoyed. I'd also like to thank Julia for finally teaching me when, and when not, to use apostrophe's!

- Thank you also to all of my office mates – for constant amusement, splendid pub lunches, fun nights not thinking about physics, and for being such pleasant company whenever I have (and haven't?!) been in the office. I'm particularly thankful to David Carretero, Malak Olamaie, James Gordon, Philip Graff, Roshina Nandra, Douglas O'Rourke, Sarah Graves, and Rosie Bolton (who makes the most delicious lemon curd).

- Further thanks go to: Anna Scaife for being such entertaining company, both during casual conversations and teleconferences in Cambridge and during the LOFAR meeting in Newcastle, and also for a wealth of insightful comments on RM Synthesis. David Titterington and Greg Willatt for always being so helpful with my extensive computing requirements and for maintaining such an excellent data reduction environment. Richard King and Helen Jobson for being such delightful and good-humoured colleagues during teaching and marking sessions (and for having such great taste in music!). Nimisha Kantharia for such pleasant and engaging conversations during observing trips at the

GMRT and for kindly spending time to collect the data that was used for analysis of the polarisation beam. Sam George for both helpful conversations and thoughtfully offering to read through this thesis and providing some excellent feedback. Russ Taylor and Ue-Li Pen for useful comments, that ultimately made this thesis better.

- Although there are far too many of you to mention, in no particular order: Paul Farnes, Eleanor Farnes, Arthur Pollestad, Ivan Barberic, Thomas 'Geordie' Bennett, Michele 'Face' Veldsman, Jodie Allen, Kristina Bluwstein, Paul Joseph 'PJ' Lennon, Duncan Needham, Laura Hurley, Angela Brooks, Emma 'Aldenatronathon' Alden, Kate 'Kate Taylor' Taylor, James Watson, Wendy Hall, Sunny Thathong, Sarah Weaver, and many others – where do I even start?! Thank you!!!

- Finally, I thank my parents for supporting me emotionally, mentally, and financially through all of my studies at University. I'm sure they have thoroughly enjoyed moving my vast collections of bric-a-brac up and down from Cornwall :) I'm so thankful to you both, and promise I'll come home from Australia to see you all frequently over the next few years!

- I thank the staff of the GMRT who have made these observations possible. The GMRT is run by the National Centre for Radio Astrophysics of the Tata Institute of Fundamental Research. The National Radio Astronomy Observatory is a facility of the National Science Foundation operated under cooperative agreement by Associated Universities, Inc. The Digitized Sky Surveys were produced at the Space Telescope Science Institute under U.S. Government grant NAG W-2166. This research has made use of the NASA/IPAC Extragalactic Database (NED) which is operated by the Jet Propulsion Laboratory, California Institute of Technology. This research has made use of NASA's Astrophysics Data System. This work has been supported by the Science and Technology Facilities Council.

Jamie Farnes

CHAPTER 1

AN INTRODUCTION TO COSMIC MAGNETISM

"Find a job you love, and you will never work a day in your life."

Patricia Wilton

1.1 The Basics

It is well known that the Earth has a magnetic field. This magnetic field is vital for navigation and shields the Earth from harmful cosmic rays, possibly allowing life to have evolved here. Such magnetic fields extend far beyond Earth, and are now known to be ubiquitous throughout the Universe on all scales from asteroids to planets, stars, galaxies, and galaxy clusters. In most cases these cosmic magnetic fields are caused by the motion of enormous electrically charged clouds of gas (e.g. Vallée 1998).

As these fields are everywhere, they play a vital role in the formation and evolution of astrophysical systems. There is enormous variation in the strength of these magnetic fields, which are typically measured in gauss (1 G = 0.0001 T). A conventional fridge magnet has a field strength of ~ 50 G while the Earth has a field strength of 0.3 G. The magnetic field strength of other planets is typically ~ 0.1 μG, while the poles of the Sun have fields of 10 G and sunspots with small surface areas can have fields up to 2000 G (Vallée 1998). Our Galaxy[1] has a regular spiral-shaped field of ~ 5 μG, while other normal spiral galaxies have an average field of 10 μG (Govoni & Feretti 2004). In some galaxies, fields as high as ≈ 80 μG have been detected

[1] In order to make a clear distinction, I will use 'galaxy' to refer to any distinct system that contains millions or billions of stars. I will use 'Galaxy' and 'Galactic' to specifically refer to our own galaxy, the Milky Way.

(Wolfe et al. 2008), and irregular fields of similar strengths also exist in elliptical galaxies (Moss & Shukurov 1996). Some neutron stars have field strengths up to 10^{15} G (Palmer et al. 2005).

These magnetic fields are likely to be affecting the large-scale structure of the Universe, as fields in clusters of galaxies are of sufficient strength to play a fundamental role in the cluster gas dynamics (Carilli & Taylor 2002). It is vital to understand the role that magnetism plays in the Universe, particularly as little is known about how these pervasive magnetic fields originated or how they evolved into the fields we observe today. Enhancing this understanding is not straightforward; magnetic fields are invisible directly and we can only detect them through the indirect effects they have on other matter.

One key process that allows for the detection of cosmic magnetic fields is that of synchrotron emission. Synchrotron emission is the dominant radiating process at low radio frequencies and is caused by cosmic rays – highly relativistic charged particles, such as electrons – that spiral around and illuminate the magnetic field lines. Synchrotron radiation is particularly suitable for observations of magnetic fields as the synchrotron emissivity, ε (the radiated power per unit volume), is very sensitive to changes in the magnetic field strength, B, since $\varepsilon \propto B^{1+\alpha}$. The spectral index, α (defined such that $S \propto \nu^{-\alpha}$, where S is the flux density at frequency ν), is another useful probe of these fields and measures the way that the flux density from an astrophysical source varies depending on the observing frequency.

Synchrotron emission is intrinsically 'polarised', with the electric field of the generated electromagnetic waves being oriented in either a single direction or rotating as the wave propagates, i.e. linear or circular polarisation respectively. Circular polarisation is typically very weak at low radio frequencies, but astrophysical sources frequently remain linearly polarised down to very low frequencies (e.g. Cotton et al. 2003). As linear polarisation relates to the geometry of the magnetic field lines, the polarisation properties serve as an ideal probe of quasi-regular fields and their structure.

The observation of radio continuum emission in total intensity can provide information on the strength of a source's magnetic field. In addition, any linearly polarised emission provides the electric vector polarisation angles, from which the magnetic field's orientation and structure perpendicular to the line of sight can be deduced i.e. $B_\perp = E + 90°$. This process of measuring polarisation properties is known as 'polarimetry'.

A key issue for polarimetry of astrophysical sources is being able to remove effects that alter the measured polarisation properties of radiation. These effects broadly fall into two categories: (1) those that occur as the radiation propagates across the Universe, and (2) those due to limitations of the measuring instrument.

The former category is dominated by 'Faraday rotation' which rotates the electric vector of linearly polarised radiation as it travels through a magnetised plasma, such as the intergalactic medium, the interstellar medium of our own Galaxy, or the Earth's ionosphere. This Faraday rotation allows for the study of magnetic fields that are oriented parallel to the line of sight i.e. $B_\parallel$ – providing yet another polarimetric view of the Universe as shown in Figure 1.1.

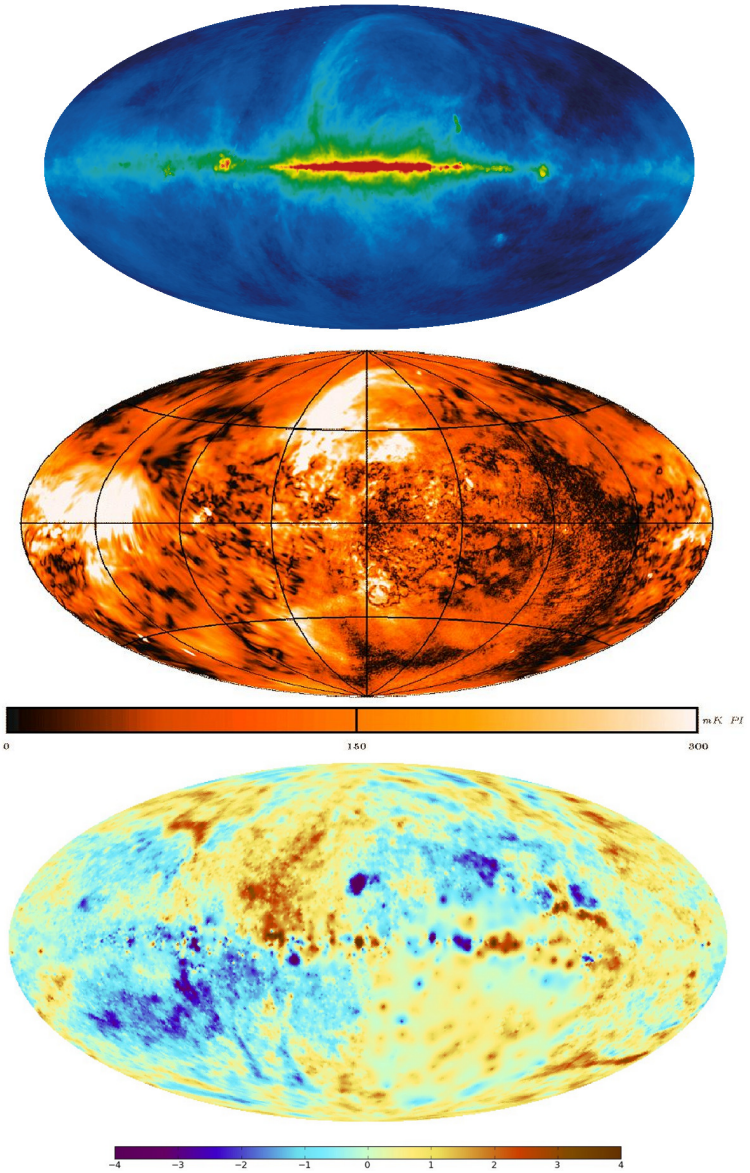

Figure 1.1: Three different all-sky views of the magnetic Universe showing: the total intensity of synchrotron emission at 408 MHz (top) (Haslam et al. 1982), the polarised intensity at 1.4 GHz (middle) (Testori et al. 2004; Wolleben et al. 2006), and the Galactic Faraday rotation (bottom) (Oppermann et al. 2011).

The effects due to limitations of the measuring instrument result from a number of systematics that begin when an incoming signal first hits the reflecting surface of a radio dish. Additional systematic changes continue to accrue while the signal is detected and processed until the final, now corrupted, measurement is recorded electronically. The process of polarisation calibration aims to remove these instrumental effects and allow for polarimetry across the entirety of an observed field of view.

The commissioning of radio telescopes for polarimetric observations requires thorough

investigation of the instrument to determine its polarisation response, and the creation of a pipeline to perform polarisation calibration. Such instrumental commissioning is essential, as circumvention of the instrumental effects is what allows for direct study of the cosmic magnetic fields in which we are interested.

1.2 Radio Interferometry

To obtain the sensitivity and resolution required to thoroughly investigate the polarisation properties of the Universe requires a radio interferometer. Although the full complexities of radio interferometry are well beyond the scope of this thesis, the basic premise is that an incoming radio signal is converted into a voltage by an antenna and then correlated with a second antenna to form a '*uv*-visibility'. This visibility is a direct sample of the spatial coherence function, which is the Fourier transform of the sky intensity – see Perley et al. (1986) for further detail.

By using an array consisting of multiple antennas and correlating together all antenna combinations, it is possible to sample the spatial coherence function well enough that a high-quality image of the radio sky can, in principle, be produced. Each pair of correlated antennas is known as a 'baseline'. If one antenna on the baseline is held in a fixed location, then changing the relative orientation of the second antenna allows for one to learn about the correlation properties of the radiation field; the necessary movement is conveniently provided by the Earth's rotation around its own axis.

Interferometers are advantageous in that they synthesise the aperture of a single dish with the equivalent size of the interferometer's longest baseline. For these reasons, radio interferometry has also been called 'Earth rotation synthesis' and 'aperture synthesis' (e.g. Kitchin 2003). Interferometry allows for the creation of images with very high angular resolution dependent on the length of the longest baseline, $L_{\rm MAX}$, and the observing wavelength, λ. The resolution is given by $\theta_{\rm HPBW} = \lambda/L_{\rm MAX}$. Radio interferometers always contain up to $n(n-1)/2$ baselines, where n is the number of antennas. As radio interferometry is dependent on the Earth's rotation, it is a prerequisite that an astronomical source remains stable over the observing period.

The field is currently entering a period of rapid expansion, with a wealth of new or upgraded facilities currently in either the development or commissioning stage. The Low Frequency Array (LOFAR), Australian Square Kilometre Array Pathfinder (ASKAP), Murchison Widefield Array (MWA), the Expanded Very Large Array (EVLA/"Karl G. Jansky Very Large Array"), and many others will all be pathfinder instruments towards building the Square Kilometre Array (SKA) – a radio telescope that when complete will be almost two orders of magnitude more sensitive than any other instrument, with a likely frequency range from 70 MHz to > 25 GHz.

Facilities mentioned or used in some form throughout this thesis include the Very Large Array (VLA) in New Mexico, USA, the Molonglo Observatory Synthesis Telescope (MOST)

near Canberra, Australia, and the Westerbork Synthesis Radio Telescope (WSRT) in the Netherlands. The thesis will focus on the use of the Giant Metrewave Radio Telescope.

1.3 The Giant Metrewave Radio Telescope

The Giant Metrewave Radio Telescope (GMRT) is a radio interferometer based near Pune, India. It is capable of observing at five frequency bands: 150 MHz, 235 MHz, 325 MHz, 610 MHz, and 1420 MHz. The array consists of 30×45 m dishes on altitude-azimuth mounts, providing a total collecting area of $\sim 48,000$ m^2. The surface of each parabolic reflector is formed by a wire mesh, with prime-focus feeds mounted onto a rotating feed turret. The polarisation basis of the feeds is circular, with the exception of the 1420 MHz feed which is linear (e.g. Chengalur et al. 1999).

The GMRT has a maximum baseline of 27 km, with the antennas arranged in a 'Y' configuration in order to maximise the *uv*-coverage (see Figure 1.2), together with a 'central square' of ~ 1 km that contains 14 antennas and provides a large number of short baselines – resulting in excellent sensitivity to large-scale radio emission.

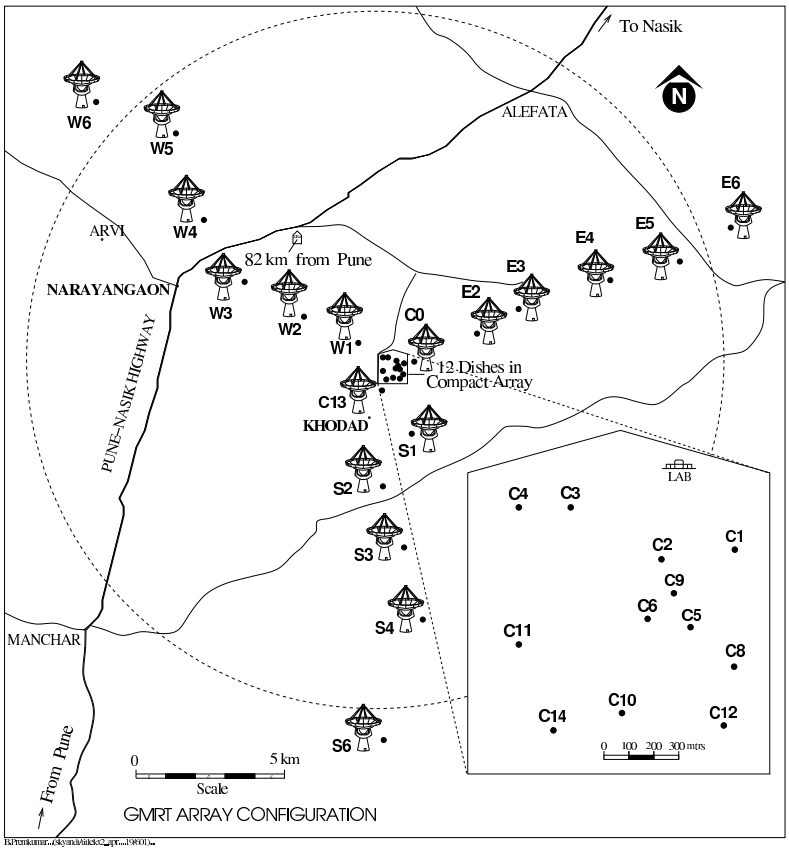

Figure 1.2: A schematic of the GMRT antenna configuration (http://gmrt.ncra.tifr.res.in).

Observations at the GMRT are taken in spectral-line mode. At low frequencies, this allows for narrow-band interference to be excised from the data baseline-by-baseline – an efficient, albeit tedious, procedure. Each observation consists of a number of scans on various calibrator sources, plus multiple scans of a desired target source. Data are typically sampled throughout this thesis with an integration time of 16.9 s.

A 'full-polar mode' became available at the GMRT in 2005 November, with the polarisation mode being enabled in the correlator software. The mode is designed to allow for polarimetric observations. In the full-polar mode, all four cross-correlation products from the circularly polarised feeds are recorded i.e. *RR*, *LL*, *RL*, and *LR*. This mode of the GMRT has not been well tested, and is currently available on an experimental basis. Commissioning and testing of the full-polar mode will allow for polarimetry with unique resolution and sensitivity, thereby providing a unique instrument with which to probe cosmic magnetism. It is therefore of paramount importance to understand the GMRT's polarisation response, and to be able to complete a high-quality polarisation calibration.

As GMRT polarimetric data are recorded in spectral-line mode, the result is a significant number of individual channels, with each channel having a relatively small bandwidth. Combined with the large field of view provided at low frequencies, the GMRT is an ideal instrument with which to conduct 'wide-field spectropolarimetry'. Spectropolarimetry allows for the unique technique of 'RM Synthesis' to be applied to the data – thereby allowing the properties of polarised sources to be investigated in Fourier space directly (see Chapter 2).

Observations at 610 MHz are a good starting point for polarimetric tests at the GMRT as there is a protected band from 608–614 MHz which attempts to keep radio interference to an absolute minimum. Furthermore, ionospheric effects and Faraday depolarisation both scale with increasing wavelength (see Section 2.6.3).

In this thesis, I use observations taken in full-polar mode to determine the GMRT's instrumental response and to design an appropriate polarisation calibration procedure. I then use the interferometer to investigate some aspects of cosmic magnetism. Some of the questions surrounding cosmic magnetism that the GMRT is well-suited to investigating are now discussed.

1.4 Evolution of Galactic Magnetic Fields

Magnetism in a galaxy's interstellar medium is dynamically important in star formation: removing angular momentum from collapsing protostellar clouds (Mellon & Li 2009), affecting the dynamics and evolution of gas clouds, and altering the energy density and distribution of cosmic rays (Wielebinski & Beck 2005). The fields observed today are thought to have originated from small initial seed fields that have been amplified via the dynamo effect.

In the dynamo effect, a conducting fluid flows past a magnetic field and induces a current which produces an additional reinforcing magnetic field. In galaxies, it has been assumed that the large scale rotation of the galactic disk amplifies the field via this mechanism. However,

assuming a galactic lifetime of 10^{10} years, a conventional mean-field dynamo model can only amplify an initial regular field by a maximum factor of 10^{17} (Arshakian et al. 2009). This may seem a significant factor, but it is actually problematic as the model then requires a rather large seed field of $\sim 10^{-16}$ μG in order for the fields to reach their current levels within the observed timescale. Similarly, this seed field may seem small, but there are no candidates for seed fields with such strength.

Current thinking is that the evolution of magnetism in galaxies has therefore taken place in multiple stages and must include other field-generating mechanisms in addition to the standard dynamo model (e.g. Beck 2006). For example, interstellar turbulence-based dynamos allow for seed fields on the order of $\sim 10^{-20}$ μG to be amplified to their current levels within the observed timescales (Arshakian et al. 2009). The origin of the seed fields themselves is also still a cause of great debate, with possibilities including the 'Biermann battery effect', primordial fields, AGN jets, and early supernova remnants (e.g. Kulsrud & Zweibel 2008; Rees 2006). The strongest seed magnetic fields are believed to have been generated in protogalaxies by the Biermann battery effect, with a strength of $\sim 10^{-18}$ μG (e.g. Arshakian et al. 2009).

As already said, the origin and evolution of cosmic magnetism is one of the major challenges to be addressed by the next generation of radio telescopes, particularly the SKA. The most important technique will be the direct observation of polarised emission, particularly from galaxies, which will be used to measure the Faraday rotation towards background sources (e.g. Gaensler et al. 2004). At the flux levels accessible to the SKA (≈ 100 nJy for a 1 h observation with $A/T_{\rm sys} = 20000$ m^2 K^{-1} at 1.4 GHz and a 350 MHz bandwidth), the polarised sources detected will be dominated by star forming galaxies. The background sources, which will form an essential 'grid' of Faraday rotation across the sky, will therefore be dominated by late-type galaxies. The observed polarisation fraction, Π, of late-types observed with the SKA will be strongly dependent on Faraday depolarisation (see Section 2.6.3). Understanding the effects of depolarisation as a function of frequency is therefore crucial if projects such as those to be undertaken by the SKA are to succeed.

An excellent environment in which to test the link between magnetism and galaxy evolution is in galaxy groups. Galaxy groups are some of the smallest and most dense associations of galaxies. These groups are gravitationally bound structures in various stages of dynamical evolution, from young and spiral-dominated to almost completely merged. They are useful for investigating the impact of galaxy interactions on the evolution of the intragroup medium, and it is known that mergers and less powerful interactions can be a significant contributor to heating of this medium via the triggering of active galactic nuclei and supernova explosions (e.g. Pompei et al. 2007).

1.5 Magnetic Fields in Supernova Remnants

As discussed in Section 1.4, supernovae play an important role in the evolution of cosmic magnetism – possibly providing the initial seed fields now detected in galaxies. The 'remnants' of material that are left over from the explosions compress magnetic fields that are 'frozen in' to the plasma and also develop magnetohydrodynamic (MHD) turbulence that gives rise to 'Rayleigh–Taylor instabilities'. These mechanisms in supernova remnants are also responsible for the amplification of magnetic fields.

Supernova remnants not only amplify magnetic fields, but also redistribute matter within the interstellar medium. The violent shockwave from these explosions can compress interstellar gas, leading to the formation of the next generation of stars. These feedback mechanisms make supernovae crucial in understanding the evolution of cosmic magnetism. Such supernova events are expected to occur in the Galaxy with a rate of two or three core-collapse supernovae per century (e.g. Diehl et al. 2006). This makes each individual remnant an important experimental laboratory for our understanding of shock physics and astrophysical magnetic field evolution.

Observations of the polarisation in shell-type supernova remnants can provide information on the physical processes driving the emission of synchrotron radiation. As this polarisation is a direct tracer of magnetic field structure, its detection can allow for the investigation of the order and orientation of magnetic fields within a remnant. This is particularly important in shocked regions – as the shocks can compress and order magnetic fields. Polarisation observations are also useful for understanding the nature of MHD turbulence in remnants. This is of particular interest in young remnants where the ordered component of the magnetic field has consistently been shown to be radial as in Cas A, Kepler, and Tycho (Milne 1987). Although Rayleigh–Taylor instabilities are frequently employed to explain this phenomenon, the mechanism that generates these radial fields is still poorly understood. The radial fields are proposed to be the consequence of an early Rayleigh–Taylor unstable evolutionary phase accompanying the onset of ejecta deceleration (Gull 1973a, 1975).

In addition to polarimetry of supernova remnants, there are also other techniques to investigate the magnetic field structure. The spectral index of these remnants is typically steep ($0.4 \leq \alpha \leq 0.8$). However, the spectral index tends to be flatter in older remnants, and also tends to vary spatially across the angular extent of a remnant. Consequently, measurement of spatial spectral variations at radio wavelengths allows the mechanisms responsible for electron acceleration to be studied, providing information about the local dynamics in remnants. Interpretation of such measurements is complicated by the typical use of different telescopes for the different observing frequencies. This results in the sampling of different spatial frequencies and can produce corresponding artefacts in any derived spectral index images (Bhatnagar 2001). Missing large scale emission due to a lack of short interferometer spacings also causes substantial differences in the base-levels of each image.

These errors can however be overcome using two key techniques: T–T plots (Turtle et al.

1962; Anderson & Rudnick 1993), and Spectral Tomography (Katz-Stone et al. 2000). T–T plots require radio surface brightness maps of a source at two different frequencies. The source can be split into regions of limited extent, and from each region in the source the surface brightness at one frequency can be plotted against that at the other frequency – from which a gradient can be determined. The magnitude of the gradient is directly related to the spectral index and can, in principle, be determined independently of the base-level variations. By splitting up the remnant into a number of regions an accurate determination of the spectral index can be made, as the variations in the different large scale base-levels will be substantially smaller than the range of emission from the remnant (e.g. Green 1990). While spectral variations within each region will tend to be smeared out, the process allows for the identification of larger scale variations across the remnant.

As the emission from remnants is generally optically thin, it is possible to confuse regions with differing spectral indices along the line of sight. The method of Spectral Tomography assists the search for spectral variations by producing a gallery of images, in which the high frequency image is scaled by a trial spectral index and then subtracted from the low frequency image. Regions with a spectral index equal to the trial value will disappear from the resulting gallery image (Katz-Stone et al. 2000). In principle, this allows for the identification of overlapping regions within the remnant – although the interpretation of such a tomography gallery is complicated by a number of factors. The technique is especially sensitive to large scale base-level differences. While it is possible to correct for the effects of a large scale DC component on the images, a gradient across the maps or small scale variations can still remain. The gallery of tomography images therefore need to be interpreted with particular care.

These spatial spectral index variations are a useful tracer of the shock wave, providing information about the energy of the electron populations and the local dynamics. More importantly, the ambient magnetic field, which was mostly undisturbed prior to the explosion, is imprinted onto the spectral index variations. The spatial variation is therefore a tracer of the original magnetic field, which can be inferred given a reasonable model of the underlying shock physics. This is not however clear cut, as current knowledge of shock physics is not well equipped to deal with the extreme conditions that exist in these exotic phenomena.

CHAPTER 2

THE LANGUAGE OF POLARIMETRY

> "There is too much at stake for us to surrender to the politics of polarisation."
>
> *Brad Henry*

In Chapter 1, I introduced the broad concepts of polarimetry and radio interferometry, and some of their many astronomical applications within the field of cosmic magnetism. I now discuss the technical jargon and mathematical concepts that underpin these polarimetric observations when using a radio interferometer.

As previously discussed, polarised radio emission is fundamentally related to the presence of magnetic fields. Observations of polarisation are arguably the best way of studying quasi-regular fields and their structure. While thinking of polarisation states in terms of electric, magnetic, and Poynting vectors is useful, the properties of an electromagnetic wave can also be described using considerably more effective forms of notation. In this chapter, I introduce this notation and then use it to explain the theory of polarisation calibration for a radio interferometer. I also describe the various limiting effects that must be considered during polarimetric observations, and explain the theory behind the tool of Rotation Measure Synthesis – which is revolutionising modern polarimetry.

2.1 Stokes Parameters

The polarisation state of a quasi-monochromatic electromagnetic wave is fully and concisely described by the four Stokes parameters. Consider the electric field of an electromagnetic

wave that is propagating in the z-direction. The wave can be decomposed into two orthogonal components that are mathematically defined by

$$E_x(t) = e_x(t)\cos[\omega t + \delta_x]\,, \tag{2.1}$$

$$E_y(t) = e_y(t)\cos[\omega t + \delta_y]\,, \tag{2.2}$$

where E_x and E_y are the amplitudes of the components of the electric field orthogonal to the Poynting vector, ω is the angular frequency, t is a measure of time, and $e_i(t)$ and δ_i are the amplitude and phase respectively for E_i. The Stokes parameters are then defined by

$$I = \langle e_x^2(t)\rangle + \langle e_y^2(t)\rangle\,, \tag{2.3}$$

$$Q = \langle e_x^2(t)\rangle - \langle e_y^2(t)\rangle\,, \tag{2.4}$$

$$U = 2\langle e_x(t)e_y(t)\cos[\delta_x - \delta_y]\rangle\,, \tag{2.5}$$

$$V = 2\langle e_x(t)e_y(t)\sin[\delta_x - \delta_y]\rangle\,. \tag{2.6}$$

The Stokes parameter I is a measure of the total power in the wave, and V represents the circularly polarised component. Q and U represent the linearly polarised component, with Q describing the polarisation state parallel to the x/y axes and U describing the polarisation state at 45° to these axes. All four parameters are scaled to be measured in jansky (1 Jy = 10^{-26} W m^{-2} Hz^{-1}).

Monochromatic waves are always fully polarised, but physically realistic waves have a finite bandwidth – only a certain fraction of these quasi-monochromatic waves are polarised. This fractional polarisation is given by

$$\Pi_{\mathrm{T}} = \frac{\sqrt{Q^2 + U^2 + V^2}}{I}\,, \tag{2.7}$$

$$\Pi_{\mathrm{L}} = \frac{\sqrt{Q^2 + U^2}}{I}\,, \tag{2.8}$$

$$\Pi_{\mathrm{C}} = \frac{V}{I}\,, \tag{2.9}$$

where Π_{T}, Π_{L}, and Π_{C} are the total, linear, and circular fractional polarisations respectively. Due to the low fraction of circular polarisation typically detected in astronomical sources, it is common practice to assume that $V = 0$. Referring to the fractional polarisation then simply relates to the linear fraction, which is commonly denoted Π. The linear polarisation is also often measured in terms of the 'polarised intensity' which is given by

$$P = \sqrt{Q^2 + U^2}\,, \tag{2.10}$$

with the electric vector polarisation angle (EVPA) of the plane of polarisation, Φ_{EVPA}, being given by

$$\Phi_{\mathrm{EVPA}} = \frac{1}{2}\tan^{-1}\left(\frac{U}{Q}\right). \tag{2.11}$$

In the case of radio interferometry, I is generally positive with the notable exceptions of sidelobes, noise, and observations of the Sunyaev–Zel'dovich effect. Q, U, and V can be either positive or negative. The Stokes parameters are useful as they allow easy retrieval of the total intensity, fractional linear polarisation, fractional circular polarisation, and the EVPA of polarisation. If we want to study an astronomical source, all we need to do is create images of each of these Stokes parameters.

2.2 The Need for Polarisation Calibration

As briefly discussed in section 1.2, the signals from an antenna's feeds are combined by a correlator to form a *uv*–visibility. For an interferometer that has feeds with a circular polarisation basis (i.e. feeds that are sensitive to right and left circular polarisations, R and L), the correlator outputs the four cross-correlation products: RR, LL, RL, and LR. For an ideal, calibrated interferometer with circular feeds, the cross-correlation products are directly related to the Stokes parameters via

$$\begin{pmatrix} RR \\ RL \\ LR \\ LL \end{pmatrix} = \begin{pmatrix} 1 & 0 & 0 & 1 \\ 0 & 1 & i & 0 \\ 0 & 1 & -i & 0 \\ 1 & 0 & 0 & -1 \end{pmatrix} \begin{pmatrix} I \\ Q \\ U \\ V \end{pmatrix} = \begin{pmatrix} I+V \\ Q+iU \\ Q-iU \\ I-V \end{pmatrix} . \tag{2.12}$$

Note that $RL = LR^*$, where * is the complex conjugate, and for most astronomical sources $RR = LL = I$ since typically $V = 0$. However, there is a significant caveat in that equation 2.12 only holds true for idealised antennas with a perfect polarisation response. Antenna feeds are never perfectly circularly polarised. This leads to detectors sensitive to R also detecting a small amount of L and vice-versa, leading to an effect known as 'polarisation leakage'. This leakage, or 'instrumental polarisation', results in impure cross-correlation products, and ultimately causes an unpolarised astronomical source to appear polarised.

Additionally, the antennas in an array such as the GMRT use an altitude–azimuth (alt-az) mount. These are sometimes referred to as azimuth–elevation mounts. These mounts cause the cardinal points of a source (N, E, S, W) to constantly rotate with respect to the feeds over the duration of an observation. The amount of this rotation, as measured from N through E, is known as the parallactic angle, χ. Due to the polarisation leakage and parallactic angle rotation, the EVPA (see equation 2.11) of any polarised emission is corrupted. Ultimately, these effects conspire such that equation 2.12 is no longer applicable. The process of polarisation calibration attempts to remove these instrumental effects from observational data so that equation 2.12 holds true.

2.3 On-axis Theory

This section is concerned with the theory governing the polarisation calibration of a radio interferometer at the phase-tracking centre, i.e. the centre of the field of view. For now, I only consider the effects of instrumental polarisation along the optical axis of the antennas. I shall call the calibration of this instrumental response the 'on-axis' corrections.

There are several models that can describe the on-axis polarisation response of an interferometer. For the sake of clarity, I shall avoid general formalisms and only concentrate on models applicable to radio telescopes with alt-az mounted circular-basis feeds.

For a radio interferometer, there are two models that suitably describe the response of antenna feeds to polarised radiation (e.g. Cotton 1999). These are the:

1. Leakage Term Model – which assumes the feed is perfectly coupled to the nominal polarisation, with the addition of a complex factor times the orthogonal polarisation. The feed can then be characterised in terms of 'leakages' or 'D-terms'.
2. Orientation/Ellipticity Model – which characterises the feed in terms of the orientation and ellipticity of the polarisation that it would transmit if the antenna were to be used as a transmitter rather than a receiver. Each feed is then parameterised in terms of the orientation and ellipticity of the polarisation to which it is sensitive.

For antennas with nearly perfect feeds observing an unresolved, weakly polarised source at the phase centre, these two models can be shown to be equivalent (Roberts et al. 1994). However, these simplifications are seldom true. Some antennas may have substantial instrumental polarisation – meaning that the assumption of nearly perfect feeds is not appropriate. In chapter 3 I discuss the observation of calibrator sources for the purpose of polarisation calibration. At low radio frequencies the polarisation properties of these calibrators are rarely known a priori. Many of these sources are also strongly polarised. The theory behind both models is now detailed.

2.3.1 Leakage Term Model

Following Hamaker et al. (1996), the response of an interferometer can be described by antenna-based response matrices, known as Jones matrices. The response of antenna j with orthogonal circularly polarised feeds (R and L) can be expressed in terms of a Jones matrix that operates on the column vector $(R, L)^{\mathrm{T}}$. Determination of the Jones matrix is intrinsically non-commutative. The multiplication order is the inverted sequence of effects that take place as the signal propagates from the source to the antenna. The Jones matrix is then given by

$$J_j = G_j D_j P_j \,. \tag{2.13}$$

G_j is the gain such that

$$G_j = \begin{pmatrix} g_{jR} & 0 \\ 0 & g_{jL} \end{pmatrix} , \tag{2.14}$$

where g_{jR}, g_{jL} are the complex gains for the two orthogonally polarised signals. This matrix represents the effects of the atmosphere and the electronics.

The D-term is given by

$$D_j = \begin{pmatrix} 1 & d_{jR} \\ -d_{jL} & 1 \end{pmatrix} \tag{2.15}$$

which models the deviations of the feed polarisation response from an idealised system. The complex leakage terms d_{jR}, d_{jL} represent the fraction of the orthogonally polarised signal 'leaking' into a given feed.

The additional P-term

$$P_j = \begin{pmatrix} e^{-i\chi} & 0 \\ 0 & e^{i\chi} \end{pmatrix} \tag{2.16}$$

describes the effects of the rotation of an alt-az mounted antenna as seen by a tracked source, where $i = \sqrt{-1}$. The parallactic angle, χ, is depicted in Figure 2.1 and is defined as the angle between the source's hour circle and the great circle passing through both the source and the zenith, as seen by an antenna. It is given by

$$\chi = \tan^{-1}\left(\frac{\cos(L)\sin(h)}{\sin(L)\cos(\delta) - \cos(L)\sin(\delta)\cos(h)}\right), \tag{2.17}$$

where L is the antenna latitude, δ is the source declination, and h is the source hour angle.

For an interferometer, there is not a direct concern with the antenna-based response described by J_j, but rather with the visibilities obtained on a given baseline j–k. These measured visibilities can be described by a Mueller matrix, ν, which gives the interferometer response to polarised radiation

$$\nu = \begin{pmatrix} \nu_{RR} \\ \nu_{RL} \\ \nu_{LR} \\ \nu_{LL} \end{pmatrix}. \tag{2.18}$$

This Mueller matrix may be expressed in terms of the outer product (also known as the tensor or Kronecker product) of the individual antennas' Jones matrices

$$\nu = \left(J_j \otimes J_k^*\right) S^{\circledcirc} s, \tag{2.19}$$

where $S^{\circledcirc}$ is the co-ordinate transformation for circular feeds given by

$$S^{\circledcirc} = \frac{1}{2}\begin{pmatrix} 1 & 0 & 0 & 1 \\ 0 & 1 & i & 0 \\ 0 & 1 & -i & 0 \\ 1 & 0 & 0 & -1 \end{pmatrix}, \tag{2.20}$$

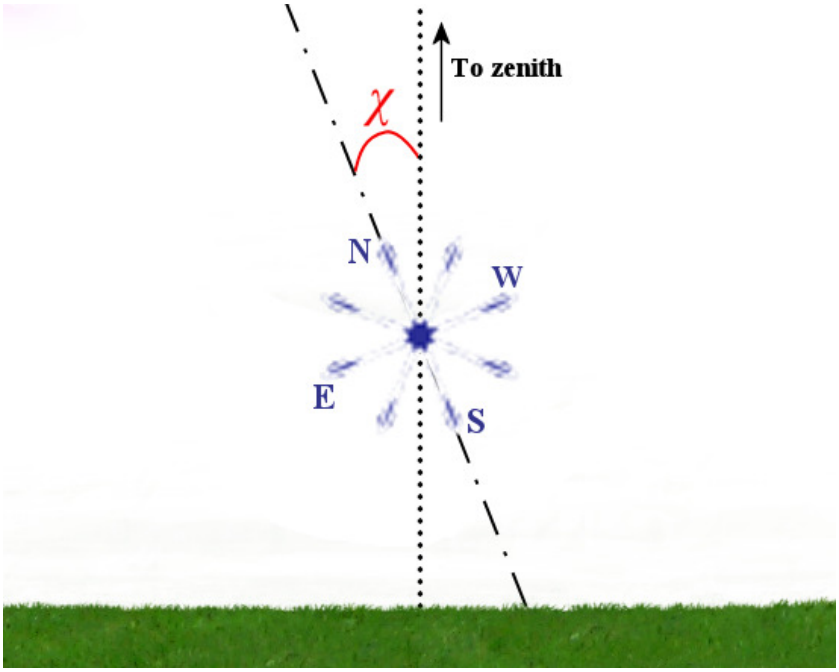

Figure 2.1: A cartoon depicting the parallactic angle, χ, as seen by an observer looking South. The source and its cardinal points are shown in dark blue. The hour circle of the source (dot-dash line) and the great circle passing through source and zenith (dotted line) are shown. χ is measured N through E from the source's hour circle. The source shown has $\chi \approx -22.5°$.

and s is the matrix of Stokes parameters

$$s = \begin{pmatrix} I \\ Q \\ U \\ V \end{pmatrix} . \tag{2.21}$$

The Stokes parameters are directly related to the observed visibilities via the relation (RR, RL, LR, LL)$^{\mathrm{T}} = 2S^{\circledcirc}s$ (as in equation 2.12), where RR, RL, LR, and LL are the amplitude and phase calibrated responses of an interferometer with perfect feeds (see equation 2.12).

For a linear approximation, it is assumed the leakage terms are small and that the source is weakly polarised, allowing us to neglect the second order terms d^2, dQ, dU, and dV. Furthermore, by assuming that $V = 0$, a greatly simplified set of equations can be obtained when expanding out equation 2.19. This yields

$$v_{RR} = \frac{1}{2} g_{jR} g^*_{kR} I \,, \tag{2.22}$$

$$v_{RL} = \frac{1}{2} g_{jR} g^*_{kL} \left[(d_{jR} - d^*_{kL}) I + e^{-2i\chi} (Q + iU) \right] , \tag{2.23}$$

$$v_{LR} = \frac{1}{2} g_{jL} g^*_{kR} \left[(d_{kR} - d^*_{jL}) I + e^{2i\chi} (Q - iU) \right] , \tag{2.24}$$

$$\nu_{LL} = \frac{1}{2} g_{jL} g^*_{kL} I \,. \tag{2.25}$$

The solution of these simultaneous equations allows for the calculation of the complex D-terms. The true visibility values, free from the effects of instrumental polarisation, can be retrieved from the data by applying the D-terms.

2.3.2 Orientation/Ellipticity Model

Following Cotton (1993), the response of a feed to an electric field can be parameterised by

$$\begin{aligned} G = \widehat{e_x} \left[\cos(\theta)\cos(\Phi+\chi) - i\sin(\theta)\sin(\Phi+\chi)\right] \\ +\widehat{e_y} \left[\cos(\theta)\sin(\Phi+\chi) + i\sin(\theta)\cos(\Phi+\chi)\right] \end{aligned} \,, \tag{2.26}$$

where $\widehat{e_x}$, $\widehat{e_y}$ are orthogonal unit vectors, θ is the feed ellipticity, and Φ is the orientation of the polarisation ellipse.

After amplitude and phase calibration, the response of a given baseline can be written as

$$\begin{aligned} F^{\rm obs}_{jk} &= g_j g^*_k \Big\{ RR \left[(\cos\theta_j + \sin\theta_j) e^{-i(\Phi_j+\chi)}\right] \times \left[(\cos\theta_k + \sin\theta_k) e^{i(\Phi_k+\chi)}\right] \\ &+ RL \left[(\cos\theta_j + \sin\theta_j) e^{-i(\Phi_j+\chi)}\right] \times \left[(\cos\theta_k - \sin\theta_k) e^{-i(\Phi_k+\chi)}\right] \\ &+ LR \left[(\cos\theta_j - \sin\theta_j) e^{i(\Phi_j+\chi)}\right] \times \left[(\cos\theta_k + \sin\theta_k) e^{i(\Phi_k+\chi)}\right] \\ &+ LL \left[(\cos\theta_j - \sin\theta_j) e^{i(\Phi_j+\chi)}\right] \times \left[(\cos\theta_k - \sin\theta_k) e^{-i(\Phi_k+\chi)}\right] \Big\} , \end{aligned} \tag{2.27}$$

where the effects of phase calibration are given by

$$g_R = \exp[-i(-\chi - \Phi_R + \Phi_{R(\rm ref)})] \,, \tag{2.28}$$

$$g_L = \exp[i(-\chi - \Phi_L + \Phi_{L(\rm ref)} + \Phi_{R-L})] \,, \tag{2.29}$$

such that $\Phi_{R(\rm ref)}$ and $\Phi_{L(\rm ref)}$ are the orientations of the R and L circular feeds of the reference antenna, and Φ_{R-L} is the right–left phase difference. Equation 2.27 can then be solved for each baseline, to determine θ and Φ. The calculated orientations and ellipticities can be applied to each antenna by expressing equation 2.27 in matrix form so that

$$F^{\rm obs}_{jk} = M_{jk} F^{\rm true}_{jk} \,, \tag{2.30}$$

where $F^{\rm obs}_{jk}$ is the matrix of observed correlations, $F^{\rm true}_{jk}$ is the matrix of true values (RR, LL, RL, LR), and M_{jk} is given by

$$M_{jk} = \begin{pmatrix} \widehat{G}_{RR} K^*_{Rj} K_{Rk} & \widehat{G}_{RR} D_{Rj} E_{Rj} D_{Rk} E^*_{Rk} & \widehat{G}_{RR} K^*_{Rj} D_{Rk} E^*_{Rk} & \widehat{G}_{RR} D_{Rj} E_{Rj} K_{Rk} \\ \widehat{G}_{LL} K^*_{Lj} K_{Lk} & \widehat{G}_{LL} D_{Lj} E_{Lj} D_{Lk} E^*_{Lk} & \widehat{G}_{LL} K^*_{Lj} D_{Lk} E^*_{Lk} & \widehat{G}_{LL} D_{Lj} E_{Lj} K_{Lk} \\ \widehat{G}_{RL} K^*_{Rj} K_{Lk} & \widehat{G}_{RL} D_{Rj} E_{Rj} D_{Lk} E^*_{Lk} & \widehat{G}_{RL} K^*_{Rj} D_{Lk} E^*_{Lk} & \widehat{G}_{RL} D_{Rj} E_{Rj} K_{Lk} \\ \widehat{G}_{LR} K^*_{Lj} K_{Rk} & \widehat{G}_{LR} D_{Lj} E_{Lj} D_{Rk} E^*_{Rk} & \widehat{G}_{LR} K^*_{Lj} D_{Rk} E^*_{Rk} & \widehat{G}_{LR} D_{Lj} E_{Lj} K_{Rk} \end{pmatrix} , \tag{2.31}$$

such that $K_{\beta k} = S_{\beta k} E_{\beta k}$, $K^*_{\beta k} = S_{\beta k} E^*_{\beta k}$, $\widehat{G}_{\alpha\beta} = g_{\alpha j} g^*_{\beta k}$, $S_{\beta k} = \cos\theta_{\beta k} + \sin\theta_{\beta k}$, $D_{\beta k} = \cos\theta_{\beta k} - \sin\theta_{\beta k}$, and $E_{\beta k} = e^{i(\chi_{\beta k} + \Phi_k)}$, where indices α and β represent R or L respectively.

Using this relationship and inverting equation 2.30 allows for the calculated corrections to be applied and for the effects of instrumental polarisation to be removed – thereby retrieving the true visibility values.

2.3.3 Practicalities of Polarisation Calibration

The equations in sections 2.3.1 and 2.3.2 show that it is, in principle, possible to calculate the instrumental polarisation by observing an unresolved source at the phase centre over a range of parallactic angles. In each of the two models, either the source or instrumental polarisation varies as a function of χ while the other remains constant. This allows for both contributions to be separated, and the effects of instrumental polarisation to be removed. Under most circumstances, a large range of χ is required in order to separate the instrumental and source response.

The linearised model provides a set of equations that can be solved easily, but only if various assumptions are valid, i.e. the calibrator is weakly polarised, the instrumental polarisation is small, and the circular polarisation is negligible. Alternatively, the orientation/ellipticity model provides a complete formulation of the feeds with no limiting assumptions. However, the resulting equations have a non-linear dependence on instrumental properties – requiring solutions to be iteratively calculated with increased computational expense.

Roberts et al. (1994) point out that for the special case of an unpolarised source ($Q = U = 0$), the orientation/ellipticity model offers no theoretical advantage over the leakage term model – even for antennas with large instrumental polarisation. Therefore as an alternative to separating instrumental and source contributions via parallactic angle variation, a short observation of a calibrator with no intrinsic polarisation can be used. This allows instrumental polarisation to be calculated for snapshot observations, albeit with a loss of accuracy due to the inherent decrease in signal-to-noise for a short scan. As a final caveat, this method also requires that the source is assumed to be completely unpolarised.

2.4 Electric Vector Polarisation Angle Calibration

Following instrumental polarisation calibration as explained in Section 2.3, the fractional polarisation of an observed astronomical source should, in principle, be accurately determined. However, while solving for the instrumental polarisation, the absolute value of the phase offset between R and L was left as an unconstrained degree of freedom. This $R - L$ phase difference has an effect equivalent to a change of parallactic angle, and equations 2.22–2.25 show that this is analogous to a rotation of $Q \pm iU$ in the complex plane. This results in the EVPA being arbitrarily offset from its nominally true value (see equation 2.11).

This offset is typically corrected by observing a highly polarised source with stable polarisation properties and a known polarisation angle. The calibrator sources 3C286 and 3C138 are generally used for this purpose at the VLA, with various assumptions made

about their 'known' intrinsic polarisation. By assuming that the $R - L$ phase difference is instrumentally stable during an observation, these sources allow EVPA calibration to be carried out. The known polarisation properties of these sources also allow for checks on the quality of instrumental polarisation calibration via measurement of their fractional polarisation. Note that there are problems with the assumptions made about the 'known' polarisation of common EVPA calibrators. I provide a more detailed explanation of these problems, and develop a new calibration technique in Chapter 6.

2.5 Faraday Rotation and the Ionosphere

A key issue for polarimetry of astrophysical sources is removal of effects that alter the polarisation properties of the radiation as it propagates across the Universe. One such effect, Faraday rotation, occurs as linearly polarised radiation travelling through a magnetised plasma undergoes a phenomenon similar to birefringence. The linear polarisation can be considered as two counter-rotating circularly polarised components which experience different refractive indices. Upon exiting the plasma, Faraday rotation will have caused the electric vector of the incoming linearly polarised wave to rotate.

Let us consider a simple model with just one source along a line of sight. This source has no internal Faraday rotation, and only a single slab of plasma exists between us and the source. In this case, the EVPA will be rotated by an amount proportional to the squared wavelength of the radiation as described by

$$\Phi_{\mathrm{EVPA}} = \Phi_0 + \mathrm{RM}\,\lambda^2\,, \tag{2.32}$$

where Φ_{EVPA} is the observed EVPA, Φ_0 is the intrinsic EVPA at the source, and λ is the wavelength of the radiation. The factor of proportionality is known as the rotation measure (RM) and is defined by

$$\mathrm{RM} = \frac{e^3}{2\pi m_{\mathrm{e}}^2 c^4} \int_0^d n_{\mathrm{e}} B_{\parallel}\, ds\,, \tag{2.33}$$

where n_{e} is generally the electron number density of the plasma and $B_{\parallel}$ is the strength of the component of the magnetic field parallel to the line of sight. The constants e, m_{e}, and c are the electronic charge, the mass of the electron, and the speed of electromagnetic radiation in a vacuum respectively. The integral from 0 to d represents the distance along the line of sight between the observer and the source. Of course, the EVPA and λ^2 can have a far more complicated relationship than this simplified model suggests – for details of this situation, see Section 2.8.

Faraday rotation is a hindrance to polarimetric observations as it limits the usable bandwidth (see Section 2.6.2) and corrupts the observed EVPA. Fortunately, attempts can be made to correct the effect by obtaining measurements at two or more radio wavelengths, allowing Φ_0 to be ascertained (e.g. Krause 2003). Measurements of the intrinsic EVPA can then provide information on the magnetic field structure in an astronomical source.

The measurement of RM is also physically useful. As equation 2.33 shows, the RM allows us to probe magnetic fields oriented along the line of sight. The interpretation of RM measurements is complicated as Faraday rotation occurs both within the source we wish to study and in the intervening magnetised plasmas between us and the source. For example, Faraday rotation from the ISM of our own Galaxy (the 'Galactic foreground') corrupts the measurement of weak magnetic fields in extragalactic sources. In addition, Faraday rotation in the Earth's ionosphere further modifies polarised signals and inhibits polarisation calibration.

Fortunately, the advent of modern correlators and new techniques such as RM Synthesis (see Section 2.8) allows for the separation of these polarised components which exist at different 'Faraday depths'. These new polarimetric tools allow investigation of the magnetic field structure along lines of sight towards large numbers of extragalactic sources. As a result, our understanding of cosmic magnetism is making significant advances.

2.5.1 Ionospheric Faraday Rotation

Ionospheric effects are always present at low radio frequencies, even during periods of solar minimum. The effects of ionospheric Faraday rotation result in the modification of equation 2.13 into

$$J_j = G_j D_j P_j F_j \,, \tag{2.34}$$

such that

$$F_j = \begin{pmatrix} e^{i\chi_{\rm ion}} & 0 \\ 0 & e^{-i\chi_{\rm ion}} \end{pmatrix} . \tag{2.35}$$

Note that $F_j \equiv P_j^*$ (see equation 2.16). Consequently, ionospheric Faraday rotation by an angle $\chi_{\rm ion}$ is analytically identical to rotating the antenna's feed by $-\chi$ (Hamaker et al. 1996). The effect of ionospheric Faraday rotation therefore manifests itself as a change in the $R-L$ phase difference, causing an apparent rotation of a source's EVPA.

As with conventional Faraday rotation, these effects depend on the ionosphere's magnetic field strength and each antenna's line of sight through the ionospheric plasma. The magnetic field of the ionosphere is only weakly variable over the duration of a typical astronomical observation (Cotton 1993), while the total electron content (TEC) can change rapidly. These changes in the TEC cause rapidly varying fluctuations in the $R-L$ phase difference: both perturbing a source's EVPA and the instrumental polarisation solutions obtained during calibration.

Faraday rotation in the ionosphere can be corrected using global maps of the TEC derived from Global Positioning Systems (GPS), as shown in Figure 2.2. Assuming a simple model of the ionosphere, the maps can be used to determine the amount of ionospheric Faraday rotation affecting an observation (see Section 3.4.4). This is an important first-order correction in order to achieve a high-quality polarisation calibration.

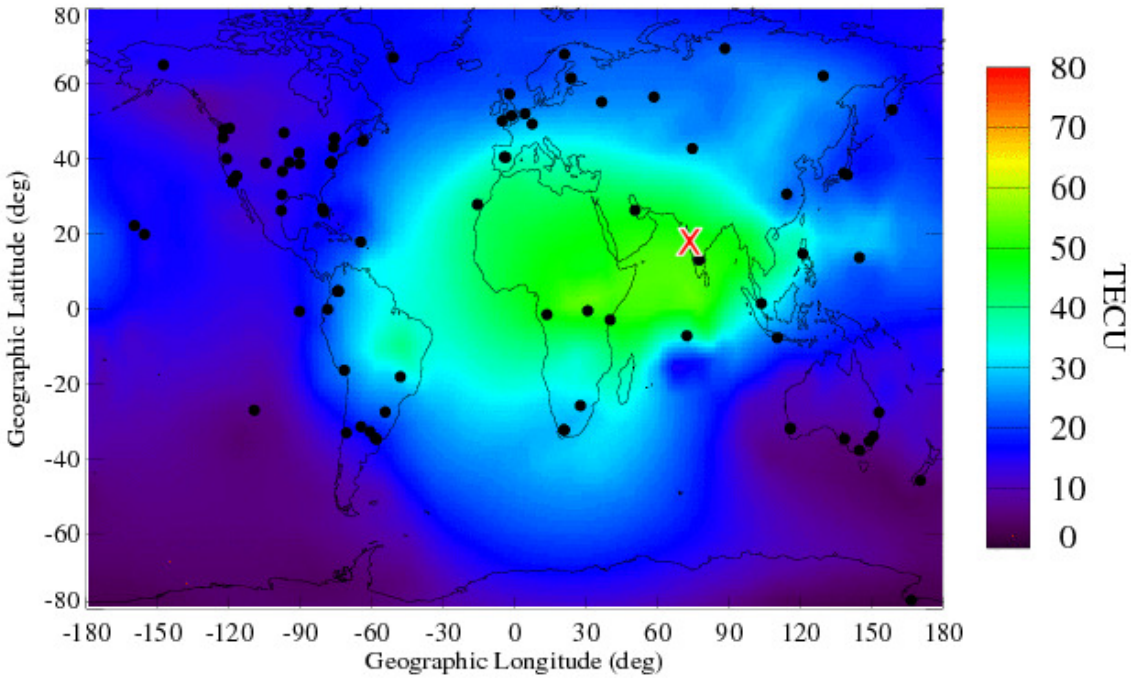

Figure 2.2: A global map of the ionospheric TEC on 2012 May 20th at 12:20 UT, as obtained from NASA's Jet Propulsion Laboratory (http://iono.jpl.nasa.gov). The position of the GPS receivers are shown by black dots, and the location of the GMRT is shown by a red cross. Note the proximity of the Hyderabad and Bangalore receivers to the GMRT. These receivers are visible as two closely spaced black dots just to the SE of the GMRT.

2.6 Depolarisation Effects

Although astronomical sources are intrinsically linearly polarised, there are a number of instrumental and physical effects that can result in the measured polarisation being less than anticipated – a phenomenon known as 'depolarisation'. There are three such effects that are important in radio astronomy: instrumental beam and bandwidth depolarisation, and the astronomical effect of Faraday depolarisation.

2.6.1 Beam Depolarisation

All interferometric observations have an intrinsic angular resolution that is determined by the size of the synthesised beam, or analogously by the length of the longest baseline. Consider an extended source which is not uniformly polarised. If the radio telescope has a resolution that is lower (i.e. a synthesised beam size that is larger) than the angular scale over which the source polarisation is coherent, then a given synthesised beam contains regions with different EVPAs. The synthesised beam therefore 'smoothes' out the polarisation of the source, and the measured polarisation will be less than the true source polarisation. This 'beam depolarisation' cannot

be corrected for, and the only way to obtain the true source polarisation is to observe with a telescope that has better angular resolution (e.g. Chengalur et al. 1999).

2.6.2 Bandwidth Depolarisation

Most modern radio observations are recorded using a correlator that has a finite number of spectral channels across an observing bandwidth. This allows for the RM of a source to be easily determined, as variations in λ^2 are typically well-sampled by these correlators (see Section 2.5). Each of these spectral channels has a finite bandwidth, and data within the channel bandwidth has been averaged together. The EVPA may rotate within the channel bandwidth to the extent that the different EVPA contributions begin to cancel out – resulting in bandwidth depolarisation. Of course, this EVPA rotation is caused by the RM. Consequently, any observation is only sensitive up to a certain maximum value of RM before bandwidth depolarisation becomes significant. The amount of this depolarisation is given by a factor

$$D_{\rm pol} = \left| \frac{\sin \Delta\Phi_{\rm EVPA}}{\Delta\Phi_{\rm EVPA}} \right| , \tag{2.36}$$

where $|\Delta\Phi_{\rm EVPA}|$ is the change in the EVPA within the spectral bandwidth which is given by

$$|\Delta\Phi_{\rm EVPA}| \approx 2{\rm RM}\,\lambda^2 \frac{\Delta\nu}{\nu} , \tag{2.37}$$

where ν is the observing frequency and $\Delta\nu$ is the bandwidth of a single spectral channel (e.g. Gardner & Whiteoak 1966).

I take bandwidth depolarisation to be significant when the EVPA rotates by ~ 1 rad in a single spectral channel, as this approximately equates to a depolarisation factor of 0.85. The effects of bandwidth depolarisation therefore become significant for,

$$|RM_{\rm depol}| \geq \frac{\nu^3}{2c^2\Delta\nu} . \tag{2.38}$$

2.6.3 Faraday Depolarisation

Whilst beam and bandwidth depolarisation are both instrumental in origin, depolarisation can also take place both internally to a source itself and along the line of sight if there is an intervening Faraday screen. Consider a radio source that is extended along the line of sight, with mixing of the emitting and Faraday rotating regions. The RM will vary along the line of sight as it is dependent on the electron density and magnetic field (see equation 2.33). The different RMs in these emitting regions will cause the rotated polarisation vectors to add up incoherently, decreasing the net observed polarisation. As the rotation of the EVPA is dependent on λ^2, the depolarisation caused by Faraday dispersion is also an increasing function of wavelength (Burn 1966).

As an example, this Faraday depolarisation makes the ISM appear 'optically thick' to polarised radio emission in galaxies. At sufficiently low frequencies, polarised emission from

the far-side of a galaxy is completely depolarised, with only the front layer remaining visibly polarised (Beck 1999). Consequently, small variations in the field strength, geometry, or thermal electron density can lead to large fluctuations in the observed Π and RM.

Faraday depolarisation effects come in a variety of different forms and occur due to internal and external Faraday dispersion, and differential Faraday rotation. Further details on these physical depolarisation mechanisms are provided in Chapter 8.

2.7 Wide-field Polarimetry

For radio interferometers, the field of view (FOV) scales as ν^{-1}. This needs to be carefully considered, as the large primary beam causes bright sources distant from the phase centre to contribute sidelobes to images of the sky. These sources need to be imaged and CLEANed.

Furthermore, assumptions of a co–planar sky no longer hold for a large FOV such as that of the GMRT. Typically, sources in the sky are assumed to lie on a single tangent plane perpendicular to the line of sight. In reality, sources are located on a celestial sphere and for a large FOV the difference becomes significant. The separation between a tangent plane and the celestial sphere is given by

$$1 - \cos\theta \approx \frac{\theta^2}{2}\,, \tag{2.39}$$

where θ is the angle between the phase centre and a point on the celestial sphere and $1 - \cos\theta$ is the corresponding maximum separation between the tangent plane and celestial sphere (e.g. Chengalur et al. 1999). Imaging a large FOV while assuming a co-planar sky increases the phase errors and results in flux being incorrectly allocated to parts of the image. Additionally, sources significantly displaced from the phase centre will exhibit position offsets if a co-planar sky is assumed. As such, new wide-field imaging techniques are required that take the curvature of the celestial sphere into account for low-frequency radio observations.

The primary beam response will affect the flux levels across such a wide-field image, but this is usually easily correctable as variations in the Stokes I beam tend to be circularly symmetric about the phase centre.

The beam response is far more complex for polarimetric observations. The on-axis instrumental response was discussed in Section 2.3, however wide-field polarimetry also requires calibration of the direction-dependent or 'off-axis' instrumental effects. As for on-axis calibration, the polarisation beam manifests itself with total intensity flux leaking into the polarisation images. These polarimetric aberrations result in an increase in the observed fractional polarisation and also alter the EVPA of sources. The effect becomes more pronounced with increasing distance from the phase centre.

Correcting the direction-dependent instrumental polarisation poses challenges, but knowledge of the polarisation beam is vital for mosaiced surveys and other observations where the science relies on wide-field polarimetric capabilities.

2.8 Rotation Measure Synthesis

The importance of RM measurements has already been explained (Section 2.5). In the simple model that I presented earlier, $\Phi_{\rm EVPA}$ had a linear dependence on λ^2. The constant of proportionality was the RM, which could be calculated by fitting a straight line to some data. In reality, many astronomical sources contain both non-thermal and thermal electron populations – leading to internal Faraday rotation. Furthermore, multiple Faraday rotating regions may exist along the line of sight between us and a source. This often leads to a non-linear dependence between $\Phi_{\rm EVPA}$ and λ^2, with the RM becoming a function of wavelength.

Despite this, the literature is littered with RM measurements that merely fit a straight line to data obtained at two or three observing frequencies. This is unacceptable in cases where Faraday rotation along the line of sight exhibits complicated behaviour. This method also gives rise to '$n\pi$ ambiguities', as the EVPA is degenerate for rotations of $\pm 180n^\circ$. The separation of the differing wavelength-dependent contributions to the RM (which exist at different Faraday depths), alongside the elimination of $n\pi$ ambiguities, is essential if we are to truly understand cosmic magnetism.

The capabilities of modern correlators allow for a single observation to typically output at least 256 frequency channels. In combination with the technique of RM Synthesis, it is possible to separate differing contributions to the RM. The technique also eliminates $n\pi$ ambiguities, and maximises the sensitivity to polarised emission.

To begin, the RM can be redefined as

$$\mathrm{RM} = \frac{\mathrm{d}\Phi_{\rm EVPA}(\lambda^2)}{\mathrm{d}\lambda^2}\,, \tag{2.40}$$

and now equation 2.33 can be redefined in terms of the Faraday depth, ϕ, so that

$$\phi(s) = \frac{e^3}{2\pi m_{\rm e}^2 c^4} \int_0^d n_{\rm e} B_\parallel \, ds\,. \tag{2.41}$$

Now the RM is simply the slope of a $\Phi_{\rm EVPA}$ versus λ^2 plot, and ϕ is defined so that it can vary along the line of sight and such that a positive value implies a B field pointing towards the observer. Sources of radiation may now exist at different Faraday depths along a line of sight. Note that the Faraday depth does not have a simple relation to physical depth.

Using this definition of ϕ and neglecting depolarisation effects, a complete model of Stokes Q and U as a function of frequency is described by

$$Q(\nu) = P_0 \left(\frac{\nu}{\nu_0}\right)^{-\alpha} \cos 2(\phi\lambda^2 + \Phi_0)\,, \tag{2.42}$$

$$U(\nu) = P_0 \left(\frac{\nu}{\nu_0}\right)^{-\alpha} \sin 2(\phi\lambda^2 + \Phi_0)\,, \tag{2.43}$$

where α is the spectral index, and P_0 is the linearly polarised flux density at frequency ν_0. The observed polarisation vector can then be expressed as a complex quantity so that

$$P = Q(\nu) + iU(\nu) = P_0 \left(\frac{\nu}{\nu_0}\right)^{-\alpha} e^{2i\Phi_0} e^{2i\phi\lambda^2} \,. \tag{2.44}$$

Integrating this complex polarisation over all Faraday depths yields

$$P(\lambda^2) = \int_{-\infty}^{\infty} F(\phi) e^{2i\phi\lambda^2} d\phi \,, \tag{2.45}$$

where $P(\lambda^2)$ is the complex observed polarisation, and $F(\phi)$ is the 'Faraday Dispersion Function' which describes the intrinsic polarisation at each Faraday depth (Burn 1966). Equation 2.45 takes the recognisable form of a Fourier Transform, allowing the relationship to be inverted into

$$F(\phi) = \frac{1}{\pi} \int_{-\infty}^{\infty} P(\lambda^2) e^{-2i\phi\lambda^2} d\lambda^2 \,. \tag{2.46}$$

Everything on the right-hand side is now an observable. However, there is still a problem; in order to retrieve $F(\phi)$ we would need to observe *all* positive (and negative) λ^2. A solution for multi-channel data was found by Brentjens & de Bruyn (2005) who introduced a weighted top-hat like function that allows $F(\phi)$ to be reasonably approximated by

$$F(\phi) \approx K \sum_{i=1}^{N} W_i P_i e^{-2i\phi(\lambda_i^2 - \lambda_0^2)} \,, \tag{2.47}$$

where i is simply a spectral channel across a finite observing bandwidth of N channels, K and W_i allow for weighting of each channel, and λ_0 is the mean observing wavelength. In essence, the mathematical derivation of the RM Synthesis technique allows for polarisation vectors that are close together in λ^2-space to be Fourier inverted into 'Faraday space' i.e. ϕ-space. The polarisation vectors are summed coherently at a number of trial Faraday depths, with the sensitivity being maximised to polarised emission at that Faraday depth.

As equation 2.47 is a Fourier inversion of a windowed function, $F(\phi)$ is convolved with a point-spread function in Faraday space following RM Synthesis. This point-spread function is known as the Rotation Measure Spread Function (RMSF), and has a FWHM given by

$$\delta\phi \approx \frac{2\sqrt{3}}{\Delta\lambda^2} \,, \tag{2.48}$$

where $\Delta\lambda^2$ is the width of the λ^2 distribution i.e. the range in λ^2 of the observing bandwidth (Brentjens & de Bruyn 2005). The RMSF can be trivially deconvolved from $F(\phi)$ using a one-dimensional clean that is analytically identical to that used during aperture synthesis imaging. In addition, the maximum observable Faraday depth (at 50% sensitivity) is given by

$$|\phi_{\max}| \approx \frac{\sqrt{3}}{\delta\lambda^2} \,, \tag{2.49}$$

and the largest scale in ϕ-space to which the instrument is sensitive is given by

$$\phi_{\mathrm{max-scale}} \approx \frac{\pi}{\lambda^2_{\mathrm{min}}}\,, \tag{2.50}$$

where $\delta\lambda^2$ is the channel width (i.e. the range in λ^2 of a single channel), and λ^2_{min} is the shortest wavelength squared. There are clearly many analogies between RM Synthesis and aperture synthesis, with the concepts of λ^2-coverage and uv-coverage, and of a RMSF and a synthesised beam. Note that future facilities will soon be moving beyond the technique of RM Synthesis to employ Faraday Synthesis, which takes uv-data and converts directly into ϕ-space. While Faraday Synthesis is currently in its infancy, it has several inherent advantages over the traditional two-step technique. These include improved sky-plane resolution, fidelity, and dynamic range (Bell & Enßlin 2011). Nevertheless, for now the RM Synthesis technique is a useful asset to the toolbox of radio polarimetry, and it will be used throughout this thesis.

2.9 Rician Bias

Polarimetry is often used to make measurements of the polarised intensity. These polarised intensity measurements are made from combined images of Stokes Q and U (see equation 2.10), both of which typically contain normally distributed noise. As images of P are created by summing Q and U in quadrature, the noise-statistics in P are instead governed by the Rician distribution.

Now, consider a source that has no intrinsic polarisation, so that $P = Q = U = 0$. As the created images of Q and U contain Gaussian noise, it is clear that a measurement of P from an image will always yield $P > 0$. This over-estimation of polarised intensity due to P being positive-definite is known as 'Rician bias'.

For higher signal-to-noise ratios, the amount of this bias becomes increasingly small; the 'Wardle–Kronberg', maximum-likelihood, and other estimators all yield similar results. Nevertheless, at lower signal-to-noise ratios an estimator of the bias is essential to retrieve the true polarised intensity, P_0. For a detailed explanation, see Simmons & Stewart (1985).

The least-biased estimator of Rician bias at low signal-to-noise ratios has been shown to be that of Wardle and Kronberg (Wardle & Kronberg 1974; Simmons & Stewart 1985). It is given by

$$P_0 = \sqrt{P^2 - \sigma^2_{QU}}\,, \tag{2.51}$$

where σ_{QU} is the best estimate of the RMS noise in the Q and U images. This works well for band-averaged images. However, there is a much stronger bias in P images made using RM Synthesis due to an additional uncertainty in Faraday depth. It has been shown (George et al. 2011) that in this case, a much more effective estimator of the true polarised intensity is given by

$$P_0 = \sqrt{P^2 - 2.3\sigma^2_{QU}}\,. \tag{2.52}$$

Corrections for the effects of Rician bias have been applied throughout this thesis. The specifics of which estimator has been used are detailed at the appropriate place in the text.

CHAPTER 3

OBSERVATIONS AND DATA REDUCTION

"Insanity: doing the same thing over and over again and expecting different results."

Albert Einstein
(who never used AIPS)

In Chapters 1 and 2, I introduced the concept of radio interferometry with the GMRT and detailed the foundations of polarimetric observations. I now progress to the practical application of these ideas to real observational data. I first list the observational parameters of the various data in Section 3.1. These observations required the removal of narrow-band interference and the application of a number of calibration techniques. I discuss the data reduction procedure in Section 3.2 and then continue to explain all the intermediary steps that were carried out up to the application of RM Synthesis to calibrated images in Section 3.7. In Chapter 4, I shall begin the analysis of these observations.

3.1 Observations

Data from the GMRT were typically taken at 610 MHz, with additional data also obtained at 325 MHz. GMRT data were always taken in 'full-polar' mode, so that the *RR*, *LL*, *RL*, and *LR* visibilities were recorded. Further complementary data were also obtained from the VLA archive at both 1.4 GHz and 4.8 GHz. These data are all clearly identified in the text, but when unspecified I am referring to 610 MHz GMRT data. All observations with the GMRT used a recently developed software correlator. The data are summarised in Table 3.1.

Table 3.1: Observational parameters of the GMRT data. The target source is not listed for observations that were only used for instrumental analysis in this thesis.

Date	Target	Obs. Code	Time on source /min	Freq. /MHz	BW /MHz	N_{CHAN}
2010 Jan 08	SCG 0141–3429	17_060_1	220	610	16	256
2010 Jan 09	G1.9+0.3	17_051	235	610	16	256
2010 Jan 09	SCG 2315–4241	17_060_2	180	610	16	256
2010 Jan 10	M51	17_052	400	610	16	256
2011 Jan 16	—	19_037_1	—	610	32	256
2011 Apr 26	Off-axis Response	TST0570	—	610	16	256
2011 Jun 05	—	20_014_1	470	610	32	256
2011 Jun 06	—	20_014_2	360	610	32	256
2011 Sep 09	Off-axis Response	TST0620	—	325	32	256
2011 Sep 11	Sagittarius A*	TST0623	133	610	32	512

A number of different sources were used for the purpose of calibration. Table 3.2 lists the primary and secondary[2], phase, and EVPA calibrators for each observation. The primary and secondary calibrators normally doubled as the bandpass calibrators. The AIPS task used for polarisation calibration is also specified (see Section 3.4.5).

Table 3.2: A list of calibrator sources used in each observation, alongside the AIPS task used for leakage calibration. The differences between the leakage calibration methods are detailed in Section 3.4.5.

Obs. Code	Primary	Secondary	Phase	EVPA	AIPS task
17_060_1	3C138	3C48	J0240–231	3C138	PCAL
17_051	3C286	3C48	J1751–253	3C286	PCAL
17_060_2	3C138	3C48	J2314–449	3C138	PCAL
17_052	3C286	3C138	J1313+549	3C286	PCAL
19_037_1	3C48	3C138	J0334–401	3C286	LPCAL
TST0570	3C147	—	3C147	—	LPCAL
20_014_1	3C147	3C138	J0713+438	3C286	PCAL
20_014_2	3C147	3C138	J1248–199	3C286	PCAL
TST0620	3C286	3C48	3C48	—	LPCAL
TST0623[3]	3C286	3C48	J1751–253	3C286	LPCAL

Additional VLA observations were also retrieved from the online data archive to complement

[2]I use the term ‘primary’ calibrator to refer to the source used for flux density scale calibration. Two such flux density calibrators were sometimes used, in which case I also refer to a ‘secondary’ calibrator.

the observations of G1.9+0.3 at 610 MHz. The VLA data are summarised in Table 3.3. Data at 1.44 GHz were obtained using the B and C configuration on separate observing runs, while the 4.86 GHz data used the C configuration. All of the VLA data used 3C286 and J1751–253 as the primary and phase calibrators respectively.

Table 3.3: Observational parameters of the VLA data for G1.9+0.3.

Date	Config.	Frequency /GHz	Bandwidth /MHz	Time on source /min
2008 May	C	4.86	100	30
2009 Mar	B	1.44	50	38
2009 Jul	C	1.44	50	36

3.2 Data Reduction

All data were processed using the Astronomical Imaging Processing System (AIPS).

There are several differences between the calibrations needed for total intensity and polarisation imaging. For a thorough explanation of GMRT calibration for total intensity imaging see Garn (2009) – similar procedures were used throughout this thesis. Here I shall focus on the steps necessary for GMRT polarisation imaging, which have not been previously documented in detail.

A number of AIPS 'tasks' were used to remove bad visibilities from the observations listed in Section 3.1, and in order to calibrate the data. The recorded visibilities are corrupted by both astronomical and instrumental effects including the antenna gains, phase stability, ionosphere, polarisation leakage, radio-frequency interference, and a number of other time- and frequency-dependent systematics. These corruptions can be largely modelled by a number of Jones matrices that transform the visibility values. Calibration aims to undo these transformations in order to retrieve the true visibilities associated with the sky.

I scripted all calibration procedures using POPS, the AIPS scripting language, in order to ensure a consistent and repeatable calibration. Tasks, scripts, and other time-intensive procedures were often run within a Python wrapper that I developed for AIPS that allows the calibration to run in the background, and notifies the user by e-mail as the script progresses. The log files output by AIPS and the Python-based wrapper are saved for later investigation by the user. This compilation of code constitutes a GMRT polarisation pipeline. Following the flagging stage, this pipeline allows for full polarisation calibration and wide-field imaging to be carried out with minimal user intervention.

The calibration procedures themselves tend to require minimal CPU time, but the imaging stage in particular is computationally expensive. Creating wide-field Stokes Q and U datacubes

[3] Bandpass calibration of this observation was instead carried out by frequent monitoring of J1822–096.

for a full-synthesis GMRT observation with 256 channels typically takes between 2–4 weeks of CPU time on a Quad-Core AMD Opteron Processor at 1.9 GHz.

3.3 Flagging

All GMRT observations are taken in spectral-line mode, which assists with identifying narrow-band interference. Radio-frequency interference (RFI), pointing errors, and problems with position control (i.e. the servo system) result in anomalous data being recorded by an interferometer. Consequently, each observation requires careful checking so that these bad data can be identified and removed. The removal process is known as 'flagging'. Full-polar data taken with the GMRT require particularly extensive flagging, as the visibilities are dominated by RFI. The RFI also frequently impinges on the protected region of the band from 608–614 MHz.

Following the loading of multi-channel GMRT data into AIPS, an initial calibration was applied (see Section 3.4) and each data set was analysed using the task TVFLG. This allows all baselines in each individual channel to be viewed as a function of time. Anomalous baselines with very high amplitudes throughout an observation were removed from the data. The first and last integrations of each scan were also flagged using QUACK as these tend to be noisy. Antennas listed in the observation log file as having problems were also flagged, and on average 27 antennas were available for Stokes *I* imaging of any given observation.

The RFI is best removed using the task SPFLG, which allows for all channels of each individual baseline to be viewed as a function of time. The data were first flagged in *RR* and *LL*, and the entire procedure then repeated for *RL* and *LR*. In principle, the weaker signal in *RL*/*LR* should allow flagging to be accomplished using these cross-correlations alone. However, checks on the data indicate that RFI remains in the *RR* and *LL* visibilities following flagging in *RL*/*LR*. All cross-correlations were therefore flagged individually. An example of completed flagging is shown in Figure 3.1 for the calibrator source 3C48.

For Stokes *I* work, it is standard procedure to assume that the majority of RFI has been removed by using user-based pattern-recognition i.e. identifying trends in already flagged RFI to locate lower-level interference. This can leave substantial amounts of RFI in individual channels. As the polarisation calibration is performed on each single channel, this lower-level RFI can result in serious errors and a poor calibration. The only way to flag full-polar GMRT data is to ensure that every baseline and channel has been checked in *RR*, *LL*, *RL*, and *LR*. This is highly tedious, but ultimately very effective. The ultimate aim is to employ automated RFI detection algorithms at the GMRT, but this is not yet a standard procedure.

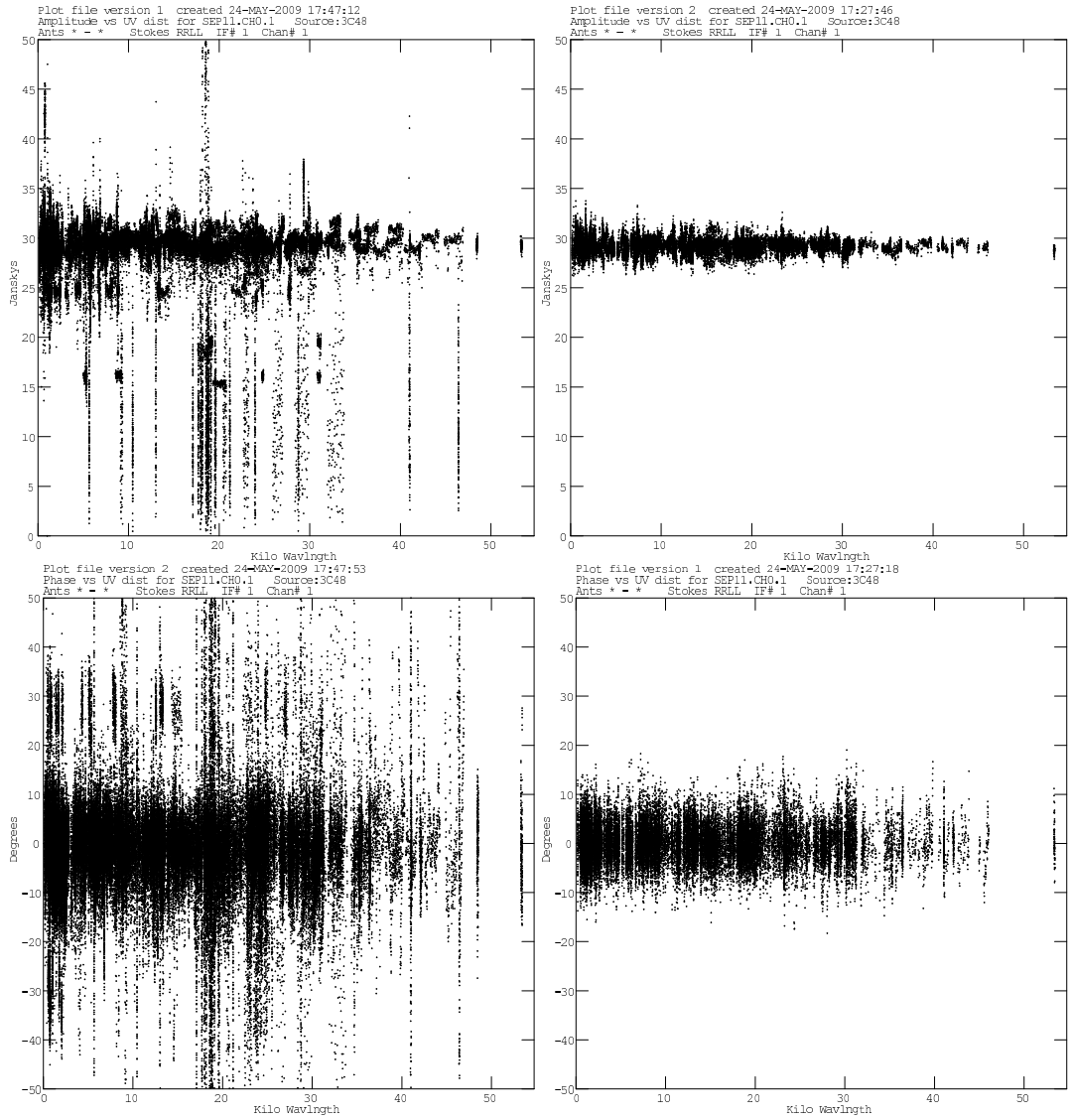

Figure 3.1: Amplitude (top row) and phase (bottom row) as a function of *uv*–distance ($\sqrt{u^2 + v^2}$) for the calibrator source 3C48, both after the initial calibration (left) and after flagging is complete (right).

3.4 Calibration

3.4.1 Bandpass Calibration

In spectral-line mode, the sensitivity differs for each frequency channel across the observing bandwidth. This frequency response, or 'bandpass', requires calibration, and was calculated for these observations as a function of time using the primary and secondary flux calibrators and the task BPASS.

The bandpass is expected to vary smoothly as a function of frequency and to remain relatively constant over time. The same primary and secondary flux calibrators were observed

throughout each observing run, and this allowed for checks on the variability of the bandpass. Plots of the calculated bandpass were also useful diagnostic tools in finding bad data. Sudden leaps or drops in the bandpass allowed for the identification of further visibilities that needed to be flagged.

The final bandpass corrections were applied to the multi-channel data, which was used to output a number of pseudo-continuum 'channel-0's'. The channel-0's were created by separating out each individual spectral channel using the task SPLAT. Channels at the edges of the bandpass were excluded due to edge effects and increased noise. For a 256 channel observation, this typically resulted in 220 expanded spectral channels; a 512 channel observation typically resulted in 470 usable spectral channels.

3.4.2 Flux Density Scale Calibration

Flux density scale calibration was carried out on each spectral channel using the primary and/or secondary flux calibrators. These calibrator sources are ideally bright (> 10 Jy), isolated, unresolved point sources and are typically distant quasars. The amplitude calibration is calculated in AIPS using a set of coefficients that describe the flux density of each source as a function of frequency; which are determined from previous monitoring observations of these sources. The calculated flux density scale is then applied to the observation. This was done using the task SETJY, with fluxes determined using the 'Perley–Butler 2010' coefficients[4] as employed in the 31DEC10 version of AIPS.

3.4.3 Amplitude and Phase Calibration

The relative gain of individual antennas varies slowly during an observation. This is seen in the data as a time-dependent variation in amplitude and phase. These variations can be caused by the correlator's electronics, inaccuracies in the co-ordinates of the antennas, or more commonly by changes in the turbulent ionosphere – with changes in the TEC and B field altering the pathlength of incoming radiation and leading to rapid phase fluctuations.

In the image-plane, the intensity of an ideal calibrator source should resemble a two-dimensional Dirac δ-function. As an interferometer observes the Fourier Transform of the sky, a calibrator source located at the phase-centre should have constant amplitude and zero phase on all baselines in the uv-plane. The task CALIB uses this property, combined with the flux density scale determined by SETJY, and adjusts the complex gains of each antenna to approximate an ideal point source using a least-squares based solution. This was done using SOLTYPE='L1R', which provides a robust solution that is less sensitive to outliers. The CALIB process was run on all observed calibrator sources, including the phase and EVPA calibrators. For these GMRT observations, which have high sensitivity at low frequency, the calibrator sources are rarely

[4] See the output of EXPLAIN SETJY within AIPS. Alternatively, see www.aips.nrao.edu/cgi-bin/ZXHLP2.PL?SETJY.

isolated in the FOV. However, if other nearby sources in the FOV have a flux density $\lesssim 10\%$ of the calibrator, then the calculated solutions should tend to vary by $\lesssim 10\%$.

In order to measure the antenna-based variations, observations of the target were interspersed with $\sim$ 5 minute scans of a phase calibrator every $\sim$ 30 minutes. The pre-calculated flux density scale and calibrator solutions were used to determine the flux of this phase calibrator. This was calculated using the task GETJY.

The phase calibrator, like the flux calibrators, must also be bright, isolated, and unresolved. Additionally, the phase calibrator must be in close proximity to the target source on the sky – typically within 10°. This ensures that phase variations originating in the sky, which affect the phase calibrator, are also applicable to the target source i.e. the sources are within the same isoplanatic patch. The solutions for the phase calibrator can then be reliably interpolated across scans of the target. The distribution of suitably bright phase calibrators is far from homogeneous, and the balance between selecting either a bright or a nearby source is a subjective one. Generally, GMRT phase calibration at 610 MHz is reliable when the source has a flux density of at least 0.5 Jy.

Amplitude and phase solutions determined using CALIB with the phase calibrator were assumed to vary smoothly with time, and were linearly interpolated across the target source. This was done using a two-point interpolation of the phase variation with the task CLCAL. This provides a data set calibrated for both amplitude and phase.

3.4.4 Ionospheric TEC Calibration

Ionospheric Faraday rotation can be a significant hindrance to calibration at low radio frequencies (see Section 2.5.1). All observations in this thesis were obtained during a period of relatively quiet solar activity. Some observations were also scheduled at night, when the ionosphere is not being excited by the Sun. Nevertheless, most of these full-synthesis observations included the periods of either sunrise or sunset, and the ionosphere is expected to have highly variable TEC during these most active periods of ionisation and recombination.

Corrections for the effect of ionospheric Faraday rotation were made using the task TECOR, which contains a basic model of the ionosphere. These corrections were made using global maps of the GPS-derived TEC, which are freely available in the IONEX format from the CDDIS data archive at NASA's Jet Propulsion Laboratory. The maps were used to correct for ionospheric Faraday rotation at the reference antenna, with differences between the antennas being removed by self-calibration.

The GPS measurements of the vertical TEC are spatially interpolated and temporally smoothed, and updated every 15 minutes. The nearest GPS receivers to the GMRT are located in Bangalore and Hyderabad – the location of these receivers is shown in Figure 2.2.

Ionospheric Faraday rotation also depends on the ionosphere's magnetic field strength and each antenna's line of sight through the medium. There is currently no widely available model

to correct for differences in the observing geometry. Nevertheless, the magnetic field is only weakly variable over the duration of a typical observation, while the TEC can be highly variable (Cotton 1993). Maps of the TEC are therefore an important first-order correction, and appear to correct GMRT data well. A plot showing the determined ionospheric Faraday rotation at the GMRT over a 10 hour duration is shown in Figure 3.2.

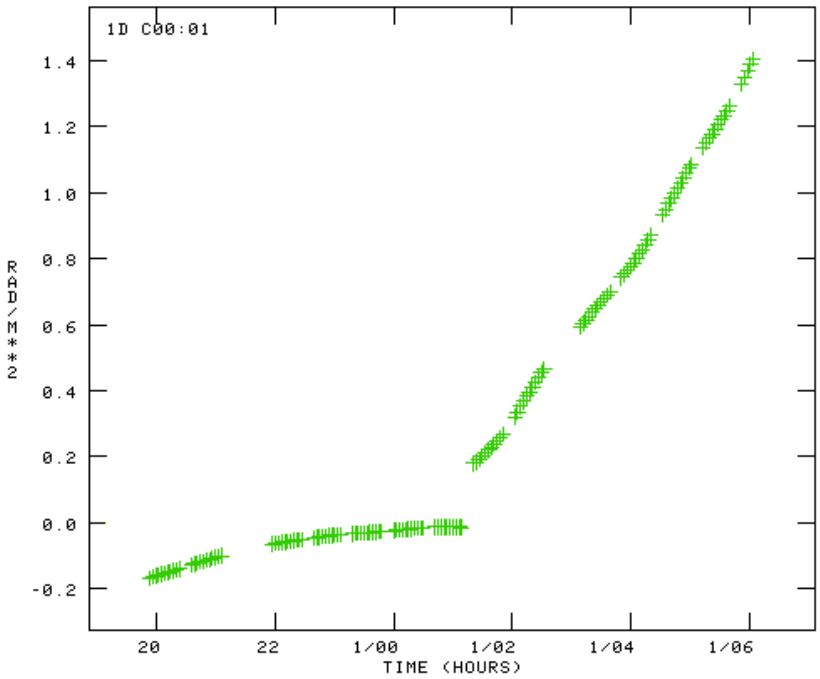

Figure 3.2: The ionospheric Faraday rotation at the GMRT as a function of time, during an observation of M51 on 2010 Jan 10. The maximum Faraday rotation due to the ionosphere was ~ 1.4 rad m^{-2}.

3.4.5 Polarisation Leakage Calibration

The effects of instrumental polarisation were removed from the data using either the AIPS task PCAL (which uses parallactic angle variation to separate the source and instrumental contributions) or the task LPCAL (which uses an unpolarised calibrator). A linear model of the feeds was used (SOLTYPE='APPR'), as it is not possible to use a full non-linearised model in AIPS.[5]

[5]In AIPS versions earlier than 31DEC09, attempts were made to calibrate using the full orientation/ellipticity model (SOLTYPE='ORI-'). Despite applying parallactic angle corrections before phase calibration, the model did not converge for GMRT data and provided unusable results. The orientation/ellipticity model is more suitable for GMRT data (see Chapter 4). As of 31DEC10 AIPS, the orientation/ellipticity model can no longer be used at all due to an error when corrections are applied to the data (DOPOL>0). I have located the nature of this problem in the underlying Fortran code. The error originates in the subroutine PDRGET, which gets the reference antenna and phase differences from the AN table when solutions are in the 'ORI' format. The details were passed on to the AIPS team, and the problem was fixed as of 31DEC12 AIPS. Nevertheless, while the task now functions, the results are

In principle, the use of a known unpolarised calibrator should be equivalent to the use of the orientation/ellipticity model (see Section 2.3). However, the inherent decrease in signal-to-noise ensures that the best calibration for GMRT data is carried out by separating the instrumental and source polarisation characteristics via observation of a source over a large range in parallactic angle. The polarisation calibration was therefore typically carried out in PCAL with the phase calibrator (using SOLTYPE='APPR'). Exceptions to this are clearly specified in the text. The data were time-averaged before calibration into 2 minute intervals (SOLINT=2). Varying the time-averaging between 1–10 minutes was found to have a negligible effect on the polarisation calibration, with artefacts only being introduced if the data were averaged over periods greater than one phase calibrator scan length.

As the linearised model loses accuracy for large leakages, the quality of calibration was limited for several antennas in the array with high leakage amplitudes. Consequently, all antennas with leakages $> 15\%$ were flagged from the data. This was typically 7–8 antennas in any given observation. There is an associated loss in sensitivity, and occasionally outer arm antennas had to be flagged – leaving relatively large holes in the *uv*-coverage. An appropriate selection of *uv*-range and/or *uv*-taper during the imaging stage can accommodate for these holes. Nevertheless, extended polarised emission remains well sampled by the over-density of antennas in the GMRT's central square. The minimum baseline length of ~ 100 m means the data is sensitive to polarised emission on scales up to $\sim 17'$.

It was found empirically that the instrumental polarisation could not be well-calibrated if the calibrator source had a flux of $\lesssim 1$ Jy, even if there was substantial parallactic angle variation. While the calibration is generally excellent for full-synthesis observations (and a corresponding large range in χ), the calibration quality decreases rapidly for shorter observations. The use of an unpolarised calibrator is much more effective in these circumstances. The flux density scale calibrators 3C48 and 3C147 have flux densities of ~ 29 Jy and ~ 37 Jy respectively at 610 MHz. Both sources are assumed to be unpolarised at this frequency.

3.4.6 Electric Vector Polarisation Angle Calibration

Following polarisation leakage calibration, the absolute value of the phase offset between R and L is left as an unconstrained degree of freedom. This needs to be corrected by observing a source of known polarisation angle. The calibrators 3C138 or 3C286 were generally used for this purpose.

At the VLA, the $R - L$ phase offset is typically determined using the AIPS task RLDIF, with the correction applied using CLCOR. At the GMRT, it was found that the matrix-based corrections determined using RLDIF did not correct the data well. The corrections were found to be significantly improved by using an image-based method, with the $R - L$ phase difference

unfortunately disappointing – subsequent runs of RLDIF displays longer baselines as having a RL/LR phase equal to 0°. Additionally, images of the calibrators 3C138 and 3C286 do not resemble a polarised point source. It appears that the task does not correctly derive the instrumental polarisation for GMRT data.

determined using integrated flux measurements of the EVPA calibrator from images in Q and U. These image-based corrections are used throughout this thesis, and are discussed in detail in Chapter 4.

3.5 Wide-Field Imaging

3.5.1 The CLEAN Algorithm

Images were created in AIPS using the task IMAGR, which FTs the *uv*-visibilities and creates a 'dirty image' of the sky. The dirty image contains the emission from the sky convolved with the point-spread function (PSF), which is determined by the *uv*-coverage of an observation. This PSF leads to sidelobes that distort the area surrounding each source.

The CLEAN algorithm attempts to deconvolve the image from the PSF. While various algorithms exist, the standard procedure is to locate the pixel of maximum intensity in the dirty image, and then remove a percentage (typically 10%) of this pixel's intensity. This contribution to the image is stored as a 'CLEAN component' (CC). This CC is then convolved with the antenna PSF, a FT carried out, and the resulting contribution is subtracted from the *uv*-data. This process is repeated iteratively by locating the next pixel of maximum intensity in the image-plane.

This causes the sidelobes to be incrementally reduced until usually only a residual image remains (typically the thermal noise). The CCs are then relocated to their original sky co-ordinates and are convolved with a Gaussian. Finally, the resulting smoothed CC image is combined with the residual image to produce a final CLEAN image.

3.5.2 Polyhedron Imaging

As mentioned in Section 2.7, the FOV scales as ν^{-1} and at 610 MHz the GMRT has a large primary beam of FWHM 0.74°. This large primary beam causes bright sources distant from the phase-centre to contribute sidelobes to images of the sky. These sources also need to be imaged and deconvolved from the PSF using the CLEAN algorithm.

As assumptions of a co-planar sky do not hold for wide-fields such as that of the GMRT, wide-field imaging techniques are needed. This was carried out in AIPS by breaking up the FOV into a 'fly's eye' of multiple facets, with each facet being of small enough size that co-planar assumptions remain sufficiently accurate. This is known as polyhedron imaging. The required facet size is given by

$$\theta \leq \sqrt{\frac{2\lambda}{L_{\mathrm{MAX}}}}, \tag{3.1}$$

where L_{MAX} is the maximum baseline length. For the GMRT at 610 MHz, with $L_{\mathrm{MAX}} = 27$ km, the maximum size of a facet is $21'$.

The synthesised beam must be well-sampled, with 4–5 cells across each beam. As the synthesised beam size of GMRT images is $\sim 5''$, a cellsize of $1.2''$ is appropriate. A facet consisting of 1024×1024 pixels therefore allows for inclusion of all the data in the *uv*–plane and gives each facet a size well below the $21'$ maximum determined using equation 3.1.

Polyhedron imaging was carried out using the task SETFC which creates a 'boxfile' that contains the co-ordinates of each individual facet and the corresponding circular CLEAN box. The boxfile was extended out to a radius of 0.75° from the pointing centre (BPARM(1)=0.75). Although the primary beam of the GMRT drops to a sensitivity of 20% at a radius of only 0.53°, the larger radius ensures sidelobes from distant bright sources are CLEANed from the map. This required that 31 facets were used. The facets were arranged in an overlapping hexagonal arrangement (1+6+12+12) across the primary beam. An overlap of 20 pixels was used between facets (BPARM(2)=20).

Imaging of the wide-field then progressed in a manner similar to single-field imaging, except that the CLEAN algorithm checked each facet to find the brightest pixel and removed the sidelobes associated with this pixel from all facets.

3.5.3 The Thermal Noise

The thermal noise, $\sigma_{\rm T}$, is the minimum RMS noise achievable in an image based on the observational parameters. For a weak source, the thermal noise can be calculated using,

$$\sigma_{\rm T} = \frac{WT_{\rm sys}}{G\eta_{\rm c}\sqrt{2n_{\rm b}n_{\rm chan}\tau\Delta\nu}}\,, \tag{3.2}$$

where W is a weighting factor (typically 1 for natural weights and ~1.2 for robust or uniform weights), $T_{\rm sys}$ and G are the system temperature and gain of a single antenna, $n_{\rm b}$ is the number of baselines, $n_{\rm chan}$ is the number of channels in a spectral-line observation, $\Delta\nu$ is the bandwidth of a single channel, τ is the total on-source integration time, and $\eta_{\rm c}$ is the efficiency of the correlator. For the GMRT, $\Delta\nu$ is in Hz, τ in seconds and $\sigma_{\rm T}$ is given in Jy. In the GMRT user manual for December 2008, $T_{\rm sys} = 102$ K and $G = 0.32$ K/Jy/antenna. $\eta_{\rm c}$ is taken as 1 for the GMRT correlator.

There is no point in CLEANing below the thermal noise. To prevent this, CLEAN has to be stopped by some pre-defined criterion. For Stokes I images, this is relatively simple: as I emission is always positive, the total CLEANed flux will increase up to a point when the algorithm will begin to add and subtract small CLEAN components on the scale of the expected thermal noise. At this point, the CLEANing should be stopped. For Q, U, and V images the criteria are not so straightforward, as the emission can be both positive and negative. For these images, a CLEAN threshold was set equal to $4\sigma_{\rm T}$, where $\sigma_{\rm T}$ is the expected thermal noise in an individual channel as calculated using equation 3.2. The CLEANing process stopped automatically when the maximum absolute value of pixel intensity was $\leq 4\sigma_{\rm T}$.

3.5.4 Recombining Image Facets

After cleaning had finished, the 31 facets were merged into a 5000 × 5000 pixel map of the sky using the task flatn. In order to avoid edge-effects in images of the faint polarised emission, pixels around the edge of each facet were excluded from the Q, U, and V images using edgskp= 40. The resulting Q and U images were combined into datacubes and into individual images of polarised intensity, $P = \sqrt{Q^2 + U^2}$. The resulting images of P were averaged together into a final image of the polarised intensity – I will refer to this type of image as 'band-averaged P'. In some cases, an additional image was created by averaging together Q and U to produce a single P image – I will refer to this type of image as 'band-averaged Q/U'. Note that neither of these methods is ideal for science, although both types of image are useful indicators of source polarisation and image-plane artefacts. RM Synthesis was also used to properly average the data (see Chapter 2 for details on Rician bias, bandwidth depolarisation, and RM Synthesis).

3.6 Self-Calibration

After creating a clean wide-field image, residual calibration errors will still remain in the data. Nevertheless, it is possible to adjust the complex gain of individual antennas in order to improve the image quality and reduce the RMS noise in the final image. This process, 'self-calibration', effectively focusses the array by using an input model of the sky to make small, iterative, time-dependent corrections to the data. Self-calibration is effective at removing a number of effects, including time-variation of the antenna gains, a slowly changing ionosphere, or inaccuracies in the antenna co-ordinates.

The image of the sky that was made initially is considered to be the best available model. Subtracting this model from the original data leaves a set of residuals that represent differences between the input model and the actual data. Self-calibration attempts to minimise these residuals by allowing the complex gains of the antennas to be free parameters. The residuals are minimised by adjusting the antenna gains so the data better represents the model. The data are then re-imaged, to produce a more accurate input model. This procedure is repeated iteratively until the image quality has been significantly improved.

The procedure is carried out in AIPS via iterative runs of imagr to produce an image model, followed by a run of calib. The task calib uses the CCs as a model of the sky. All available CCs from the model image were used for the data presented in this thesis, as the clean algorithm is a non-linear process and will attempt to correct itself if too much flux was removed from a given pixel on an earlier iteration. Additionally, if clean encounters a source located between two adjacent pixels, the algorithm will pass flux back and forth between the pixels in an attempt to image the source. This can result in negative CCs which are not representative of image noise (e.g. Garn 2009). Consequently, limiting the number of CCs used in the model is subjective.

The best prescription found for self-calibration of GMRT data agreed with previous efforts

(see Garn (2009)). This consisted of four consecutive iterations, using the Stokes I images. The first three iterations were used to make phase-only corrections (SOLMODE='P') to the data in CALIB. Each iteration solved for the antenna gains over progressively shorter time intervals, ten minutes, then three minutes, and finally one minute solution intervals. The set parameters only allowed solutions with a minimum signal-to-noise ratio of four (APARM(7)=4). A 'L1 solution' was used so that the gain solutions were less influenced by anomalous data points (SOLTYPE='L1'). The final iteration solved for both amplitude and phase (SOLMODE='A&P') over ten minute intervals. This allowed corrections for slow variations in the antenna-based amplitude sensitivities. The gains were also normalised (CPARM(2)=1) during amplitude self-calibration, in order to prevent drifting of the flux density scale.

For the self-calibration process, each image model contained 5×10^4 CCs. The images were checked at each stage to ensure that the image quality had improved. The effectiveness of the procedure differs depending on the field that was observed. Nevertheless, for some fields the process can reduce the RMS noise by a factor of ≈ 5 and also increase the dynamic range by a factor of ≈ 5. Following self-calibration, a final Stokes I image was created. This typically required 5×10^5–2×10^6 CCs to reach the thermal noise. The self-calibration solutions were then copied over to each polarisation calibrated spectral channel. The solutions were applied to the data using CLCAL before images in Q, U, and V were created.

3.7 Applying RM Synthesis

After the creation of a GMRT datacube in Stokes Q and U, it was possible to apply the technique of RM Synthesis (see section 2.8) using a code that I developed in Python. The code is capable of processing 220 channel datacubes of Q and U, each being 512×512 pixels, into 201 Faraday depths in ≈ 3 hours using a Quad-Core AMD Opteron Processor at 1.9 GHz.

This code also implemented a form of RM-clean to deconvolve the Faraday dispersion function from the RMSF. There is currently some question over the capability of RM-clean to fully reconstruct the Faraday dispersion function along the line of sight (Frick et al. 2010; Farnsworth et al. 2011), and it is possible that modelling of $Q(\lambda^2)$ and $U(\lambda^2)$ is advantageous under many circumstances (O'Sullivan et al. 2012). Nevertheless, the RM-clean implemented here considers the effects of the residuals, and uses complex cross-correlation in order to locate the peak in Faraday space (Heald et al. 2009). RM-cleaning was performed down to a 1σ limit. The cleaned Faraday spectrum was convolved with a FWHM equal to that of the expected RMSF for the individual observations (see equation 2.48). This varied from $\sim$ 140–320 rad m^{-2}, depending on the observational set-up. Unless otherwise specified, the polarisation was summed up coherently across the band for trial Faraday depths ranging from -2000 rad m^{-2} to $+2000$ rad m^{-2}. The 'RM-cubes' generated by RM Synthesis were always sampled to at least twice the Nyquist rate, which is $\Delta\phi = 10$ rad m^{-2} for a 32 MHz bandwidth at 610 MHz. Sampling of $\Delta\phi = 1$ rad m^{-2} was often used. Noise levels of ~ 50 μJy beam^{-1} rmsf^{-1} were

frequently achieved.

Attempts were made to weight the Q/U input datacubes by a factor of $1/\sigma^2$, where σ was the noise in each individual channel. This provided only a small improvement in the quality of the output, with the use of weighting typically reducing the noise in ϕ-space by a factor of 1.02. Although such small improvements are useful, the increase in computational expense (a factor of ~ 2) meant that the decision was made not to weight the data.

The data are not limited by the RM Synthesis observational set-up. For a typical experiment at the GMRT which uses a 16 MHz bandwidth, with 62.5 kHz channel spacing at 610 MHz, the maximum Faraday depth to which one is sensitive is $|\phi_{\rm max}| \sim 35000$ rad m^{-2}. Bandwidth depolarisation will affect these data for a |RM|≥ 20000 rad m^{-2}.

The maximum scale in Faraday space to which the data are sensitive is 14 rad m^{-2}, consequently the data are not sensitive to Faraday thick emission. Faraday thick emission would present itself in these data as two Faraday thin peaks at the edges of a Faraday thick slab.

CHAPTER 4

THE ON-AXIS POLARISATION RESPONSE OF THE GMRT

> "I do not think there is any thrill that can go through the human heart like that felt by the inventor as he sees some creation of the brain unfolding to success. Such emotions make a man forget food, sleep, friends, love, everything."
>
> *Nikola Tesla*

In Chapter 3, I discussed the observations obtained at the GMRT and the reduction procedures used for these data. I now use these data to investigate the instrumental polarisation response of the GMRT at 610 MHz – placing constraints on variations in the instrument that arise due to both frequency- and time-dependent effects. I show that the leakages are highly frequency-dependent, and that this gives rise to an 'instrumental RM' which must be corrected. I also identify two antennas in the array with significant time-dependent instrumental polarisation. The data are then used to create images of the calibrator sources. This allows me to quantify the residual instrumental polarisation and show that the linear and circular polarisation fractions are as expected. I then use empirical methods to optimise the polarisation calibration, showing that 'image-based' corrections are a superior method of EVPA calibration at the GMRT. Finally, the images of the calibrator sources are used to test my developed RM Synthesis code.

4.1 The On-axis Instrumental Polarisation

There are two essential steps for the polarisation calibration of an alt-az mounted interferometer with circular feeds, such as the GMRT:

1. Firstly, the orthogonal polarisations of antenna feeds are never perfectly isolated, and corrections must be made for this polarisation leakage between R and L. This is typically carried out by observing an unresolved point source at the phase-centre over a range of parallactic angles, allowing for the separation of instrumental and source polarisation.
2. When solving for the instrumental leakage, the absolute value of the phase offset between R and L is left as an unconstrained degree of freedom. This needs to be corrected by observing a source of known polarisation angle. At the VLA and WSRT, the calibrators 3C138 and 3C286 are frequently used for this purpose.

This calibration will correct for the effects of 'on-axis' instrumental polarisation i.e. the polarisation response at the phase-centre. The polarisation response may also vary across the FOV, and an investigation of this 'off-axis' instrumental polarisation is presented in Chapter 6. For now, I only consider the on-axis response.

Following the procedures set out in Section 3.4.5, it was possible to calculate the instrumental polarisation of the GMRT. Example plots showing the typical leakages for an observation at 610 MHz are shown in Figures 4.1–4.3. The 325 MHz leakages have been found to have similar properties, as is shown in Section 4.2.2.

The leakages are of significant amplitude – up to 40% for some antennas, and are highly frequency-dependent with both the amplitude and phase varying smoothly across the band. There is also substantial phase-wrapping across the band.

The high leakage amplitude is problematic when using a linear model to solve for the instrumental polarisation, as there is a loss of accuracy for leakages $\gtrsim 5\%$. This suggests that a full non-linear treatment of the feeds is more appropriate for GMRT data, although it has not been possible to apply this calibration algorithm (see Section 3.4.5). Consequently, all antennas with leakages > 15% were flagged from the data. As an upper limit, residuals due to uncorrected second-order leakage terms are then < 2.25% (15% × 15% = 2.25%). In practice the residuals are frequently less than this. For example, following the removal of antennas with leakage > 15% there were 23 remaining antennas in observation 17_052. The mean leakage of these remaining antennas was 6.65%, leaving a mean residual of 0.44% due to second-order leakage terms.

The phase behaviour of some antennas (for example E04 and S02) appears erratic and undergoes significant phase-wrapping across the band. These rapid variations are to some extent a consequence of the choice of reference antenna, as the phase leakage is relative to that of another antenna in the array. The selection of reference antenna is important for any underlying phase relationship, as the R phase of the reference antenna is left undetermined during the leakage calibration process.

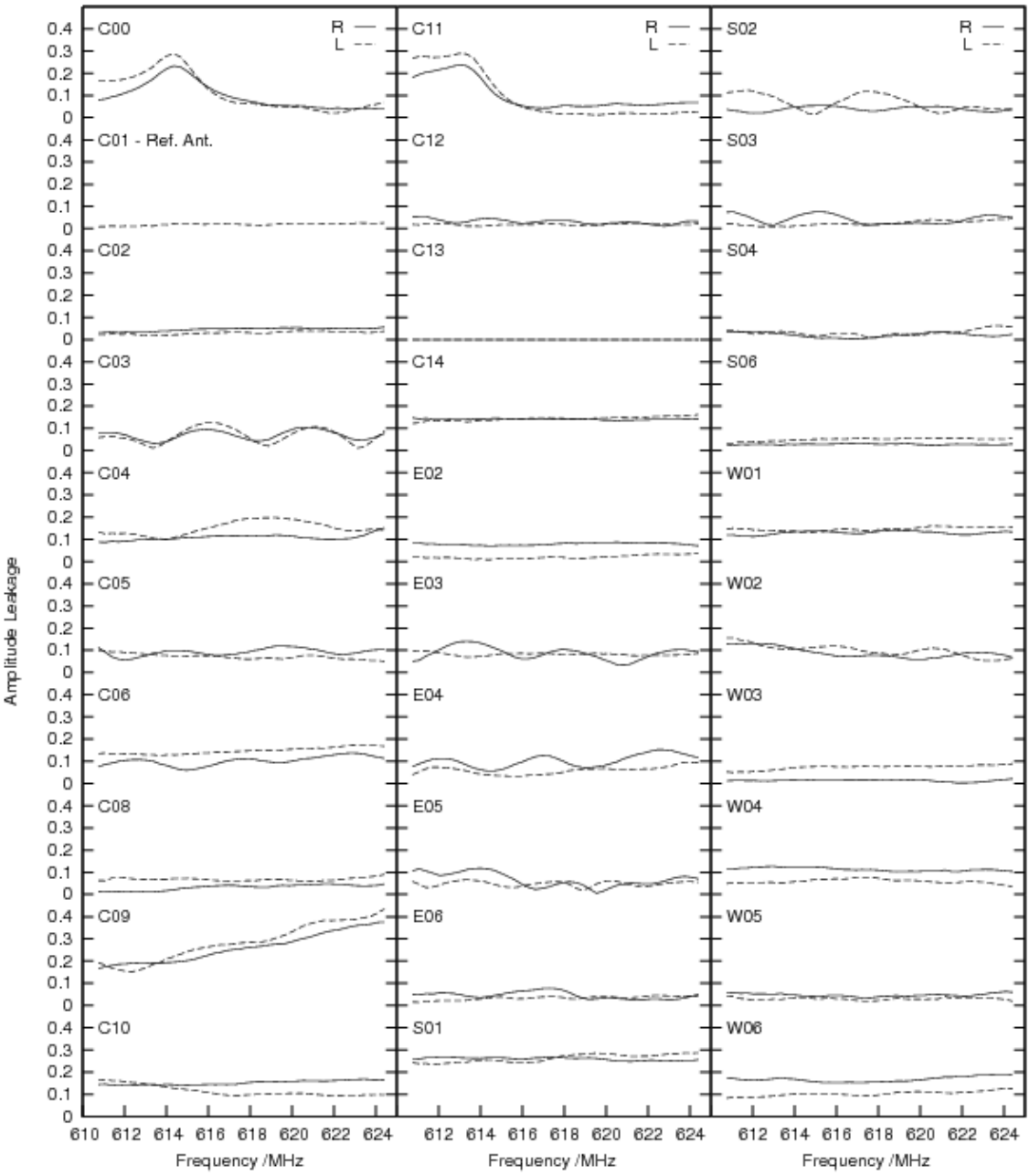

Figure 4.1: Amplitude of the antenna leakages, as calculated for observation 17_060_2. All data displayed with an amplitude of zero are a consequence of flagging. The reference antenna is C01.

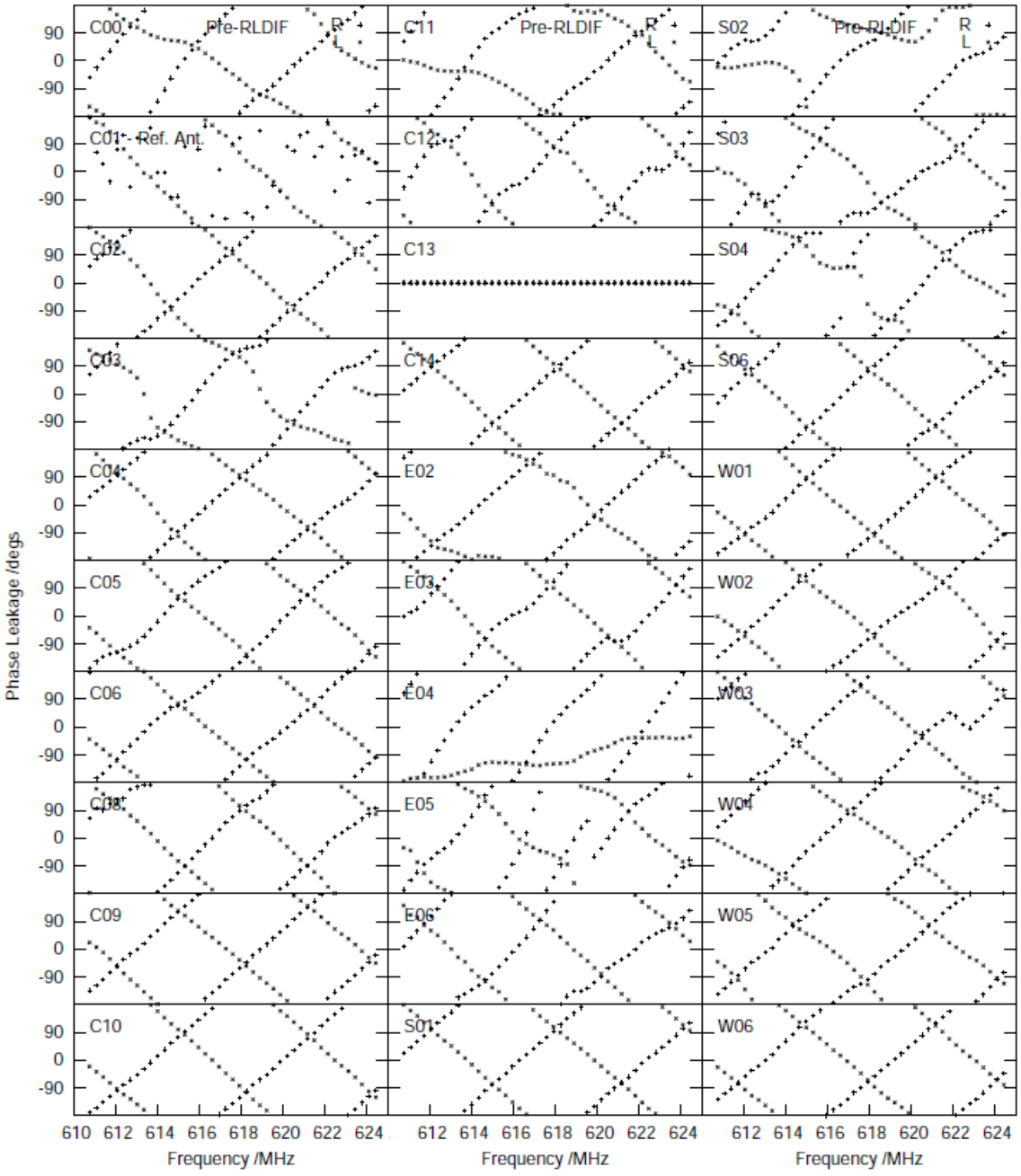

Figure 4.2: Phase of the antenna leakages as calculated for observation 17_060_2, *before* EVPA calibration had been applied (see Section 4.4). All data displayed with a phase of zero are a consequence of flagging. The reference antenna is C01.

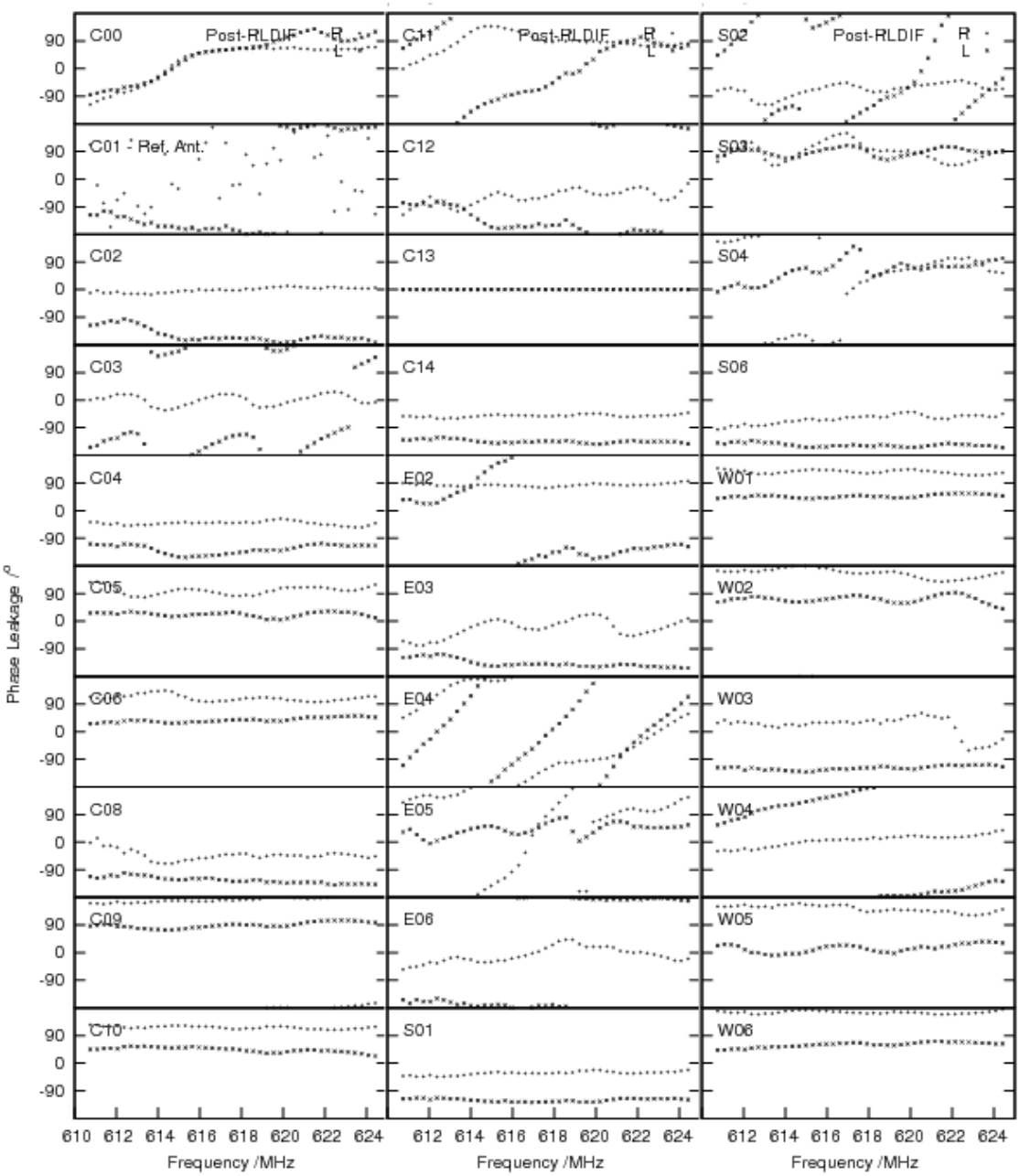

Figure 4.3: Phase of the antenna leakages as calculated for observation 17_060_2. The plot is similar to that of Figure 4.2, but *after* EVPA calibration had been applied (see Section 4.4). All data displayed with a phase of zero are a consequence of flagging. The reference antenna is C01.

As shown in Figure 4.3, for many antennas the phase of the leakage is almost constant, i.e. C14, W06, S06. These antennas tend to have a $\sim 90^\circ$ phase offset between the R and L circularly polarised signals. Such an offset is anticipated due to the quarter-wave plate in the 610 MHz feed, which is expected to provide a $\pi/2$ phase lag between both polarisations.

Some antennas display a smoothly varying decrease in the R phase with frequency, along with a corresponding increase in the L phase, or vice-versa. For example, see C05 and W02. This is possibly a consequence of reflections within the feed, with the sense of circular polarisation inverting at each reflection and the change in phase being dependent on the additional path-length.

4.1.1 Channel Averaging

The instrumental polarisation varies rapidly with frequency at 325 MHz and 610 MHz – with significant phase-wrapping across the band. Consequently, channel averaging should not be carried out on these GMRT data prior to polarisation calibration.

If channel averaging is applied before polarisation calibration, antennas which have phase leakage that crosses the $\pm 180^\circ$ threshold do not calibrate well within the channel average. If the size of the dataset does need to be reduced, it is possible to average channels following the application of EVPA calibration. This will, of course, increase bandwidth depolarisation effects and reduce the sampling in λ^2-space, and is therefore not recommended.

4.2 Time-Dependence of the Leakages

I wish to use these calculated leakages in order to calibrate GMRT data. Due to signal-to-noise constraints, it is generally only possible to calculate a *single* leakage for each antenna in a full-synthesis observation. Each observation typically takes place over many hours. In order to calibrate the data, I must therefore make the critical assumption that the antenna's on-axis response is sufficiently stable that it can be parameterised by a single complex leakage for the duration of an observation.

Time-dependent leakages will result in uncorrected 'residual' instrumental polarisation. This residual polarisation will cause emission in Stokes I to leak into and corrupt Q and U. It is therefore important to check that time-dependent effects are negligible.

4.2.1 Short-Term Stability

The short-term time-stability of the leakages was investigated by initially solving for the instrumental and source polarisation simultaneously – using the phase calibrator over the full range in parallactic angle. The source polarisation determined via this process was then used as an input model for future calculations of the instrumental polarisation. This allowed for

the instrumental polarisation to be calculated in a manner similar to when a source of known polarisation is used.

This method allowed the leakages to be calculated for each individual ~ 5 minute scan of the phase calibrator throughout four consecutive observations, 17_051, 17_060_1, 17_052, and 17_060_2. This yielded 49 calculations of the instrumental leakage in each spectral channel during the two day observing period. The RMS variation in these leakages will be a consequence of two effects: a contribution due to thermal noise, and an additional component due to time-variability of the leakages. An analysis of the time-variability is therefore reliant on the ability to separate out these two contributions. As the observations use four separate phase calibrators, the data also allow for any significant elevation-dependence to be identified.

The methodology used by Sault & Perley (2009) was adopted, and they find that the uncertainty due to system noise is approximately given by

$$\sigma_D^2 = \frac{1}{N}\frac{\sigma_C^2}{I^2}\,, \tag{4.1}$$

where σ_D^2 is the variance of the real or imaginary parts of the leakages, σ_C^2 is the variance of the correlation data, and N is the number of antennas. σ_C^2/I^2 can be estimated from the RMS of the closure phase, which is expected to be equal to $3\sigma_C^2/I^2$. The RMS of the closure phase was therefore extracted from the data using the AIPS task SHOUV, and was found to be approximately constant across the band. Equation 4.1 is derived using the approximation that the error in each leakage term is independent. This is incorrect as the leakages are derived using the various baselines j–k, but this only affects the results by a factor of order $1/N$.

A plot showing the RMS leakage variability across the band is shown in Figure 4.4. An example of the typical raw data for all antennas in a single channel is shown in Figures 4.5–4.7.

It is clear from Figure 4.4 that the best, median, and 80th percentile antennas have similar RMS leakage variability. The RMS variability of the 80th percentile antenna is almost twice that of the RMS expected due to thermal noise, but is well within the limits expected due to Gaussian noise statistics. The RMS leakage variability for most antennas appears consistent with that expected due to thermal noise alone. The observed variations in the best, median, and 80th percentile antennas are therefore simply a consequence of statistical error.

However, there are a number of anomalous antennas which seem to have significant time-dependent leakage. Across the entire band, the worst antenna is always C09 – with an RMS leakage variability ~ 8 times larger than that expected due to thermal noise. Antennas C06 and E02 also possibly display statistically significant time-dependent leakage, and typically have a variability ~ 4 times that expected due to noise. The effect of C06 and E02 on the interferometric images was investigated. C06 appeared to be well calibrated within the data, and removal of the antenna has the sole effect of increasing the noise in the subsequent images. This leads me to conclude that antenna C06 is simply a noisy outlier. Nevertheless, the removal of E02 visibly reduced image artefacts surrounding polarised sources. This suggests that the leakage of E02 is not sufficiently stable with time.

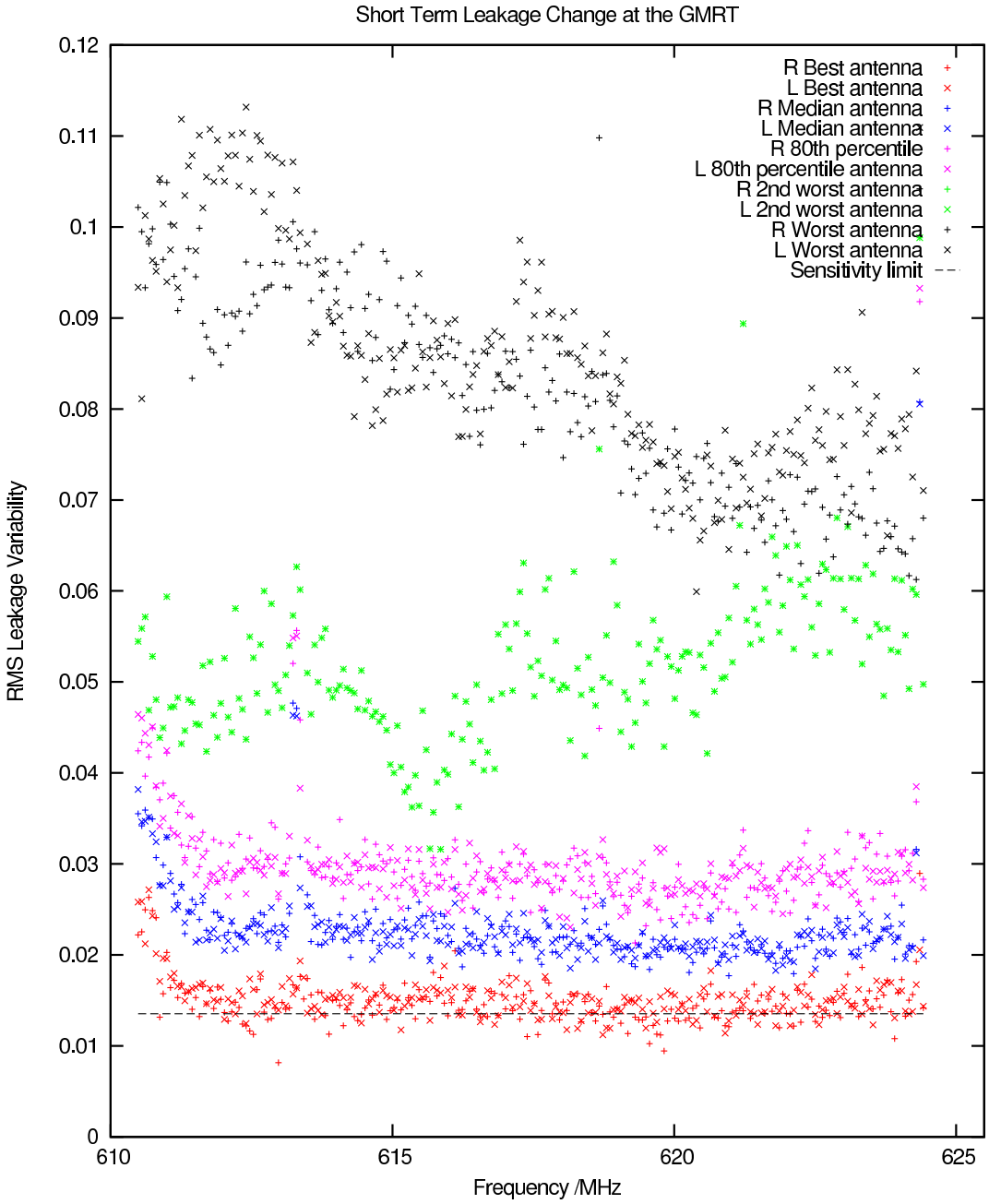

Figure 4.4: A plot of the short-term time-variability of instrumental polarisation across the GMRT band at 610 MHz. The 'RMS leakage variability' has been calculated about the mean of the derived solutions. The best, median, 80th percentile, 2nd worst, and worst antenna, in terms of their RMS variability have been plotted. A line showing the sensitivity limit of the four observations is also displayed and shows the expected RMS variation due to thermal noise; this was found to be approximately constant across the band.

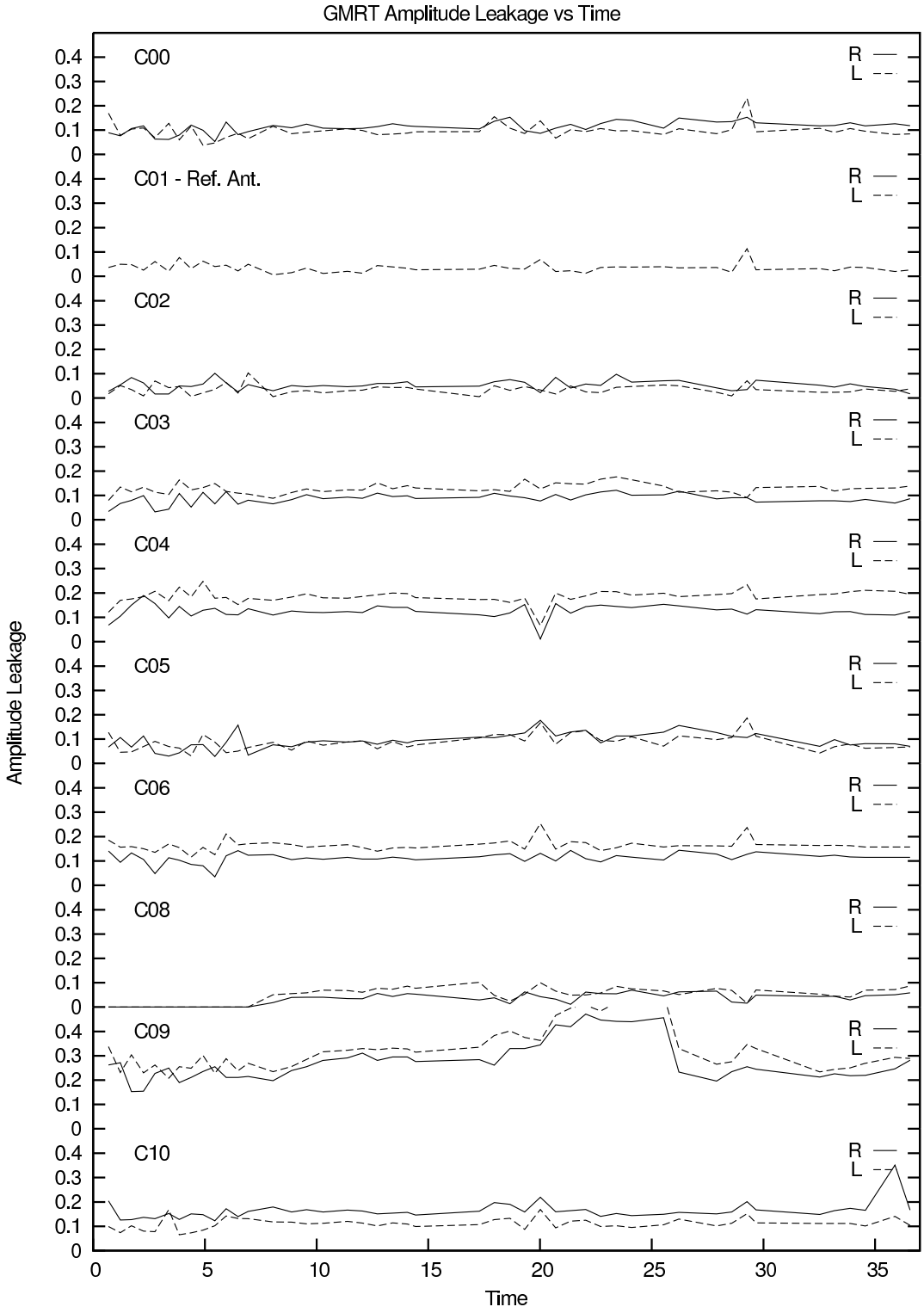

Figure 4.5: A plot of the short-term time-variability of the leakages across the GMRT band at 610 MHz for a single channel near the centre of the bandwidth. The variation in the amplitude leakage of antennas C00–C10 is shown as a function of time throughout the four consecutive observations. The time axis is in hours starting from 2010 Jan 09, 8:00 IST. Data with amplitudes of zero are a consequence of flagging – these data have been excluded from the RMS calculations.

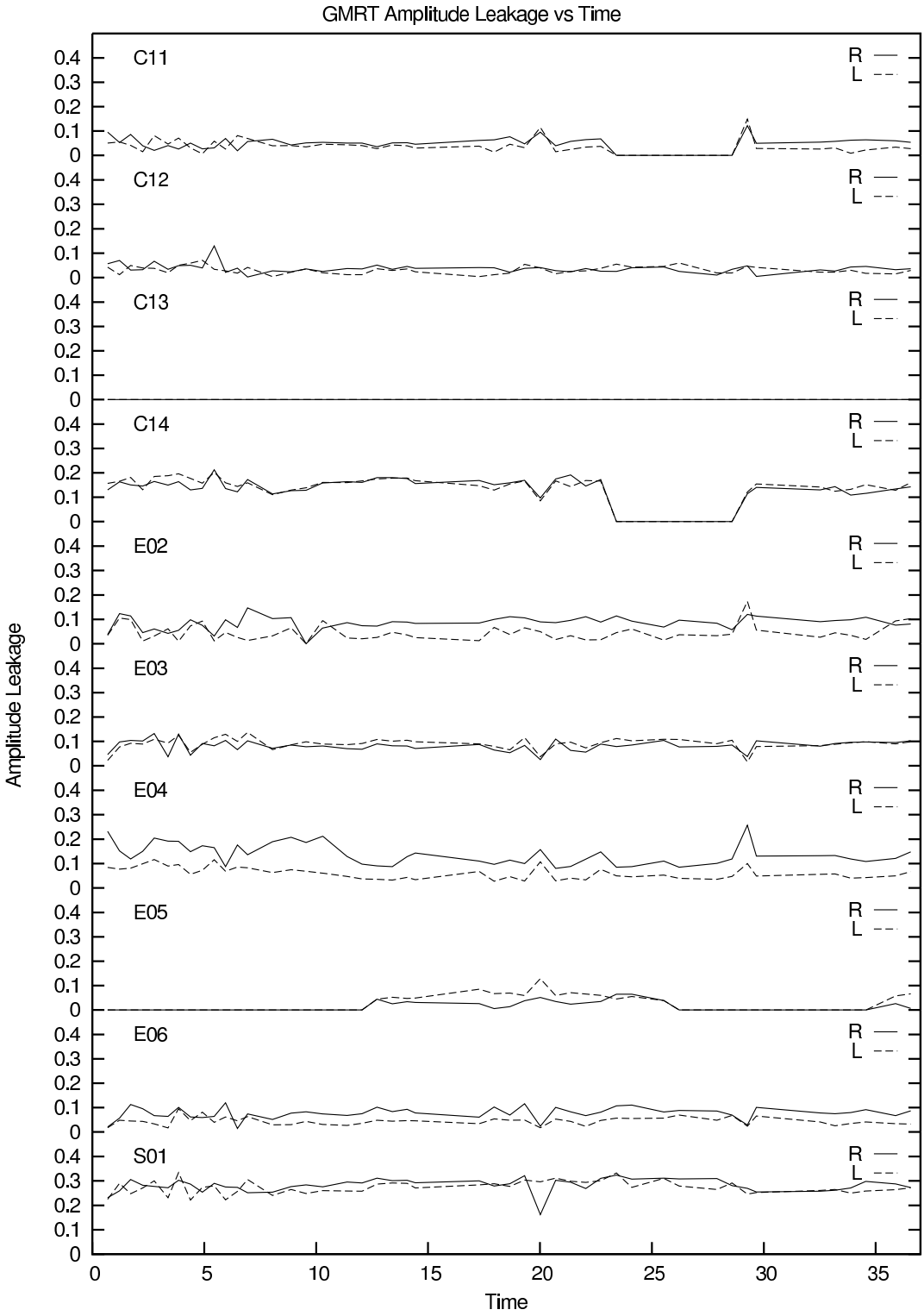

Figure 4.6: Similar to Figure 4.5, but for antennas C11–S01.

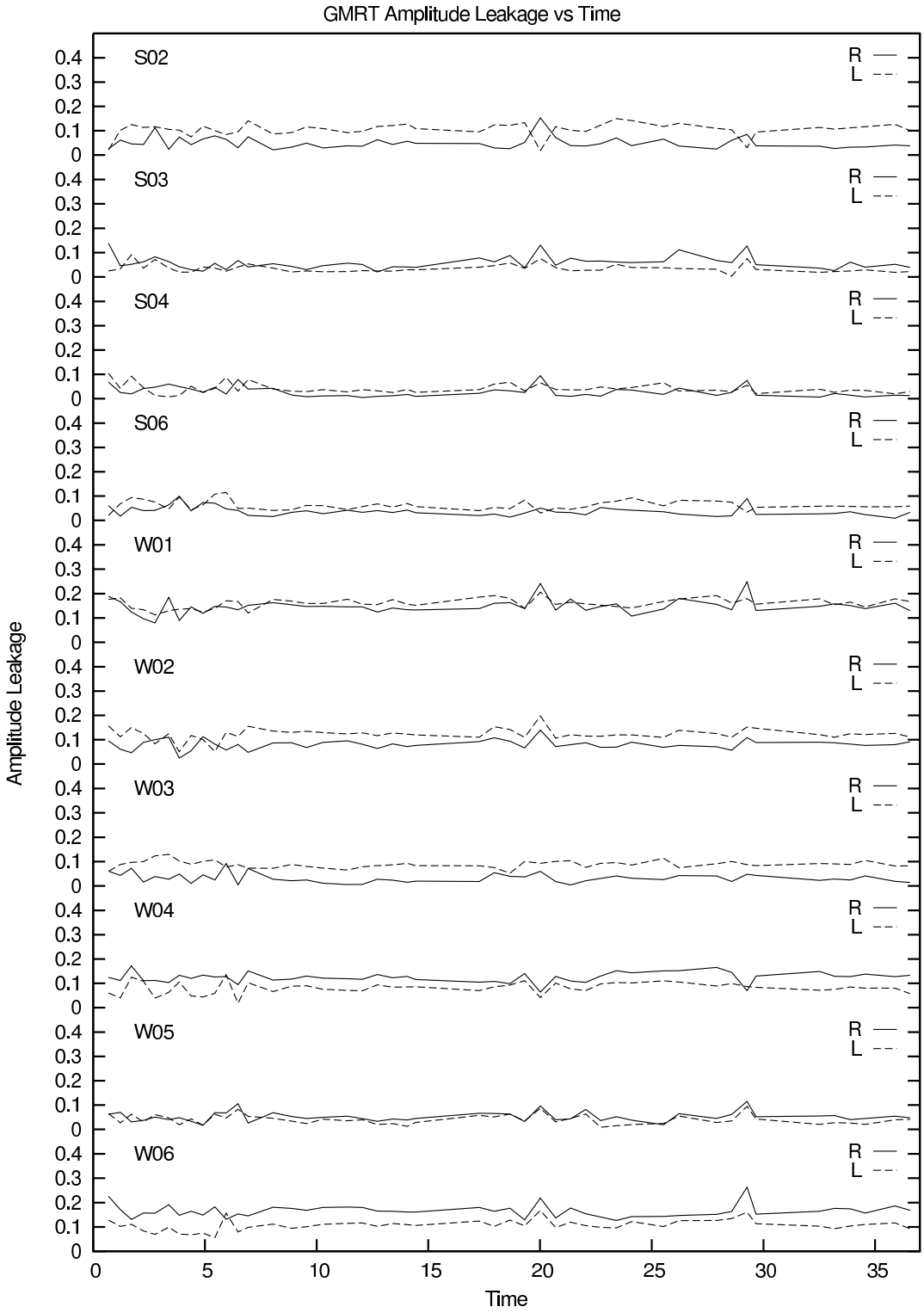

Figure 4.7: Similar to Figure 4.5, but for antennas S02–W06.

After polarisation calibration, the matrix of *RL* and *LR* phases displayed by RLDIF shows that the mean phase of antennas C09 and E02 is offset from the matrix average. This offset can also be seen in plots of the real versus imaginary values of the *RL* and *LR* visibilities, as shown in Figure 4.8. The offset is present in all four of the observations used for the analysis. While C09 has the highest leakage of all antennas during these observations, E02 has leakage below the mean level. The data appear consistent with the effects of residual time-dependent instrumental polarisation. The cause of this time-dependent instrumental polarisation at 610 MHz is unknown. Nevertheless, both antennas were flagged – with the *RL* and *LR* visibilities being removed from every observation. Both antennas are physically located within or near to the central square, which fortunately minimises the size of the gaps in the *uv*-coverage that results from antenna removal.

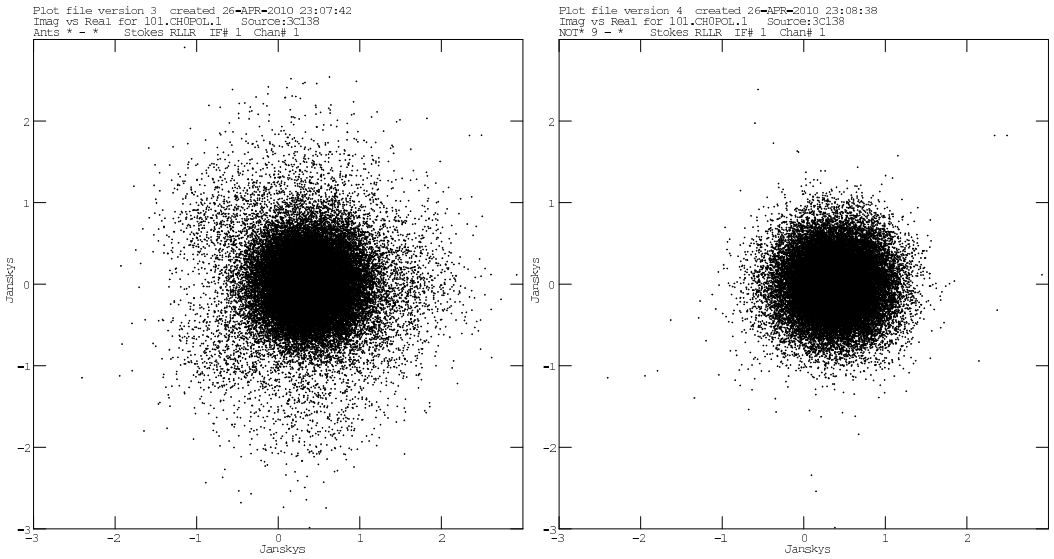

Figure 4.8: Real and imaginary plots of 3C138's visibilities, with antenna's C09 and E02 remaining in the data (left) and with both antennas flagged (right).

This information was provided to staff at the GMRT in 2010. Although the analysis of time-dependence has not been repeated, the offset in *RL* and *LR* phase was no longer present for either antenna as of observing cycle 19 (as determined from observations taken in 2011 January – see Chapter 3). However, similar offsets have occasionally been identified in more recent observing cycles. Systematic offsets in the matrix of *RL* and *LR* phases should therefore be identified, with such antennas removed from the data analysis.

Taking into account the sensitivity limit of these observations, the analysis shows that the instrumental polarisation of the median antenna is essentially independent of time. Leakages vary by $< 2\%$ over several days and $\lesssim 0.5\%$ over the length of a typical observation. It is therefore feasible that instrumental polarisation solutions from one observation can be copied to another in an adjacent observing block.

4.2.2 Long-Term Stability

The GMRT leakages at 610 MHz vary substantially over long time scales. The amplitude of the instrumental polarisation in four observing epochs, between cycle 17 to 21, is shown in Figure 4.9. The cycle 17 and 19 data both use antenna 2 as the reference antenna, antenna 8 is used as the reference antenna in cycle 20, while the cycle 21 observations use an unpolarised calibrator for polarisation calibration. The cycle 19 leakages are not well-determined due to a faint calibrator source. Nevertheless, there are clear similarities with the cycle 20 leakages – despite both observations using different reference antennas. This is a reassuring indication that the reference antennas were good choices with low leakages.

Qualitatively, it could be argued that the leakages of the central square and western arm tend to be of higher magnitude and show more time-dependence. This could be related to RFI, which intrinsically affects short baselines more substantially. The RFI environment may be impacted by the nearby town of Narayangaon (for the western arm) and the GMRT laboratory and other buildings on site (for the central square). High levels of RFI can indeed affect the leakages – as shown in cycle 21, where three affected channels have discrepant leakages. Nevertheless, narrow-band interference fails to explain the similarities between the cycle 19 and 20 observations, which were both subject to very different RFI patterns. There appears to be another mechanism responsible for the leakages changing from one maintenance cycle to the next, although there is currently insufficient evidence to conclude what causes these variations.

Some of the most dramatic leakage variations are understood. Antenna 29 (W05) required a 'Turn buckle' replacement 10 days after the cycle 19 observations, while antenna 30 (W06) was equipped with an experimental wide-band feed during this same period. In cycle 21, antenna 21 (S02) required a new feed to address the poor polarisation isolation at 610 MHz (Nimisha Kantharia: priv. comm.) – this is seen in Figure 4.9.

The cause of more subtle variations is not clear. The cause of the high leakage amplitudes and long-term fluctuations necessitate further investigation. GMRT staff are currently enhancing their monitoring of the polarisation isolation as a consequence of these long-term fluctuations. They have recently extended their procedures so that data across the entire band is now analysed (Nimisha Kantharia: priv. comm.). It is hopeful that these new procedures will allow further understanding of the long-term stability and for the high leakage of several antennas to be consistently reduced.

The leakages at 325 MHz also vary on long time scales, as shown in Figure 4.10.

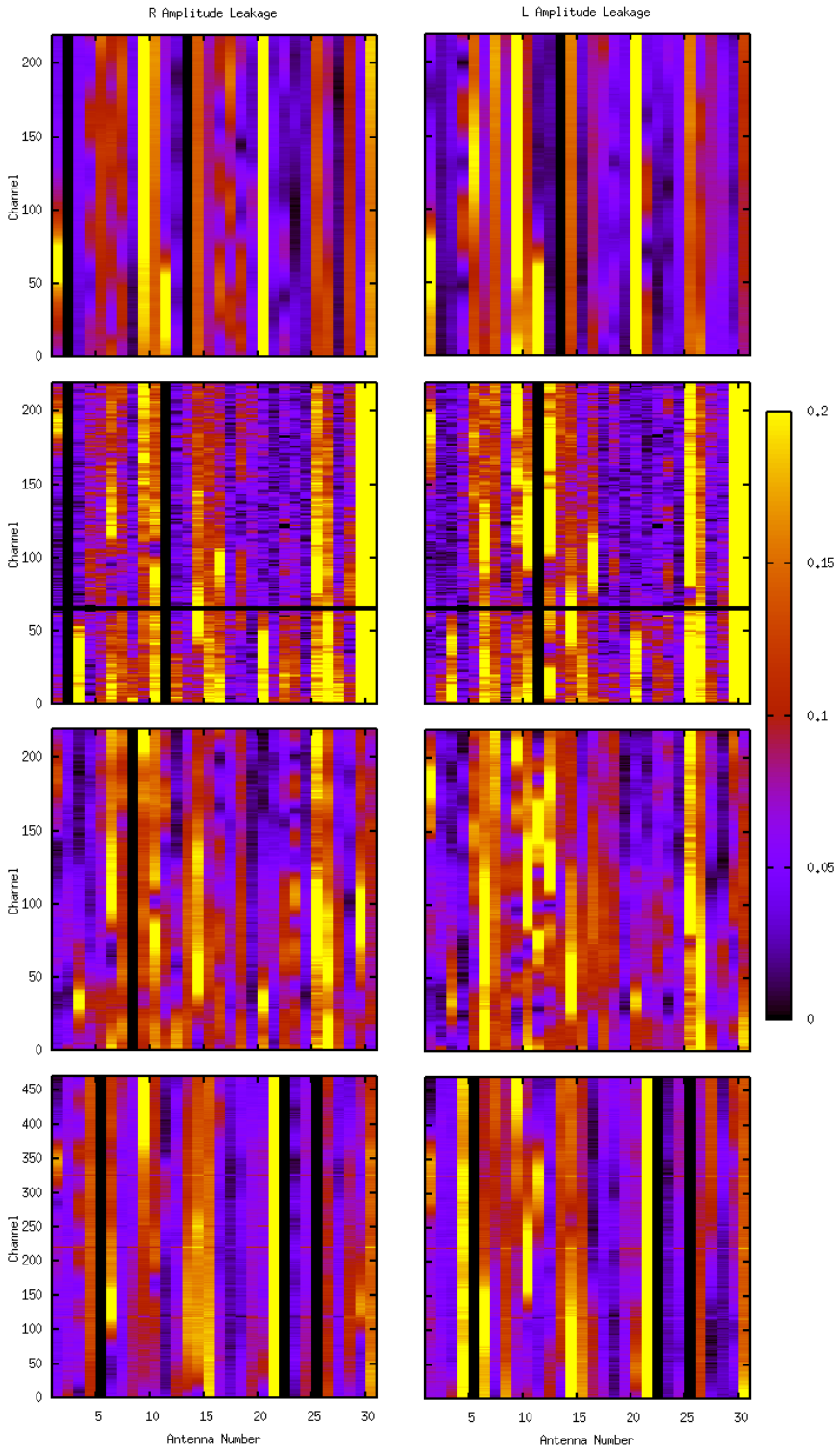

Figure 4.9: The amplitude of 610 MHz GMRT leakages at different observing epochs. The plots show the antenna number (x-axis) versus the channel number (y-axis). The pseudo-colour scale indicates the leakage from 0–20%. The R leakage (left column) and L leakage (right column) are shown for observing cycle 17 (top row), 19 (second row), 20 (third row), and 21 (bottom row). Antennas shown in black across the band in both R and L have been flagged from the data.

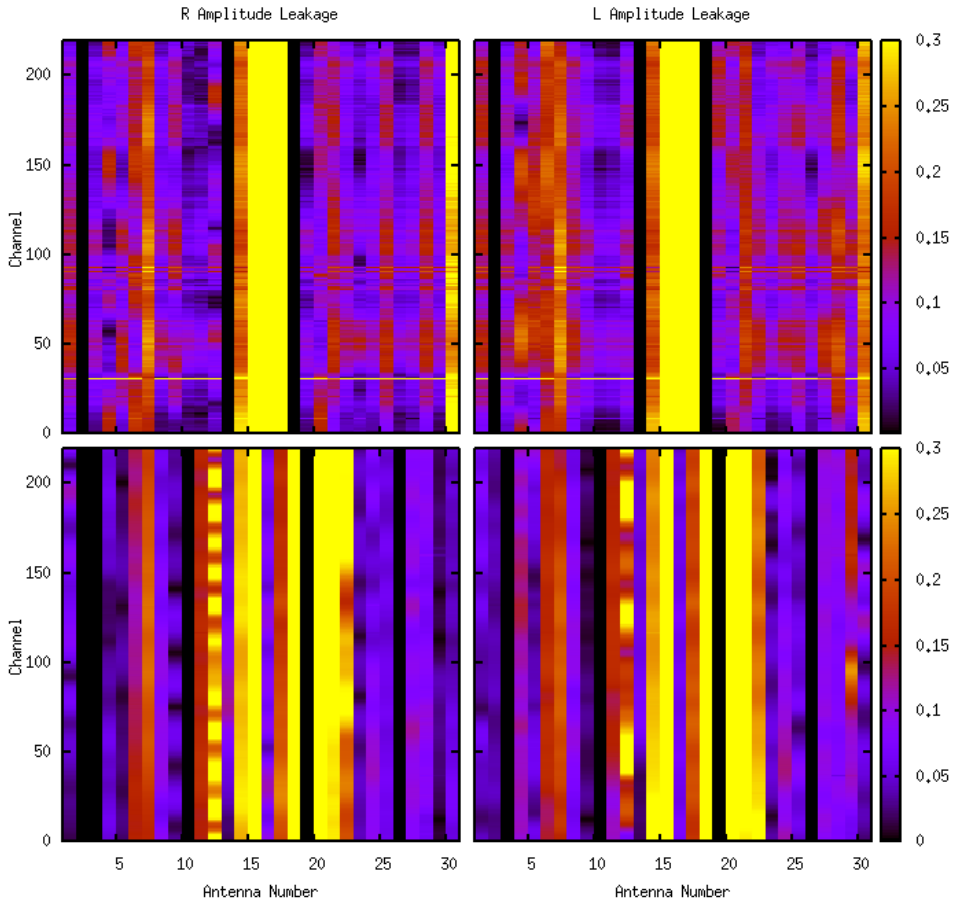

Figure 4.10: The amplitude of 325 MHz GMRT leakages at different observing epochs. The plots show the antenna number (x-axis) versus the channel number (y-axis). The pseudo-colour scale indicates the leakage from 0–30%. The R leakage (left column) and L leakage (right column) are shown for observing cycle 17 (top row), and 20 (bottom row). Antennas shown in black across the band in both R and L have been flagged from the data.

4.3 Applying Instrumental Polarisation Solutions

4.3.1 In the *uv*-plane

In Section 4.1, I calculated the instrumental polarisation of the GMRT at 610 MHz. I now investigate the effect of applying these leakages to GMRT data.[6]

The effects of applying instrumental polarisation solutions to *uv*-data are shown in Figure 4.11. Solutions were applied to the unresolved point source 3C138, which is expected to be polarised at 610 MHz. The amplitude of the *RL* and *LR* visibilities becomes essentially constant as a function of *uv*-distance. The phase is also essentially constant, with the *RL* and *LR*

[6]The leakages were applied in AIPS using DOPOL=1, which also removes the effects of χ-rotation at the phase-centre from the data.

visibilities being split into two distinct contributions – indicative of a polarised source.

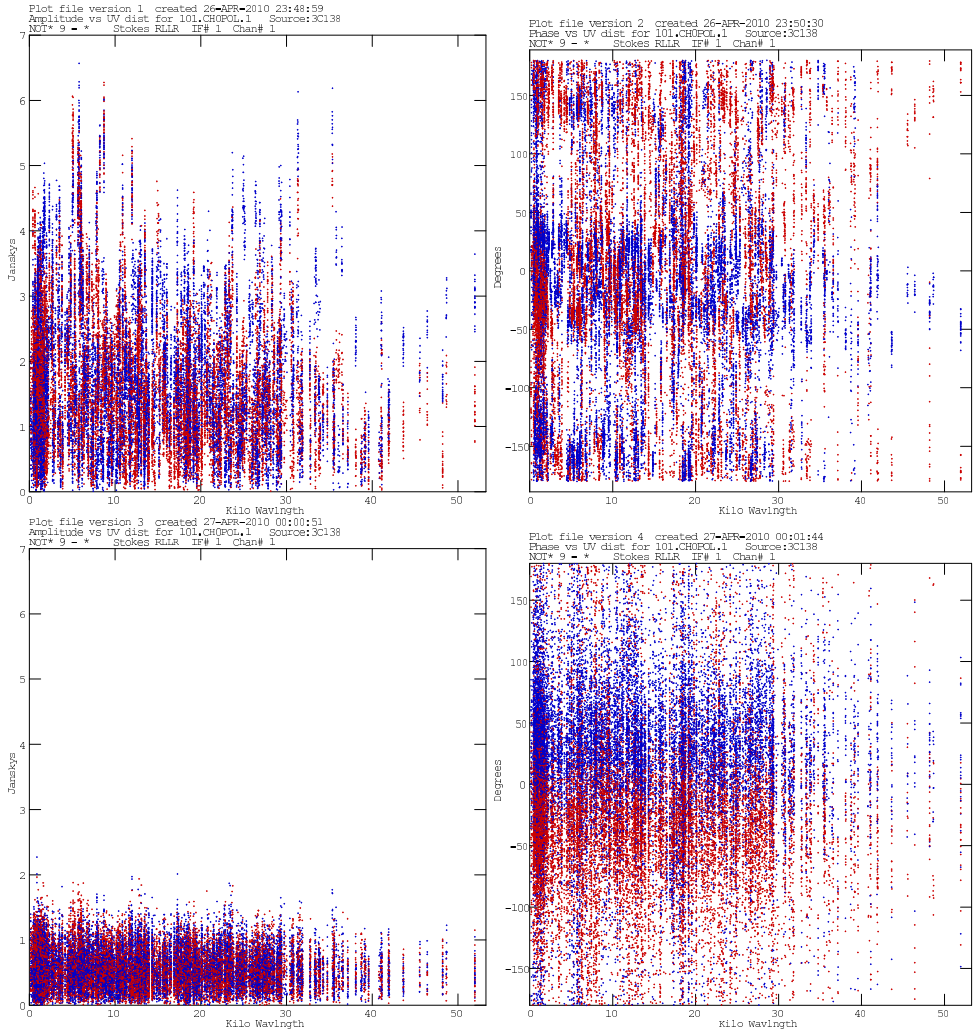

Figure 4.11: Amplitude (left column) and phase (right column) of the *RL* (red) and *LR* (blue) visibilities as a function of *uv*-distance ($\sqrt{u^2 + v^2}$) for calibrator source 3C138 in the 17_060_2 observation. Shown with instrumental polarisation solutions: (i) not applied (top row), and (ii) applied (bottom row).

The spread of the *RL* and *LR* phases (σ_{RL}) can be investigated using the task RLDIF. This was done for various observations using the sources 3C138 and 3C286. σ_{RL} is typically 10–30° for these sources at 610 MHz. As antennas with high leakages have been flagged from the data, the high σ_{RL} values are likely due to the source's weak polarised emission at these frequencies, and the highly frequency-dependent instrumental polarisation.

The frequency-dependent instrumental polarisation has been averaged together within each spectral channel of finite bandwidth. This means that only the average instrumental polarisation in each channel can be calibrated. The mean difference in leakage phase between two adjacent spectral channels was found to be $17.9 \pm 2.0°$ in observation 17_052, with a minimum difference

of 5.3° and a maximum of 42°. This suggests the average antenna can only be accurately calibrated within ∼ 9°, with some antennas only being calibrated to within ∼ 20°. The only way to improve this would be to observe with increased spectral resolution. Nevertheless, increased spectral resolution would be at the expense of a decrease in signal-to-noise (s/n).

The value of σ_{RL} also varies for different sources. Lower values are consistently found for 3C138, and in some observations approaches ∼ 5°. Generally, following instrumental polarisation calibration, 3C138 has $\sigma_{RL} \approx 10°$, while 3C286 has $\sigma_{RL} \approx 25°$.

This difference could feasibly be caused by s/n considerations but the polarised flux densities of 3C138 and 3C286 are ∼ 0.379 Jy and ∼ 0.562 Jy respectively at 610 MHz, i.e. the polarised flux from 3C138 is less than from 3C286. There must be another explanation. One possibility is increased levels of low-level RFI for sources that are located closer to the horizon. The declination at the zenith is always equal to the latitude on Earth, and the GMRT is located at a latitude of 19d06′(N). 3C286 has a declination of 30d30′, and 3C138 has a declination of 16d38′. 3C138 will therefore move closer to the zenith, and rise further from the horizon. This may partially explain the observed values – indeed σ_{RL} for 3C286 tends to increase when the source is rising or setting. Nevertheless, σ_{RL} tends to remain approximately constant for 3C138 – regardless of the source's location in the sky.

The isolation of these sources in the FOV could also be responsible, with other nearby sources complicating the measurements of 3C138 and 3C286. Nevertheless, as shown in Figures 4.15–4.16, 3C286 appears to be more isolated than 3C138. While the cause is not fully understood, the measurements do indicate that 3C138 is a better choice for EVPA calibration (see Section 4.4).

In addition, any variation in the mean *RL* and *LR* phase during an observation is indicative of residual time-dependent effects. These can be caused by uncorrected instrumental polarisation, time-dependent instrumental polarisation, the $R - L$ phase stability of the reference antenna, low-level RFI, or ionospheric Faraday rotation. Repeated observation of 3C286 over a full-track observation places an upper limit of $< 4.5°$ on the time-dependent contribution to the EVPA at 610 MHz, while observation of 3C138 gives an upper limit of $< 0.3°$.

4.3.2 In the image-plane

The *uv*-data have now been calibrated for the effects of instrumental polarisation, and it is possible to perform a Fourier transform to create polarimetric images. These images can also be used as a diagnostic of the GMRT's instrumental properties.

The calibrators 3C48, 3C138, and 3C286 were imaged in Stokes Q, U, and V. Images of the band-averaged P and V were created using the individual images from each spectral channel. For the calibrators, diagnostic images of the band-averaged Q and U were also made. The band-averaged Q/U images were also combined into a P image. No corrections for the EVPA had yet been applied.

4.3.2.1 Residual Instrumental Polarisation

The source 3C48 is believed to be depolarised at 610 MHz, and the VLA calibrator manual reports $\Pi < 0.5\%$ at 20 cm. Any detection at 610 MHz is therefore due to residual instrumental polarisation. Measuring the magnitude of this uncorrected instrumental polarisation places an upper bound on the quality of the calibration. Images of 3C48 in I and band-averaged P are shown in Figure 4.12.

The Π peak for the brightest pixel in Stokes I is 0.23%, after correction for the Rician bias using the mean noise in a single channel. This suggests the calibration procedure limits residual intrumental polarisation to $< 0.25\%$ in terms of percentage polarisation. This quantity varies between observations, although a residual instrumental polarisation of $< 0.5\%$ is frequently obtained. Under most circumstances, analysis should be conservatively restricted to sources with $\Pi > 0.5\%$.

The multiple artefacts in the P image, as shall be shown, are likely the result of residual phase leakage errors and the limited *uv*-coverage of this snapshot observation.

4.3.2.2 Fractional Polarisation Checks

Images of calibrator sources with a known polarisation fraction are a useful check that Π is as expected. 3C138 is polarised with $\Pi \approx 3\%$ at 49 cm (Tabara & Inoue 1980), and 3C286 has been found to have $\Pi \approx 2.4\%$ at 608.5 MHz (Spoelstra 1997). The Rician bias corrected values of measured fractional polarisation for 3C138 and 3C286 at 610 MHz are shown in Figures 4.13 and 4.14 respectively.

Images of 3C138 and 3C286 in Stokes I, band-averaged P, and P using band-averaged Q/U are presented in Figures 4.15 and 4.16 respectively. Using the band-averaged P images, 3C138 has $\Pi = 3.09 \pm 0.02\%$ and 3C286 has $\Pi = 2.73 \pm 0.02\%$. Given the residual instrumental polarisation of 0.23%, these values are in reasonable agreement with previous observations.

The band-averaged P images contain more artefacts than the P images from band-averaged Q/U. The cause of these artefacts must therefore change with frequency. Two possible effects are: (i) the *uv*-coverage which varies due to the flagging and is also severely limited for these short calibrator scans, and (ii) residual phase leakage errors that change across the band. To show which of these effects is dominant, Figure 4.17 displays an image of the phase calibrator in I and P. Note that the substantially increased *uv*-coverage removes the artefacts from the image. The peak fractional polarisation of the source is $\Pi = 0.143 \pm 0.004\%$, and therefore consistent with residual instrumental polarisation. Residual phase leakage errors are still present close to the source. As can be seen in the images of 3C138 and 3C286, these residual errors quickly become buried in the noise for sources with higher fractional polarisation.

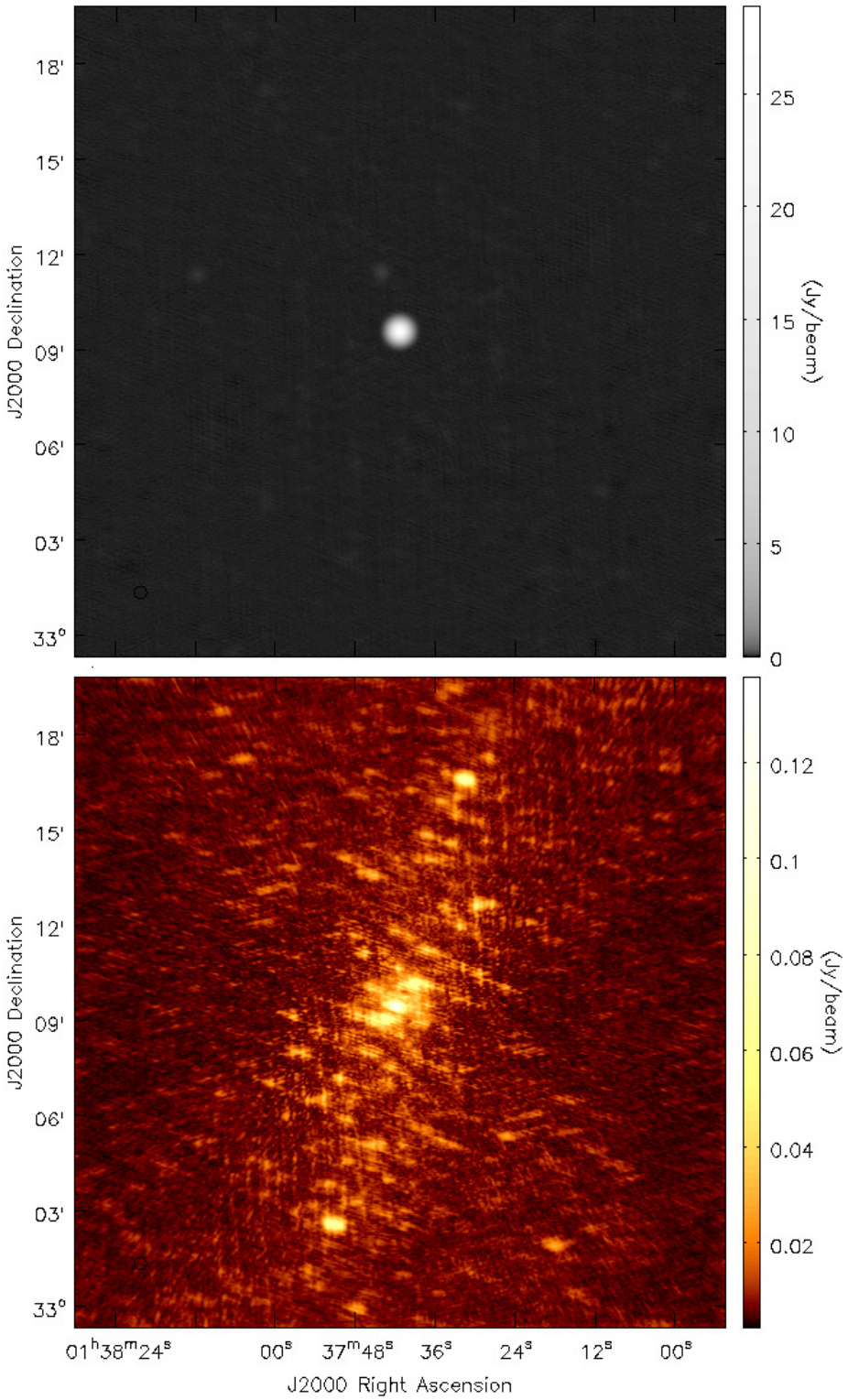

Figure 4.12: Images of the unpolarised flux calibrator 3C48 from observation 17_060_1 in Stokes I (top) and band-averaged P (bottom). The band-averaged P image shows the residual instrumental polarisation. The brightest pixel in Stokes I has $\Pi = 0.23\%$. Both images have a resolution of $24'' \times 24''$. The P image has not been corrected for the effects of Rician bias.

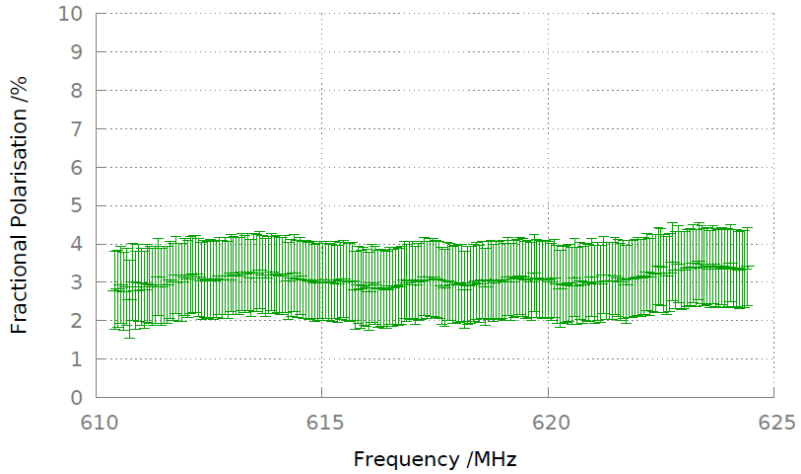

Figure 4.13: The fractional polarisation, Π, of the calibrator 3C138 from observation 17_052 as a function of observing frequency. The values have been corrected for the effects of Rician bias using σ_{QU} for each individual channel.

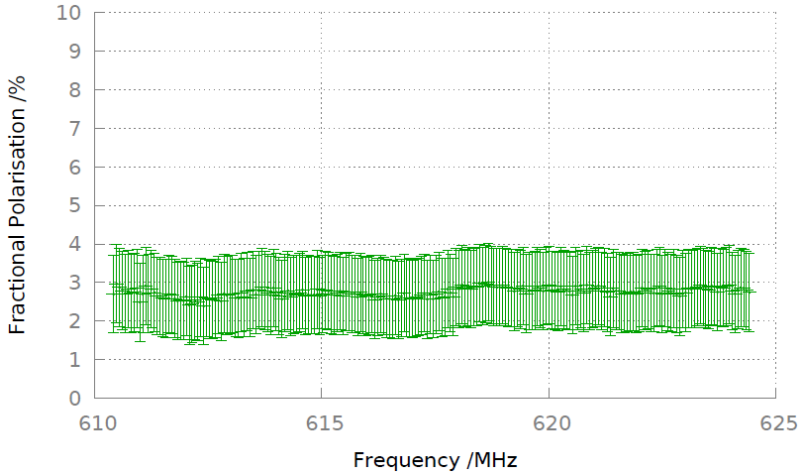

Figure 4.14: The fractional polarisation, Π, of the calibrator 3C286 from observation 17_052 as a function of observing frequency. The values have been corrected for the effects of Rician bias using σ_{QU} for each individual channel.

4.3.2.3 Circular Polarisation

Circular polarisation is weak in most radio sources at low frequencies (e.g. Cotton et al. 2003). Checks on the Stokes *V* images therefore provide another useful diagnostic of the GMRT's polarisation response.

Measurements of circular polarisation are dependent on being able to accurately measure the difference between *R* and *L*. This is notoriously difficult for circular feeds, and is subject to a large number of errors due to the delicate measurement of differences between the *RR* and *LL* visibilities. These errors include amplitude calibration errors, gain variations with time, beam

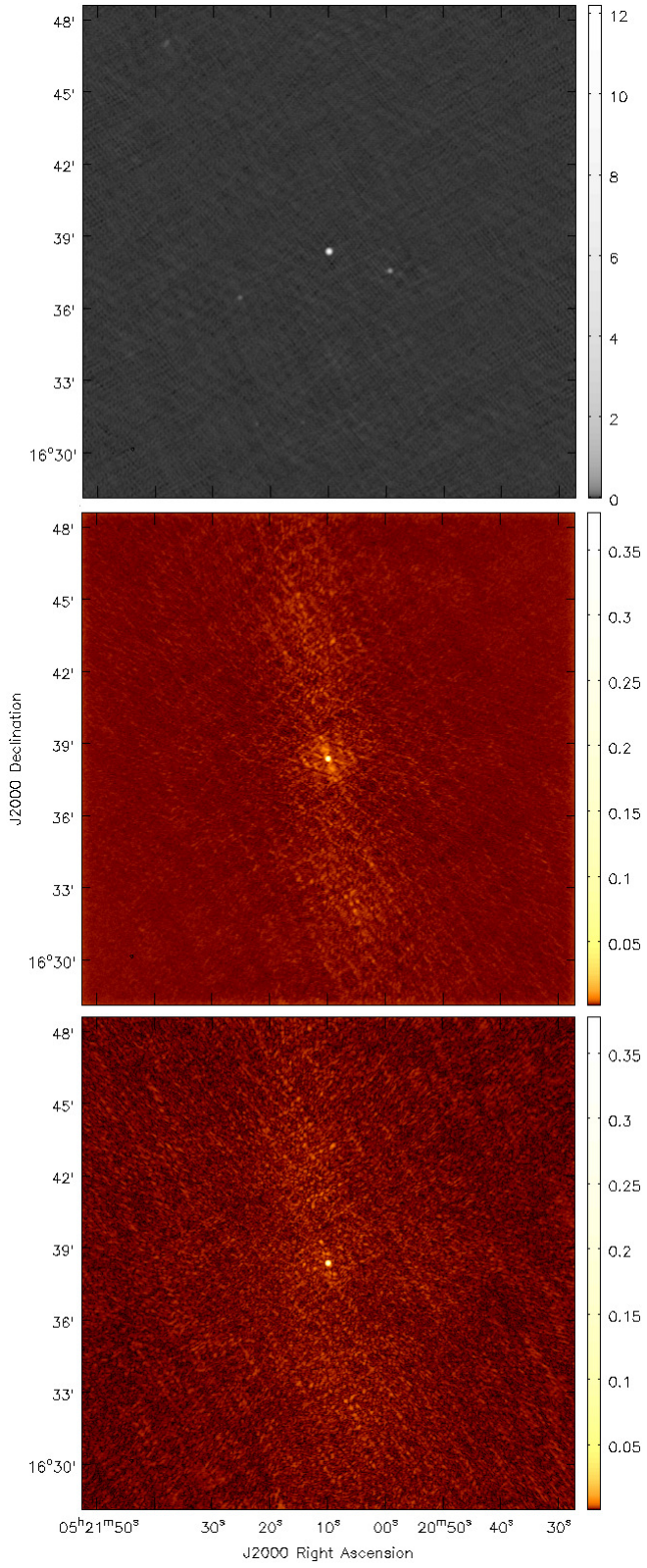

Figure 4.15: Images of the flux calibrator 3C138 from observation 17_052 in Stokes I (top), band-averaged P (middle), and P from band-averaged Q/U (bottom). All images have a resolution of $7'' \times 7''$. The P images have not been corrected for the effects of Rician bias, and the pseudo-colour scales are in units of Jy beam^{-1}.

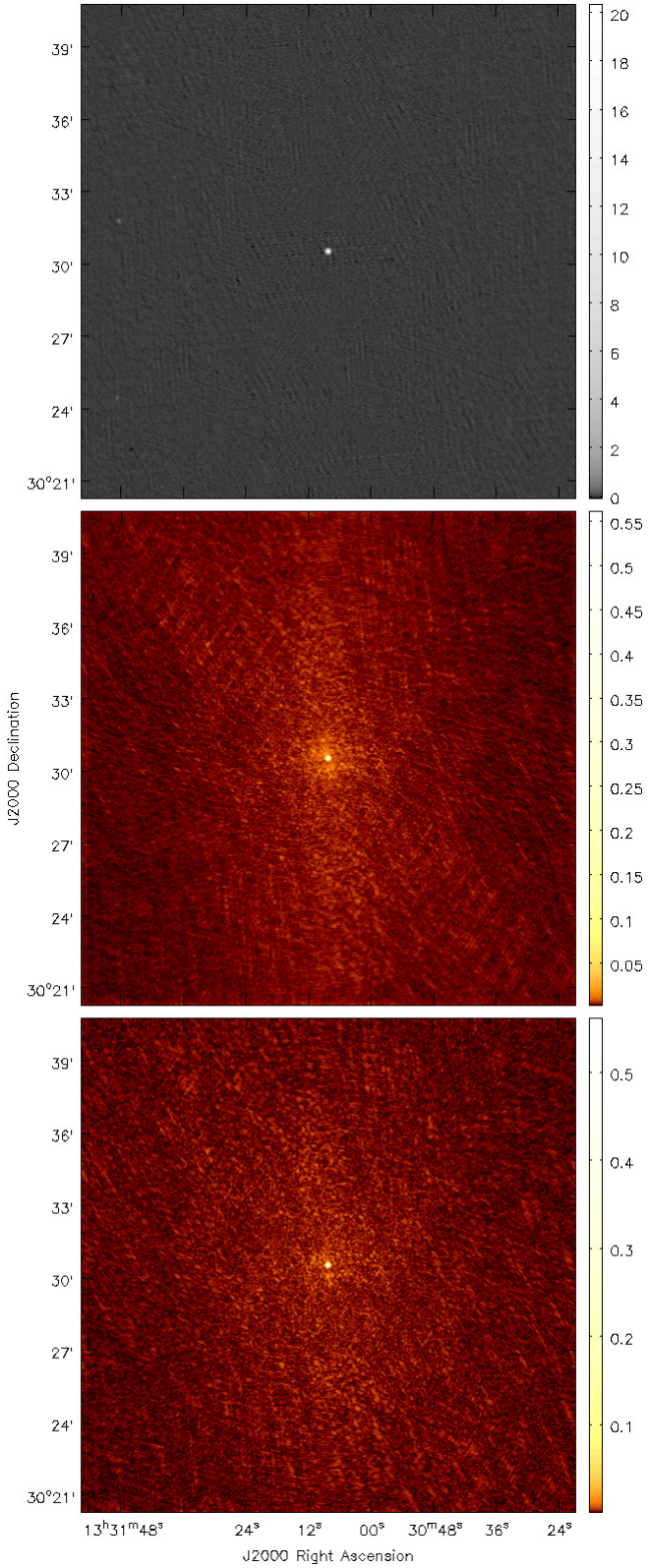

Figure 4.16: Images of the flux calibrator 3C286 from observation 17_052 in Stokes I (top), band-averaged P (middle), and P from band-averaged Q/U (bottom). All images have a resolution of $7'' \times 7''$. The P images have not been corrected for the effects of Rician bias, and the pseudo-colour scales are in units of Jy beam^{-1}.

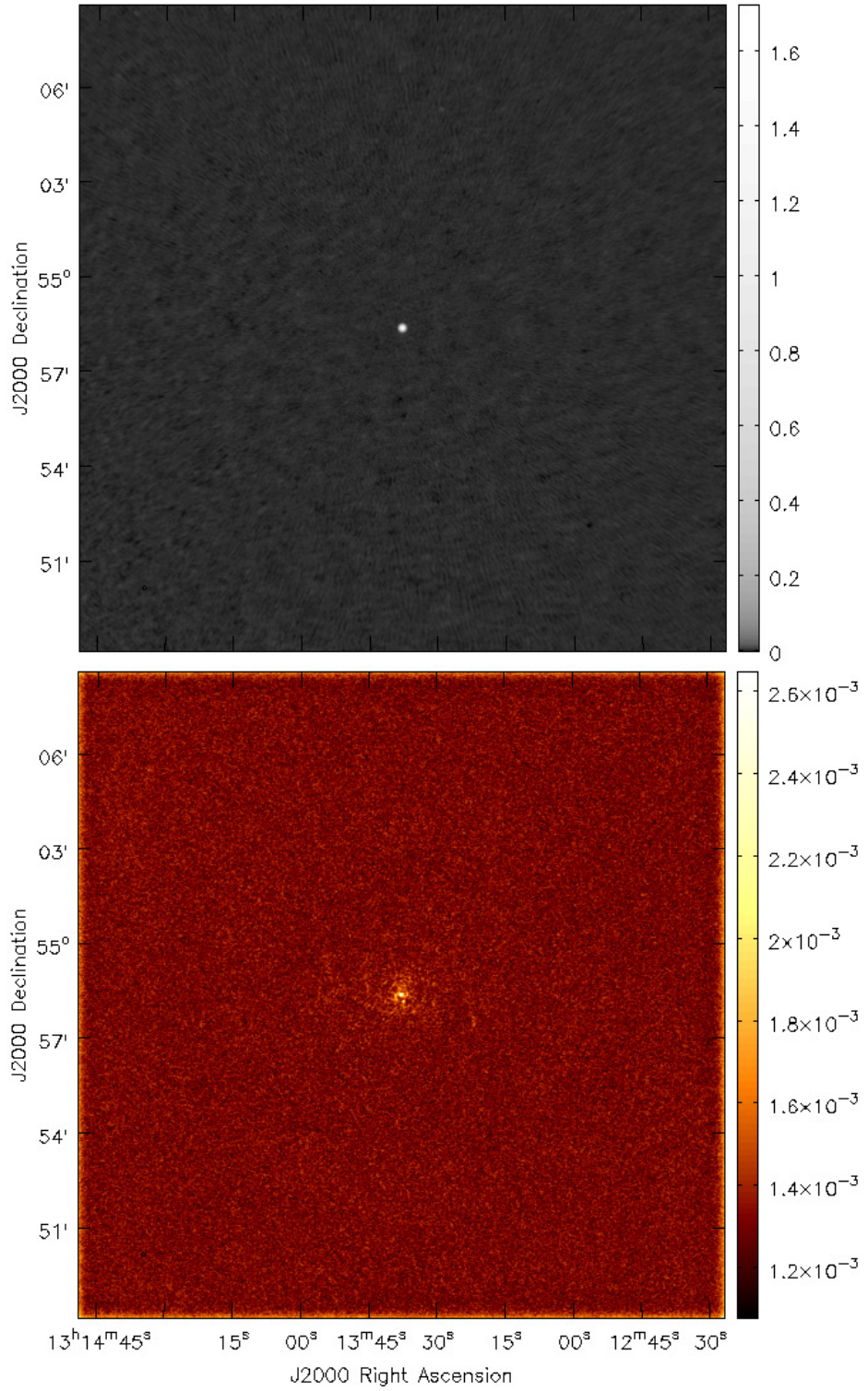

Figure 4.17: Images of the phase calibrator J1313+549 from observation 17_052 in Stokes I (top) and band-averaged P (bottom). Both images have a resolution of $7'' \times 7''$. The P image has not been corrected for the effects of Rician bias, and the pseudo-colour scales are in units of Jy beam^{-1}.

squint, second-order polarisation leakage effects, and the effects of RFI.

Stokes V images of calibrator sources are shown in Figure 4.18. Independent measurement of sources such as 3C138 suggest there is no intrinsic circular polarisation at low frequencies (Cenacchi et al. 2009). The images shown here are in agreement with this. The circular polarisation fraction, Π_C, for the brightest pixel in Stokes I is 0.001% (0.3σ), 0.003% (0.9σ), 0.007% (1.3σ), and 0.005% (0.4σ) for 3C138, 3C286, 3C48, and J1313+549 respectively. While the on-axis behaviour for Stokes V is clearly excellent, numerous high intensity artefacts are visible off-axis in locations with no corresponding Stokes I emission (see Chapter 6).

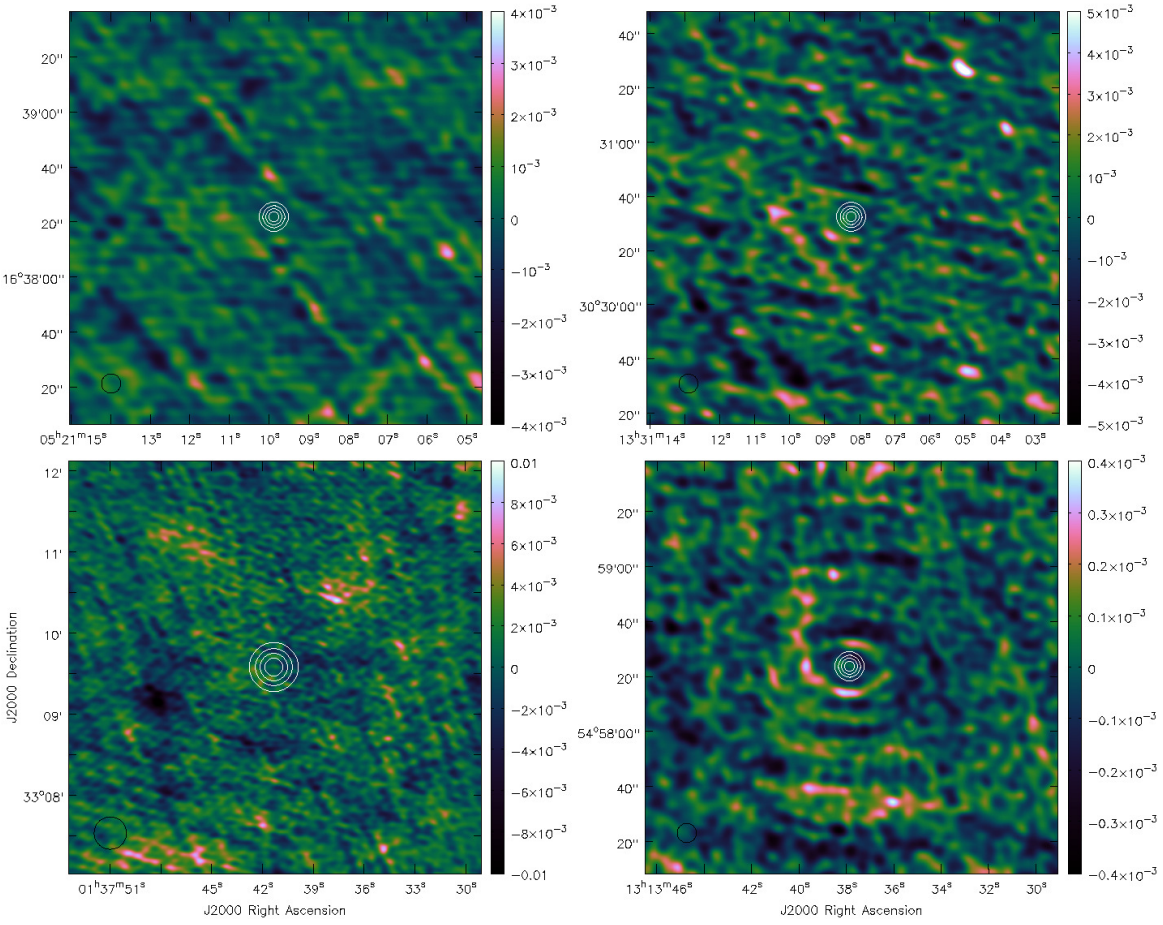

Figure 4.18: Stokes V images of the four calibrator sources overlaid with Stokes I contours. The pseudo-colour 'cube-helix' scales are in units of Jy beam^{-1} (Green 2011). Contours are at 0.2, 0.4, 0.6, and 0.8 times the peak brightness. The calibrators shown are 3C138 (top left), 3C286 (top right), 3C48 (bottom left), and J1313+549 (bottom right). All images have a resolution of $7'' \times 7''$, with the exception of 3C48 which has a resolution of $24'' \times 24''$.

4.3.2.4 Instrumental Rotation Measure

No corrections have yet been made for the EVPA. I therefore extract the EVPA for 3C138 from every channel by taking the brightness in Q and U from the pixel of peak brightness in Stokes I. The EVPA is then calculated using equation 2.11. A plot of the EVPA versus λ^2 across the observing band for 3C138 is shown in Figure 4.19. The GMRT has a large instrumental RM. In the plot shown, the instrumental RM is -678 ± 5 rad m^{-2}. This has been found to vary slightly depending on the observation, but is always of a similar magnitude. The true EVPA of a source on the sky is lost during the calibration process because the phase of the leakage of the reference antenna is set to zero during leakage calculation. As the leakages vary rapidly with frequency, it is essentially unsurprising that a large instrumental RM is present.

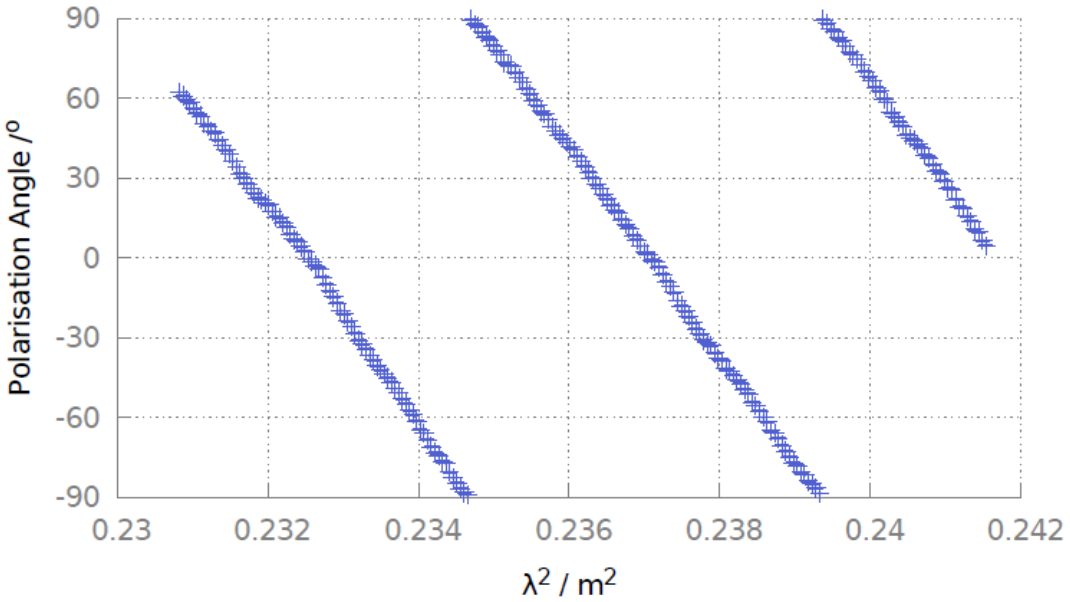

Figure 4.19: A plot of the EVPA versus λ^2 across the observing band for 3C138. No EVPA correction had yet been applied. 3C138 has a low intrinsic RM and the shown variation is a result of the GMRT's instrumental RM. Errors in Φ_{EVPA} are plotted but not visible, they are roughly 1–2°.

4.4 EVPA Calibration

When solving for the instrumental leakage, the absolute value of the phase offset between R and L is left as an unconstrained degree of freedom. A change in this $R - L$ phase difference is equivalent to a change of parallactic angle, and equations 2.22–2.25 show that this will cause a rotation of $Q \pm iU$. The EVPA, Φ_{EVPA}, is related to Q and U through equation 2.11 – resulting in a rotation of the apparent EVPA of a source. This is important for GMRT measurements due

to the instrumental RM (see Section 4.3.2.4), which causes rapid EVPA variations across the observing band. These variations need to be calibrated so that source RMs can be retrieved.

If the $R - L$ phase difference is constant during an observation, EVPA calibration can be carried out using a short observation of a highly polarised calibrator with known, stable polarisation properties. The $R - L$ phase difference does not vary significantly with time at the GMRT, as measured in Section 4.3.1. At the VLA, the EVPA is typically calibrated using an observation of 3C138 or 3C286. The correction to be applied to VLA data is determined using a 'matrix method' i.e. by examining the matrix of *RL* and *LR* phases via the task RLDIF. This correction is then applied using the task CLCOR.

As the corrections are dependent on a source's RM and Φ_0, these must be known a-priori and interpolated across the observing band using equation 2.32. Both 3C138 and 3C286 have been shown to have low intrinsic integrated RMs at higher frequencies. 3C138 has been shown to have a RM= -2.1 ± 0.7 rad m^{-2} and $\Phi_0 = 170 \pm 1°$, while 3C286 has been shown to have a RM= -1.2 ± 0.8 rad m^{-2} and $\Phi_0 = 33 \pm 1°$ (Tabara & Inoue 1980). Other measurements have provided consistent values for RM and Φ_0 (Simard-Normandin et al. 1981; Broten et al. 1988), although all assume the RM can be determined from a single straight line fit and are also subject to $n\pi$ ambiguities. Nevertheless, these values for 3C138 and 3C286 were assumed initially.

Preliminary attempts were made to correct the EVPA of the GMRT using the matrix method. This method is known to lose accuracy for sources with substantial resolution or for data with low s/n (Cotton 1993). In these cases, the correction can be calculated using an 'image method'. The image method allows the sum of the Q and U clean components to be taken from images of the EVPA calibrator. For data with low s/n, the Q and U values from the brightest Stokes I pixel can be used. These values can be used to calculate the necessary correction, and are applicable to GMRT data given the large standard deviation in the *RL* and *LR* phases (Section 4.3.1). The correction to be applied to each spectral channel using CLCOR is therefore given by

$$\mathrm{clcorprm}(1) = 2\left[\Phi_0 + \mathrm{RM}\left(\frac{c}{\nu_{\mathrm{LOW}}}\right)^2 - 2\mathrm{RM}\lambda_0^2\frac{\Delta\nu}{\nu_0}\frac{i_{\mathrm{CHAN}}}{N_{\mathrm{CHAN}}}\right] - \arctan\left(\frac{\sum U}{\sum Q}\right), \tag{4.2}$$

where RM and Φ_0 are those of the EVPA calibrator, ν_{LOW} is the lowest observing frequency of the band, λ_0^2 is the mean value of the squared wavelength within the bandwidth, $\Delta\nu$ is the bandwidth, ν_0 is the mean observing frequency, i_{CHAN} is the spectral channel number, N_{CHAN} is the total number of spectral channels output by the correlator, and $\sum Q/\sum U$ are the Q and U values determined from the images. A two-argument arctan function should be used to avoid any quadrant ambiguities. A comparison of the matrix- and image-based methods is shown in Figure 4.20. Due to the improved results using the images, this method was used for EVPA calibration.

The effect of EVPA calibration is to flatten the highly-frequency dependent leakage phase, as shown in Figure 4.3.

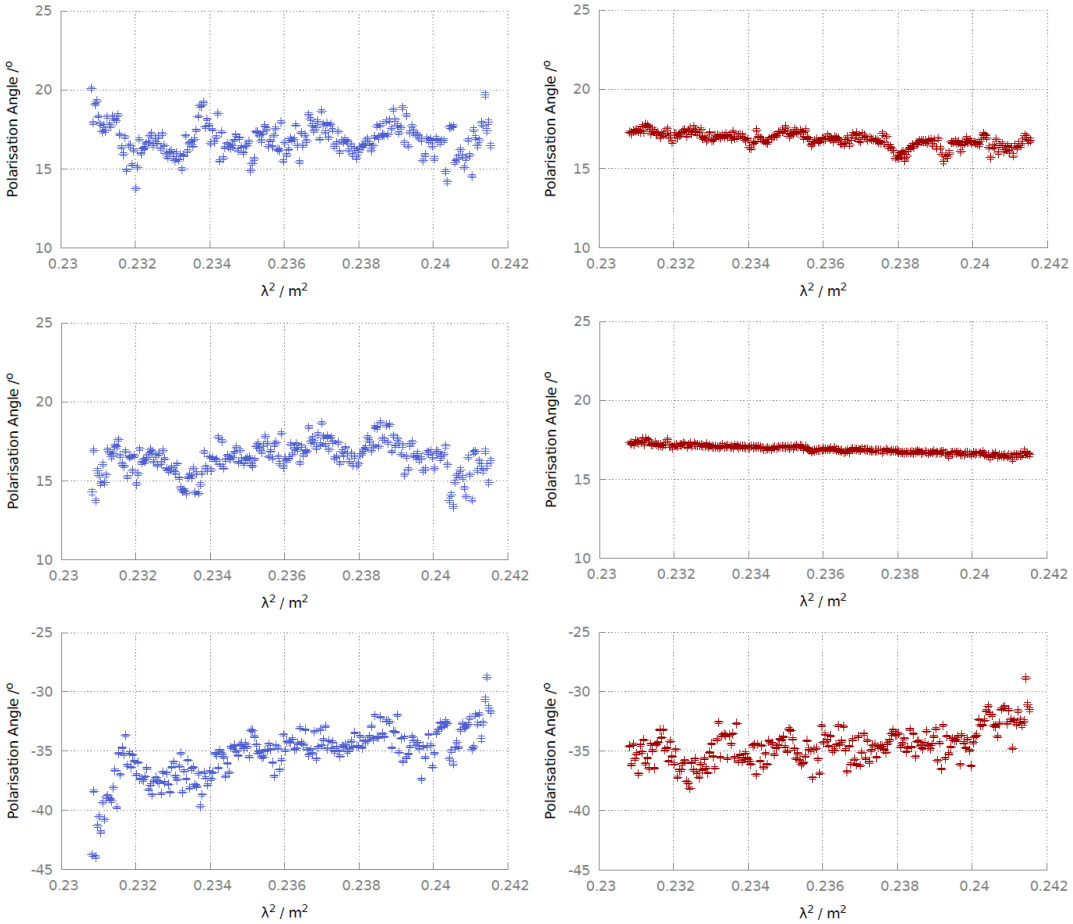

Figure 4.20: A comparison of the EVPA vs λ^2 for the two EVPA calibration methods. The effect of giving 3C286 a RM= -1.2 rad m^{-2} is shown after one iteration (top) and three iterations (middle), for the matrix-based (left column – in blue) and image-based (right column – in red) methods. The effect on the derived RM of 3C138 is also shown (bottom). All images were made with constant resolution across the band and excluded baselines smaller than 1 kλ, which are more prone to interference.

4.5 RM Ambiguities

Following EVPA calibration relative to 3C286, the RM of test sources were extracted from the data. The source 3C138 was expected to have a RM= -2.1 ± 0.7 rad m^{-2}, but the RM was found to be positive as shown in Figure 4.20. Initial RMs varied between observations, e.g. 6.1 ± 0.4 rad m^{-2} in cycle 17 and 11.5 ± 0.8 rad m^{-2} in cycle 20. This appears to be partially due to low-level RFI, as implementing a cut-off for small baselines (UVRANGE=1,0) during imaging provided RMs of 4.0 ± 0.4 rad m^{-2}, 4.5 ± 0.9 rad m^{-2}, and 10.2 ± 0.8 rad m^{-2} in cycle 17, 19, and 20 respectively.

Attempts to correct for systematics due to the delay-rate were made using the task FRING, although this only changed the RM by a maximum of 0.3 rad m^{-2} and did not lead to a noticeable

improvement of the images. In addition, the cycle 20 observations were subject to the highest ionospheric Faraday rotation, with a maximum of ~ 5 rad m^{-2} determined by the simple model used. There is no simple way to test that the applied ionospheric corrections assist in removing any ionospheric component. Although the corrections do appear to improve the data, it is possible that the model underestimates the amount of Faraday rotation.

As the RM of 3C138 is small, the data could also be interpreted as a change of sign somewhere within the instrument. A swap in R and L could cause such a sign-inversion, and could go unnoticed in Stokes I observations. To rule this out, further observations were performed on the source 3C66B. The source has an integrated RM of -67 rad m^{-2} (Simard-Normandin et al. 1981), although a constant RM of -93.4 rad m^{-2} has frequently been assumed as this is the mean in some areas of the source (Leahy et al. 1986; Hardcastle et al. 1996). A plot of the EVPA versus λ^2 at 610 MHz is shown in Figure 4.21. Two discrepant data points were excluded from the RM calculation as the leakages in these channels were severely affected by strong RFI. The RM of 3C66B was found to be -95.8 ± 1.3 rad m^{-2}.

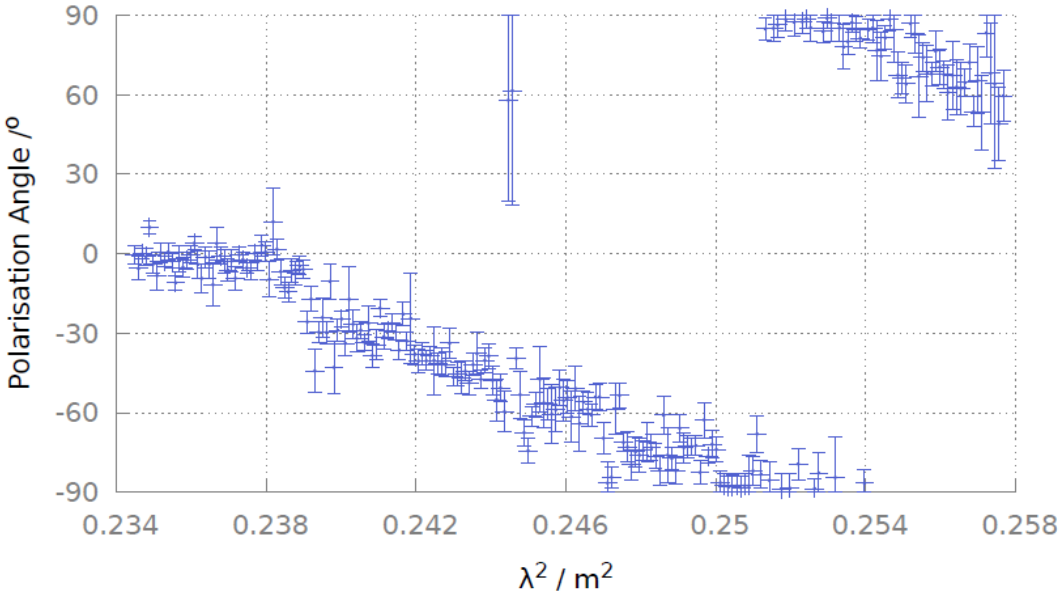

Figure 4.21: A plot of the EVPA versus λ^2 across the observing band for the brightest polarised emission detected from 3C66B. The two discrepant data points were excluded from the RM calculation as the leakages in these channels were severely affected by strong RFI.

The measured RM in 3C66B rules out a swap or change of sign in the instrumentation. The difference in the measured RM is due to the detected emission coming from a different part of the source at low frequencies, thereby causing a discrepancy between the measured and integrated RMs. The RM varies in a similar manner across the surface of 3C138, which also contains positive regions (Dallacasa et al. 1995; Cotton et al. 1997). RMs measured at low frequencies may differ from those at higher frequency due to relations between the depolarisation and

RM, the non-linear connection between EVPA and λ^2, or variation in the integrated RM as a function of frequency due to a different dominant emission region. Despite the best efforts of the calibration procedures, these RMs may also be affected by time-dependent systematics such as the magnitude of ionospheric Faraday rotation.

In the worst case scenario, all RMs measured with the GMRT may be inaccurate by up to 5 rad m^{-2}. As the intrinsic EVPA, Φ_0, is highly sensitive to systematic errors across the band (see equation 2.32), no attempt to retrieve this has been made for any source. All RMs derived with the GMRT at 610 MHz are tied to that of 3C286, which I take to have a RM of $= -1.2$ rad m^{-2}. Consequently, a RM of 4.0 rad m^{-2} was assumed for 3C138 when used as the EVPA calibrator, this is in agreement with the RM during cycle 17.

CHAPTER 5

PRELIMINARY OBSERVATIONS USING THE POLARISATION PIPELINE

> "We're thirty thousand light years from galactic central point, we go round every two hundred million years, and our galaxy is only one of millions of billions, in this amazing and expanding universe."
>
> *Monty Python*

The on-axis response of the GMRT has now been investigated and the polarisation calibration routine has been optimised using the procedures detailed in Chapter 4. This polarisation pipeline can now be used to study the properties of candidate target sources. In this chapter, I use a version of the pipeline to test the polarisation calibration procedure. I first test my RM Synthesis code and then investigate the properties of two well-studied regions of the sky – the Galactic centre and the nearby galaxy M51. These observations also serve as further diagnostics of the GMRT's instrumental response. Observations of the Galactic centre region prove to be a useful test for the pipeline, finding no linear polarisation in the region and showing that the calibration quality at the GMRT is frequently too poor for polarimetric imaging when using an unpolarised calibrator to solve for the leakages. I also find that M51 is depolarised at 610 MHz to below the sensitivity limit of the presented observations, although a number of polarised sources are located across the FOV.

5.1 Previous Observations

The preliminary observations presented in this chapter are not the first at the GMRT. Polarisation studies with the GMRT began with the observations 14DAG01 and 14DAG02[7]. Preliminary results that I obtained for these data are presented in Figure 5.1, which shows band-averaged polarised intensity images that are dominated by artefacts. Initial results showing the instrumental polarisation for these data are also presented by Taylor (2009).

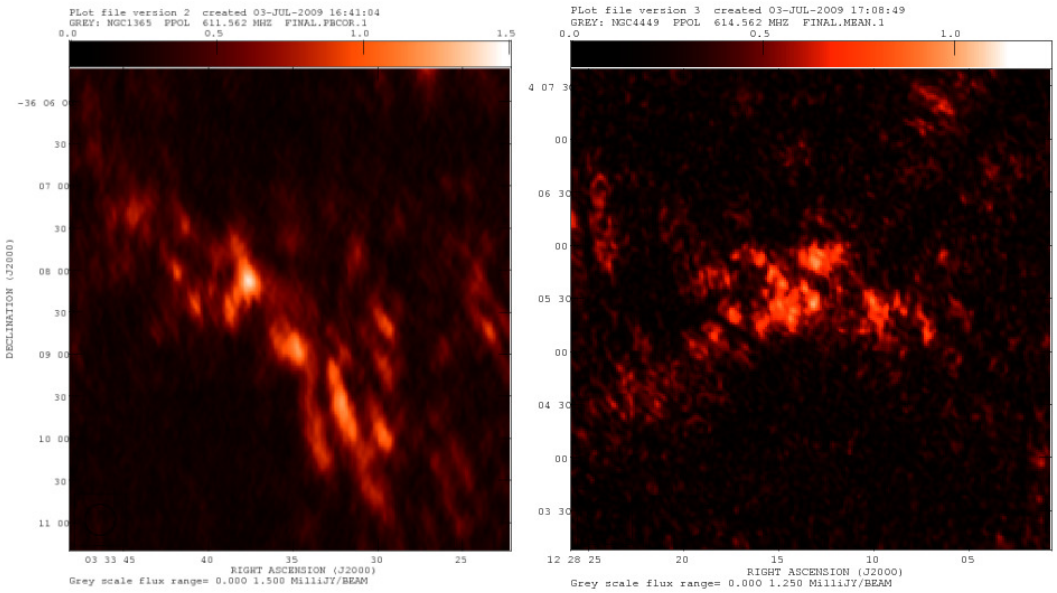

Figure 5.1: Early GMRT polarised intensity images made with the hardware correlator. The images are zoomed into the phase-centre of a field surrounding NGC 1365 (left) and NGC 4449 (right). The images are dominated by artefacts, which arise from poorly constrained instrumental polarisation solutions.

The GMRT still made use of a hardware-based correlator when these earliest observations were taken, and there were several issues that prevented a high-quality polarisation calibration being obtained. There were many adjacent groups of four baselines that were poorly recorded by the hardware correlator. This was the result of burnt out hardware components, loose connections, failed cables, and bad earthing of the electronics[8]. These groups of baselines had to be flagged from the data.

The hardware correlator also tended to record noisier visibilities. When combined with the essential flagging for removal of RFI, and the further flagging of antennas with high leakage[9], the heavily flagged data resulted in poorly constrained instrumental polarisation solutions. Nevertheless, these preliminary results showed that the calibration of GMRT polarimetric observations was possible at 610 MHz.

[7] These observations were taken by Dave Green and Rosie Bolton in September 2008.

[8] http://gmrt.ncra.tifr.res.in/gmrt_hpage/sub_system/corr/IMH/main/digtl_status.html.

[9] Due to the lack of a non-linear algorithm – see Chapter 3.

The GMRT has now implemented a software backend (see Roy et al. (2010) for further details). This vastly improves the quality of the data, and vastly reduces the amount of bad data that needs to be flagged. The observations presented throughout this thesis were obtained using the software backend.

5.2 Testing the RM Synthesis Code/RM-clean

To ensure that the implemented RM Synthesis code is fully functional, observations of the calibrator sources were processed using the developed Python script (see Chapter 3). The observation of 3C138 prior to EVPA calibration is ideal for this purpose, as the large instrumental RM shown in Figure 4.19 appeared to have only a single component. This should become clearly visible in ϕ-space. The output images for 610 MHz observations, after RM Synthesis only, and after RM Synthesis followed by RM-clean, are shown in Figures 5.2 and 5.3 respectively.

It is clear that RM-clean effectively reduces the sidelobes in ϕ-space. Tests were performed to ensure that the ϕ peak was as expected – the spectrum was extracted from the brightest pixel in Stokes I. The spectra, both before RM-clean and after, are shown in Figures 5.4 and 5.5 respectively.

The Gaussian fit to the cleaned spectrum shown in Figure 5.5 yields a peak in ϕ-space at -675.96 ± 0.19 rad m^{-2}, in excellent agreement with the single component measured at -678 ± 5 rad m^{-2} in the plot of EVPA versus λ^2. The peak brightness, corrected for the effects of Rician bias using equation 2.52, was measured as 0.3648 ± 0.0005 Jy beam^{-1} rmsf^{-1} – providing a polarisation fraction for 3C138 of $\Pi = 2.980 \pm 0.005\%$.

RM Synthesis was also tested on the pulsar B1937+21, as observed with the GMRT at 325 MHz. The cleaned output at a Faraday depth of 8 rad m^{-2} is shown in Figure 5.6. Note that in Figure 5.3 at 610 MHz, there are visible residuals within the FOV at the peak Faraday depth of the source. These residuals are far less substantial at 325 MHz, despite both images being from snapshot observations. This is a consequence of the residuals at Faraday depths away from the emission peak being convolved with a RMSF of FWHM=321 rad m^{-2} at 610 MHz, while at 325 MHz the RMSF has a FWHM=22.2 rad m^{-2}. This increases the residuals more substantially in the ϕ-cubes at 610 MHz. A significant contributor to these residuals is likely uncorrected instrumental polarisation. Nevertheless, this does not differ substantially between 325 MHz and 610 MHz. Following flagging of antennas with instrumental polarisation $> 15\%$, the mean instrumental polarisation of all antennas is typically $\approx 6.5\%$ at 610 MHz and $\approx 7.5\%$ at 325 MHz.

The smaller FWHM of the RMSF means that observations at 325 MHz are less affected by residual instrumental polarisation – at least for snapshot observations. For observations taken over a large range in parallactic angle, the effects of uncorrected residual instrumental polarisation will average down to some extent.

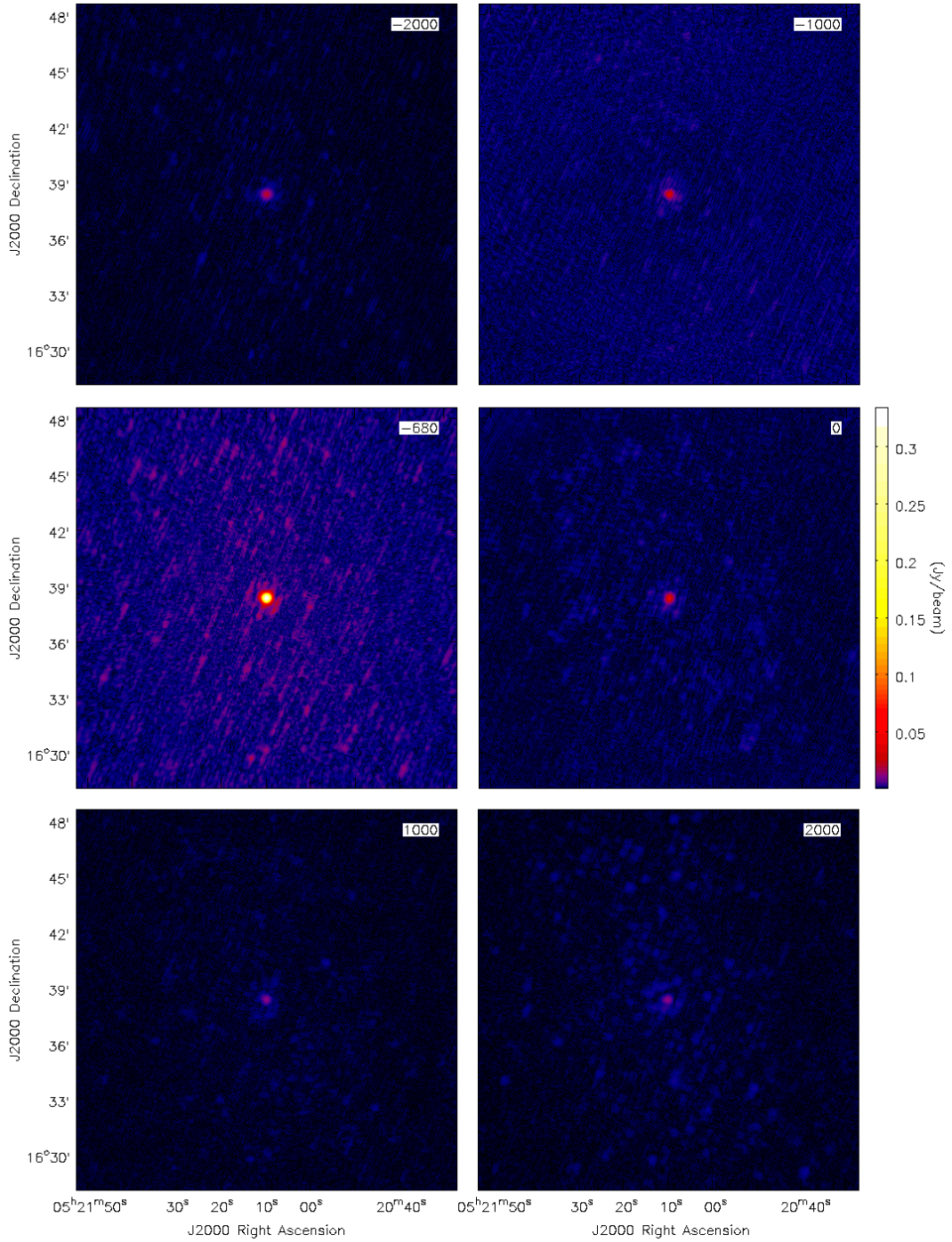

Figure 5.2: Images of the polarised intensity of 3C138, prior to EVPA calibration, at a number of Faraday depths as output by the RM Synthesis code. The Faraday depths shown are at −2000, −1000, −680, 0, 1000, and 2000 rad m^{-2}. The RM-clean algorithm has not been applied.

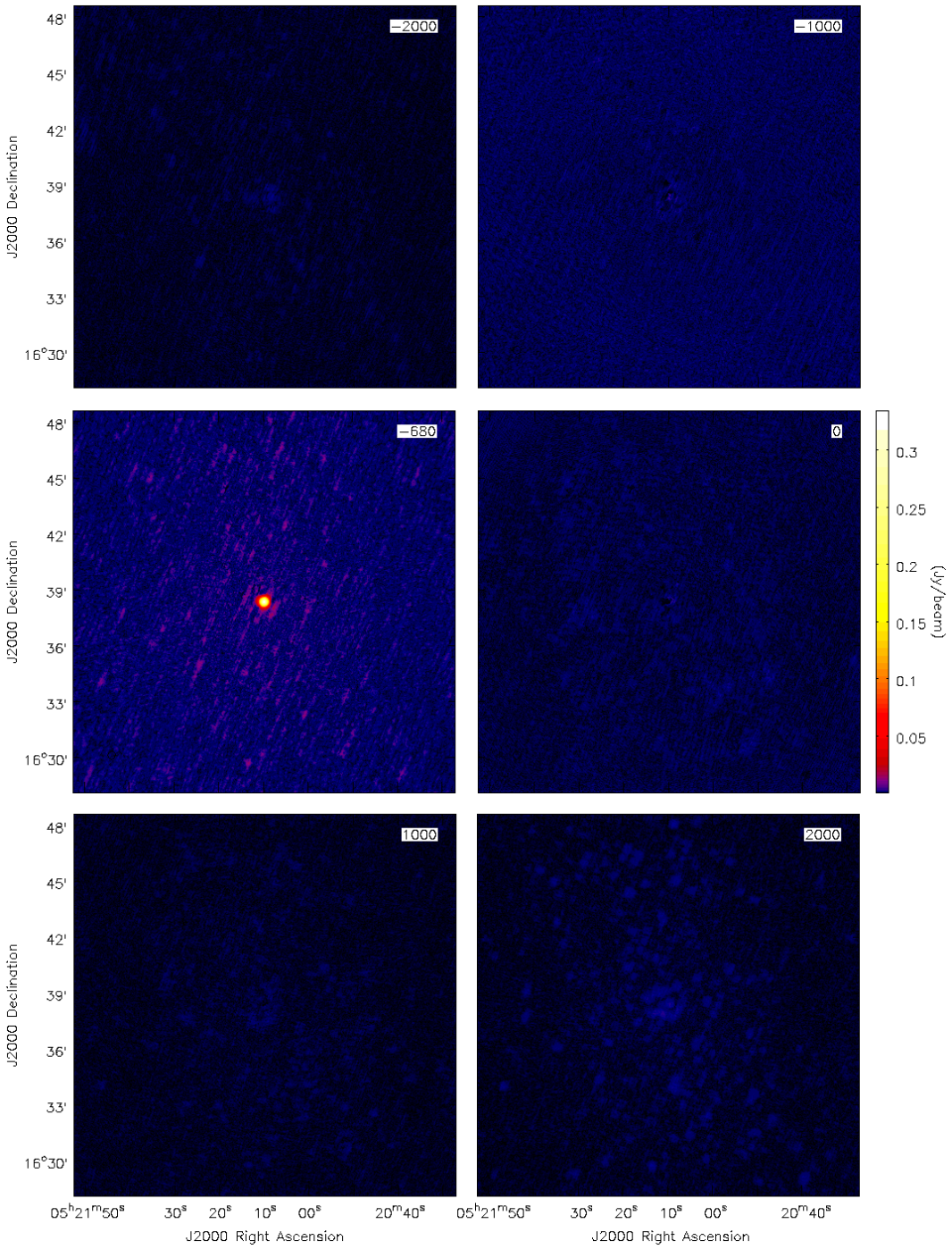

Figure 5.3: Similar to Figure 5.2, but the RM-clean algorithm has been applied.

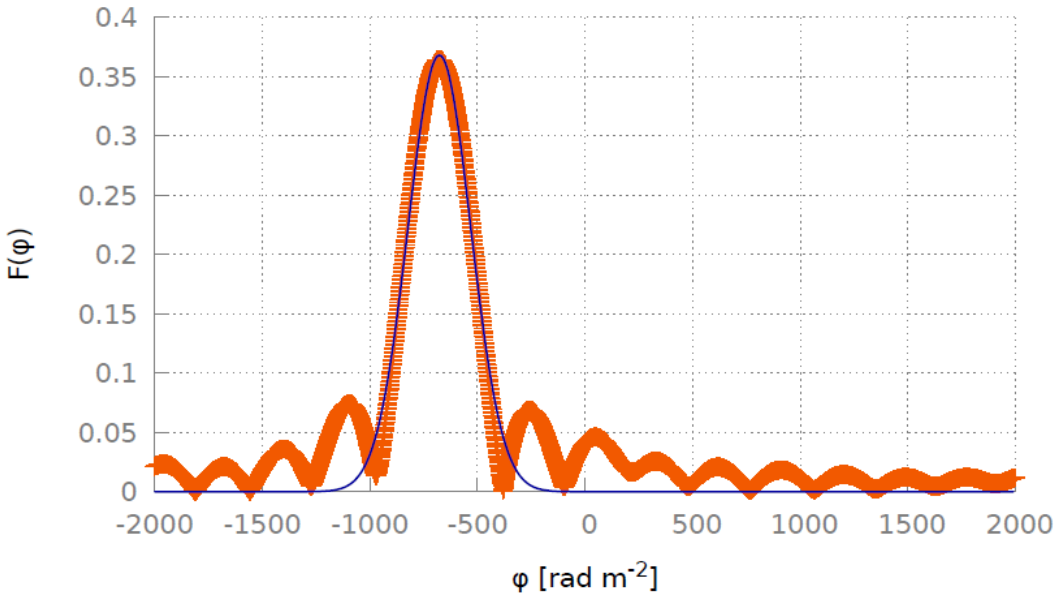

Figure 5.4: A plot of the Faraday dispersion function as a function of Faraday depth for 3C138 *before* EVPA calibration. This Faraday spectrum was extracted from the uncleaned ϕ-cube shown in Figure 5.2. The datum extracted at each trial Faraday depth is shown in orange – samples were taken at every 1 rad m^{-2}. A Gaussian fit to the main lobe of the spectrum is shown in blue. The spectrum is clearly still convolved with the RMSF.

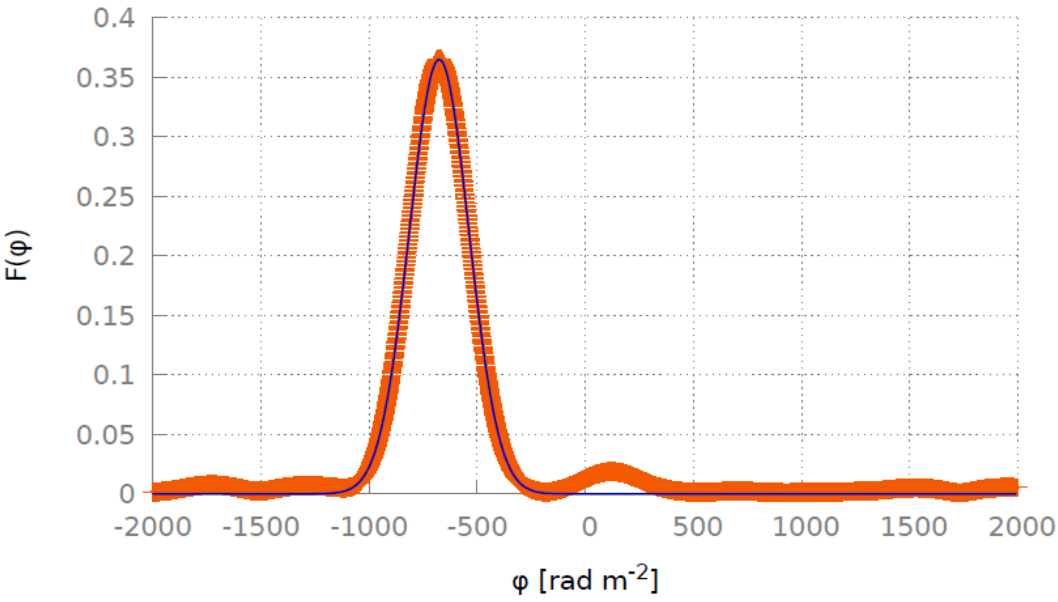

Figure 5.5: Similar to Figure 5.4, however this Faraday spectrum was extracted from the ϕ-cube following the application of RM-clean as shown in Figure 5.3. The datum extracted at each trial Faraday depth is shown in orange – samples were taken at every 1 rad m^{-2}. A Gaussian fit to the main lobe of the spectrum is shown in blue.

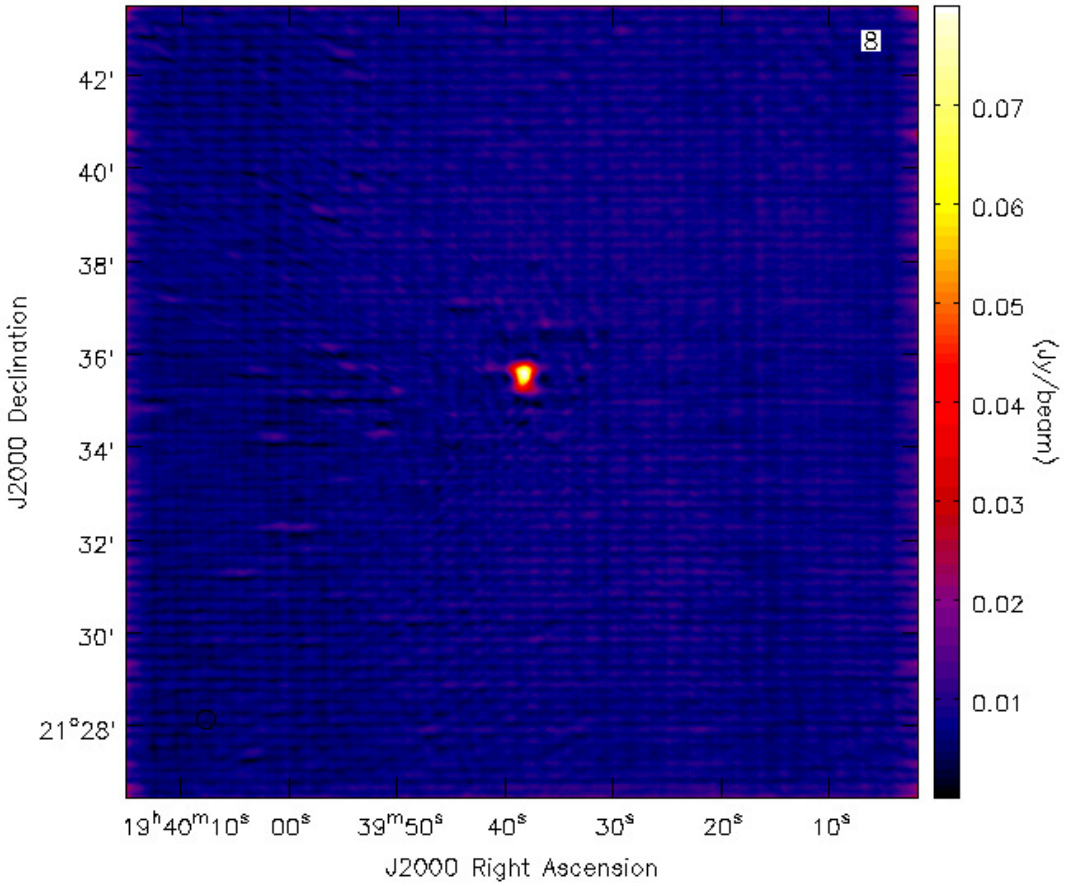

Figure 5.6: An image of the polarised intensity of pulsar B1937+21 as observed at the GMRT at 325 MHz, after EVPA calibration, at a Faraday depth of 8 rad m^{-2}. The RM-clean algorithm has been applied.

5.3 Preliminary Observations of the Galactic Centre

The Galactic centre (GC) is a unique region in the Galaxy and is amenable to observations with a resolution and sensitivity that is unattainable for the central regions of other galaxies.

The discovery of pulsars close to Sagittarius A* (Sgr A*) would give rise to the exciting possibility of using the timing information to derive the local gravitational potential and to test general relativity in the strong-field regime. However, the electron density is very high in the local ISM within several arcminutes of Sgr A* – giving rise to large dispersion, scattering measure, and pulse broadening. It is estimated that the pulse broadening is so high that no pulsar could be detected by their pulsations below several GHz in frequency as the pulse broadening $\propto \nu^{-4}$ (Cordes & Lazio 1997). However, pulsars typically exhibit very steep spectral indices ($\alpha \sim 1.5$, $S \propto \nu^{-\alpha}$), resulting in much lower flux levels at high frequencies. Consequently, the success of pulsar detection in high frequency searches has been quite low. Indeed, only a few pulsars have been discovered using Parkes and the Green Bank Telescope at GHz frequencies

(Johnston et al. 2006; Deneva et al. 2009), and none of the four nearest pulsars are seen through the central 10′ region in projection from the GC.

Pulsars are known to be highly polarised. Although the linear polarisation fraction goes down due to pulse averaging, pulsars are still typically polarised to ∼ 20% (Gould & Lyne 1998). Observing the GC region therefore allows for an attempt to detect polarised emission from compact sources near Sgr A*, serving to identify pulsar candidates in the region. This technique has already been used at 1.4 GHz, identifying several strong pulsar candidates in the central 1° of the GC (Law et al. 2008).

The RM close to Sgr A* is known to be very high ($\sim 5 \times 10^5$ rad m^{-2}) at frequencies of ∼ 300 GHz (Macquart et al. 2006). This high RM is believed to be a consequence of infalling ionised material to the $4 \times 10^6 M_\odot$ black hole. Polarised emission from pulsars in the region could also suffer high RM. Such high RMs would result in complete bandwidth depolarisation to all of the existing VLA continuum observations at 1.4 GHz, leading to non-detection of polarised emission close to Sgr A*.

While such high RMs are problematic for the majority of modern correlators, the GMRT software backend (GSB) allows for 512 spectral channels across a bandwidth of 32 MHz. These observations are therefore sensitive to RMs up to $\approx 6 \times 10^4$ rad m^{-2} at an observing frequency of 610 MHz. These will therefore be the first low-frequency observations with high enough RM sensitivity to probe the GC region – providing an unprecedented opportunity to locate pulsar candidates in the central 40′ of the Galaxy. More importantly, such observations provide a useful technical test to demonstrate the feasibility of obtaining a full-synthesis of the GC with the GMRT.

Several challenges need to be addressed. The target was to find a polarised point source, scatter broadened to 3.2″. Source confusion can arise from polarisation leakage, as well as the presence of diffuse polarised emission, and extragalactic background point sources. The background will be scatter broadened to at least twice the pulsar size i.e. > 6″, and possibly 2′ if the scattering screen is close to the GC – so these effects should be readily distinguishable.

The confusion problem can be further overcome by using the previously mentioned technique of RM Synthesis. It is known that diffuse emission in the galactic plane is Faraday depolarised beyond the Faraday horizon at RM $\lambda^2 \gg 1$. In the data, lots of confusion is expected at zero RM, with diffuse structure up to the RM horizon at ≤ 100 rad m^{-2}. Beyond this, isolated pulsars are expected to appear as point sources in the three dimensional maps.

The data were calibrated using the phase and bandpass calibrators J1751–253 and J1822–096. Checks on the EVPA calibrator, 3C286, suggests that the residual instrumental polarisation is ≤ 1%. See Chapter 3 for further details of the observations.

From the obtained time on source of 133 minutes, a thermal noise of ∼ 35 μJy beam^{-1} would typically be expected at the GMRT in Stokes *I*. However, the sky temperature increases near to the GC by a factor of ∼10–12 (Haslam et al. 1982). This increases the system temperature substantially and decreases the flux levels by a similar order of magnitude (Bhatnagar 2001).

Corrections for such an effect can be made in order to retrieve the true flux levels of sources (see Chapter 8). Such a correction has not been carried out for this preliminary observation.

5.3.1 Extended Stokes I Emission

The obtained Stokes *I* image, sensitive to all scales of emission accessible to the GMRT, is shown in Figure 5.7. An image zoomed in towards the GC is shown in Figure 5.8. The images have a rms noise of ~ 3.5 mJy beam^{-1}.

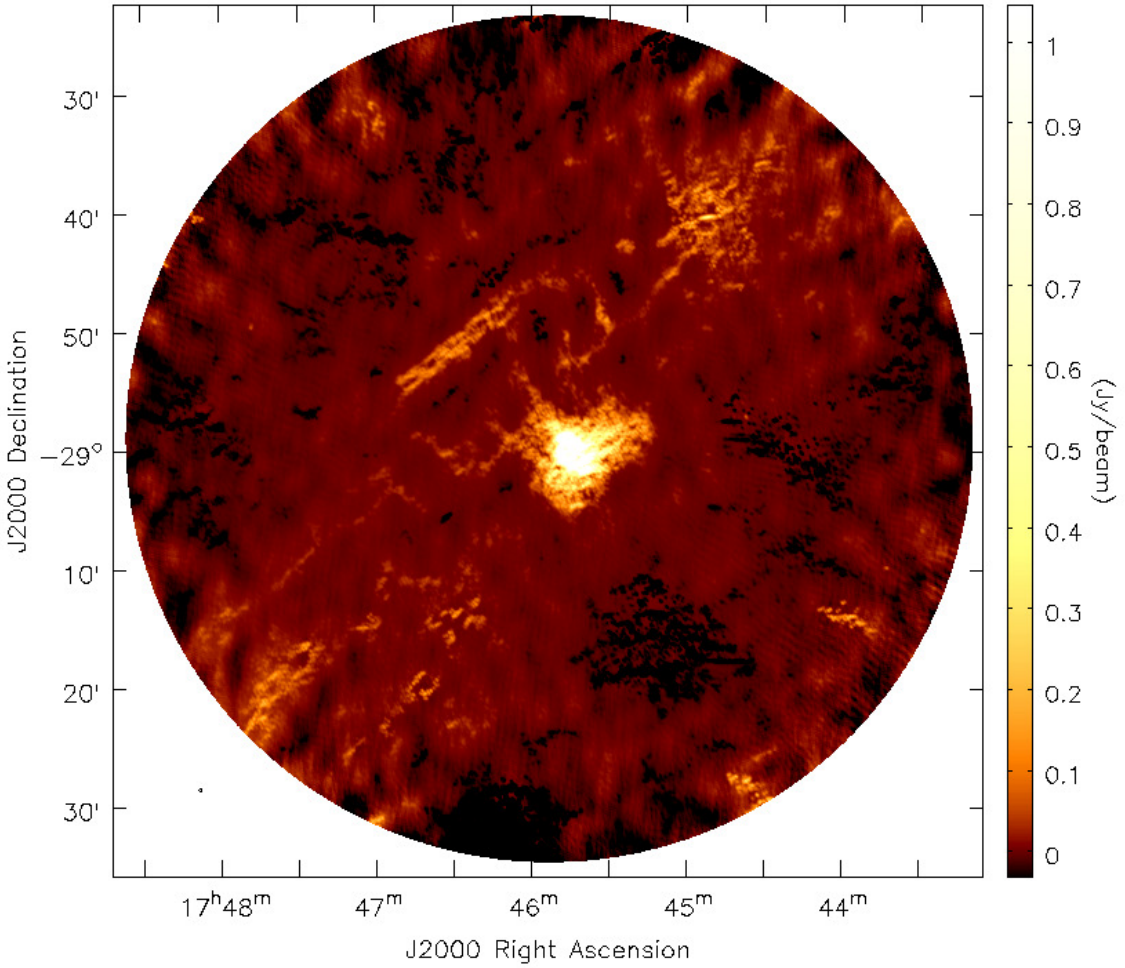

Figure 5.7: The full FOV surrounding the Galactic centre in Stokes *I* at 610 MHz. All available spatial scales were used. The image has a resolution of $17.04'' \times 12.07''$ with a position angle of $36.6°$.

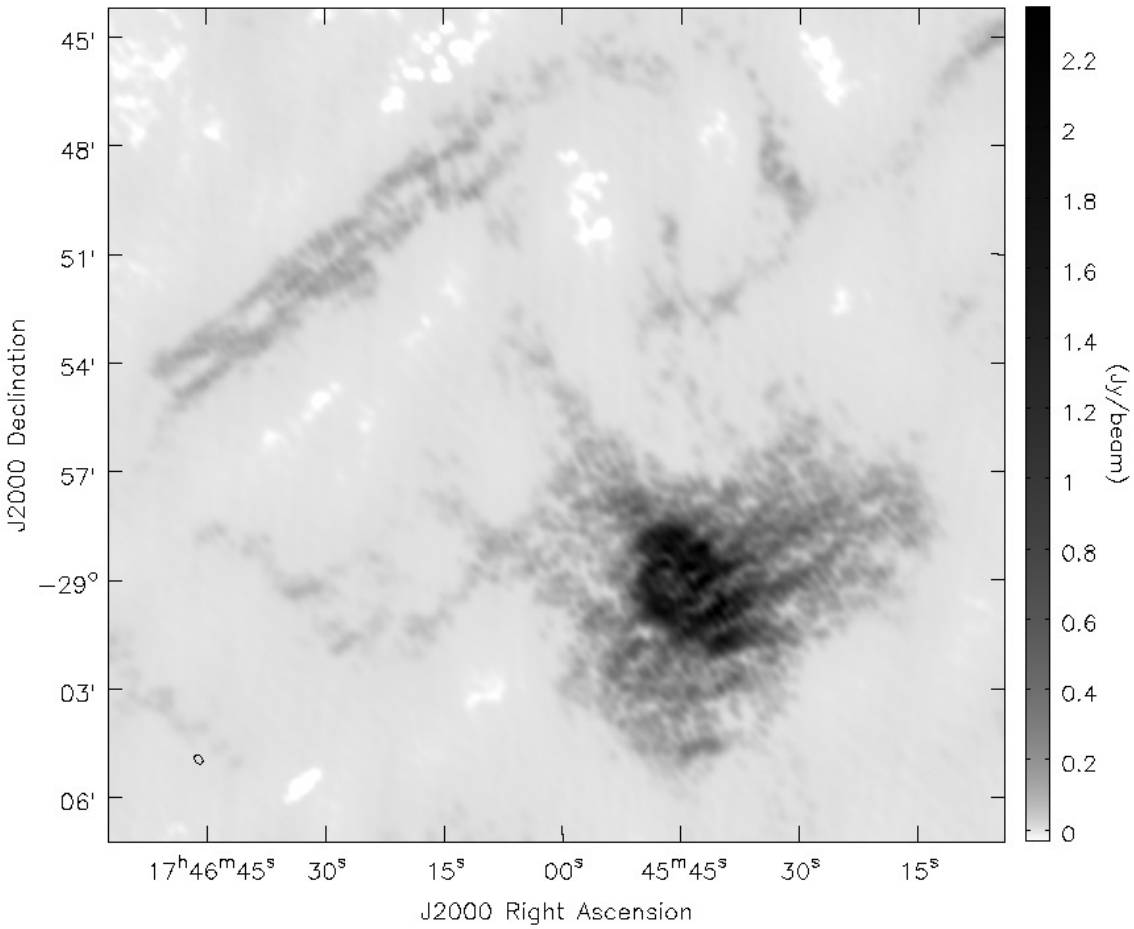

Figure 5.8: An enlarged view of the region directly surrounding Sgr A* in Stokes *I* at 610 MHz. The image is the same as that in Figure 5.7.

5.3.2 Locating Compact Sources

In order to get a better handle on the compact sources in the FOV, large-scale emission was removed using a *uv*-cut. All data below 4 kλ were excluded and the images are insensitive to emission with spatial scales $\gtrsim 0.86'$. The initial *uv*-cut images were severely limited by low-level phase errors emanating from the GC region, likely resulting from the limited *uv*-coverage in this observation. Consequently, the final 'amplitude and phase' step of self-calibration was skipped (see Chapter 3) as this re-introduced errors which had been eliminated earlier in the self-calibration process.

Due to the effects of increased system temperature and the 'negative-bowl' resulting from a lack of short *uv*-spacings, the flux levels of sources are not well-estimated. Nevertheless, a number of small-diameter sources and thin filamentary structures (non-thermal 'threads', e.g. Lang et al. (1999)) are detected in Stokes *I*. The wide-field image obtained is shown in Figure

5.9. A rms noise of 0.4 mJy beam^{-1} was achieved.

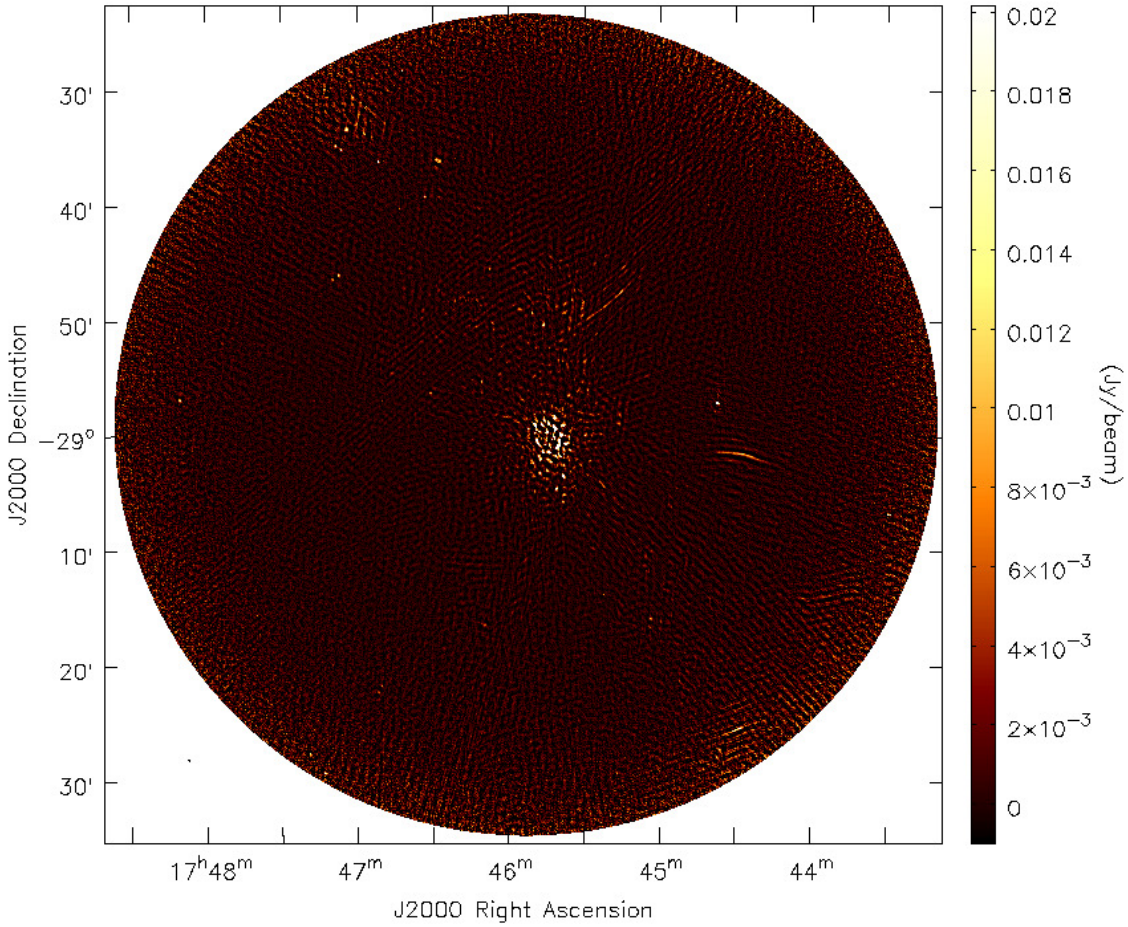

Figure 5.9: The full FOV surrounding the Galactic centre in Stokes *I* at 610 MHz, with a *uv*-cut excluding all spatial scales $\gtrsim 0.85'$. The image has a resolution of $7.47'' \times 3.76''$ with a position angle of 34.2°.

A number of pulsars have previously been detected in the GC region. Of these, the pulsar likely in closest radial proximity to Sgr A* is J1746–2850II (Deneva et al. 2009).

Deneva et al. (2009) report that the pulsar J1746–2850I, near to J1746–2850II, is located at 17h 46m 06.6s(2), −28° 50′ 42″(5). A small-diameter source is detected in the GMRT images at 17h 46m 05.9s, −28° 50′ 45″. The off-source rms noise in this region is ∼1.2 mJy beam^{-1}. The measured peak surface brightness of this source is 6.8 mJy beam^{-1}, yielding a 5.6σ detection. Note the aforementioned systematics that affect estimates of the flux density from these images. No candidate for the pulsar J1746–2850II, previously identified at 17h 46m 03.7s(1), −28° 49′ 19″(21), is detected in the GMRT images. The region surrounding the two pulsars is shown in Figure 5.10.

The region surrounding a third pulsar J1745–2910, that Deneva et al. (2009) report as being

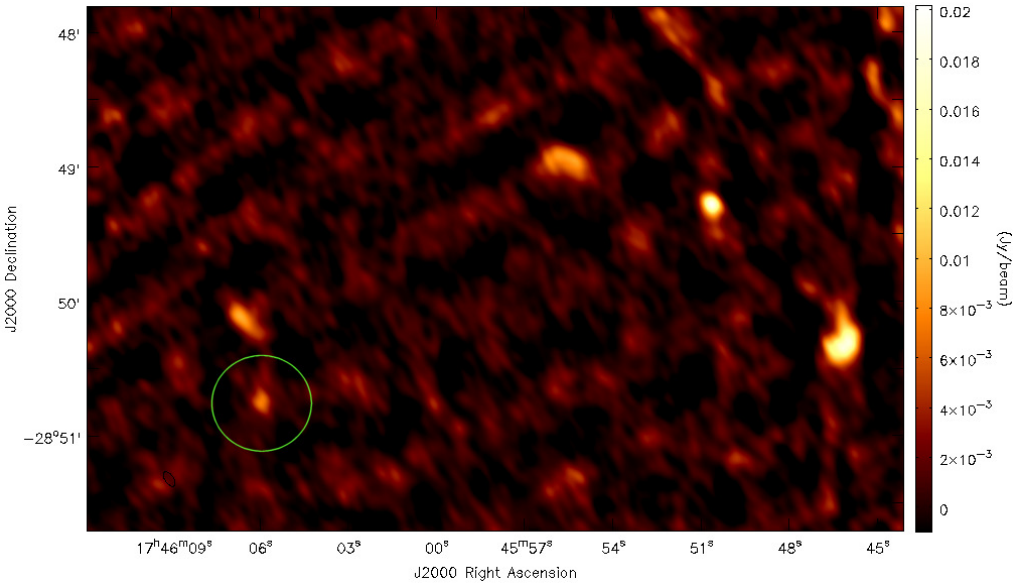

Figure 5.10: An enlarged view of the region directly surrounding J1746–2850I and J1746–2850II at 610 MHz. The candidate detection of J1746–2850I is indicated by the green circle. The image is the same as that in Figure 5.9.

located at 17h 45m 16s(34), −29° 10′(3), is shown in Figure 5.11. Small-diameter sources are detected in this region, although it is difficult to identify the nature of these sources, due to the lack of complementary data at another frequency. The pulsar can not be easily identified or otherwise in these images without strong constraints on the spectral index, particularly due to the large uncertainty in the source's previously identified co-ordinates.

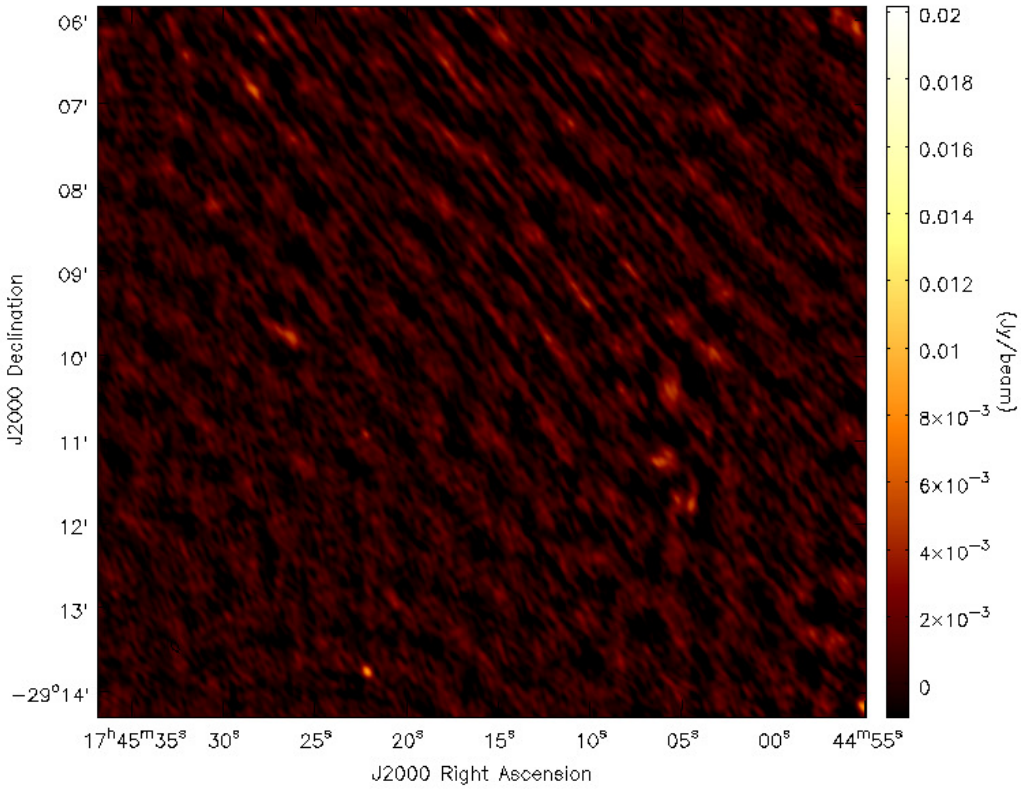

Figure 5.11: An enlarged view of the region directly surrounding J1745–2910 at 610 MHz. The image is the same as that in Figure 5.9.

5.3.3 Linear Polarisation Measurements

An image of the bandwidth-averaged polarised intensity, P, and a set of Q/U image cubes were created. The images were convolved to a common restoring beam of $10'' \times 10''$. The majority of high leakage antennas were located within the GMRT's central square. A noise level of ~ 250 μJy beam^{-1} was obtained in P, with the positive-definite image being governed by Rician statistics.

All *uv*-scales below 4 kλ were excluded in the polarisation images. Such a *uv*-cut is not essential due to intrinsic polarisation from the extended total intensity emission, which is expected to undergo strong Faraday depolarisation near to the GC. However, this procedure reduces instrumental polarisation as it prevents the diffuse Stokes I emission from leaking into the polarisation images. The *uv*-cut was found to reduce the instrumental polarisation by a factor of ~ 1.5.

When creating the P image, the use of Q and U from each noisy individual channel provides a large Rician bias. Such images are nevertheless useful for quick identification of polarised emission without suffering from bandwidth depolarisation effects. Attempts to retrieve the polarised flux density should always be carried out via RM Synthesis (see Chapter 2).

The data were Nyquist-sampled during RM Synthesis up to Faraday depths of ± 20000 rad m^{-2}. The effects of bandwidth depolarisation and the finite width of each spectral channel makes the data insensitive to RM's higher than 63000 rad m^{-2}. Following RM Synthesis, an implementation of RM-clean was used. The clean was carried out down to a 2σ limit, where σ was found to be 370 μJy beam^{-1} rmsf^{-1}. The cleaned Faraday spectrum was convolved with a Gaussian with a FWHM equal to that of the main lobe of the RMSF for these observations, which has a FWHM of 142 rad m^{-2}. The RMSF is shown in Figure 5.12.

Direction-dependent instrumental polarisation is not anticipated to be significant at the location of either Sgr A* or J1746–2850I, which are displaced from the phase-centre by $\sim 3'$ and $\sim 9'$ respectively. Given the low parallactic angle coverage, the direction-dependence should be similar to the 'snapshot' instrumental polarisation (see Chapter 6). Off-axis effects are therefore at most $\lesssim 1\%$ in fractional polarisation for both sources.

Residual instrumental polarisation from the on-axis calibration is significant near to the GC. The estimated residual of $\leq 1\%$ contributes a substantial amount of polarised flux into the images due to the significant brightness in total intensity near to Sgr A*. The highest fractional polarisation detected across the FOV correlates with the brightest emission in Stokes I, with a peak polarisation of 1.2%. Following RM Synthesis, this emission appears at a Faraday depth of 0 rad m^{-2} along with additional large-scale artefacts. The Faraday depth is consistent with the artefacts having originated from uncorrected frequency-independent residual instrumental polarisation. The results of RM Synthesis at a number of selected Faraday depths across the entire field are shown in Figure 5.13. No small-diameter sources that are detected in Stokes I are detected in polarised intensity. The polarised intensity is dominated by residual instrumental

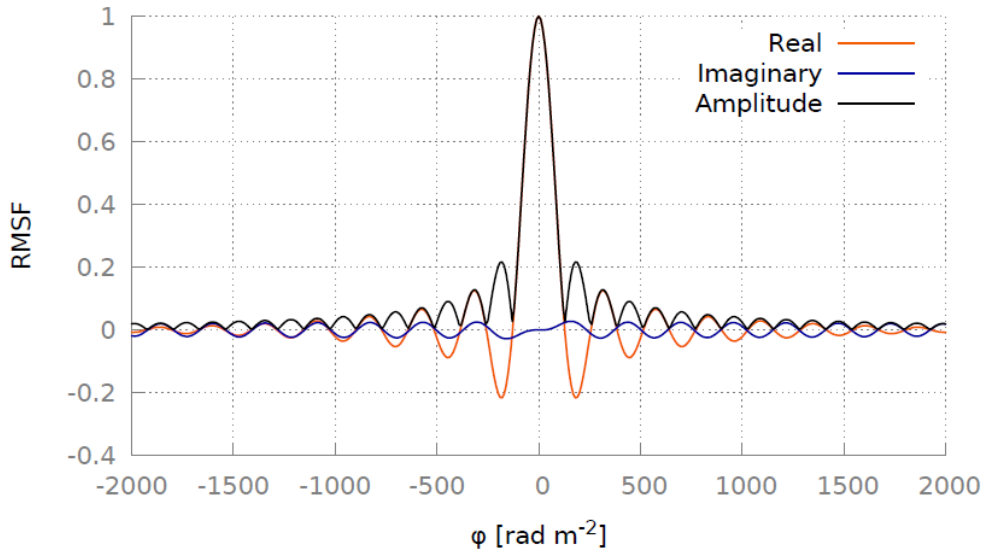

Figure 5.12: The RMSF for this observation, showing the real and imaginary components, Q and U respectively, and the amplitude, $P = \sqrt{Q^2 + U^2}$, as a function of Faraday depth.

effects.

The spectrum at the position of J1746–2850I in Faraday space is shown in Figure 5.14. Peaks occur at Faraday depths of -6920 ± 1 rad m^{-2} and 14760 ± 1 rad m^{-2} on the order of 3σ. The highest peak at 3050 ± 1 rad m^{-2} is 3.8 times the local noise level. It should be noted that the detection thresholds in RM Synthesis differ from typical images, and a s/n of 3 has a false-detection rate of up to 44% (George et al. 2011). The spectrum is therefore consistent with no polarisation being detected. Nevertheless, the peak at 3050 rad m^{-2} provides an upper limit for the pulsar's polarisation fraction of $\leq 19 \pm 7\%$.

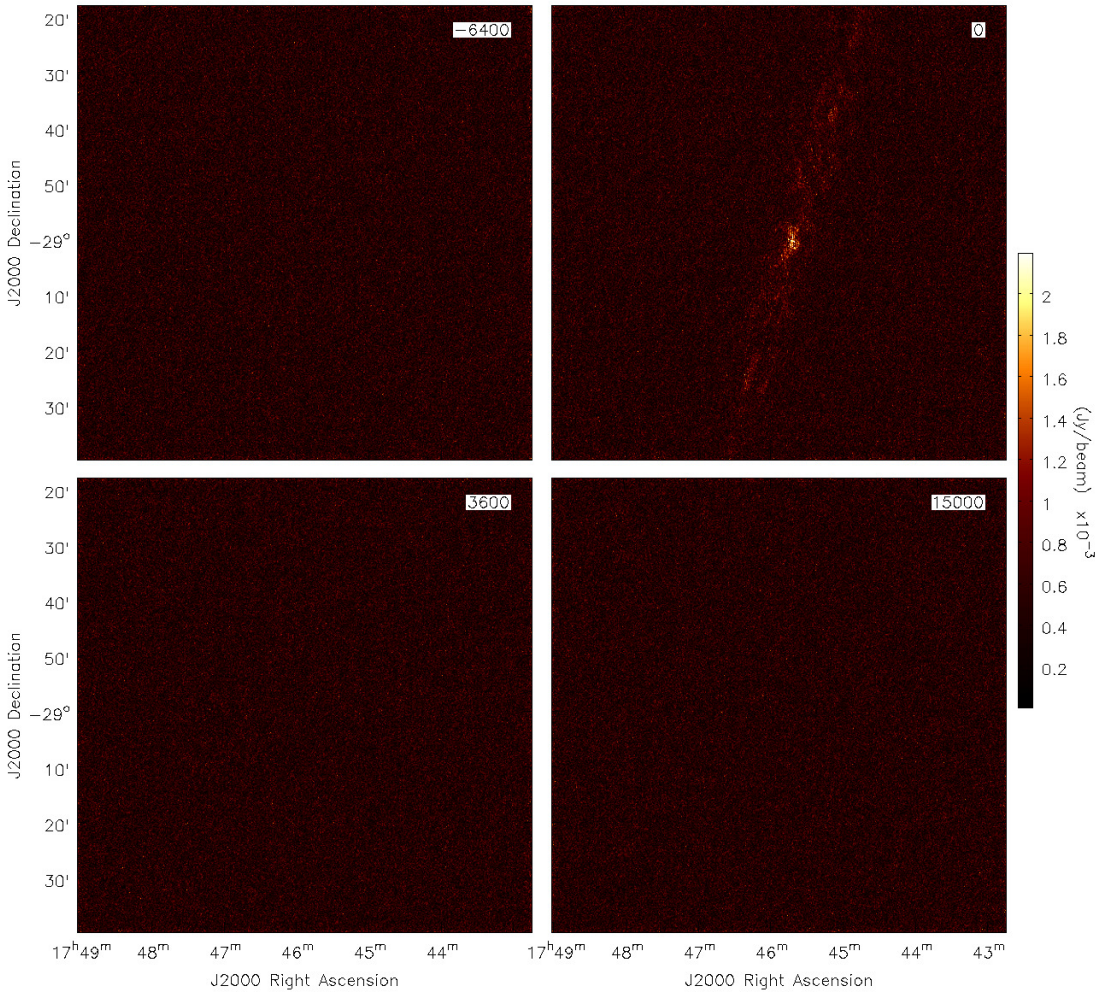

Figure 5.13: The results of RM Synthesis across the FOV. Faraday depths of −6400, 0, 3600, and 15000 rad m^{-2} are shown. The only emission detected is at a Faraday depth of 0 rad m^{-2} – consistent with frequency-independent residual instrumental effects.

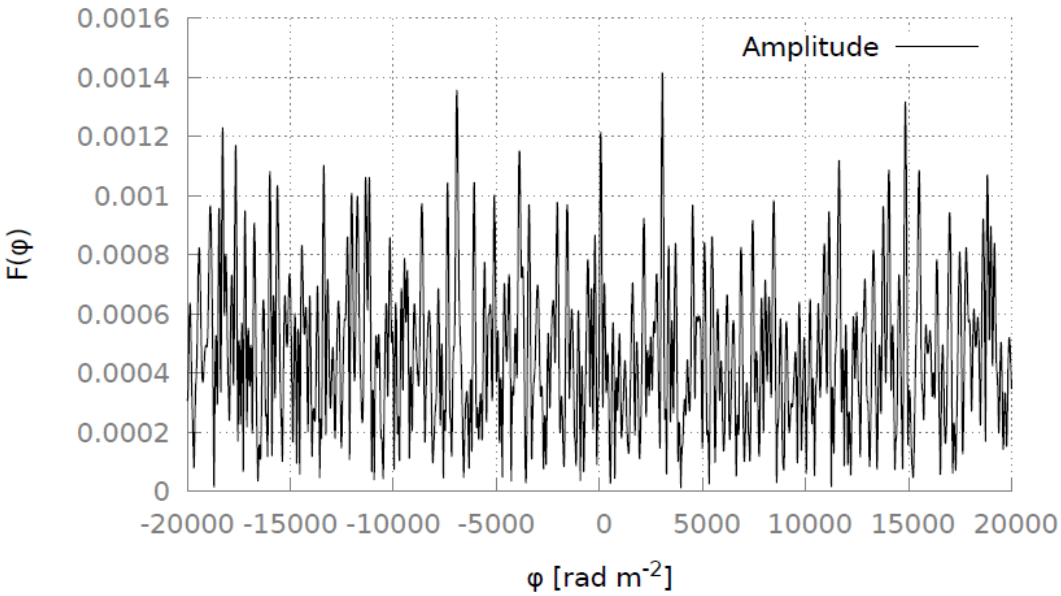

Figure 5.14: The spectrum from RM Synthesis at the brightest pixel in Stokes I for the possible pulsar detection of J1746–2850I. The amplitude, $P = \sqrt{Q^2 + U^2}$, of the Faraday Dispersion Function is shown as a function of Faraday depth.

5.4 Assessing the Pipeline through Observation of M51

The galaxy M51 also provides the opportunity to assess the quality of polarisation calibration. The galaxy and its linear polarisation properties have been well-studied at a number of frequencies (see e.g. Horellou et al. (1992); Fletcher et al. (2011) and references therein). The galaxy has a famously well-defined spiral structure that is the result of interactions with a nearby companion galaxy, NGC 5195.

In the observations presented in this chapter, the phase calibrator J1313+549 was found to have a derived flux density of 1.719 ± 0.008 Jy. Checks on the flux calibrator, 3C48, and the EVPA calibrator, 3C286, suggest that the residual instrumental polarisation is $\leq 0.25\%$.

5.4.1 Stokes I emission

An image zoomed in towards M51 is shown in Figure 5.15 at full resolution. The image has a rms noise of ~ 23 μJy beam^{-1}.

5.4.2 RM Synthesis of M51

The galaxy has previously been well studied in polarisation (e.g. Fletcher et al. 2011). Nevertheless, I am primarily interested in testing the polarisation pipeline. Polarisation images were created using a *uv*-taper and natural weighting. This increases the sensitivity to extended emission, while also removing the impact of holes in the *uv*-coverage that result from the flagging of antennas with leakages > 15%. The final polarisation images have a resolution of $24'' \times 24''$. I therefore perform RM Synthesis on the entire field. A noise level of 44 μJy beam^{-1} rmsf^{-1} is achieved in the cleaned ϕ-cubes. The RMSF has a FWHM of 321 rad m^{-2}. The RMs of the sources in the field were all found to be low. Due to the large FWHM of the RMSF, all of the polarised sources are visible at, or near, a Faraday depth of 0 rad m^{-2}. The wide-field image in Stokes I and at a Faraday depth of 0 rad m^{-2} are shown in Figures 5.16 and 5.17, along with the wide-field image in Stokes I. Note the lack of instrumental artefacts from residual instrumental polarisation, and the substantial number of discrete polarised sources.

Nevertheless, the galaxy M51 is completely depolarised down to the sensitivity limit at 610 MHz. The bright active nucleus is depolarised to a 3σ upper limit of $< 0.14\%$. The brighter spiral arms to the N and E of the galaxy are depolarised to a 3σ upper limit of $< 1.1\%$, while the fainter arms to the S and W are depolarised to $< 8.7\%$. The bright emission detected in Stokes I from the companion galaxy NGC 5195 is depolarised to $< 0.4\%$.

5.4.3 Faraday Depths of Compact Sources

Note that the effects of direction-dependent instrumental polarisation have not yet been analysed. It is therefore not yet possible to confirm if the detected discrete polarised sources are due to an

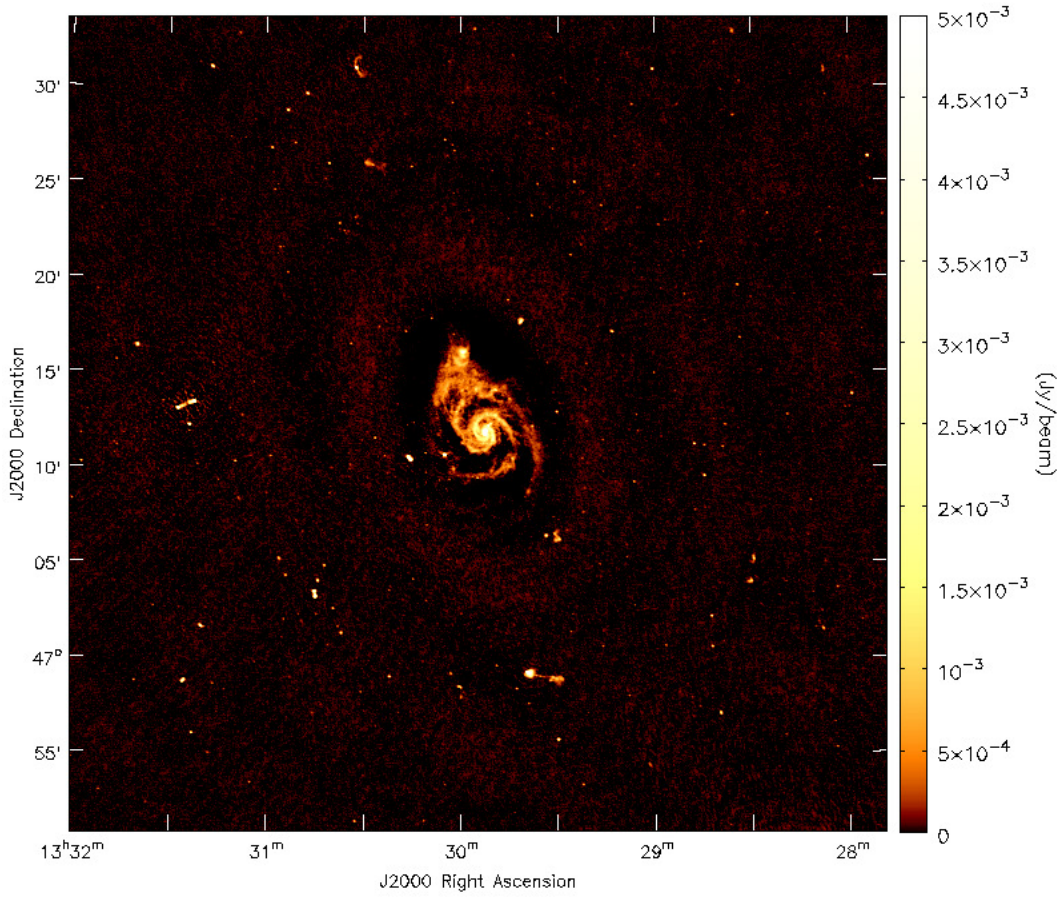

Figure 5.15: Stokes *I* image of the central portion of the field surrounding M51. The companion galaxy, NGC 5195, is clearly visible as the location of bright emission at the outer edge of the spiral arms to the N of M51. The pseudo-colour scale is in units of Jy/beam. The image has a resolution of $5.7'' \times 4.6''$ with a position angle of 66°.

off-axis instrumental response. Such effects are investigated in Chapter 6. Nevertheless, some examples of the polarised sources in the field are shown in Figure 5.18.

Using RM Synthesis, I now extract the polarised peak brightness and Faraday depth of all sources with a peak $\geq 8\sigma$ in the Faraday spectrum. The right ascension, declination, radius from the phase-centre, fractional polarisation, and Faraday depth as measured using the GMRT, WSRT, and VLA respectively are listed in Table 5.1. The listed co-ordinates are for the brightest pixel in Stokes *I*. The polarisation fraction was only calculated for sources within the 10% point of the Stokes *I* beam, i.e. at a radial distance $\leq 35.6'$ from the phase-centre. Off-axis effects likely cause an overestimation of Π for several of these sources (see Chapter 6). The calculated Π should be considered an upper limit, particularly for sources beyond the half-power points, i.e. at a radial distance $\geq 22.2'$ from the phase-centre. Measurements of Π and the Faraday depth were calculated by fitting a Gaussian to the points immediately surrounding the peak in ϕ-space. The Π measurements were corrected for the effects of Rician bias using the estimator

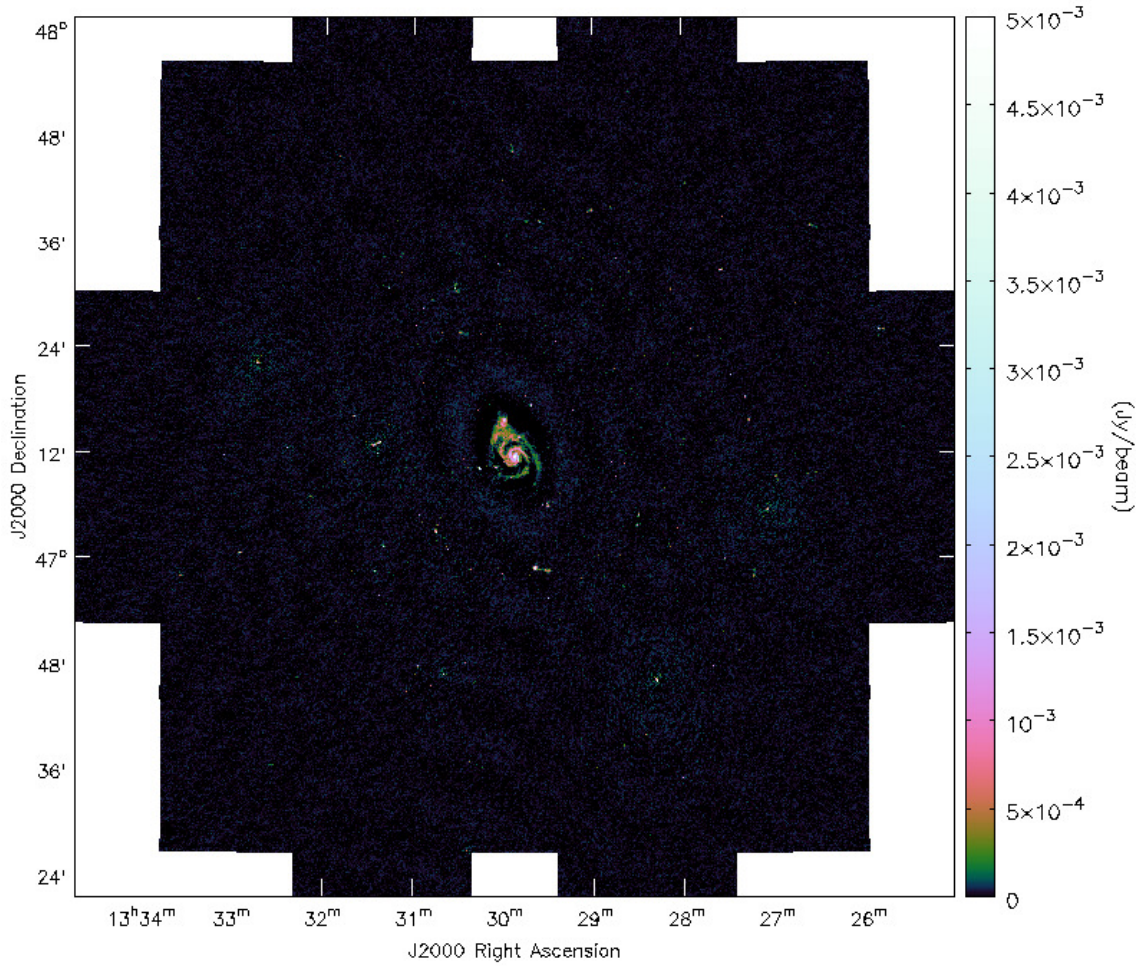

Figure 5.16: The wide-field Stokes *I* image of the field surrounding M51 at 610 MHz. A correction for the effects of the Stokes *I* beam has not been applied. Also see Figure 5.17.

in equation 2.52. Where available, previous Faraday rotation measurements determined from NVSS data at 1.4 GHz (Taylor et al. 2009), and WSRT data at 18 cm and 22 cm (Heald et al. 2009) are also displayed. Sources are considered to correspond when the recorded co-ordinates are separated by less than one synthesised beam. All listed errors are the 1σ uncertainties.

5.4.4 Circular Polarisation

The galaxy was also imaged in circular polarisation as a further check of the GMRT's instrumental properties. No circular polarisation is expected to be present, and the presence of any is indicative of instrumental systematics.

An image of M51 in band-averaged Stokes *V* is shown in Figure 5.19. The *V* image has a noise level of 26 μJy beam^{-1}. The highest peak in *V* is at the 4.5σ level, to the NW of M51's nucleus. The apparent circular polarisation fraction is 1.4%. This is the result of instrumental

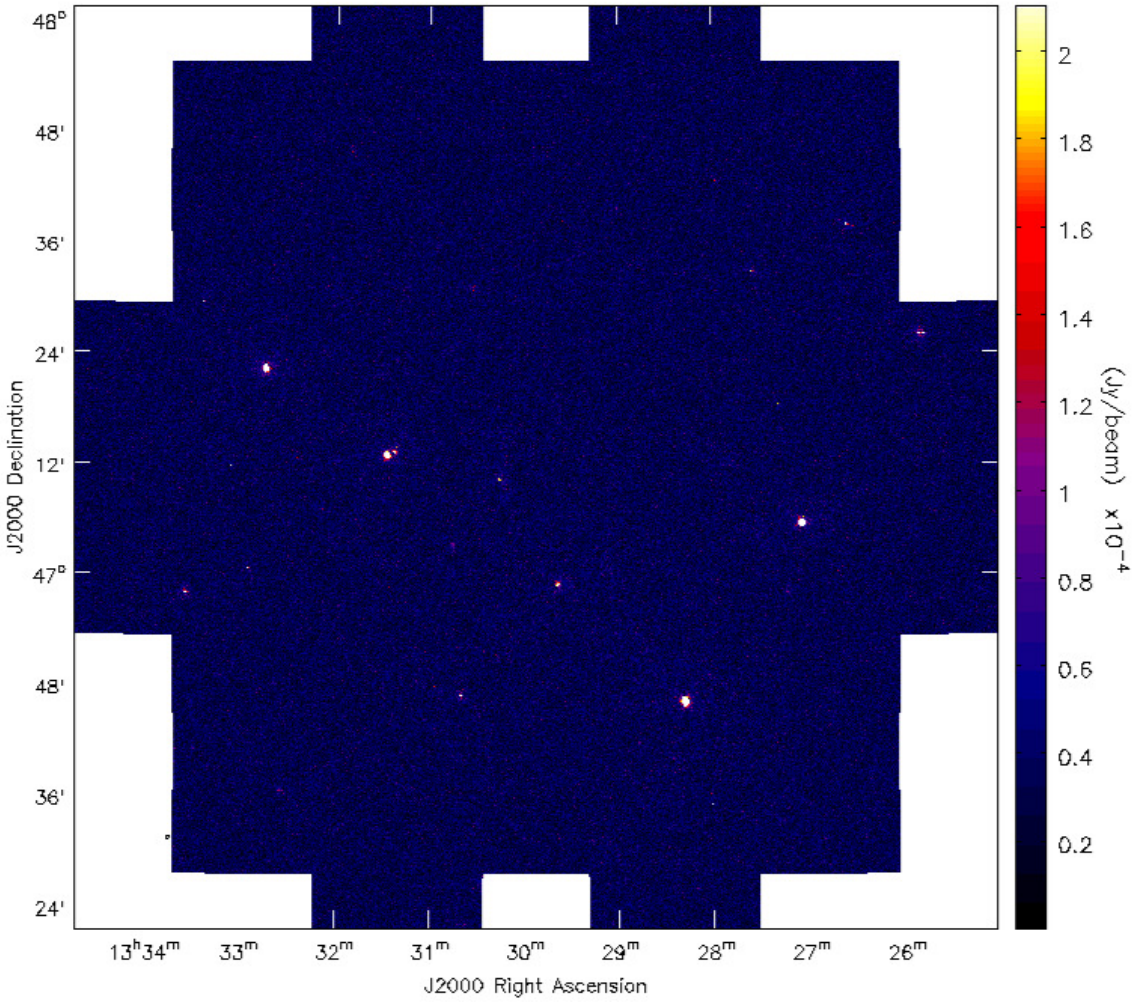

Figure 5.17: The wide-field image of the field surrounding M51 at 610 MHz in polarised intensity for a Faraday depth of 0 rad m^{-2}. The lack of instrumental artefacts, combined with the large FWHM of the RMSF mean that a Faraday depth of 0 rad m^{-2} is useful for displaying the polarised sources. A correction for the effects of the Stokes *I* primary beam has not been applied. Also see Figure 5.16.

systematics, as is shown by the fact that the most significant artefacts appear to surround the emission that is brightest in Stokes *I*.

It should be stressed that the detection of circular polarisation using an interferometer with circular feeds requires careful calibration and is subject to a large number of errors due to the delicate measurement of the difference between the *RR* and *LL* visibilities. These errors can include amplitude calibration errors, gain variations with time, beam squint, second-order polarisation leakage effects, and the effects of RFI.

Amplitude calibration errors and gain variations with time should in principle manifest as spurious Stokes *V* signal that correlates with the Stokes *I* emission. I shall also show in Chapter

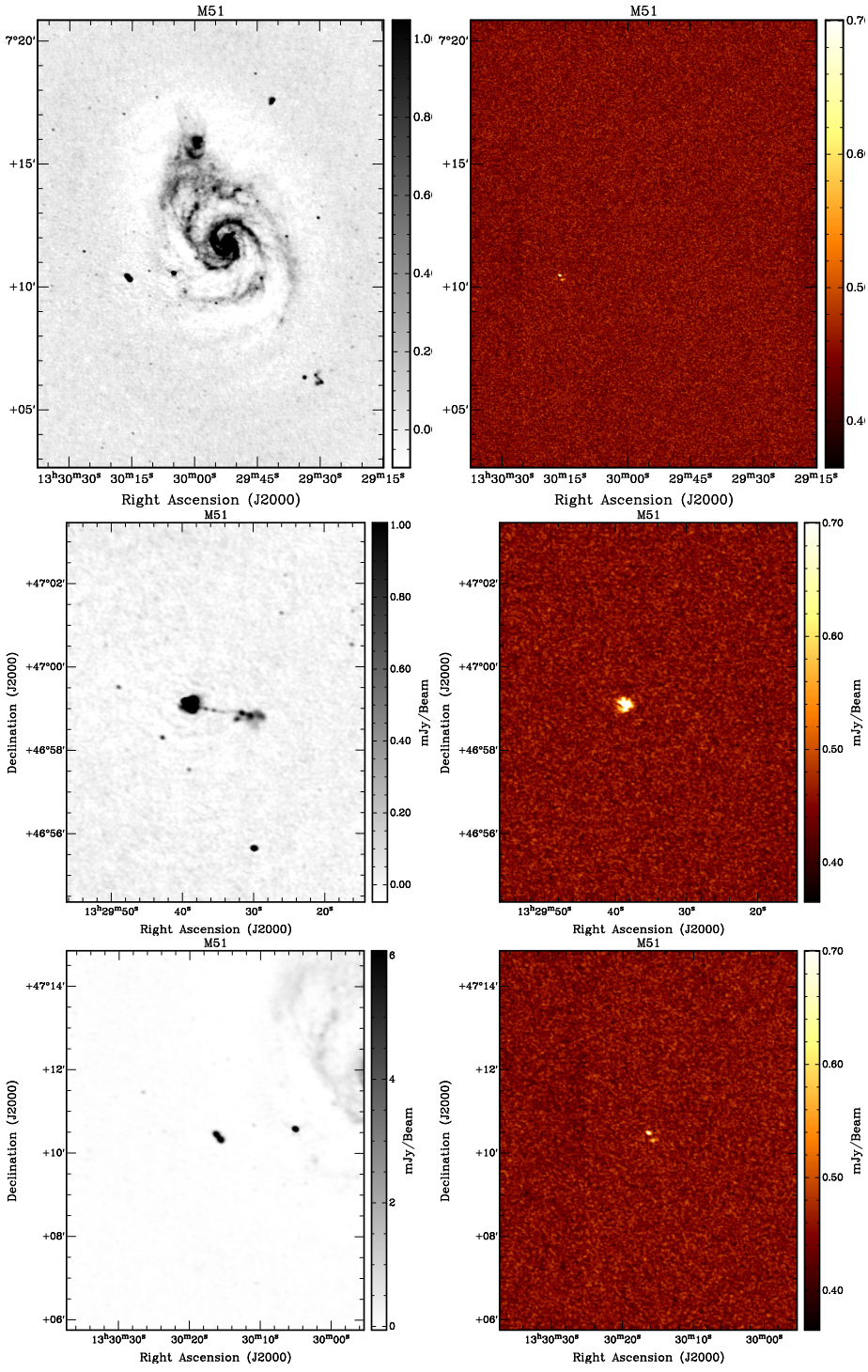

Figure 5.18: Images of the various polarised sources in the field surrounding M51 at 610 MHz. The pseudo-colour scales are in mJy/beam. The Stokes I images (left) have an RMS of 23 µJy/6″ beam. The images of the band-averaged polarised intensity (right), $P = \sqrt{Q^2 + U^2}$, have been smoothed to a 24″ beam. The images have not been corrected for the effects of Rician bias.

Table 5.1: Position, fractional polarisation, and Faraday depth of polarised sources in the field of M51.

RA (J2000)	Dec.	r /arcmin	Π_{610} /%	FD_{GMRT}	FD_{WSRT}	RM_{NVSS}
13h25m47.7s	47d26′04.9″	43.9	—	−16.97 ± 0.03	—	—
13h27m03.3s	47d05′43.3″	29.4	6.32 ± 0.14	−8.11 ± 0.07	—	—
13h27m57.2s	47d42′51.1″	36.7	—	16.83 ± 0.13	—	—
13h28m17.8s	46d46′17.4″	30.1	2.49 ± 0.07	−6.638 ± 0.013	—	10 ± 10.3
13h29m39.4s	46d59′10.2″	12.8	1.72 ± 0.09	11.15 ± 0.05	14 ± 1	−16.2 ± 16.8
13h30m16.1s	47d10′28.1″	4.2	1.79 ± 0.16	33.52 ± 0.03	28 ± 4	—
13h30m32.4s	47d30′53.1″	20.3	6.9 ± 0.5	1.494 ± 0.026	—	—
13h30m39.9s	46d47′04.9″	25.9	14.7 ± 0.7	−5.434 ± 0.019	—	—
13h30m44.9s	47d03′08.3″	12.4	1.98 ± 0.20	−3.24 ± 0.04	17 ± 2	—
13h30m45.2s	47d03′25.1″	12.3	2.74 ± 0.24	−15.97 ± 0.03	—	—
13h31m22.4s	47d13′22.5″	15.3	6.84 ± 0.17	11.51 ± 0.03	9 ± 1	—
13h31m27.4s	47d13′00.6″	16.2	7.22 ± 0.25	7.67 ± 0.04	3 ± 1	—
13h32m45.1s	47d22′22.6″	31.1	6.83 ± 0.24	−1.41 ± 0.03	—	—
13h33m24.9s	47d29′35.3″	40.2	—	1.71 ± 0.28	—	—
13h33m35.2s	46d58′07.5″	40.3	—	0.93 ± 0.23	—	16.6 ± 17.6

6 that beam squint is not substantial near to the phase-centre. In addition, careful data reduction has reduced the impact of RFI – although low-level interference may remain. As the observed systematics *surround* the regions that are brightest in I, they are likely due to second-order polarisation leakage effects.

5.5 Discussion

In this chapter, I have tested the RM Synthesis code. I have shown that the code provides results in line with those anticipated. The application of RM-clean further improves the results, and clearly deconvolves the Faraday dispersion function from the RMSF. Furthermore, although I shall continue to focus on 610 MHz data, the results also indicate that the smaller FWHM of the RMSF at 325 MHz (see Chapter 4) reduces the impact of noise and residual instrumental polarisation within the ϕ-cubes.

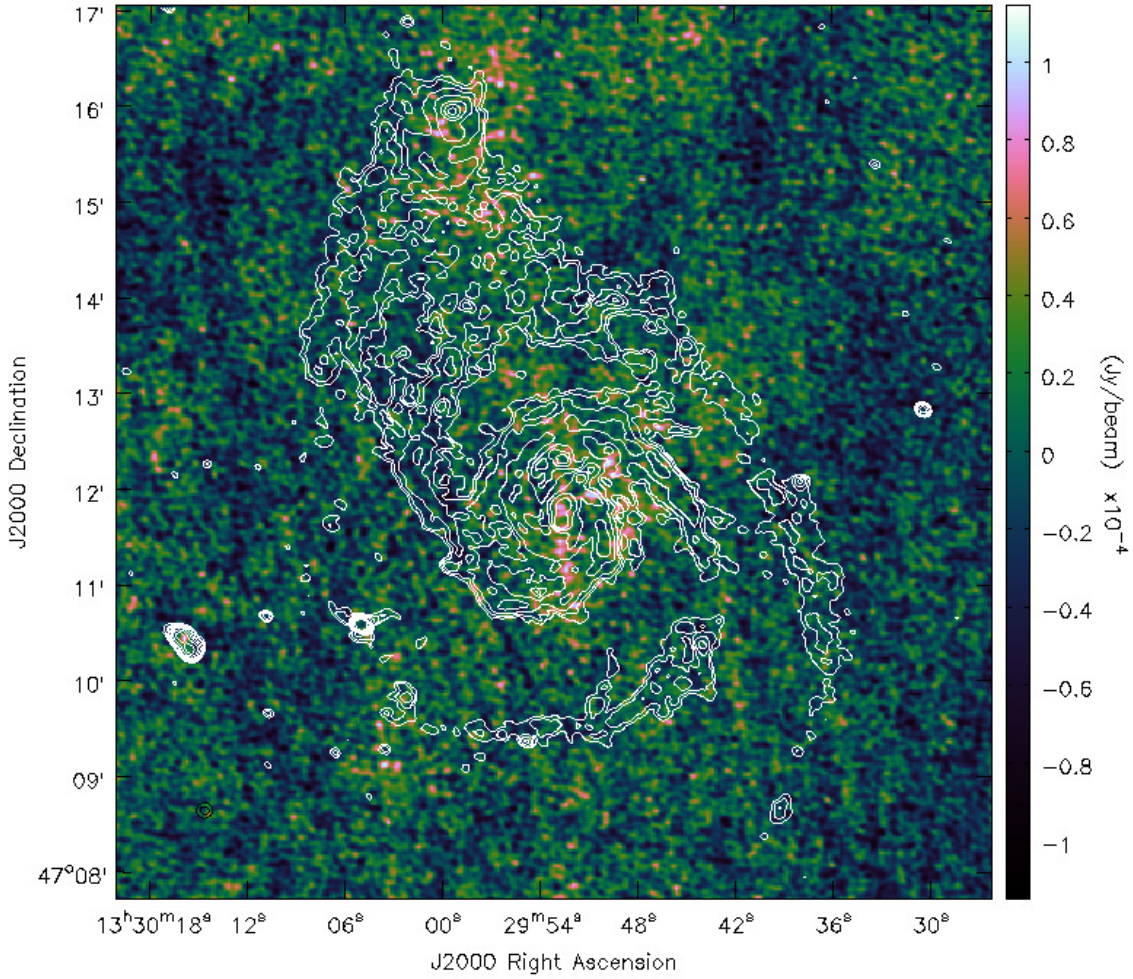

Figure 5.19: Image of the band-averaged Stokes *V* emission in the region surrounding M51. The image is overlaid with Stokes *I* contours, with levels at (1, 2, 4, 8, 16, 32, 64) × 0.125 mJy beam^{-1}. The pseudo-colour scale is in units of 10^{-4} Jy beam^{-1}.

I have also used a version of the polarisation pipeline to test the calibration procedure on two target sources at 610 MHz – the Galactic centre region and the nearby galaxy M51. Both sources are well studied at low frequencies (e.g. Nord et al. 2004; Fletcher et al. 2011). Observations of the Galactic centre region were a useful test for the pipeline. No linear polarisation was detected in the region. The test did however show that the calibration quality at the GMRT is too poor for polarimetric imaging when there is not a substantial range in parallactic angle. This resulted in solutions for the leakages being determined using a short observation of an unpolarised calibrator. Consequently, the Faraday spectrum is largely dominated by residual instrumental polarisation. Polarimetric observations with the GMRT should therefore always have a large range in parallactic angle. Shorter observations are not worthwhile, and result in a low calibration quality.

Nevertheless, despite the limitations from the reduced *uv*-coverage, the Stokes *I* data has

allowed for a small-diameter source to be detected in the GMRT images at 17h 46m 05.9s, −28° 50′ 45″. This appears to correlate with the previously reported location of the pulsar J1746–2850I (Deneva et al. 2009). In addition, a number of small-diameter sources and thin filamentary structures (non-thermal 'threads', e.g. Lang et al. (1999)) are also detected in Stokes *I*. This test observation was therefore worthwhile, and such an experiment should be repeated – albeit with a large range in parallactic angle. The reduction in residual instrumental polarisation and the related systematics would allow for reliable constraints on the presence of linearly polarised pulsars in the GC region at 610 MHz.

Investigation of the nearby galaxy M51 has shown that the polarisation calibration procedures work well – Figure 5.18 shows that some sources that are bright in Stokes *I* are also weakly polarised, while nearby sources of similar brightness in *I* have high fractional polarisation. It is difficult to comprehend an instrumental mechanism by which this can occur, the measurements must be indicative of varying source polarisation properties. Nevertheless, the galaxy itself is completely depolarised down to the sensitivity limit at 610 MHz. The bright active nucleus is depolarised to a 3σ upper limit of $< 0.14\%$. The brighter spiral arms to the N and E of the galaxy are depolarised to a 3σ upper limit of $< 1.1\%$, while the fainter arms to the S and W are depolarised to $< 8.7\%$. The bright emission detected in Stokes *I* from the companion galaxy NGC 5195 is depolarised to $< 0.4\%$. However, a number of bright polarised point sources are detected in linear polarisation. The calculated Faraday depths of sources that have been previously detected in polarisation are in excellent agreement with results obtained at higher frequencies (Heald et al. 2009).

Of the 15 compact linearly polarised sources that have a peak in the Faraday spectrum $> 8\sigma$, 4 of these sources are beyond the 10% point of the Stokes *I* beam and are possibly the result of direction-dependent instrumental polarisation (see Chapter 6). After discarding these sources, 5 of the sources have not had their polarisation properties reported previously – the Faraday depth and polarised intensity are reported here for the first time at 610 MHz.

The source located at 13h 30m 32.4s, 47° 30′ 53.1″ is coincident with the galaxy cluster WHL J133032.6+473053 located at a redshift of $z = 0.32$ (Hao et al. 2010). The detected source has a polarisation fraction of $6.9 \pm 0.5\%$, although the source of the polarised emission along the line of sight can not be investigated given the limited resolution. Furthermore, the source located at 13h 32m 45.1s, 47° 22′ 22.6″ is coincident with the radio galaxy B3 1330+476 located at a redshift of $z = 0.67$ (Schneider et al. 2005).

The preliminary observation of M51 shows that spectropolarimetry is possible with the GMRT. Nevertheless, the observations presented here make it clear that using an unpolarised calibrator source to solve for the instrumental polarisation is inadequate – a large range in parallactic angle is needed for GMRT data. As shown, the ability to calibrate the GMRT, and the instrument's unique sensitivity, has allowed for new sources to be detected in polarisation and for their Faraday depths to be measured via RM Synthesis. The observations have also allowed for new constraints to be placed on the linear polarisation in M51 and its companion

galaxy, NGC 5195, at 610 MHz. The results also highlight the GMRT's circular polarisation response. Spurious circularly polarised emission frequently surrounds the off-axis sources that are brightest in Stokes *I*. Circular polarisation measurements should be carried out at the GMRT with caution.

While the adopted calibration procedures clearly work well at the phase-centre, it is not yet clear whether the GMRT has the potential for wide-field spectropolarimetric observations. The direction-dependent instrumental polarisation response still needs to be thoroughly investigated. In order to perform full science observations, further constraints need to be placed on wide-field instrumental effects across the FOV. In the next chapter, I explore this direction-dependent instrumental polarisation in detail.

CHAPTER 6

CONSTRAINING DIRECTION-DEPENDENT INSTRUMENTAL POLARISATION

> "An expert is a man who has made all the mistakes which can be made, in a very narrow field."
>
> *Niels Bohr*

In Chapter 5, I presented the first GMRT polarisation observations taken in interferometry mode that were suitable for the extraction of Π and RM at 610 MHz. The applied polarisation calibration minimised residual instrumental polarisation at the phase-centre. Nevertheless, the instrumental polarisation is known to vary across the FOV of an interferometric observation. Any such direction-dependent effects are therefore currently uncalibrated. In this chapter, I present results from observations of the GMRT primary beam in full-polarisation and find evidence that the Stokes *I* beam has a squircle[10] geometry within the main lobe. In addition, I show that the direction-dependent polarisation at 325 MHz and 610 MHz is largely independent of the feed and is dominated by the curvature of the dishes' reflecting mesh – causing the polarisation beams to scale with the Stokes *I* FWHM. This direction-dependent polarisation averages down considerably for observations with a large range in parallactic angle. I use the developed beam model to remove direction-dependent effects directly from 610 MHz *uv*-data. Furthermore, I then develop a new technique for EVPA calibration using the wide-field response of an interferometer. This technique has the advantage that it calibrates the EVPA independently of both ionospheric variation and source variability, and also avoids a flaw in

[10] A square-circle (http://mathworld.wolfram.com/Squircle.html) (Fernandez Guasti et al. 2005)

current methods which could erroneously yield multiple Faraday components for sources that are well-parameterised by a single RM. It also removes the need for known polarised sources on the sky – which are scarce at low frequencies.

6.1 Background

The response of an interferometer varies across the primary beam, and wide-field polarimetry requires calibration of these 'direction-dependent' or 'off-axis' instrumental effects. Similar to the case of on-axis calibration, the 'polarisation beam' manifests itself with flux in total intensity leaking into the polarisation images.

These polarimetric aberrations result in an increase in the observed fractional polarisation and also alter the absolute EVPA of sources – with the effect becoming more pronounced with increasing distance from the phase-centre. Direction-dependent effects therefore limit the dynamic range of low-frequency interferometric images – restricting the region of the primary beam that is useful for scientific measurement.

Following Heiles (1999), there are two kinds of beam polarisation that are theoretically expected:

1. Beam squint: this occurs when the two circular polarisations point in different directions by a certain angle. Beam squint tends to produce a 'two-lobed' pattern, with the beam having one positive and one negative region.
2. Beam squash: this occurs when the beamwidths of the two linear polarisations differ by a certain amount. Beam squash tends to produce a 'four-lobed' pattern, in which two regions on opposite sides of the beam centre have a positive sign and two lobes rotated by 90° have a negative sign. This quadrupolar pattern tends to give rise to instrumental linear polarisation that is oriented radially with respect to the phase-centre.

Knowledge of the pattern of beam squint and beam squash across the FOV, and the ability to correct for the resulting direction-dependent effects, is vital for mosaiced surveys and other observations where the science relies on wide-field polarimetric capabilities.

In this chapter, an observational analysis of the GMRT beam is provided in full-polarisation at both 325 MHz and 610 MHz. The obtained polarisation beam model is then used to correct for the effects of direction-dependent instrumental polarisation at 610 MHz. Details of the holography observations used to obtain the beam constraints are described in Section 6.2. As a consistency check, the beam properties at 610 MHz are also inferred from a full-track synthesis in Section 6.3. The process used to retrieve the beam response from the holography data is detailed in Section 6.4, while two-dimensional maps of the full-Stokes beam at 610 MHz are presented in Section 6.5 along with an analysis of the 325 MHz beam. The obtained beam maps are then applied in order to correct the direction-dependent response. The theory behind these corrections and the impact on wide-field GMRT images is detailed in Section 6.6. A new

technique for EVPA calibration using an interferometer's wide-field response is detailed in Section 6.7. A discussion of the results is provided in Section 6.8.

6.2 Holography Observations

The test observations TST0570 and TST0620 used for analysis of the GMRT full-Stokes beam were taken in modified holography mode. This means that two reference antennas remained fixed on an unpolarised calibrator while the remaining antennas were slewed in azimuth and/or elevation to a co-ordinate such that the calibrator source was observed offset from the phase-centre. In all cases, the two reference antennas were excluded from the data analysis so that only the offset antennas were used – allowing the power pattern[11] to be directly retrieved, rather than the voltage pattern.

A number of offsets were used, such that a grid of 'raster scans' were observed. The grid used for observing these off-axis raster scans is shown in Figure 6.1. Note that all four axes were only observed at 610 MHz, and the 325 MHz observations excluded the diagonal axes Azimuth-X and Elevation-X.

Each axis of the observing grid included an on-axis scan of the holography source. These on-axis scans were used to solve for the complex gains of each antenna, with the solutions being interpolated across the other raster scans – essentially using the on-axis scans for phase calibration. The effects of instrumental polarisation (and parallactic angle variation at the phase-centre) were removed from the data by solving for the leakages using all on-axis observations of the unpolarised calibrator.

An EVPA calibration was applied to obtain the Q and U beam in the calibrated antenna frame. The correction to the holography data was applied so that the raster scans of the derotated azimuth axis displayed an EVPA that was oriented radially. Evidence to justify this assumption is provided in Section 6.3.

[11] The power pattern is 'superimposed' onto interferometric observations of the sky, and is therefore more fundamental for studying the effect that the beam has on measured source properties.

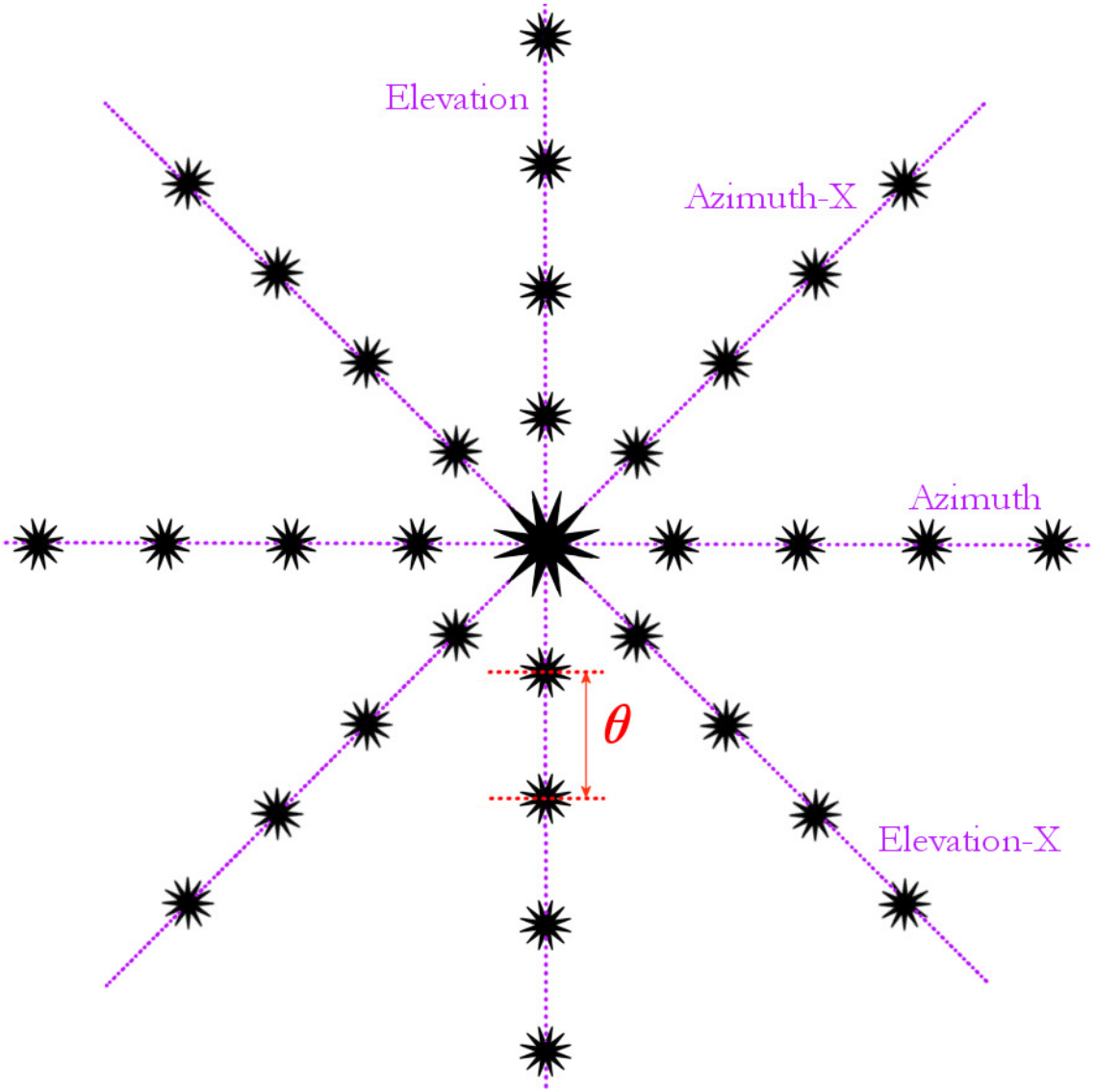

Figure 6.1: The grid used for observing the off-axis raster scans. Each axis is labelled on the end that I define as positive. Note that the Azimuth-X and Elevation-X axes were only observed at 610 MHz. For the 610 MHz observation, $\theta = 10'$, with 9 raster scans along each axis and a maximum offset of $40'$. The grid for the 325 MHz observation is similar, but uses $\theta = 20'$ to compensate for the larger beam, with a maximum offset of $80'$. The FWHM of the primary beam, as measured at the observatory, is $85.2'$ at 325 MHz and $44.4'$ at 610 MHz.

6.3 Inferring Direction-Dependent Beam Properties at 610 MHz

A lot can be inferred about the GMRT's off-axis response from a conventional observation. Observation 17_052 (see Chapter 5) has ~ 6 hours on source, with parallactic angle variation ranging from −86° to +89°. This observation was used to investigate the effects of direction-dependent instrumental polarisation. Stokes I and P images of the field are shown in Chapter 5.

The off-axis circular polarisation can also be investigated by looking at calibrator sources. As can be seen in Figure 4.18 in Chapter 4, the direction-dependent instrumental polarisation can be very high in Stokes V – numerous high intensity artefacts occur in locations with no corresponding Stokes I emission. In addition, as shown in Chapter 5, it appears that second-order polarisation leakage results in artefacts that surround the brightest emission in Stokes I. For the sake of completeness, constraints on the Stokes V beam are obtained in Section 6.4 but no further attempt is made to correct for this response. Unless specified otherwise, I use the term 'polarised' to refer to linear polarisation throughout this chapter.

6.3.1 Polarised Intensity

RM Synthesis was performed on the entire FOV surrounding M51, using images that were uncorrected for the Stokes I beam. The Faraday spectrum was processed between ±2000 rad m^{-2} with sampling every 1 rad m^{-2} (see Chapter 3). Sources with peak brightness above a 5σ threshold in Stokes I were manually identified. From the brightest pixel in Stokes I, those sources with a peak brightness $\geq$ 8σ in the amplitude of their Faraday spectrum[12] were considered polarised. These sources had their peak brightness in P calculated by fitting a Gaussian to data points surrounding the peak. The calculated peak in P was corrected for the effect of Rician bias using equation 2.52 and σ from the cleaned Q/U ϕ-cubes. The corrected values were used to calculate the fractional polarisation, $\Pi = P_0/I$. This procedure tends to underestimate the polarisation fraction, as sources may have polarisation structure that is offset from the peak in Stokes I. Nevertheless, the calculated values still provide a good estimate of the polarised intensity resulting from off-axis effects.

Sources with a peak brightness less than 8σ in the Faraday spectrum were considered unpolarised down to the sensitivity limit. The peak in the P image created from band-averaged Q and U was used to place an upper limit on the polarisation fraction of unpolarised sources. This is acceptable as I have shown the Faraday depths to be small (see Chapter 5). Bandwidth depolarisation will only be significant in this field for a RM> 40 rad m^{-2}. The calculated peak was corrected for Rician bias using equation 2.51 and σ from the Q/U images. This procedure tends to overestimate the polarisation fraction, as the bias correction does not work well for low

[12]The detection statistics differ in Faraday space. A 7σ detection threshold in ϕ-space has an equivalent false-detection rate to the ≈ 2.5σ level in total intensity. At 8σ, the false-detection rate is less than 1 in 33,000 (George et al. 2011).

s/n levels (Simmons & Stewart 1985). Nevertheless, the calculated values provide a reasonable upper limit on the polarisation fraction.

A plot of the fractional polarisation of polarised and unpolarised sources as a function of increasing distance from the phase-centre is shown in Figure 6.2. The plot provides a crude estimate of the direction-dependent instrumental polarisation. It must be remembered that M51 is located near the phase-centre with an angular size covering several arcminutes. The galaxy behaves as a depolarising Faraday screen. If I therefore only consider data beyond 10′, there is no clearly discernible increase in Π out to the half-power point. Between half-power to 10% of the Stokes *I* beam, the direction-dependent response does appear to steadily increase. The interpretation is hindered by the two polarised sources with $\Pi > 10\%$ in this region of the beam, as it is not clear if these are intrinsically of higher polarisation or are instead affected by beam effects. Beyond the 10% point of the beam, Π increases rapidly.

A direction-dependent response is therefore apparent, with the spurious polarised intensity of sources visibly increasing as a function of distance from the phase-centre. A conservative 'upper limit' on the effect of the polarisation beam at 610 MHz appears to be $\leq 2.5\%$ at the half-power point, with a rapid increase beyond this to $> 20\%$ at the edge of the beam. However, these 'upper limits' truly provide a lower bound. If the polarisation beam is oriented radially, it would be expected that this observation's large range in parallactic angle will have caused the direction-dependent instrumental effects to average down considerably. The 'snapshot' instrumental polarisation is actually best investigated via observation of an off-axis calibrator and is considered in Section 6.4.

6.3.2 Frequency-Dependence

It is essential to check the frequency response of the off-axis polarisation. Although different instruments, the WSRT is known to have a frequency-dependent beam pattern with a period of $\sim$ 17 MHz (Farnsworth et al. 2011). The VLA also showed a strong change in off-axis characteristics as a function of IF (Cotton 1994), while the EVLA beam polarisation is essentially frequency-independent across an observing band[13].

The application of RM Synthesis to the field of M51 can also be used to study the frequency-dependence of the direction-dependent polarisation. RM Synthesis is particularly useful as frequency-independent instrumental effects show up at a Faraday depth of 0 rad m^{-2} (Brentjens & de Bruyn 2005). The resulting output at a Faraday depth of 0 rad m^{-2} is shown in Figure 6.3. The Faraday depths of the sources are low (see Chapter 5) and no additional response was identified at high Faraday depths. This suggests the direction-dependent instrumental polarisation does not change rapidly with frequency.

The frequency-dependence of the beam polarisation can be further examined using bright, apparently spuriously polarised sources located far from the phase-centre (see Section 6.3.1). If

[13] http://www.ira.inaf.it/meetings/rm2010/talks/Cotton.pdf

significant frequency-variation in the beam properties exist, this will manifest as anomalous RMs for sources located off-axis. An NVSS catalogue of source RMs within 1.5 degrees of M51 show that the galaxy is located in an area with a mean RM of 0.06 rad m^{-2}, with σ of $\sim$ 12 rad m^{-2} (Taylor et al. 2009). All sources in the field were found to have consistently low RMs, with no discernible correlation as a function of distance from the phase-centre. The variation in Stokes Q and U for an example source located 30′ off-axis at 13h 28m 17.9s, 46° 46′ 21″ is shown in Figure 6.4. The source is clearly visible as the brightest spuriously polarised source to the SW of Figure 5.16. There is a slight decrease in Stokes Q at the low end of the band as a consequence of the bandpass, but the Q/U response otherwise appears stable with frequency.

In combination with the lack of direction-dependent instrumental polarisation at non-zero Faraday depths, the stable Q/U response as a function of frequency suggests that the wide-field polarisation beam has no significant frequency-dependence across an observing band at 610 MHz.

6.3.3 Polarisation Vector Orientation

The RM Synthesis performed on the field of M51 can also be used to study the geometry of the direction-dependent polarisation.

The results of RM Synthesis suggest that the off-axis instrumental response is oriented in a predominantly radial manner, as shown in Figure 6.3. Pen et al. (2009) show that this is anticipated and that leakage across the beam is expected to vary in a quadrupolar pattern. This is due to the GMRT's prime-focus feeds being mounted on four support legs which each have a width comparable to the observing wavelength. Consequently, one expects unpolarised sources within the first null to appear radially polarised, with sources beyond the null being tangentially polarised.

The radial orientation of the polarisation beam is useful for observations obtained during a full-track synthesis, as the radial polarisation will tend to average down over long integrations. This averaging down reduces the direction-dependent response within the half-power points at 610 MHz and assists considerably in reducing spurious polarisation. Nevertheless, I shall show that the snapshot direction-dependent effects are more substantial. The implication is that observations with a science goal requiring wide-field polarimetry should always observe over the full available range in parallactic angle, χ. This can help to reduce direction-dependent effects considerably.

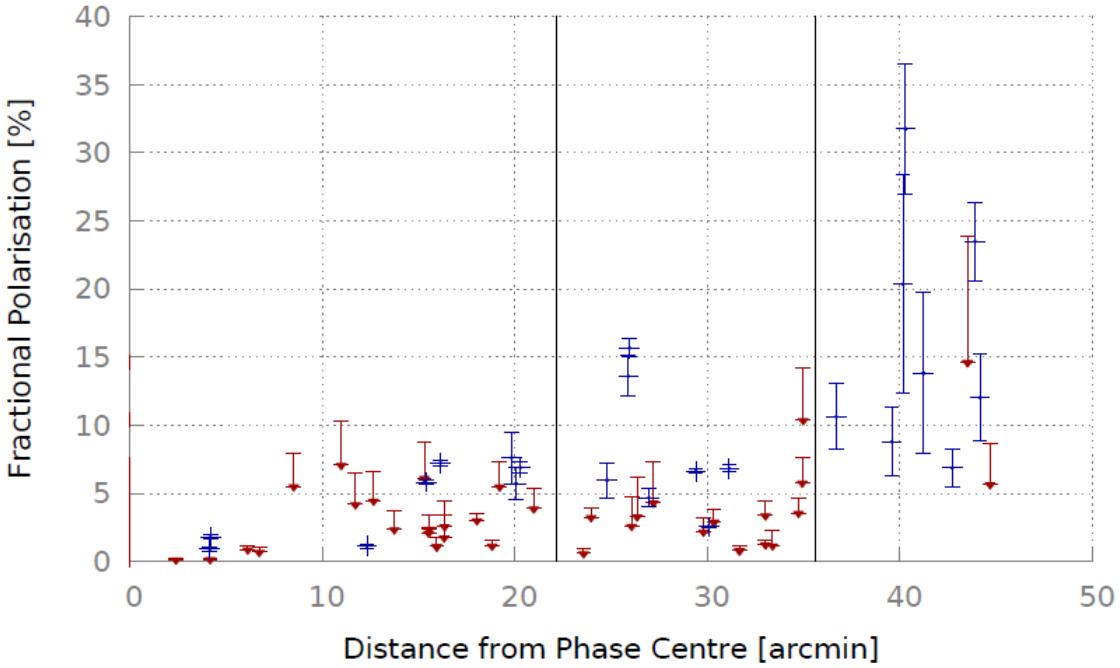

Figure 6.2: The fractional polarisation, Π, of sources surrounding M51 as a function of distance from the phase-centre. Sources detected above an 8σ limit following RM Synthesis are shown in blue. Sources undetected in polarisation within the sensitivity limit ($P < 8\sigma$) have an upper bound shown in red. The half-power and 10% points of the Stokes *I* beam are indicated by the solid vertical lines.

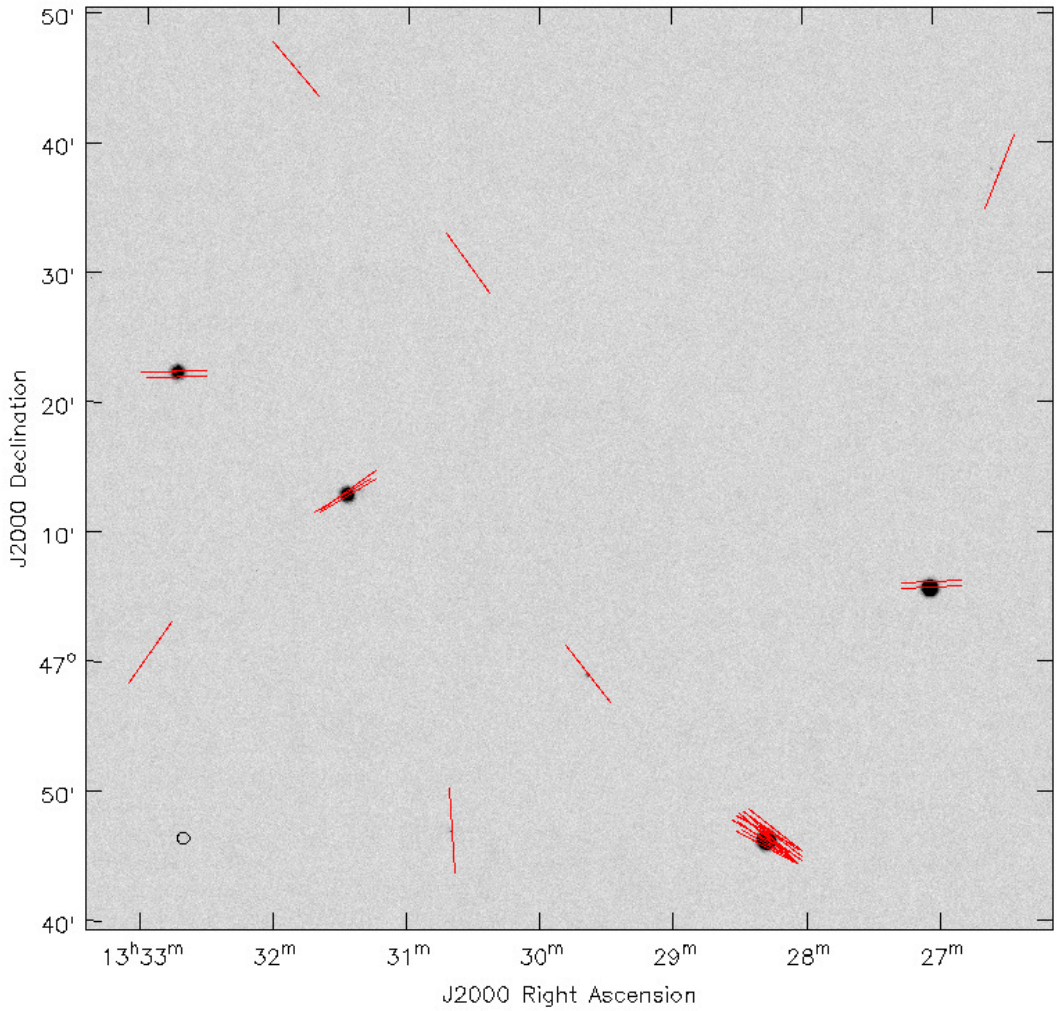

Figure 6.3: Grayscale image of the bandwidth averaged polarised intensity, $P = \sqrt{Q^2 + U^2}$, of the field surrounding M51 – the image has not been corrected for the Stokes I beam. The centre of the image is also the phase-centre of the observation. Red vectors indicate the orientation of the direction-dependent instrumental polarisation. The vectors are those at a Faraday depth of 0 rad m^{-2}, as obtained via RM Synthesis. The vectors are not proportional to polarised intensity – variations in polarised intensity across the 610 MHz primary beam are shown in Figure 6.2.

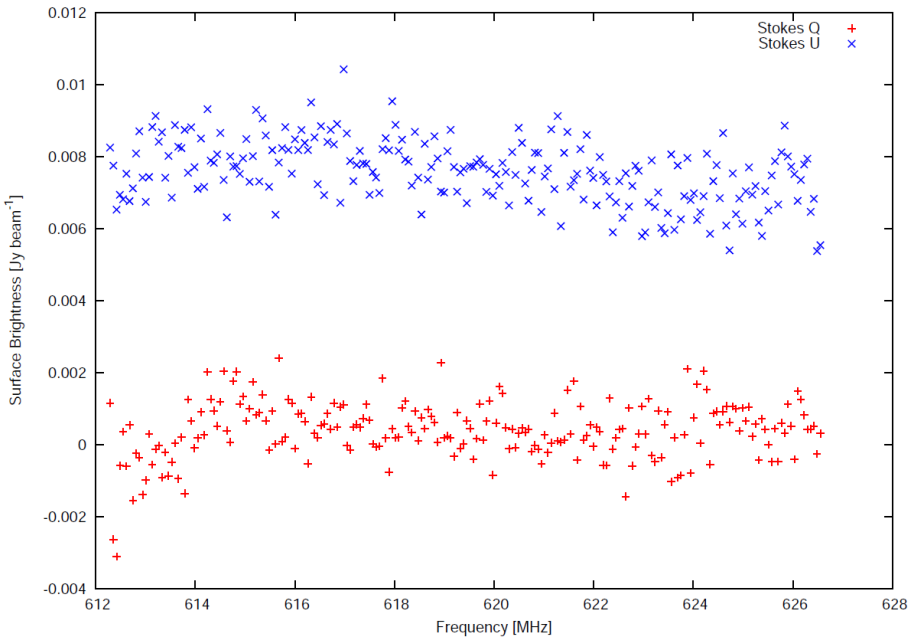

Figure 6.4: A plot showing the variation in polarised brightness as a function of frequency for a source located 30′ off-axis at 13h 28m 17.9s, 46° 46′ 21″. Stokes Q and U data are in red and blue respectively.

6.4 Retrieving the full-Stokes beam from holography rasters

The intention is to measure the direction-dependent instrumental polarisation response so that corrections can be applied to the *uv*-data. Optimal corrections may ultimately require individual beam models for each antenna, however the computational expense would be highly prohibitive. As such, the effect of the polarisation beam is best represented here by the response of the *average* antenna.

The AIPS task LISTR was used to output the average amplitude and phase of all visibilities, for each holography raster in all four cross-correlations. For an ideal, calibrated interferometer with circular feeds, the cross-correlations are complex quantities defined as

$$RR = \mathcal{A}(RR)e^{i\psi_{RR}} = I + V\,, \tag{6.1}$$

$$LL = \mathcal{A}(LL)e^{i\psi_{LL}} = I - V\,, \tag{6.2}$$

$$RL = \mathcal{A}(RL)e^{i\psi_{RL}} = Q + iU\,, \tag{6.3}$$

$$LR = \mathcal{A}(LR)e^{i\psi_{LR}} = Q - iU\,, \tag{6.4}$$

where $\mathcal{A}(jk)$ and ψ_{jk} are the amplitude and phase respectively. For a calibrated point-source, $\psi_{RR} = \psi_{LL} = 0$, so the phase terms of equations 6.1 and 6.2 can be neglected. However, the terms ψ_{RL} and ψ_{LR} cause mixing of Q and U and cannot be ignored.

By applying Euler's formula to equations 6.3 and 6.4, and then substituting into $RL = LR^*$ yields

$$\{\mathcal{A}(RL)\cos\psi_{RL} - \mathcal{A}(LR)\cos\psi_{LR}\} + i\,\{\mathcal{A}(RL)\sin\psi_{RL} + \mathcal{A}(LR)\sin\psi_{LR}\} = 0\,, \tag{6.5}$$

which has the solution

$$\mathcal{A}(RL)\cos\psi_{RL} - \mathcal{A}(LR)\cos\psi_{LR} = 0\,, \tag{6.6}$$

$$\mathcal{A}(RL)\sin\psi_{RL} + \mathcal{A}(LR)\sin\psi_{LR} = 0\,. \tag{6.7}$$

These solutions can be used to show that for real data, normalised for the effects of the Stokes I primary beam, the fractional polarimetric beam response at a given raster is

$$\frac{Q}{I} = \frac{\Re(RL + LR)}{RR + LL}\,, \tag{6.8}$$

$$\frac{U}{I} = \frac{\Im(RL - LR)}{RR + LL}\,, \tag{6.9}$$

$$\frac{V}{I} = \frac{RR - LL}{RR + LL}\,. \tag{6.10}$$

The Stokes I response itself can be obtained from

$$I = \frac{RR + LL}{2}\,. \tag{6.11}$$

A code was written in Python and used to calculate the polarisation beam response from the amplitude and phase output by AIPS, in conjunction with equations 6.8–6.11. This was done for each holographic raster in each of the individual 220 channels across the band. All of the holography sources are assumed to be unpolarised at these frequencies, so no correction for source polarisation was required.

The instrumental polarisation and effects of χ-rotation have only been corrected at the phase-centre. These effects are actually direction-dependent and due to the GMRT's alt-az mount, any residual instrumental polarisation will display an EVPA that rotates with χ. All off-axis holographic raster scans had to be corrected for the effects of this χ-dependent mixing of Q and U. This complication of the earlier on-axis calibration has to be undone by derotating Q and U, so that

$$(Q' + iU') = (Q + iU)e^{-2i\chi} \,. \tag{6.12}$$

The derotated Q' and U' can then be used to form a final beam profile in full-Stokes. The obtained beam profiles in full-polarisation across the band are shown at 325 MHz in Figure 6.5, and at 610 MHz in Figure 6.6.

The mean response across the band was obtained for each holography raster, so that the beam was described by a single datum per raster – creating a set of nine data per beam axis. Each axis was then fitted with a 5th order polynomial in Stokes I, Q, U, and V using an ordinary least-squares fit. All of the one-dimensional slices through the beam and the corresponding fits are shown at 325 MHz in Figure 6.7, and at 610 MHz in Figures 6.8–6.9. The general shape of each beam slice is well described by the fits.

Beyond the sampling limits of 40′ or 80′ at 610 MHz or 325 MHz respectively, the unconstrained polynomial fits deviate from the likely beam response. This has led to the introduction of artefacts in the beam maps at radii further away from the phase-centre than the sampling limit.

6.4.1 FWHM of the Stokes I beam

Following polynomial fitting, the FWHM of the Stokes I beam axes at 610 MHz were found to be (46.5′ ± 0.8′), (50.0′ ± 0.9′), (46.5′ ± 0.8′), and (49.8′ ± 0.8′) in Azimuth, Azimuth-X, Elevation, and Elevation-X respectively. This suggests the main lobe of the Stokes I beam has a squircle-shaped geometry at 610 MHz, with the FWHM of the beam increasing by ∼ 7.5% along the diagonal axes.

The FWHM of the Stokes I beam at 325 MHz was found to be (92.3′ ± 1.2′) and (93.1′ ± 1.2′) in Azimuth and Elevation respectively.

The measured FWHM of the primary beam differs from the values determined at the observatory of 85.2′ at 325 MHz and 44.4′ at 610 MHz. This is likely a consequence of both the fitting procedure and expected variations in the Stokes I beam – see Section 6.8 for additional detail.

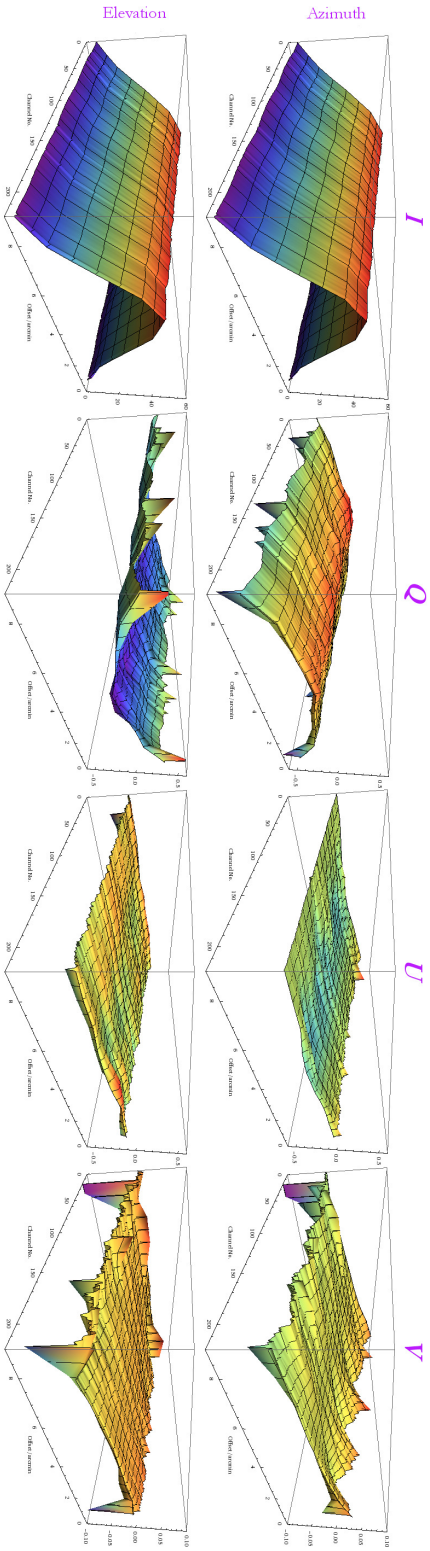

Figure 6.5: The beam profiles across the band at 325 MHz. The x-axis displays the offset from the phase-centre, the y-axis displays the beam response and is in units of 0–60 Jy for the unnormalised Stokes I beam, and units of fractional polarisation for the other Stokes parameters – the scales range from ±60% for Q and U, and ±10% for V. The z-axis displays the channel number across the band.

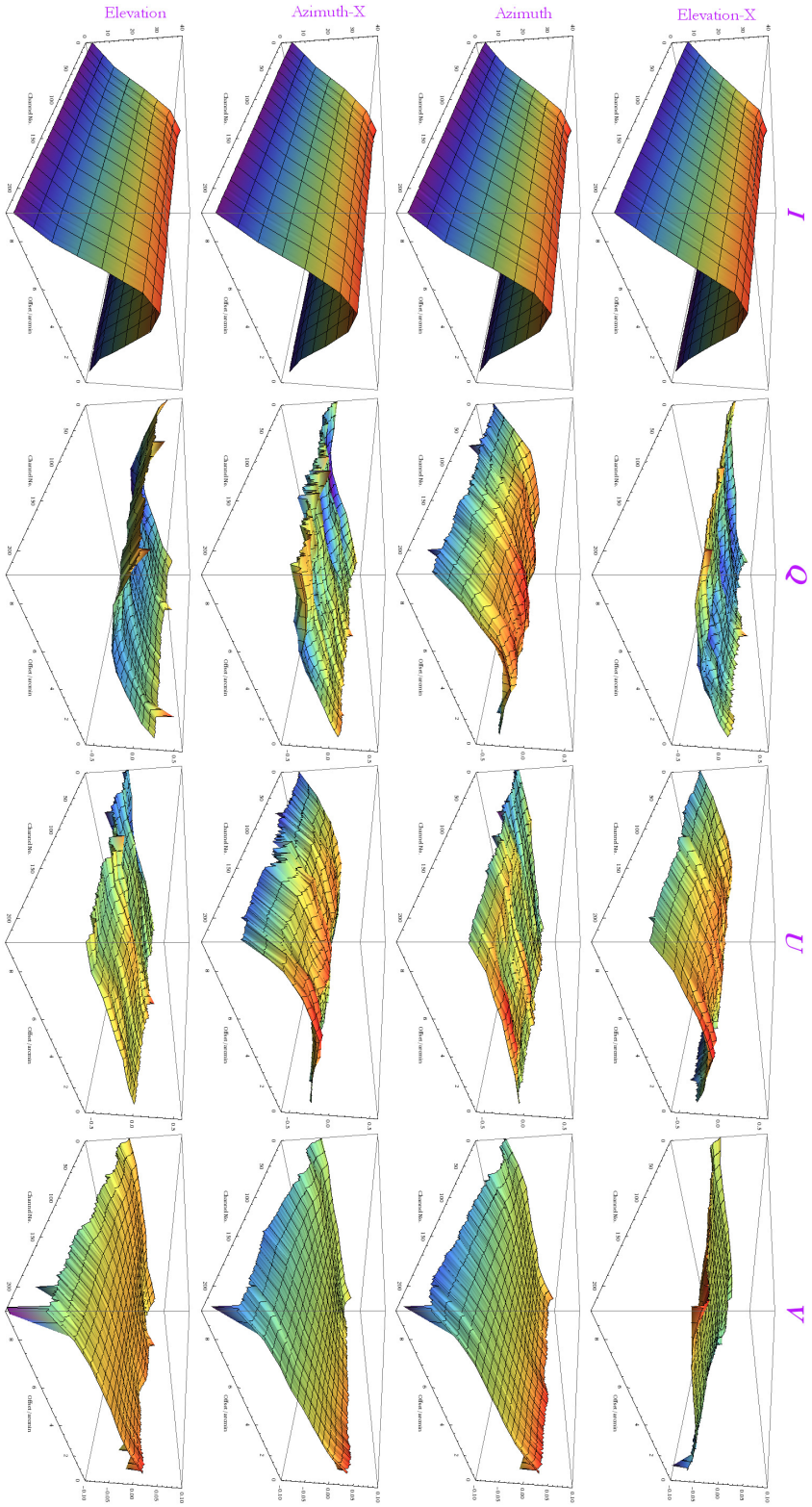

Figure 6.6: The beam profiles across the band at 610 MHz. The x-axis displays the offset from the phase-centre, the y-axis displays the beam response and is in units of 0–40 Jy for the unnormalised Stokes I beam, and units of fractional polarisation for the other Stokes parameters – the scales range from ±60% for Q and U, and ±10% for V. The z-axis displays the channel number across the band.

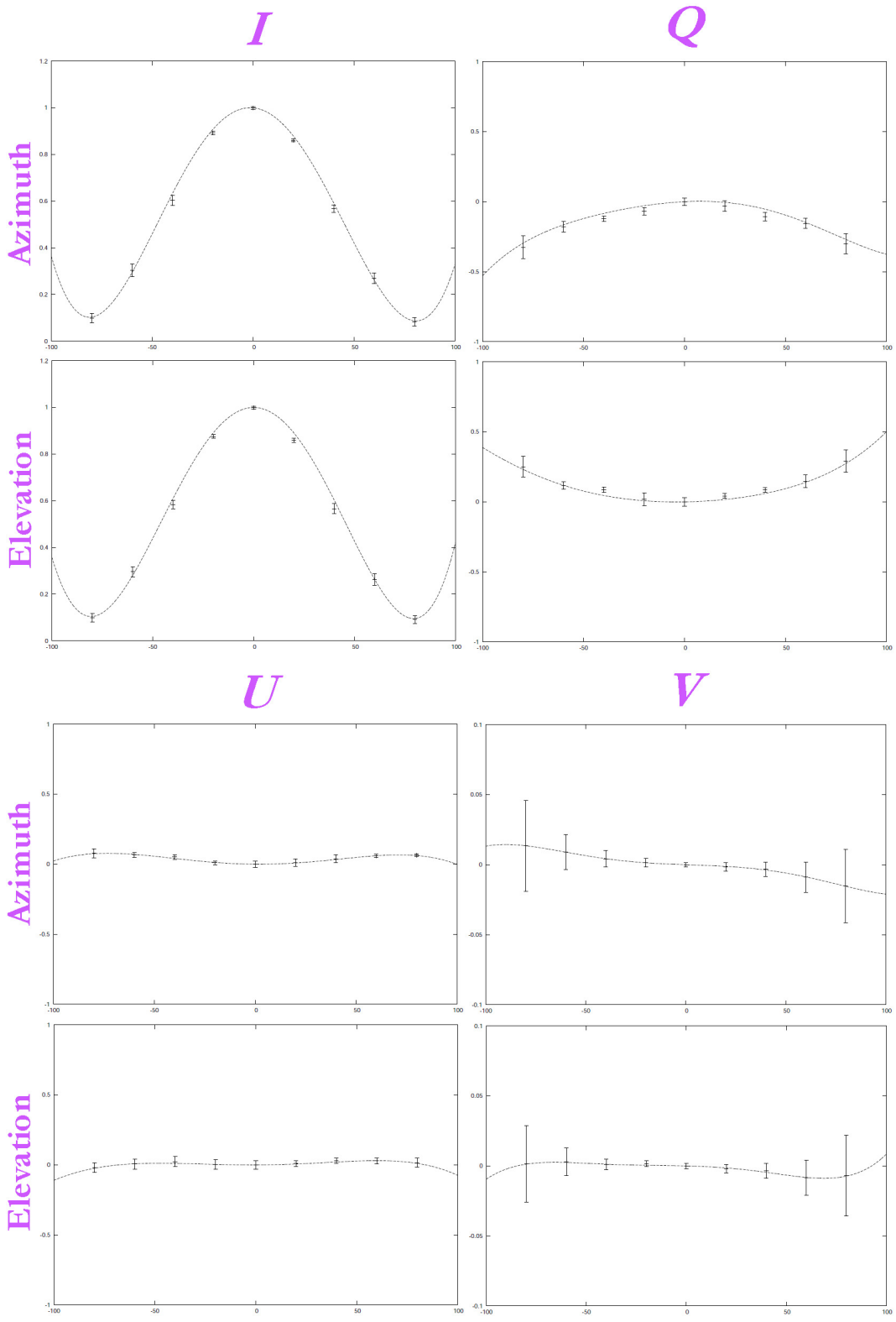

Figure 6.7: The 5th order polynomial fits to both beam axes for all Stokes parameters at 325 MHz, showing the normalised fractional response as a function of distance from the phase-centre. Stokes I has scales from 0–1.2, Q and U have scales from ±1, and V from ±0.1. Note that the data were sampled out to 80′.

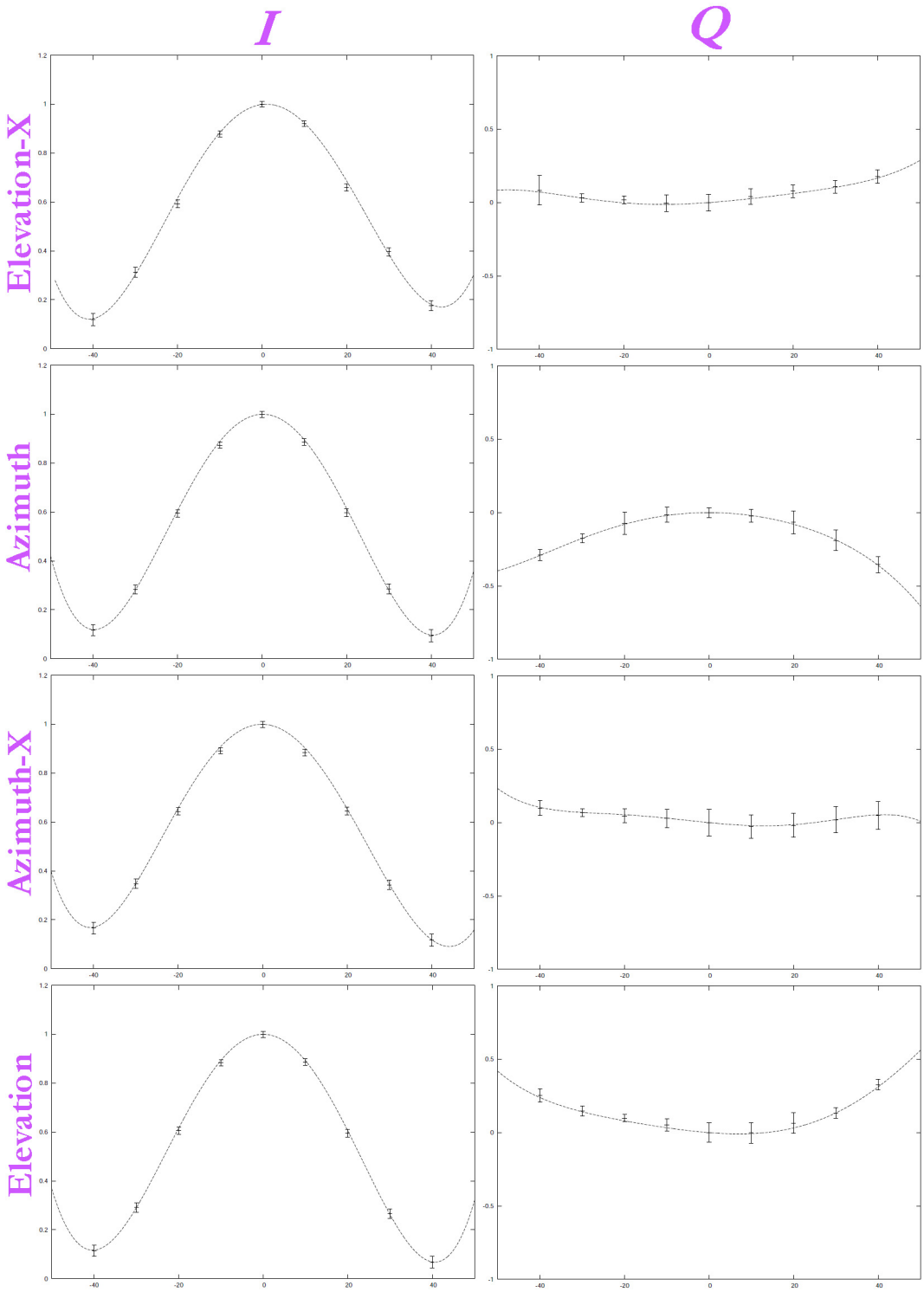

Figure 6.8: The 5th order polynomial fits to each beam axis for Stokes parameters I and Q at 610 MHz, showing the normalised fractional response as a function of distance from the phase-centre. Stokes I has scales from 0–1.2, while Q has scales from ±1. The fits to U and V are shown in Figure 6.9. Note that the data were sampled out to 40′.

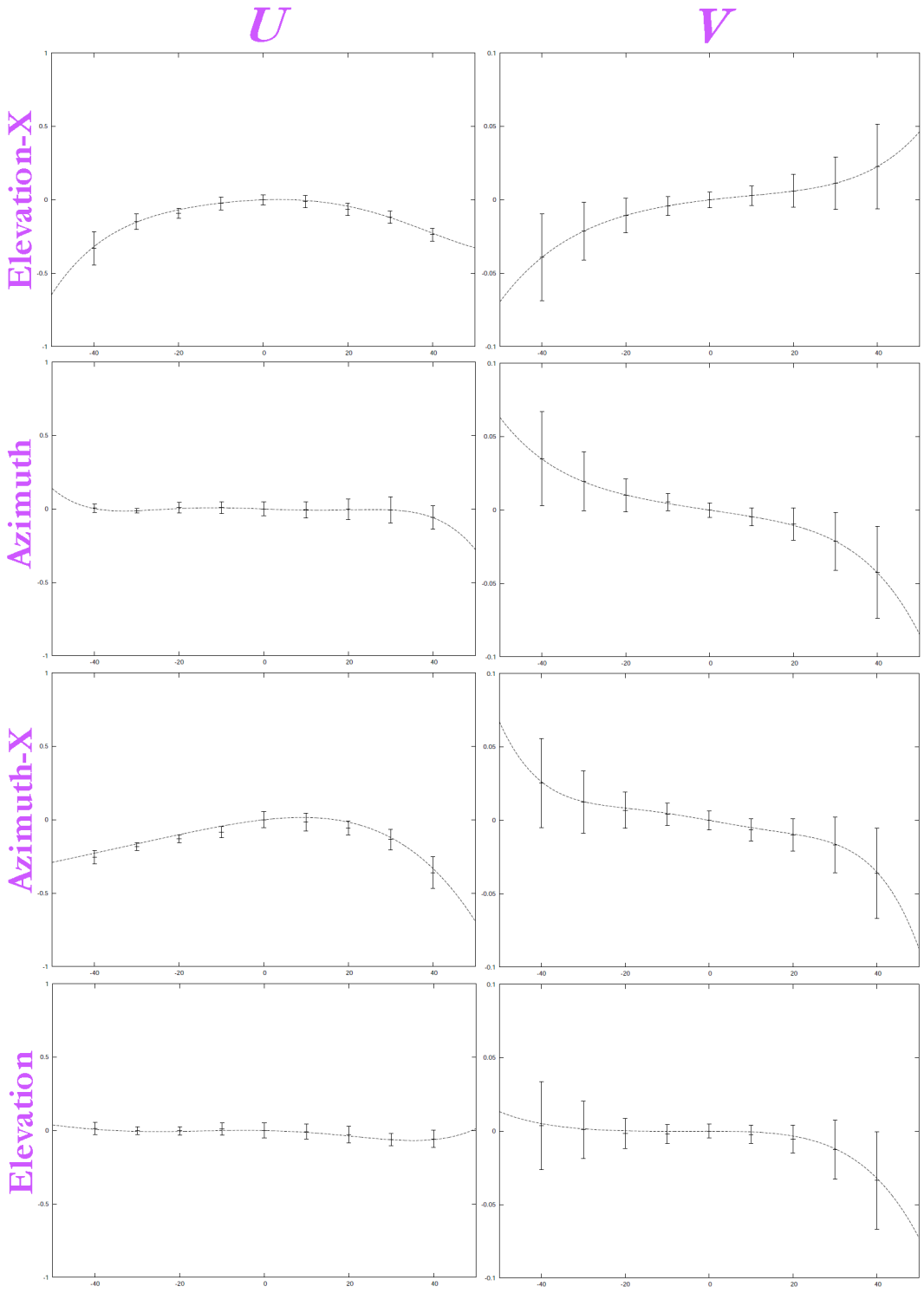

Figure 6.9: The 5th order polynomial fits to each beam axis for Stokes parameters U and V at 610 MHz, showing the normalised fractional response as a function of distance from the phase-centre. Stokes U has scales from ±1, and V from ±0.1. The fits to I and Q are shown in Figure 6.8. Note that the data were sampled out to 40′.

6.5 Two-dimensional mapping of the full-Stokes beam

The polynomial fits from Section 6.4 were used in order to create two-dimensional maps of the GMRT beam at 610 MHz. As the 325 MHz beam was not sampled along the diagonal axes, it was not possible to create a two-dimensional map at this frequency.

The polynomials describe the off-axis response for each Stokes parameter as a function of radius from the phase-centre, and so were used to tangentially interpolate and grid the beam response around the phase-centre at a given radius. This was carried out using cubic spline interpolation in order to smoothly interpolate the sparsely sampled data over the large tangential distances. Polynomial fitting may have given rise to significant Runge's phenomena.

Further consideration of the 610 MHz polarisation beam response along the diagonal axes suggests a significant problem with the Elevation-X axis. The direction-dependent response along this axis, as displayed in Figures 6.8–6.9, appears similar to the Azimuth-X axis. Consequently, polarisation vectors along the Elevation-X axis were oriented tangentially about the phase-centre in the initial Q and U maps – in disagreement with the results of RM Synthesis and the expected quadrupolar response of the GMRT polarisation beam, as discussed in Section 6.3.

Attempts to correct GMRT direction-dependent instrumental polarisation (see Section 6.6) failed using this initial beam model, with the polarisation of all sources tending to increase. Images made in AIPS of the off-axis holography sources confirmed that the unusual beam response was a result of the observation itself. As a test, the orientation of polarisation vectors along the Elevation-X axis were rotated so that they were forced to be oriented radially – this rotation was equivalent to a change of sign for both Q and U. The resulting maps are consistent with the response of the GMRT inferred using RM Synthesis, and appear to adequately correct direction-dependent effects. No explanation for this anomaly has been found, and it is crucial that this be checked by further observation.

The final two-dimensional beam at 610 MHz, interpolated under the assumption that the polarisation vectors are oriented radially along all axes, is shown in Figures 6.10–6.11.

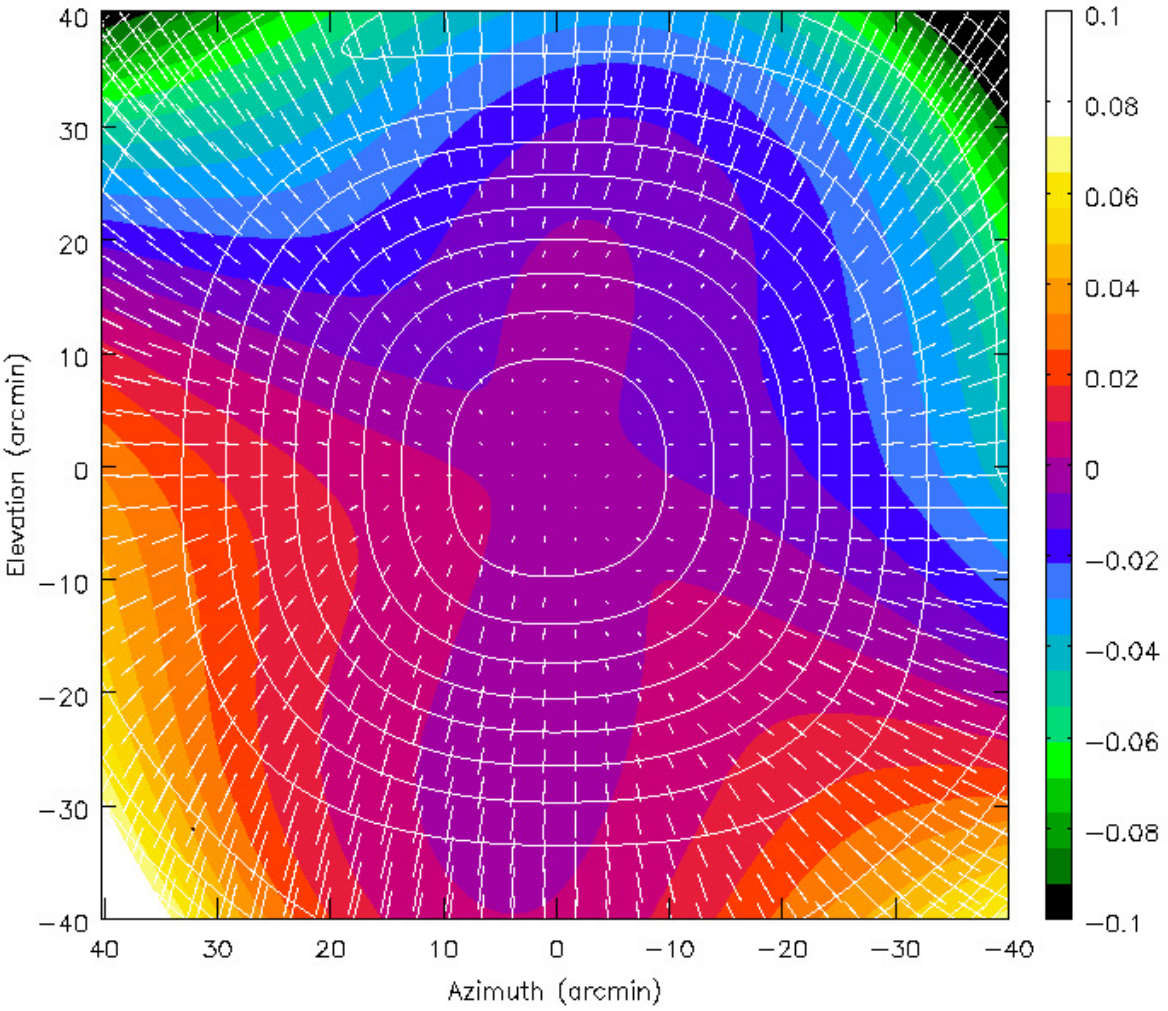

Figure 6.10: The main lobe of the GMRT primary beam in full-Stokes at 610 MHz. White contours show the Stokes I response with contour levels at 10, 20, 30…90%. White polarisation vectors are proportional to the linearly polarised intensity and indicate the orientation of the linearly polarised response. The Stokes V response is shown by the pseudo-colour scale, which ranges from ±10%.

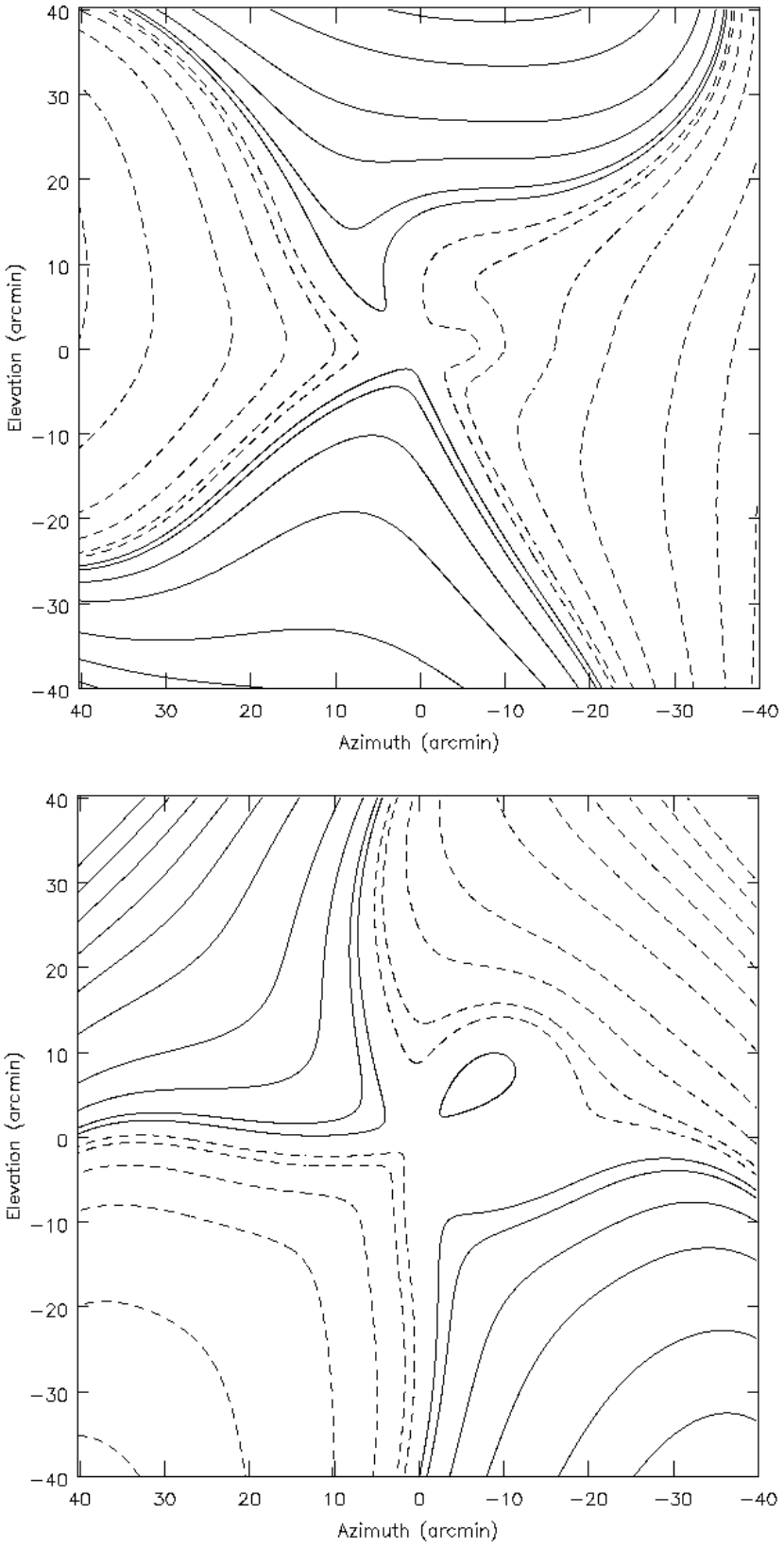

Figure 6.11: The Stokes Q (top) and U (bottom) fractional instrumental polarisation beam of the main lobe of the GMRT at 610 MHz. Contour levels are at ±1, 2, 5, 10, 20, 30...70%.

6.6 Correcting the Wide-field Response

The wide-field response of a radio interferometer is modulated by the full polarisation beam. In order to perform wide-field polarimetry, it is essential to be able to correct for these direction-dependent beam effects. No attempt was made to correct for the effects of spurious circular polarisation.

For linear polarisation observations with alt-az mounted circular feeds, the introduced aberrations are a consequence of three effects. For simplicity, I first consider a 'snapshot' observation, such that the data can be considered as of constant parallactic angle. For this case, polarimetric aberrations are introduced by:

1. The Q and U beam being rotated in the sky-plane by an amount equal to the parallactic angle.
2. Mixing of the Q/U beam response as a consequence of the parallactic angle.
3. The resulting rotated and mixed Q and U fractional polarisation beams allow a fraction of the total intensity to leak into the Q and U images.

For a single snapshot, it is possible to correct for these effects by first rotating the derived Q and U fractional polarisation beams, shown in Figure 6.11, by χ. The mixing of Q and U is introduced by the on-axis polarisation calibration and the associated correction for parallactic angle variation at the phase-centre – causing any spurious polarisation to rotate in the complex-plane as a function of χ. Similar corrections have previously been applied in the image-plane to VLA data for snapshot observations (Cotton 1994).

As most GMRT polarimetric observations are full-track observations, this procedure is clearly not ideal. As Cotton points out, it is possible to remove direction-dependent effects from full-track observations by independently correcting and imaging each snapshot of constant parallactic angle and averaging the resulting images. However, as CLEAN is a non-linear algorithm, the average of separately imaged 'chunks' of uv-data is not identical to a single image of averaged uv-data. This limitation has been overcome using a novel technique whereby the clean components from a Stokes I image are scaled by the previously mentioned χ-dependent effects, and the response removed in the uv-plane.

Having interpolated the beam model derived in Section 6.5 to the same geometry as the Stokes I image, the direction-dependent response, $R(x, y, \chi)$, for k clean components is described by

$$R = \sum_{i=1}^{k} I_i(x,y)\left\{Q(x',y') + iU(x',y')\right\} e^{2i\chi} \ni \begin{bmatrix} x' \\ y' \end{bmatrix} = \begin{bmatrix} \cos\chi & \sin\chi \\ -\sin\chi & \cos\chi \end{bmatrix} \begin{bmatrix} x \\ y \end{bmatrix}, \qquad (6.13)$$

where $I_i(x, y)$ is the Stokes I flux of the i-th clean component and $Q(x', y')$ & $U(x', y')$ are the fractional polarisation response obtained from the beam model. The pixel co-ordinates (x, y) and (x', y') are integers as a consequence of pixel quantisation in both the beam model and clean component list positions, and are related through the given rotation matrix. The centre

of the map is defined as pixel $(x, y) = (0, 0)$. The mixing of Q and U is analytically identical, but of opposite sign, to that in equation 6.12. The factor of 2 in the exponential originates from degenerate solutions for rotations of $\pm 180n$ degrees.

The response is calculated for each chunk of approximately constant parallactic angle throughout the full-synthesis, and the Fourier Transform of the scaled clean components is then subtracted from the data. The entire *uv*-data is then re-imaged. This method should have the advantage that the associated sidelobes of the spurious instrumental polarisation are also removed from the final images, thereby increasing the dynamic range.

The impact of the corrections on selected off-axis sources is shown in Figures 6.12–6.14. The corrections shown here allowed each chunk to have a maximum parallactic angle variation of $\Delta\chi = 10°$.

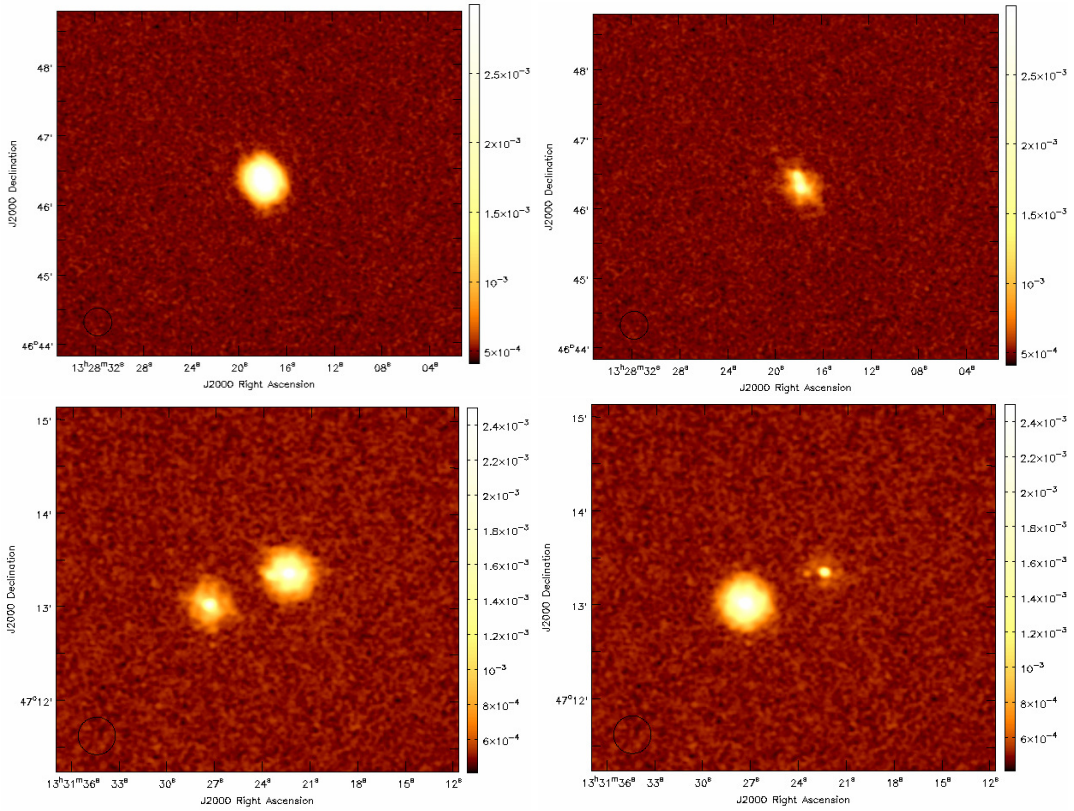

Figure 6.12: Images of the band-averaged polarised intensity both before (left) and after (right) the corrections for direction-dependent instrumental polarisation effects. Images are shown for two individual sets of sources as displayed to the top and bottom. These sources are located 25.4′ and 15.3′ off-axis respectively. One source (bottom) has its polarised intensity modified in an unusual way (see Section 6.8). The pseudo-colour scales are in units of Jy beam^{-1}, and the scales are identical for the before and after image of each source.

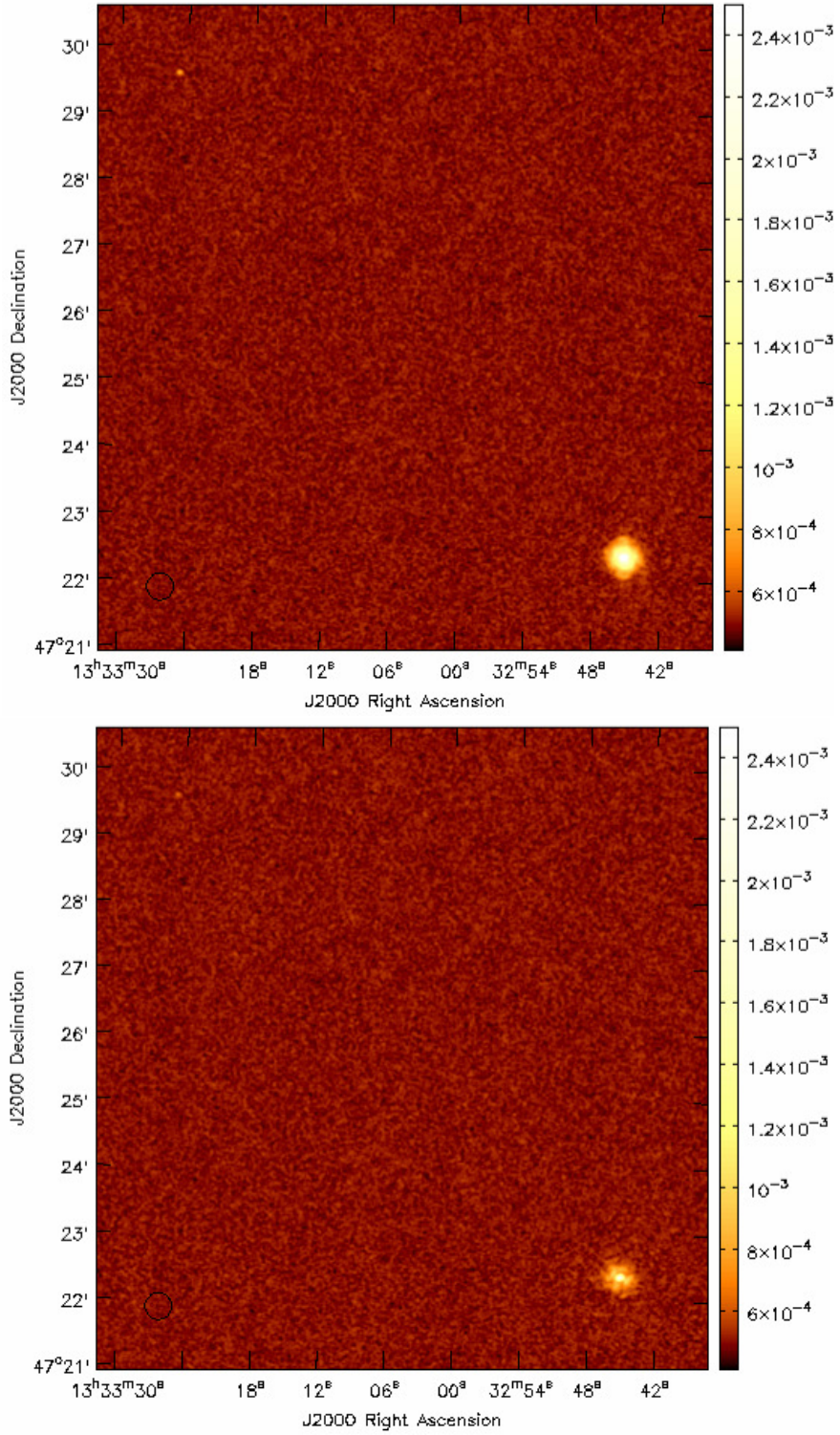

Figure 6.13: Similar to Figure 6.12, showing an image of the band-averaged polarised intensity both before (top) and after (bottom) the corrections for direction-dependent instrumental polarisation effects. Two sources – one in the NE and another in the SW – show reduced wide-field effects. The pseudo-colour scales are in units of Jy beam^{-1}, and the scales are identical for the before and after image. The sources are located 14.1′ off-axis.

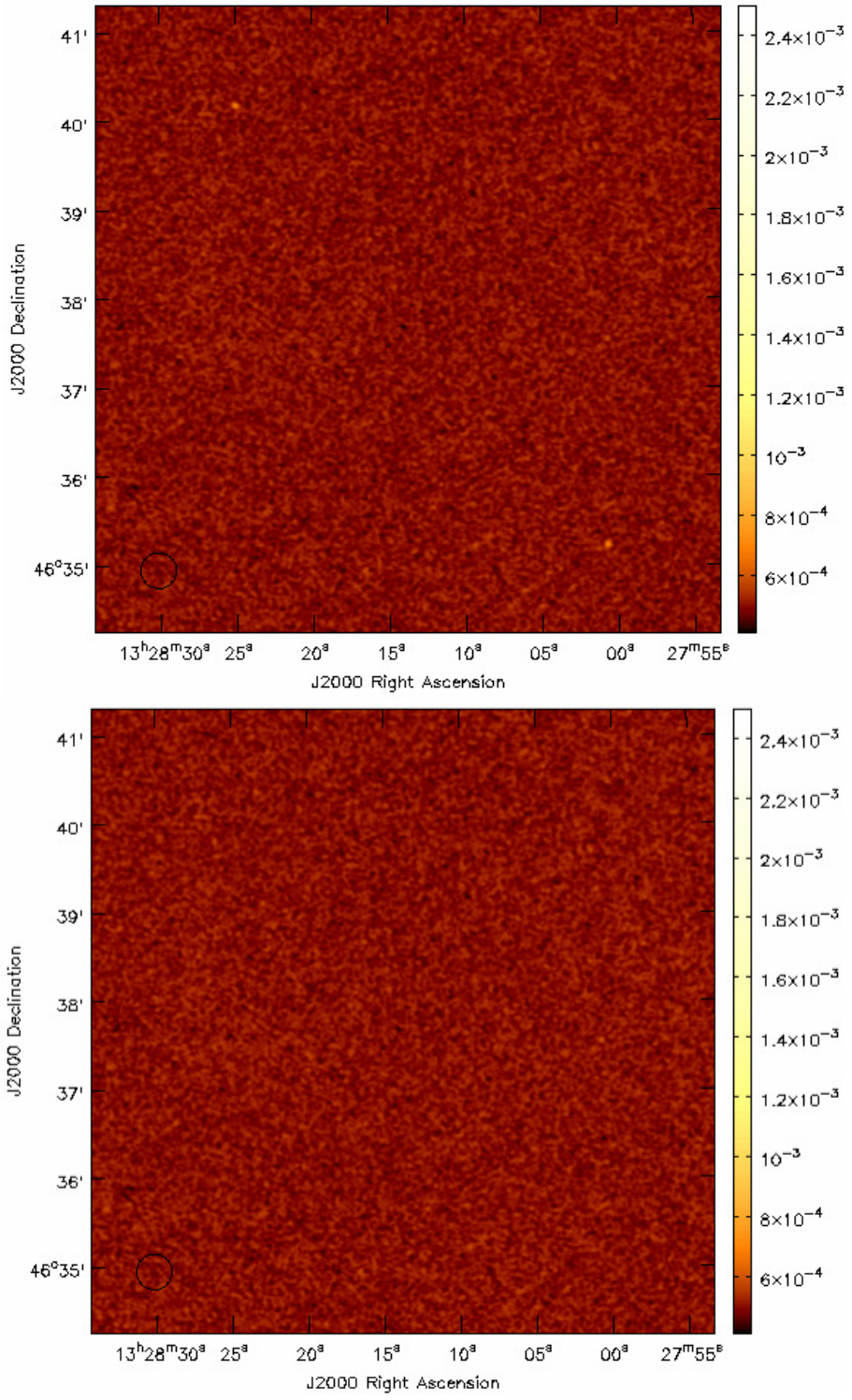

Figure 6.14: Similar to Figure 6.12, showing an image of the band-averaged polarised intensity both before (top) and after (bottom) the corrections for direction-dependent instrumental polarisation effects. Two apparently polarised sources – one in the NE and another in the SW – are completely removed from the image. The pseudo-colour scales are in units of Jy beam^{-1}, and the scales are identical for the before and after image. The sources are located 34.3′ off-axis.

6.7 A New Technique for EVPA Calibration

After solving for the instrumental leakage during polarisation calibration, the absolute value of the phase offset between R and L is left as an unconstrained degree of freedom. This needs to be corrected by observing a source with a known EVPA. The calibrators 3C138 and 3C286 are generally used for this purpose, with the RM and intrinsic EVPA measured at high frequency being used for interpolation to lower frequencies. This limits the quality of EVPA calibration, with errors in these *a priori* values cascading into measurements of RM from a target source. Furthermore, no source on the sky has had its RM directly measured using circular feeds; as is typical of interferometry, all RM measurements with circular feeds are *relative* to pre-determined values for an EVPA calibrator source.

This is particularly problematic for wide-band spectropolarimetry, as the assumed EVPA and RM of a calibrator source will be used to calibrate the source of interest. Consider an EVPA calibrator that is naively assumed to be well described by a single RM, but actually consists of multiple components at different Faraday depths. The single RM is then used to calibrate an observation of a target source, which is actually fundamentally described by a single RM. The flawed assumptions made about the EVPA calibrator will propagate into the target field, and RM Synthesis of the 'calibrated' target will erroneously yield multiple Faraday components along the line of sight.

Furthermore, ionospheric variations and source variability also have an impact on the current techniques used for EVPA calibration. As depolarisation is significant at low frequencies, there are substantial limitations to the number of sources with both a known, and a stable, intrinsic EVPA and RM. Overcoming this currently involves active searches for sources with 'low variability' – although these calibrator sources are rarely frequently monitored. Even in cases where the calibrators are monitored for variability, the variation is again only determined relative to yet another EVPA calibrator. It is clear that ideally, calibration would be improved if we could manufacture a polarised source in the sky with extremely well-defined and stable properties.

Having a suitable model of the wide-field response of an interferometer allows for EVPA calibration to be applied using the spurious off-axis polarisation of any bright unpolarised source. As the calibrator's 'polarisation' is a consequence of the antenna, such a correction process is independent of ionospheric variation. The process removes the need for calibration relative to any reference source, and instead makes the calibration relative only to the interferometer's beam.

In the case of the GMRT, the beam model has shown the wide-field response to be both frequency-independent and oriented radially. In order to correct the data, the off-axis mixing of Q/U as described in equation 6.12 has to be taken into account. Hence the correction to be enacted in the AIPS task CLCOR is given by

$$\text{CLCORPRM}(1) = 2\chi - 180 - \psi_{RL}\,, \tag{6.14}$$

where χ is the parallactic angle of the off-axis scan of the unpolarised source, and $\psi_{RL} = \psi_{LR^*}$ is the RL-phase as either output by task RLDIF or determined from the integrated Q and U flux in the images such that

$$\psi_{RL} = 2\phi = \arctan\left(\frac{\Sigma U}{\Sigma Q}\right). \tag{6.15}$$

Taking equation 6.12 and substituting in $Q = p_0 \cos 2\phi$ and $U = p_0 \sin 2\phi$ yields

$$(Q' + iU') = p_0 \{\cos(2\phi - 2\chi) + i \sin(2\phi - 2\chi)\} \tag{6.16}$$

and so following calibration the measured EVPA of the off-axis source is given by ϕ, while the EVPA of the source in the antenna frame (i.e. independent of parallactic angle effects), ϕ', is given by

$$\phi' = \phi - \chi\,. \tag{6.17}$$

This method was tested at the GMRT, with knowledge of the full-Stokes beam used to correct the EVPA using 3C48 at 325 MHz, and 3C147 at 610 MHz. The calibrated data were then used to determine the RMs of B1937+21 at 325 MHz, and 3C138 at 610 MHz. The corrections yield a RM=+8.2 ± 0.4 rad m^{-2} for B1937+21 – in excellent agreement with the previously determined value at this frequency of +8.5 ± 0.5 rad m^{-2} (Brentjens 2008). The variations in the EVPA as a function of λ^2 is shown for B1937+21 at 325 MHz in Figure 6.15. The RM of 3C138 was found to be +11.5 ± 0.9 rad m^{-2} at 610 MHz – a positive RM consistent with 'discrepant' values measured relative to 3C286 (see Chapter 4 for further detail).

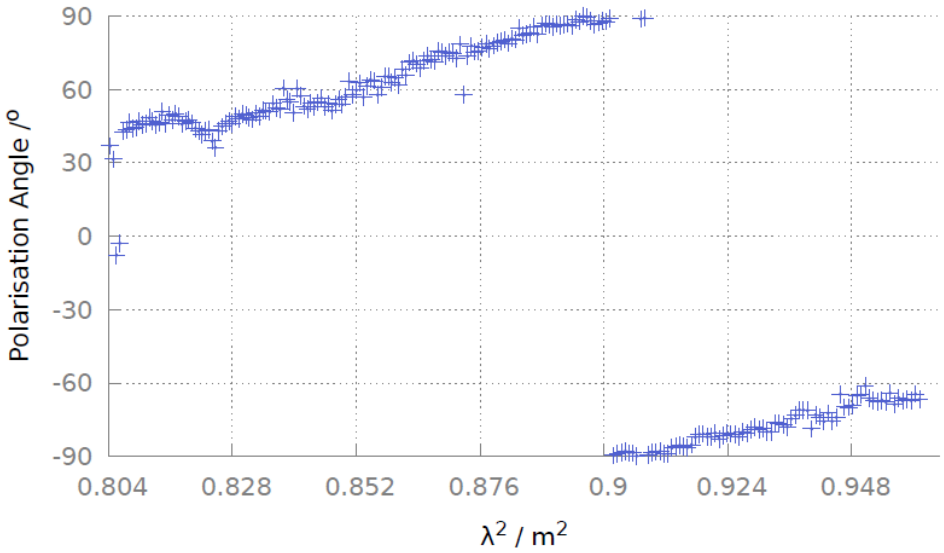

Figure 6.15: A plot of the EVPA as a function of λ^2 for B1937+21 at 325 MHz, following EVPA calibration using the direction-dependent response of the GMRT.

Using the direction-dependent response of an interferometer to calibrate the EVPA may be particularly useful for facilities such as LOFAR and the MWA – where the science requires

highly accurate determination of source RMs, with ionospheric effects eliminated from the data. The corrections are limited only by knowledge of the beam model. The caveat is that the interferometer that is being calibrated must have significant direction-dependent instrumental polarisation.

6.8 Discussion

A classical model of beam squint/squash in prime-focus feeds suggests that beam squash can arise in Q/U due to two effects: the interaction of the linearly polarised vectors with the curvature of the reflecting surface, and the difference between the two polarisations in illumination of the primary surface (which occurs from pseudo-waveguide modes in a feed). Similarly, beam squint should arise in V due to the feed not pointing directly at the vertex of the paraboloid. There is no anticipation of beam squint in Q/U or beam squash in V (Heiles et al. 2003).

The fundamental cause of direction-dependent instrumental linear polarisation is the curved reflecting surface, which slightly changes the direction of an incident electric vector upon reflection. For on-axis sources, these polarimetric aberrations cancel out. For off-axis sources, the path length to the source from different parts of the reflecting surface are not all equal. These distortions increase with curvature (Heiles 2002; Tinbergen 1996). Reassuringly, the instantaneous Q/U beams deduced at 325 MHz and 610 MHz are compatible with this model, as the direction-dependent effects appear to scale with the FWHM of the Stokes I beam – implying that the beam squash is a result of interaction with the curved reflecting mesh, and not a consequence of the feed itself.

The constraints placed on direction-dependent effects across the GMRT beam show that the snapshot 610 MHz instrumental response increases to $\sim 10\%$ at the half-power point, and increases rapidly to $> 30\%$ beyond 10% of the Stokes I beam. The measured beam squash suggests that mosaicing snapshot observations would not be sufficient to overcome off-axis effects at the GMRT, as the half-power point snapshot P of $\sim 10\%$ at 610 MHz is greater than the expected median source polarisation of $\sim 2.5\%$ at this frequency. Nevertheless, the full-track observation of M51 shows that this instantaneous instrumental polarisation can average down substantially over a large range in parallactic angle. The 325 MHz snapshot instrumental polarisation is similar to that at 610 MHz, and increases to $\sim 10\%$ at the half-power point, and to $\sim 30\%$ at 10% of the Stokes I primary beam.

Consequently, full-track observations should be used to reduce direction-dependent effects at the GMRT. The use of mosaicing would reduce these off-axis effects further by an additional factor of ~ 2. As a conservative upper limit for observations taken over a large χ-track, the instrumental polarisation at 610 MHz is at most $\sim 2.5\%$ at the half-power point, increasing steadily to $> 20\%$ beyond 10% of the Stokes I beam. Previous analyses of the 150 MHz GMRT beam are also possibly consistent with the off-axis response averaging down as a function of χ, with an instrumental polarisation of $\sim 2.5\%$ at the half-power point for a full-track observation

(Pen et al. 2009). However, no measurements of the instantaneous 150 MHz beam are currently available. Given the previously discussed scaling of direction-dependent effects with frequency, it is likely that the 150 MHz instantaneous beam is also simply a scaled version of the 610 MHz beam model shown in Figure 6.10.

Although not derived here, this scaling with frequency should in principle allow for the beam to be parameterised by a single mathematical function across all observing bands. This leads to the possibility that the GMRT Stokes I beam can also be defined by a single model for all frequencies, similar to the $\cos^6(c \times n \times r)$ derived for the WSRT (Popping & Braun 2008). Variations in the Stokes I beam-width at the GMRT are expected, and the FWHM at 610 MHz is known to range from 42.3′–47.2′ in elevation, and from 42.3′–47.0′ in azimuth (Nimisha Kantharia: priv. comm.). However, the beam results suggest that the 610 MHz primary beam has a squircle-like geometry, with the FWHM increased by $\sim 7.5\%$ along the diagonal axes – coincident with the location of the feed support legs. Peeling is often required at the GMRT at this frequency, and may be a result of time-variable direction-dependent gains caused by the Stokes I beam rotating on the sky with varying χ. It would be interesting to employ more refined beam models in a-projection algorithms, which are able to remove such effects (Bhatnagar et al. 2008).

The classical model of beam squint suggests that for observations of circular polarisation with a parabolic reflector and a feed perfectly aligned with the vertex of the paraboloid, there is perfect circular symmetry and therefore no beam structure in V. However, if the feed deviates slightly from the vertex along the x-direction, then the two circularly polarised beams will point in slightly different directions along the y-direction, i.e. with the y-direction oriented perpendicularly to the x-direction (Heiles 2002). This suggests that spurious V emission could be more significant in azimuth at the GMRT, as the rotating feed turret (which rotates about the elevation axis) may not lock exactly into place and point directly towards the vertex of the dish. Indeed, the Stokes V beam measured here is increased marginally in azimuth compared to elevation, by a magnitude of $\sim 1.5\%$. It is likely the Stokes V beam therefore changes slightly with each rotation of the feed turret.

The results from RM Synthesis at 610 MHz are consistent with the instrumental linear polarisation being oriented radially with respect to the phase-centre. The analyses of the beam, at both 325 MHz and 610 MHz, are also largely consistent with a radial orientation, with the notable exception of data from the Elevation-X axis at 610 MHz. This anomaly could feasibly be a result of gravitational deformation of the feed support legs, however why this should only afflict one axis is unclear. Nevertheless, such flips in the beam are not unprecedented. Although a very different instrument, the Green Bank Telescope (GBT) has a polarisation beam that undergoes random rotations of $Q + iU$ by 90°, which is equivalent to a change in sign (Heiles et al. 2003). This is analogous to the flip observed at the GMRT. The flip along the Elevation-X axis may therefore indicate that the beam is not constant at different epochs. If this is the case at the GMRT, this will inhibit wide-field polarimetric observations as an unfeasible amount of

preparatory time will be required to monitor a possibly unstable beam response. It could also be that blockage from the feed support legs lead to a localised change in the EVPA directly along the Elevation-X axis – if this is the case, the beam must exhibit rapidly varying properties near to the diagonal axes. The lack of a flip along the Azimuth-X axis (which would also be subject to blockage from the feed supports) is contrary to this. Ultimately, all of these possibilities amount to speculation as there is insufficient evidence to firmly conclude the nature of the beam flip – an unknown error during data collection cannot be ruled out. It is important to re-observe the beam and provide more constraints. Nevertheless, rotation of the Elevation-X axis so that it is oriented radially allows for direction-dependent effects to be removed successfully from *uv*-data.

The polarisation beam corrections implemented in Section 6.6 are novel in that they directly correct the *uv*-data using a Stokes *I* model of an observed field. These corrections have been used to successfully correct for direction-dependent instrumental polarisation – although by far less than had been hoped and with a number of limitations. The spurious linear polarisation is typically reduced by a factor of ∼2. Although useful, the beam corrections work best at correcting instrumental effects beyond the half-power point. The computational expense is therefore unlikely to be worthwhile, particularly when an equivalent or better reduction of the instrumental effects could be achieved via the combination of large parallactic angle ranges and mosaicing. Nevertheless, the corrections could be improved by implementing a cut-off for the Stokes *I* clean components, as noise and low-level artefacts that are cleaned in Stokes *I* currently get added into the linear polarisation images. Additionally some sources increase in *P* as shown in Figure 6.12. This can be expected depending on the precise combination of source and instrumental polarisation, but may also suggest that the beam model is not sufficiently accurate. The latter is likely as the direction-dependent corrections implemented here reduce the instrumental polarisation most effectively at distances $> 30'$ from the phase-centre i.e. where the corrections are of a larger magnitude. Limitations to the corrections may result from the decrease in signal-to-noise of rasters near to the phase-centre, significant beam variation between individual antennas, the coarse sampling used, or because of assumptions of χ constancy in each snapshot. In the corrections presented in this report, each chunk has $\Delta\chi < 10^{\circ}$, and no attempt to test the effects of different $\Delta\chi$ has been made. Nevertheless, reasonable wide-field polarimetry is possible at the GMRT via the use of full χ-tracks. Such direction-dependent corrections will be most useful in efforts to retrieve the intrinsic EVPA of sources, which is clearly corrupted by the instrumental beam – as shown in Figure 6.3.

New data are needed to improve the beam model and consequently the corrections. An attempt to monitor the beam out to the first sidelobe, with more axes, and less sparsely-sampled rasters would significantly enhance the model. The recommendation would be that tests are performed, the feed turret rotated, and the tests repeated in order to rule out epoch-dependent variations due to locking of the feed turret mechanism. This would also allow for checks on the observed change in sign along the Elevation-X axis. Such observations, if taken for all

GMRT bands, may provide the possibility of describing the beam with a unified model which is a function of frequency.

Knowledge of a telescope's beam is extremely important, as demonstrated by the ability to calibrate the EVPA using the direction-dependent response – allowing for corrections that are independent of ionospheric effects. Improving the beam model at the GMRT is one of the most important endeavours that could currently be carried out to refine the instrumental response, and follow-up observations should be strongly considered. Such observations may lead to improvements in the pointing model and dynamic range at all frequencies.

CHAPTER 7

TWO SOUTHERN COMPACT GROUPS: THE GRUS QUARTET AND USCG S063

> "I don't believe in Astrology. I'm a Sagittarius and we're sceptical."
>
> *Arthur C. Clarke*

In Chapter 6, I placed constraints on the direction-dependent instrumental polarisation at the GMRT. Here I present full wide-field spectropolarimetric GMRT observations of two Southern Compact Groups of galaxies at 610 MHz. The GMRT data are used alongside Sydney University Molonglo Sky Survey (SUMSS) data at 843 MHz, and near infra-red data from the DSS-2 survey. These data allow for companion sources at other wavelengths to be identified, and allow for a search for evidence of hydrodynamical interactions within the groups. The full-polar radio data also allow for measurements of the group members' spectral index, polarisation fraction, Faraday depth, and RM.

7.1 Background

Galaxy groups are some of the smallest and most dense associations of galaxies. These groups are gravitationally bound structures in various stages of dynamical evolution, from young and spiral-dominated to almost completely merged. They are amongst the best natural laboratories for investigating the impact of galaxy interactions on the evolution of the intragroup medium (IGM). It is known that mergers and less powerful interactions can be a significant contributor to heating of the IGM via both supernova explosions and the triggering of active galactic nuclei (AGN) (e.g. Pompei et al. 2007).

Hickson (1982) presented a sample of compact groups that have since been well-studied. Multi-wavelength observations of Hickson's Compact Groups (HCGs) have shown that many of these groups are physically bound and in different stages of evolution (Hickson 1982). Tidal interactions have been shown to occur frequently in HCGs, with ~50% of the galaxies showing signs of morphological disturbances. It is likely that these tidal interactions play a substantial role in the evolution of the galaxies and their morphological type (e.g. Pompei et al. 2007). Verdes-Montenegro et al. (2001) suggests a classification scheme for the state of dynamical evolution based on the HI properties. In phase 1, the gas is mainly centred on the member galaxies. In phase 2, the galaxies have extended tidal tails and a perturbed gas distribution. In phase 3a, almost no or very little HI is left in the group galaxies. In the last and least common phase, phase 3b, all the HI gas is distributed in the group potential well and not centred on any single galaxy (Pompei et al. 2007). However, the HCG sample shows a significant lack of spiral galaxies, and most of the HCGs appear to be in an advanced stage of evolution (Ponman et al. 1996; Coziol et al. 1998; Ribeiro et al. 1998).

A more recent sample of galaxy groups are the Southern Compact Groups (SCGs), which few studies have analysed in detail. The sample consists of 121 groups over ~25% of the southern sky (Iovino 2002). The automated algorithm used to select the SCG sample follows criteria that are similar to that used for HCGs, but also avoids one of the biases of the HCG catalogue – as fainter galaxy members with a magnitude close to the cut-off limit were discarded by the eyeball search used for the identification of HCGs. The selection criteria for the SCGs are based on richness, isolation, and compactness in order to identify groups in the blue plates from the COSMOS survey – for further detail, see Iovino (2002).

The SCG sample is believed to be younger than HCGs due to a higher number of spiral galaxies. This is likely as the blue plates from the COSMOS survey tend to highlight younger galaxies in comparison to the red plates used for the HCGs (Pompei et al. 2007). Nevertheless, evolutionary trends in SCGs based on the properties of the warm IGM are similar to what has been found for HCGs.

Here I present radio continuum observations of two groups from the SCG sample. The groups, the Grus Quartet and USCG S063 (also known as SCG 2315–4241 and SCG 0141–3429 respectively), are studied using the GMRT at 610 MHz alongside near-IR data from the Digital Sky Survey (DSS). Other observations suggest that both groups are in phase 2 of their evolution, with extended tidal tails and a perturbed gas distribution (Pompei et al. 2007; Dahlem 2005). The radio observations were carried out in full-polar mode, allowing for constraints on the observed source's polarisation and RM.

Additional details of the observations are provided in Section 7.2. The identified compact sources and their spectral indices are derived in Section 7.3. The group galaxies are investigated in Section 7.4, while extended sources unrelated to the groups are studied in Section 7.5. A discussion of the results is provided in Section 7.6. Throughout this chapter a ΛCDM cosmology has been assumed with $\Omega_M = 0.27$, $\Omega_\Lambda = 0.73$, and $H_0 = 71$ km s^{-1} Mpc^{-1}. The spectral index,

α, is defined such that $S \propto \nu^{-\alpha}$. All stated Faraday depths and RMs are the observed values – a rest-frame correction of $(1 + z)^2$ has not been applied.

7.2 Observations

The GMRT data consisted of observations 17_060_1 and 17_060_2 (see Chapter 3 for further detail). Observation 17_060_1 used the phase calibrator J0240–231, while 17_060_2 used J2314–449. The derived fluxes were found to be 5.23 ± 0.06 Jy and 3.05 ± 0.04 Jy respectively, and are in agreement with values determined previously at the GMRT to within ±5%. The data were limited by significant phase errors surrounding strong sources offset from the phase-centre. These artefacts were improved substantially using the AIPS task PEELR, which performed a direction-dependent self-calibration with SOLINT= 1 min. Nevertheless, unpeeled images were used for the calculation of all spectral indices as the peeling was found to have reduced the flux levels in the images. Varying trial values of SOLINT did not correct the problem. Checks on the calibrators 3C48 and 3C138 suggests that the residual instrumental polarisation is conservatively $\leq 0.5\%$ (see Chapter 4).

The GMRT data were combined with images from the SUMSS (Bock et al. 1999) at 843 MHz in order to retrieve the peak brightness and spectral index of sources. The GMRT data were reconvolved to a restoring beam of $45'' \times 45'' \csc |\delta|$, where δ is the declination of each observation (Mauch et al. 2003). The SUMSS images were then regridded to the same geometry as the GMRT images. The SUMSS data had an rms noise of 2.2 mJy beam^{-1} in the field of USCG S063, and 1.8 mJy beam^{-1} in the field of the Grus Quartet. All compact sources in the images appear aligned to $\leq 1.2''$.

Note that errors in the derived spectral indices are otherwise dominated by flux calibration errors, which are assumed to be 5% and 3% for the GMRT and SUMSS data respectively. There are further systematics originating from the limited accuracy of the beam model at the GMRT. All images were corrected for the effects of primary beam attenuation using PBCOR in AIPS and the coefficients that have been determined at the observatory[14].

RMs were retrieved using a typical least-squares fit to plots of the EVPA versus λ^2. As most features in polarisation are unresolved, polarised regions are suitably parameterised by a single RM. There is no evidence for deviations from a straight line in the fits.

In addition, the technique of RM Synthesis was applied (see Chapter 2). The RMSF had a FWHM of 321 rad m^{-2} due to the 16 MHz bandwidth. The RMSF is shown in Figure 7.1. An implementation of RM-clean was also applied and cleaning performed down to a 2σ limit.

[14] http://ncra.tifr.res.in/~ngk/primarybeam/beam.html

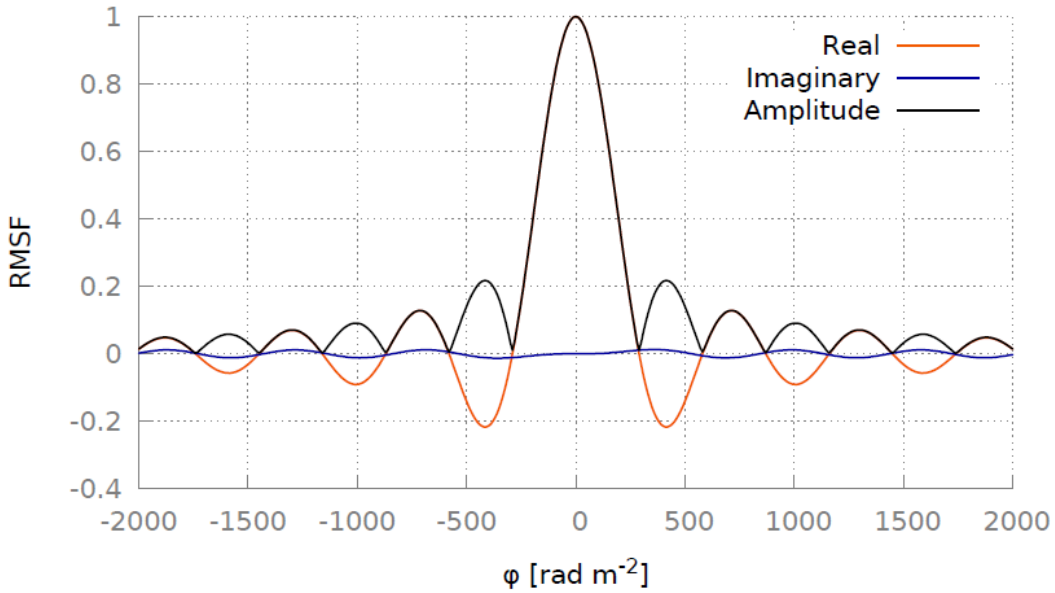

Figure 7.1: The rotation measure spread function (RMSF) for these GMRT observations. The real and imaginary components ($Q + iU$) and the amplitude ($P = \sqrt{Q^2 + U^2}$) are shown.

7.3 Compact Sources

Compact sources with peak intensity $\geq 6\sigma$ at both 610 MHz and 843 MHz were identified in Stokes I. Measurements of the peak flux were obtained by fitting a two-dimensional elliptical Gaussian to each source using the AIPS task JMFIT. The Gaussian fits did not solve for the zero level, however the listed uncertainties show that the data are predominantly limited by the minimal separation between the observing frequencies. Sources detected in the fields of USCG S063 and the Grus Quartet are listed in Table 7.1. The right ascension, declination, flux densities at 610 MHz/843 MHz, and the spectral index are given for each source. The stated 1σ uncertainties in the flux density measurements are the combined error from the Gaussian fit and flux calibration systematics. Calibration errors are taken to be 5% for GMRT and 3% for SUMSS data. The use of 610 MHz and 843 MHz data provides substantial uncertainty in the estimates of α. The estimated values are included for the sake of completeness, but the noted errors show that the measurements are generally unreliable except for the very brightest of sources.

Table 7.1: Measured parameters of compact sources in the fields of USCG S063 and the Grus Quartet.

RA (J2000)	Dec.	S_{610} /mJy	S_{843} /mJy	α
01h44m02.8s	−34d13′03.6″	536 ± 27	466 ± 15	0.4 ± 0.4
01h44m06.5s	−34d05′59.9″	40.5 ± 2.2	39 ± 5	0.2 ± 0.9
01h43m33.8s	−34d15′49.7″	111 ± 6	91 ± 6	0.6 ± 0.6
01h41m59.1s	−34d39′08.4″	860 ± 50	542 ± 17	1.4 ± 0.5
01h46m09.8s	−34d17′32.2″	111 ± 6	61 ± 5	1.8 ± 0.7
01h46m08.9s	−34d11′41.4″	35.4 ± 1.9	30 ± 5	0.5 ± 1.2
01h45m30.2s	−34d08′33.8″	24.7 ± 1.5	17 ± 5	1.1 ± 1.9
01h43m24.5s	−33d57′08.0″	111 ± 6	124 ± 6	−0.3 ± 0.5
01h43m02.1s	−34d36′44.1″	36.2 ± 2.0	27 ± 5	1.0 ± 1.3
01h43m25.3s	−34d44′44.7″	56.6 ± 2.9	35 ± 5	1.5 ± 1.0
01h43m10.6s	−34d29′59.6″	28.7 ± 1.6	30 ± 5	−0.1 ± 1.2
01h43m08.0s	−34d29′58.8″	27.6 ± 1.6	28 ± 5	0.0 ± 1.2
01h44m47.0s	−34d42′44.1″	26.3 ± 1.5	28 ± 5	−0.2 ± 1.2
23h16m54.4s	−42d15′11.5″	166 ± 9	152 ± 6	0.3 ± 0.5
23h17m53.8s	−42d21′23.9″	11.6 ± 2.0	13 ± 4	−0.4 ± 2.2
23h18m14.9s	−42d31′37.2″	87 ± 5	77 ± 4	0.4 ± 0.6
23h16m44.2s	−42d6′28.2″	34.8 ± 2.6	37 ± 4	−0.2 ± 0.9
23h17m29.9s	−42d2′59.6″	23.8 ± 2.3	32 ± 4	−0.9 ± 1.0
23h20m17.8s	−42d16′00.6″	60 ± 4	58 ± 4	0.1 ± 0.7
23h18m32.3s	−42d9′14.9″	21 ± 3	23 ± 4	−0.2 ± 1.3
23h15m52.3s	−42d9′26.5″	13.6 ± 2.0	14 ± 4	0.0 ± 2.0
23h17m16.4s	−42d29′19.9″	13.7 ± 2.0	13 ± 4	0.2 ± 2.1
23h17m43.7s	−42d17′19.4″	40.9 ± 2.8	43 ± 4	−0.1 ± 0.8
23h18m50.2s	−42d46′40.9″	17.0 ± 2.1	12 ± 4	1.1 ± 2.2
23h20m18.8s	−42d37′21.9″	45 ± 3	40 ± 4	0.4 ± 0.8

7.4 Group Galaxies

The group name, distance, number of galaxies, and galaxy names, alongside the respective label, red-shift, inclination, and Hubble type of the known galaxies are provided in Table 7.2. The inclinations of galaxies in the Grus quartet are taken from Dahlem (2005). Inclinations in USCG S063 are calculated using the relation

$$\cos(i - 3^\circ) = \sqrt{\frac{(b/a)^2 - p^2}{1 - p^2}}, \tag{7.1}$$

where the inclination, i, is calculated using the ratio of the minor to major axes, b/a, alongside a correction factor of $p = 0.2$ to correct for a galaxy's oblate spheroid geometry (Hubble 1926; van den Bergh 1988). The correction of 3° is added in accordance with documented 'empirical recipes' (Tully 1988).

The individual groups are discussed in further detail in Sections 7.4.1 and 7.4.2. Supplementary images of the various galaxies are shown in Appendix A.

Table 7.2: The physical parameters of the observed SCGs. The group name, the distance[15], the number of galaxies in the group, and the galaxy names, labels, redshifts[16], inclinations, and type[17] are all listed.

Group	D /Mpc	N_{Gal}	Galaxy Name	Label	z	i	Type
USCG S063	54.5	5	IC 1724	*A*	0.01268	77°	$S0^+$
			IC 1722	*B*	0.01377	68°	SAB(s)bc
			ESO 0353–G036	*C*	0.01274	75°	SB(rs)0, SFG
			IRAS F01415–3433	*D*	0.01253	90°	S0
			ESO 0353–G039	*E*	0.01305	79°	Sc, SFG
Grus Quartet	22.5	4	NGC 7552	*a*	0.00537	46°	SB(s)ab, HII Liner
			NGC 7582	*b*	0.00525	64°	SB(s)ab, Sy2
			NGC 7590	*c*	0.00526	68°	S(r?)bc
			NGC 7599	*d*	0.00551	72°	SB(s)c

[15]The co-moving distance, assuming a flat cosmology with $\Omega_M = 0.27$, $\Omega_\Lambda = 0.73$, and $H_0 = 71$ km s^{-1} Mpc^{-1}.

[16]From the NASA/IPAC Extragalactic Database (NED) (http://ned.ipac.caltech.edu).

[17]Dahlem (2005); Pompei et al. (2007). Note that NGC 7552 is listed as a HII Liner. However, other evidence suggests that it is in fact a starburst galaxy with a giant nuclear HII region (Forbes et al. 1994; Forbes & Norris 1998). Similarly, NGC 7582 has also been classified as Sy1 by other authors (Ricci et al. 2010).

7.4.1 USCG S063

The group USCG S063 contains 5 galaxies, all of which are either lenticular or spiral as shown in Figure 7.2.

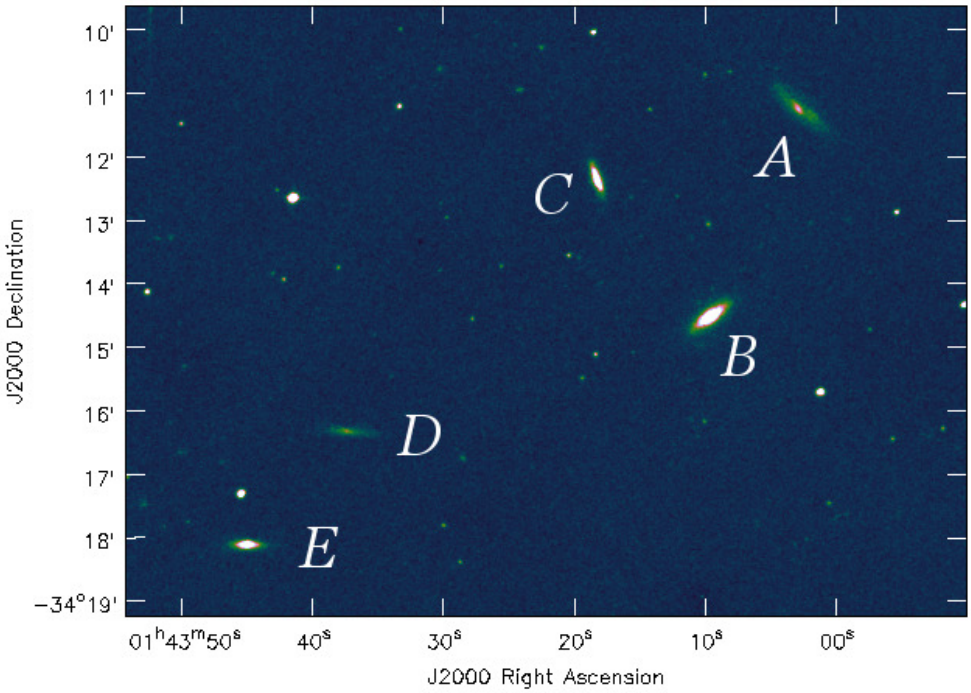

Figure 7.2: The near-IR DSS-2 image of the five group galaxies in USCG S063.

The 610 MHz data from observation 17_060_1 achieved a noise-level of σ = 270 μJy beam^{-1} near the phase-centre at full-resolution in Stokes *I*. The field was strongly affected by residual phase errors from an off-axis source located 8.5′ from the phase-centre with a peak brightness of 213 mJy beam^{-1} at full-resolution. Despite mild improvement following peeling, the source limits the obtainable dynamic range in the region surrounding the source. The Rician noise level in the band-averaged *P* image was ∼23 μJy beam^{-1} at a resolution of 24″ × 24″. The removal of antennas with leakages > 15%, some of which were located in the GMRT's outer arms, meant that the data had to be tapered in the *uv*-plane in order to avoid large holes in the *uv*-coverage (see Chapter 3). The cleaned ϕ-cubes had σ = 43 μJy beam^{-1} rmsf^{-1}. The Stokes *I* field of view is shown in Figure 7.3.

At 610 MHz, galaxies *A*, *B*, *D*, and *E* were all undetected in Stokes *I* to a 5σ upper limit of < 1.35 mJy. Galaxy *C* was detected and found to have a peak brightness of 15.4 mJy beam^{-1}. The peak of radio emission from galaxy *C* appears to be offset from the emission in the near-IR, with the offset directed towards galaxies *D* & *E*. This offset of 0.3″ corresponds to ∼80 pc at the location of the galaxy, and a similar offset was also found in the SUMSS data at 843 MHz. However, it should be noted that this is just a quarter of the pixel size of 1.2″ in the GMRT

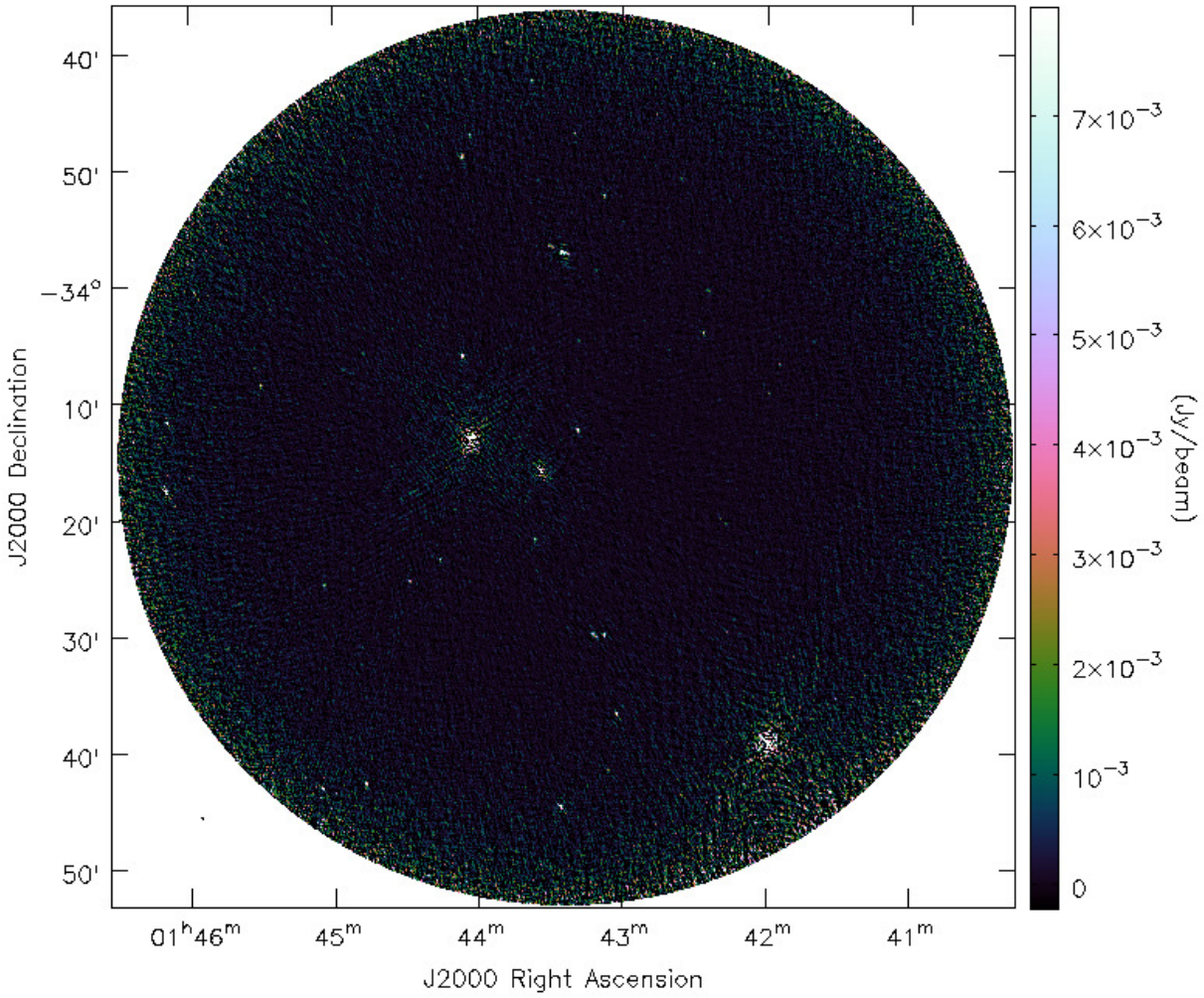

Figure 7.3: The Stokes *I* GMRT image of the field surrounding USCG S063 at full-resolution of 9.7″ × 5.6″ with a position angle of 37°. The pseudo-colour 'cube-helix' scale is in units of Jy beam^{-1} (Green 2011).

images. Nevertheless, the emission is also extended towards the E, and reaches beyond the extent of the disk that is visible at near-IR wavelengths. The spectral index of the galaxy could not be usefully constrained ($\alpha_{610}^{843} = 0.1 \pm 1.8$).

None of the group galaxies were detected in polarisation. No polarisation was detected from galaxy *C* to a 3σ upper limit of $< 0.4\%$.

7.4.2 The Grus Quartet

The Grus Quartet contains 4 galaxies, all of which are spirals as shown in Figure 7.4.

The 610 MHz data from observation 17_060_2 achieved $\sigma = 85$ μJy beam^{-1} near the phase-centre at full-resolution in Stokes *I*, and a Rician noise level in the band-averaged

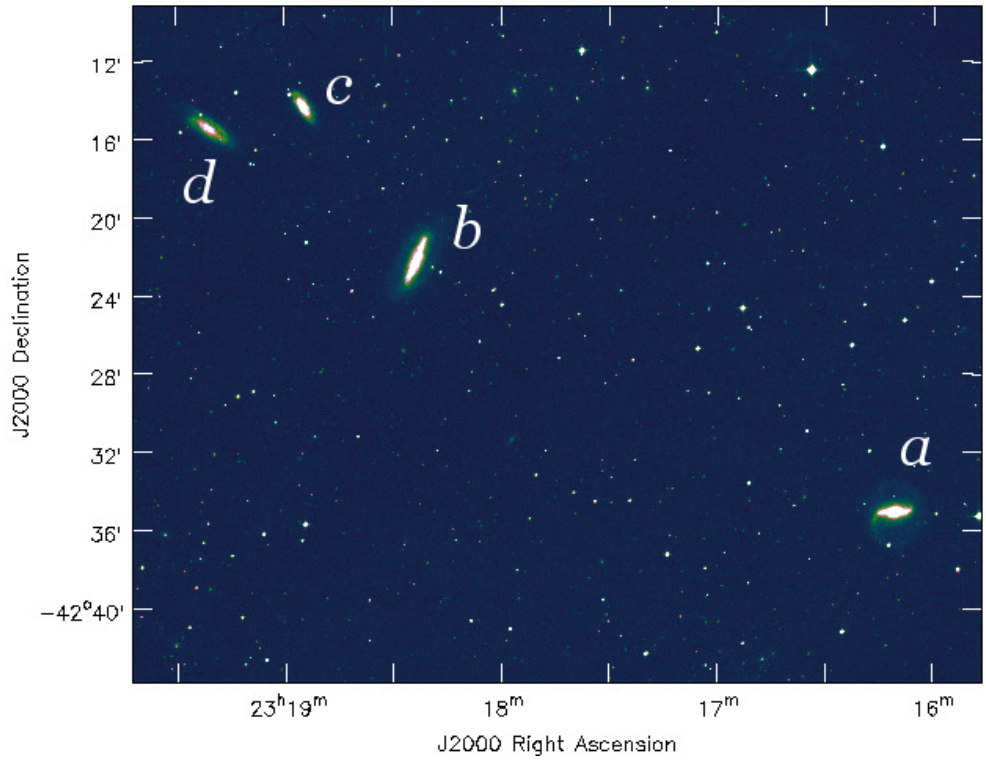

Figure 7.4: The near-IR DSS-2 image of the four group galaxies in the Grus Quartet.

P of ~36 μJy beam^{-1} at a resolution of 24″ × 24″. The cleaned ϕ-cubes had σ = 54 μJy beam^{-1} rmsf^{-1}. The Stokes I field of view is shown in Figure 7.5.

At 610 MHz, all four group galaxies were detected in Stokes I. Galaxy a, b, c, and d were found to have a peak brightness of 133 mJy beam^{-1}, 197 mJy beam^{-1}, 2.5 mJy beam^{-1}, and 3.0 mJy beam^{-1} respectively.

The brightest emission emanates from the nuclei of galaxies a and b. Extended emission is detected at 610 MHz along the bar of galaxy a. The bar of Galaxy b shows knots of emission with point-like sources at the outer northern edge of the galaxy. Emission is detected across most of the disk of galaxy c, while the peak brightness in galaxy d is located towards the W of the outer disk.

There was insufficient resolution to investigate spatial α-variations in these galaxies, and the spectral index systematics are large (see Section 7.3). Nevertheless, α_{610}^{843} of the brightest emission was found to be 0.3 ± 0.4 in galaxy a and 0.4 ± 0.3 in galaxy b. This bright emission comes from the cores in both of these galaxies. The spectrum is not usefully constrained in galaxies c and d, which were found to have α_{610}^{843} of 0 ± 6 and 0 ± 10 respectively.

Galaxies c and d were undetected in polarisation to 3σ upper limits of < 0.9% and < 1.4% respectively. Bright polarisation was detected from the nucleus of a and b (see Table 7.2). As direction-dependent instrumental polarisation has not been removed from this data, it is

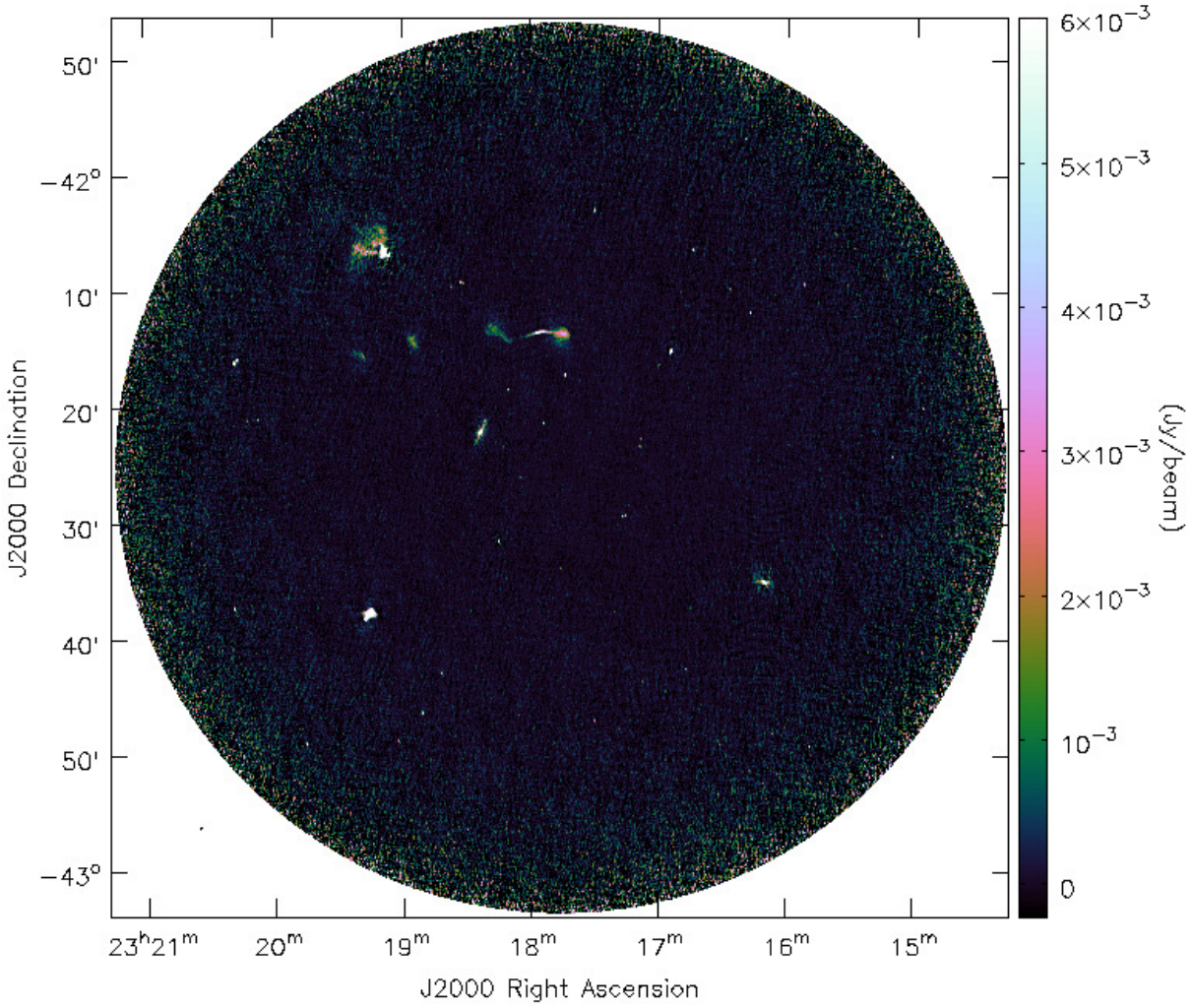

Figure 7.5: The Stokes *I* GMRT image of the field surrounding the Grus quartet at full-resolution of $9.5'' \times 4.6''$ with a position angle of 16°. The pseudo-colour scale is in units of Jy beam^{-1}.

important to compare the detected polarised emission to that expected from instrumental effects alone – especially for these two 'polarised' galaxies which are both displaced from the phase-centre. This comparison is complicated by a number of factors, especially since the amount of spurious polarisation is dependent on both the position of the source within the primary beam and the precise values of source and instrumental polarisation at this location. It is important to note that for observations with a long track in χ, the direction-dependent instrumental polarisation averages down substantially (see Chapter 6). This averaging is somewhat limited for observations of these galaxy groups due to the low declination. Nevertheless, USCG S063 was observed with parallactic angles ranging from −32° to +51°, while the Grus Quartet was observed with parallactic angles ranging from −29° to +31°.

The P peak brightness and Faraday depth were measured by fitting a Gaussian to the points surrounding the peak of the Faraday spectrum. Only pixels with a peak in ϕ-space greater than 8σ were analysed, where σ is the noise in the cleaned ϕ-cubes. The P measurements were corrected for the effects of Rician bias using equation 2.52. The corrected values were then used to calculate the fractional polarisation, $\Pi = P_0/I$. The fractional polarisations are $0.87 \pm 0.02\%$ and $0.70 \pm 0.01\%$ for a and b respectively. The Stokes I, near-IR data, and polarised intensity at 610 MHz for galaxy a (NGC 7552) are shown in Figure 7.6. Other images are available in Appendix A.

Galaxy a and b are located $20.1'$ and $7.6'$ from the phase-centre, yielding crude estimates for the direction-dependent instrumental polarisation of 2.0% (a) and 0.3% (b) (see Chapter 6). The estimated instrumental polarisation at the location of galaxy a is large enough to account for the polarisation detection as an instrumental effect. As instrumental effects tend to accumulate at Faraday depths (FDs) of 0 rad m^{-2} following RM Synthesis, the technique was applied in order to diagnose the nature of the emission. The peak in the Faraday dispersion function is at a FD of 7.71 ± 0.29 rad m^{-2} – a plot of the Faraday spectrum is shown in Figure 7.7. Surrounding pixels have varying FDs from $\sim$ 4–14 rad m^{-2}. The RM of the pixel of peak polarisation, as determined from a least-squares fit, was found to be 7.8 ± 0.5 rad m^{-2}. The polarisation to the W of the nucleus has a 'smudged' appearance and does not coincide with a distinct feature of the galaxy in Stokes I. It is likely that errors in the determination of the leakage phase arising from the use of a linear model have led to this spurious polarisation to the W of the nucleus (see Chapter 4).

Consideration of the direction-dependent instrumental response suggests that the detected polarisation in galaxy b is intrinsically on the order of 0.4%. Note that measurements suggest the residual instrumental polarisation at the phase-centre is reduced to $\leq 0.5\%$. Following RM Synthesis of the brightest polarised pixel, the peak in Faraday space occurs at a FD of -1.83 ± 0.22 rad m^{-2} – a plot of the Faraday spectrum is shown in Figure 7.8. FDs in the immediately surrounding bright pixels are all negative, varying between -9 rad m^{-2} to -1 rad m^{-2}. Approximately $6''$ away (a quarter of the beam size), the FD changes sign and increases in magnitude up to 31.8 ± 0.9 rad m^{-2}. The areas with positive FDs typically have $\Pi \approx 0.2\%$. The low Π and the apparent symmetry around a FD of 0 rad m^{-2} is indicative of the polarisation resulting from frequency-independent instrumental effects.

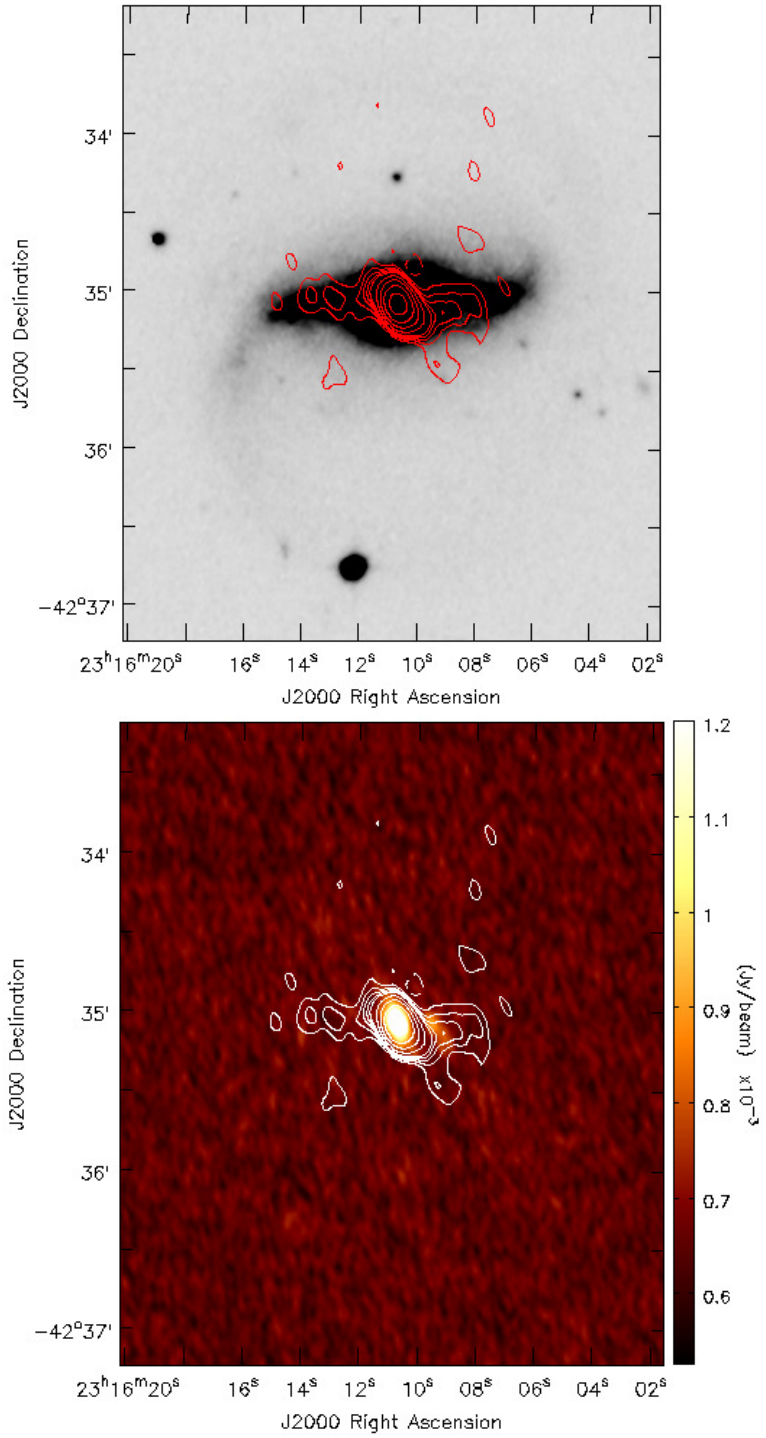

Figure 7.6: Top: Stokes *I* contours at 610 MHz overlaid on the near-IR DSS-2 image of NGC 7552, galaxy *a*, in the field of the Grus Quartet. The contours are at (−2, −1, 1, 2, 3, 4, 5, 10, 20, 40, 80) × the off-source 4σ level, where σ is 295 μJy beam^{-1}. The 610 MHz image is at full resolution of 9.5″ × 4.6″ with a PA of 16°. Bottom: Stokes *I* contours at 610 MHz overlaid on the image of the band-averaged *P* of NGC 7552. The pseudo-colour scale is in units of mJy beam^{-1}. The *P* image has a resolution of 24″ × 24″, and has not been corrected for the effects of the primary beam or for Rician bias.

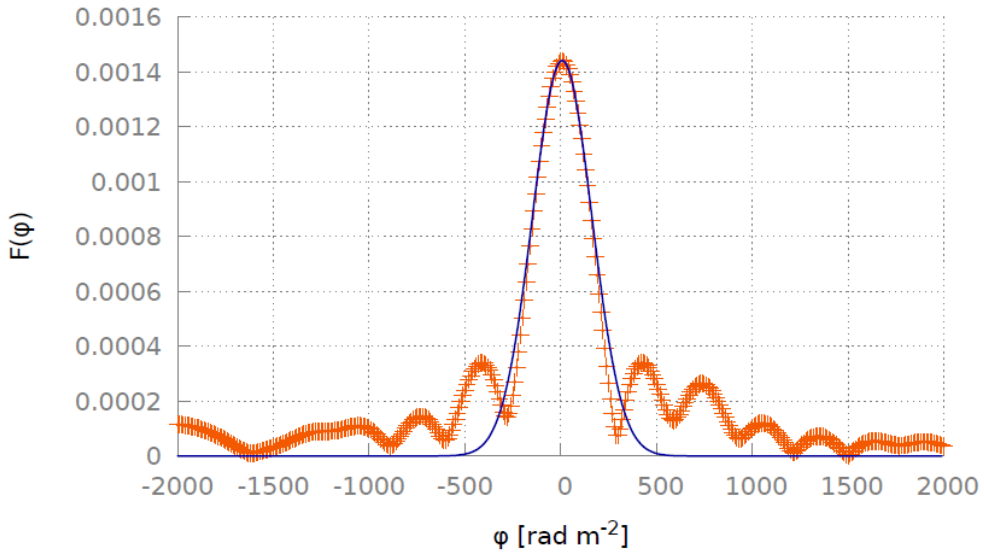

Figure 7.7: A plot of the Faraday dispersion function as a function of Faraday depth for the brightest polarised pixel in galaxy *a* (NGC 7552). The datum extracted at each trial Faraday depth is shown in orange. A Gaussian fit to the peak of the spectrum is shown in blue.

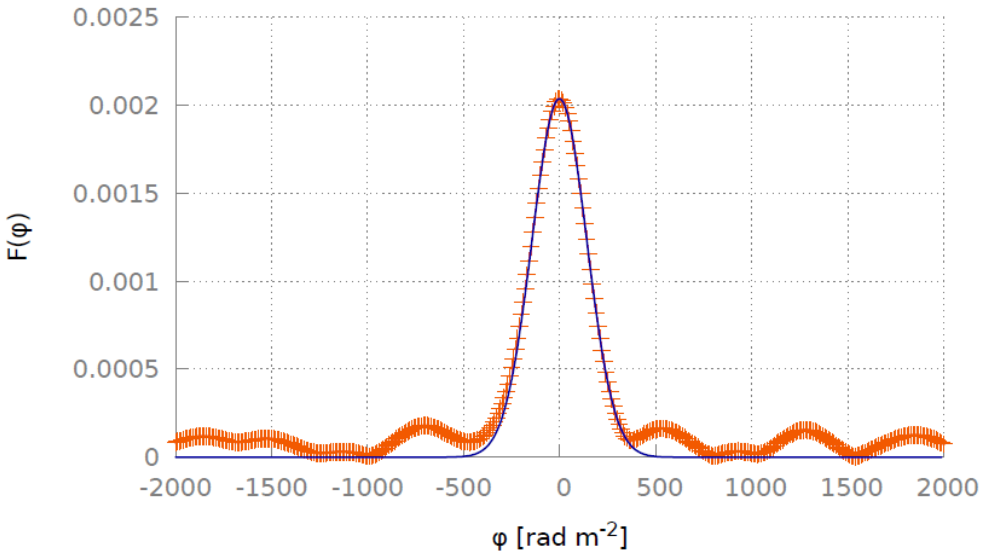

Figure 7.8: A plot of the Faraday dispersion function as a function of Faraday depth for the brightest polarised pixel in galaxy *b*. The datum extracted at each trial Faraday depth is shown in orange. A Gaussian fit to the peak of the spectrum is shown in blue.

7.5 Other Extended Sources

Three spatially extended sources were detected in the field of the Grus quartet that are unrelated to the group galaxies themselves. These three sources J2317.9–4213, MCG–07–47–031, and PKS 2316–429 have all been detected previously but are largely unstudied (Perlman et al. 1998; Ewald & Hjellming 1980; Massaro et al. 2009; Large et al. 1981). In this section, these individual sources are described in further detail. Supplementary images of these extended sources are shown in Appendix A.

7.5.1 J2317.9–4213

The complex radio galaxy J2317.9–4213 is located ∼1′ to the W of galaxy *c* at 23h 17m 55.7s, −42° 13′ 29″. It has previously been detected as an X-ray source, indicating the presence of an AGN (Ewald & Hjellming 1980).

In the near-IR DSS images is an apparent companion source coincident with the brightest 610 MHz Stokes *I* emission. This companion has $z = 0.056$ and is therefore in the background of the galaxy group, with the emission from the jets extending across 43 kpc. The general morphology, in combination with the presence of low brightness regions towards the galaxy periphery is indicative of the FR-I class. The 610 MHz polarisation is brighter in the western jet and the contrasting lack of polarised emission to the E is likely a consequence of the Laing–Garrington effect (e.g. Garrington et al. 1988). This suggests the eastern jet is located more distantly along the line-of-sight and therefore subject to stronger Faraday depolarisation.

No polarisation was detected from the AGN, to a 3σ upper limit of $< 0.2\%$. However, there are two polarised hotspots located on both the E and W side of the nucleus, as shown in Figure 7.9. The hotspots to the E have fractional polarisations of $5.2 \pm 0.4\%$ and $4.0 \pm 0.3\%$, and the hotspots to the W are polarised to $3.2 \pm 0.3\%$ and $2.2 \pm 0.2\%$. The lesser of each of these values is associated with the hotspot that is in closer proximity to the AGN. These values also show that the polarisation is ∼2% higher on the E side of the nucleus.

Moving from the hotspot furthest to the E, through to the W, the RMs extracted from the datacubes are 15.9 ± 1.3 rad m^{-2}, 12.7 ± 0.5 rad m^{-2}, 22.1 ± 0.6 rad m^{-2}, and 27.4 ± 1.1 rad m^{-2}. The RMs are clearly higher on the W side.

The RM of the four brightest regions of extended polarisation in the W jet are moving from E to W: -11.7 ± 2.4 rad m^{-2}, -2.0 ± 1.1 rad m^{-2}, -10.9 ± 1.1 rad m^{-2}, and 4.7 ± 1.4 rad m^{-2}. There appears to be a large scale change of sign relative to the RMs near to the nucleus.

7.5.2 MCG–07–47–031

The blazar or BL Lac, MCG–07–47–031, is located ∼10′ to the N of galaxy *D* at 23h 19m 5.8s, −42° 06′ 49″. The bright AGN appears to have a near-IR companion in the DSS images, which is located at $z = 0.055$, or 228 Mpc away.

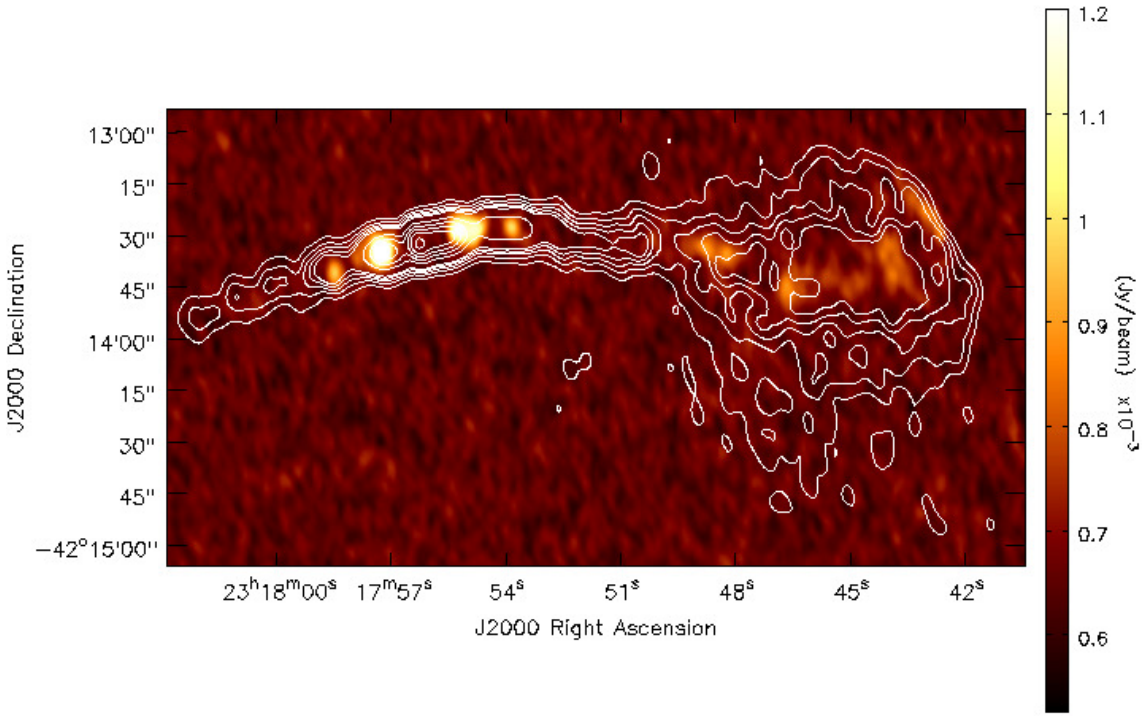

Figure 7.9: Stokes I contours at 610 MHz overlaid on the image of the band-averaged P of J2317.9–4213 in the field of the Grus Quartet. The pseudo-colour scale is in units of mJy beam^{-1}. The contours are at (−2, −1, 1, 2, 3, 4, 5, 10, 14, 18, 22, 28) × the off-source 3σ level, where σ is 185 μJy beam^{-1}. The Stokes I contours are at full resolution as in Figure A.3. The P image has a resolution of $24'' \times 24''$, and has not been corrected for the effects of the primary beam or for Rician bias.

Near the core in Stokes I, there are at least 3 other point-like regions of emission that appear associated with the blazar – although foreground/background sources can not be ruled out. At the faintest levels in the images, there is a 3σ detection of two jet-like features leading from the AGN – one directly N, and another to the E. There is also some indication of a bridge of emission connecting the two jets.

The nucleus was found to have $\alpha_{610}^{843} = 0.29 \pm 0.25$, and is detected in linear polarisation with a fraction of 7.03 ± 0.11%. A point-like source to the E of the nucleus is also polarised to 1.88 ± 0.05%, although instrumental effects are anticipated to be on the order of at most ∼2.5% at 23.7′ from the phase-centre. The nucleus itself has a RM of 6.5 ± 0.1 rad m^{-2}. No polarisation was detected from the jets to a 3σ upper limit of < 0.7%.

7.5.3 PKS 2316–429

This previously unclassified radio source is located ∼25′ S of galaxy d at 23h 19m 15.9s, −42° 37′ 53″. The radio morphology has a central point-like core, with two bright hotspots to

the NW and SE periphery.

It is believed that two near-IR sources enclosed within the Stokes I emission are in the background and unrelated to the radio source, as their location bears no relevance to the radio structure. The source is also detected in the SUMSS, and comparison with the 610 MHz data shows the source to have a non-thermal spectrum with $\alpha_{610}^{843} = 0.57 \pm 0.13$.

The two hotspots themselves exhibit offset peaks in polarisation of $3.86 \pm 0.07\%$ and $6.7 \pm 0.3\%$ to the NW and SE respectively. Direction-dependent effects are estimated to be at most $\sim 2.0\%$. The RM is similar for both polarisation peaks, being 15.39 ± 0.15 rad m^{-2} and 16.56 ± 0.19 rad m^{-2} to the NW and SE. No polarisation was detected from the core to a 3σ upper limit of $< 0.6\%$.

The non-thermal spectrum, polarisation properties, and radio morphology – particularly the bright outer hotspots – is typical of a barely resolved FR-II radio galaxy.

7.6 Discussion

A study of two SCGs at 610 MHz has found Stokes I emission from 5 galaxies in a sample of 9.

Furthermore, the three galaxies ESO 0353–G036, NGC 7590, and NGC 7599 were found to be depolarised to $< 0.4\%$, $< 0.9\%$, and $< 1.4\%$ respectively. Further still, extended sources that are unrelated to the groups themselves have allowed for the classification of a FR-I and FR-II radio source, with the detection of polarisation allowing for diagnostics of the source properties.

Of the five galaxies detected in Stokes I, two show bright radio peaks from their core and extended emission across the bar, with knots of emission being detected that are likely from supernovae or HII regions. A further two galaxies show emission across the disk. For example, NGC 7599 shows knots of radio emission that are displaced from the nucleus of the near-IR disk – likely indicating regions of enhanced star formation.

Attempting to interpolate a selected sample of nine galaxies across a population is obviously unreliable. Nevertheless, there are some reasons to suggest that the sample presented here is not completely unrepresentative. Previous analyses of the SCG catalogue have found the fraction of late-type galaxies as 59% (Prandoni et al. 1994), compared to 66% in this sample. Similarly, AGN activity has been reported in 25% of the SCG catalogue (Coziol et al. 2004; Pompei et al. 2007) and is present in 11% of the galaxies presented here.

The star formation rates (SFRs) in these galaxies can be estimated by first applying k-corrections to determine the rest-frame luminosity via

$$L_{610} = 4\pi d_{\mathrm{L}}^2 S_{610}(1+z)^{\alpha-1}\,, \tag{7.2}$$

where d_{L} is the luminosity distance. The corrected luminosities were used to calculate the SFR in the observed galaxies that were not AGN-like or undergoing a starburst, assuming $\alpha = 0.8$ and using the 610 MHz data (Condon 1992; Garn 2009). This suggests that galaxies NGC 7590 and NGC 7599 in the Grus quartet have a SFR of 0.093 ± 0.003 $\mathrm{M}_\odot$ yr^{-1} and 0.115 ± 0.003 $\mathrm{M}_\odot$ yr^{-1} respectively. Similarly, the detection of galaxy ESO 0353–G036 in USCG S063 suggests a SFR of 1.54 ± 0.03 $\mathrm{M}_\odot$ yr^{-1}. As a consequence of their non-detection, the other galaxies in USCG S063 must be producing stars at a rate of < 0.26 $\mathrm{M}_\odot$ yr^{-1}. Nevertheless, the large uncertainty in measurements of the spectral index, α_{610}^{843}, for these galaxies means that a flat or steep spectrum can not be easily distinguished. The radio continuum could feasibly be produced by thermal free–free emission. Free–free emission in normal galaxies typically emerges directly from HII regions that contain ionising stars (Condon 1992). This may complicate the calculation of the SFRs, due to difficulties in separating a thermal component from steep-spectrum synchrotron emission. Nevertheless, these values serve as useful upper bounds to the SFR.

One galaxy (ESO 0353–G036 in the field of USCG S063) was found to have a displaced peak of radio emission that is extended beyond the disk towards the E in comparison to the near-IR disk. This is interestingly in the direction of the galaxies IRAS F01415–3433 and

ESO 0353–G039, and could also be considered to be a displacement towards the gravitational centre of the group. This can be tentatively considered as evidence for hydrodynamic interactions within the group. Indeed, Pompei et al. (2007) show that HI is being stripped from the disk due to interactions with the group members. This process is dominated by the galaxies IC 1722 and IC 1724 – resulting in enhanced HI to the W of the disk. The detection of the extended gas disk with respect to the near-IR disk in ESO 0353–G036 at 610 MHz is possibly from recent star formation taking place to the E of the galactic disk. While HI traces gas being pulled out of galaxies that are taking part in gravitational interactions, the radio continuum traces star formation that is triggered by radial flows in the disturbed gravitational potential of the group members. As the emission appears displaced towards the group centre, it is a distinct possibility that this radio disturbance is a consequence of hydrodynamic interactions within the group. In a simple case, tidal interactions would lead to bridges and tails, ram pressure stripping would lead to a smooth swept-up morphology and displaced gas disks, while turbulent viscous stripping would lead to effects on the entire gas disk (Cayatte et al. 1994). While ram pressure stripping could result in the extended emission beyond the near-IR disk, the inclination of the galaxy and the complex interactions between the different physical processes which govern the gas dynamics will likely mean the situation is considerably more complicated. An increased sample of Southern Compact Groups is needed in order to truly begin understanding the signatures of various processes that influence the radio emission. Similar processes to those taking place in ESO 0353–G036 may also be occuring in NGC 7599, in which the brightest region of radio continuum emission is located towards the NW periphery of the disk – in the direction of the adjacent group member NGC 7590.

At 610 MHz, linear polarisation was detected from the core of one starburst galaxy, NGC 7552. The polarisation fraction was determined via RM Synthesis to be $0.87 \pm 0.02\%$. The RM of the brightest emission was found to be 7.8 ± 0.5 rad m^{-2}, and has not been measured before. The RM is in good agreement with the calculated peak Faraday depth of 7.71 ± 0.29 rad m^{-2}, making it likely that the Faraday rotation is taking place in the 'Faraday screen' provided by the Milky Way, i.e. a non-emitting plasma containing ions and magnetic fields that lies somewhere between us and the galaxy along the line of sight. The Seyfert galaxy, NGC 7582 (Ricci et al. 2010), was found to have a polarisation peak in the core, but this detection can be entirely explained as a consequence of instrumental effects. The results of RM Synthesis appear to further justify this conclusion.

The origin and evolution of cosmic magnetism is one of the major challenges to be addressed by the next generation of radio telescopes, particularly the Square Kilometer Array (SKA) (see Chapter 1). The most important technique that will be used is the direct observation of polarised emission, particularly from galaxies, which will be used to measure the RM from background sources (e.g. Gaensler et al. 2004). At the flux levels that will be accessible to the SKA, the polarised source counts will be dominated by star forming galaxies. The background sources, which will form an essential 'RM grid' will therefore be dominated by late-type galaxies.

The observed polarisation fraction, Π, of late-types observed with the SKA will be strongly dependent on inclination and Faraday depolarisation effects.

Current models predict a broad maximum in Π for inclinations between 50° and 80° at 4.8 GHz (Stil 2007). Conveniently, the probability density function for a set of randomly inclined spirals has a maximum near to the highest possible value of Π, as 47% of randomly oriented galaxies will have an inclination between 50° and 80°. The data presented here are not reassuring, as the three galaxies ESO 0353–G036, NGC 7590, and NGC 7599 were found to be unpolarised to $< 0.4\%$, $< 0.9\%$, and $< 1.4\%$ respectively. This is particularly unfortunate as 78% of the nine galaxies are oriented at angles between 50° and 80°. Polarisation was detected in only one galaxy inclined at $i = 46°$, NGC 7552, and this was from its nucleus. The lack of a polarisation detection in these galaxies, combined with the lack of available complementary data for these Southern galaxies, inhibits the opportunity to study the depolarisation mechanism in these galaxies. Beam depolarisation effects and Faraday depolarisation mechanisms can not be easily investigated.

The SCG sample is well known to show differences in contrast to field galaxies, so whether the SCG sample can be used to reliably interpret the impact on polarised source populations is uncertain. Interpolating the sample of nine galaxies across the population is certainly unreliable. Nevertheless, more must be done to understand the dominant Faraday depolarising mechanisms at low frequencies, and to predict how polarised galaxies should be at lower frequencies. At present, all reliable models are at frequencies of ≥ 4.8 GHz. Understanding the effects of depolarisation as a function of frequency is crucial if projects such as those to be undertaken by the SKA are to succeed. Upcoming polarimetric surveys such as those to be carried out by the SKA pathfinders will help to finally constrain these problems (see Chapter 1 and Stil (2007); Stepanov et al. (2008) for further details).

CHAPTER 8

THE YOUNG SUPERNOVA REMNANT: G1.9+0.3

"The world's still spinning round, we don't know why? Why? Why? Why? Why?"

Champagne Supernova, Oasis

The youngest known Galactic supernova remnant, G1.9+0.3, provides a unique opportunity to study the evolution of remnants in an early epoch. In this chapter, I use the GMRT at 610 MHz and complementary VLA data at 1.44 GHz to identify large-scale spectral variations across the remnant. I find a systematically flatter spectrum in the NW and SE of the remnant. Consideration of theoretical models of cosmic ray acceleration at oblique shocks suggests that the variation of α across G1.9+0.3 is most consistent with an ambient magnetic field running perpendicularly to the axis of bilateral symmetry. However, neither a parallel or perpendicular scenario can be ruled out.

For the first time, the presence of polarised emission in G1.9+0.3 at the $\sim$ 10% level is detected using the VLA at 4.86 GHz, with increased ordering of the magnetic field towards the NW of the remnant. The presence of linear polarisation is further investigated using GMRT spectropolarimetry at 610 MHz, and the VLA at 1.44 GHz. These polarimetric observations show that the remnant undergoes rapid depolarisation as a function of increasing wavelength. Strong Faraday depolarisation effects must be present.

It has not been possible to correct for the effects of Faraday rotation along the line of sight. Nevertheless, the B field vectors retrieved at 4.86 GHz are not oriented radially with respect to the centre of the remnant. This most likely implies a systematic gradient in RM across the source. It is suggested that a gradient of $\sim$ 140 rad m^{-2} from N to S across the remnant is

enough to explain the depolarisation and to provide a radially-oriented field, with just a small contribution from internal Faraday effects being required. Such a RM gradient may be the consequence of anisotropic regular magnetic fields either within the remnant or in an intervening Faraday screen. However, the present lack of strong constraints on the RM, in combination with the remnants current evolutionary stage, leaves open the possibility that Rayleigh–Taylor instability formation has not yet fully taken place.

8.1 Background

The youngest known Galactic supernova remnant (SNR) G1.9+0.3 is a 'missing link' in our knowledge of supernovae (SNe) evolution. At only 100–150 years old, as confirmed by both its expansion and Fe Doppler width, it is less than half the age of the otherwise youngest known SNR Cas A at $\sim$ 300 years old (e.g. Green 2004).

As the only known example of a very young SNR, G1.9+0.3 also hosts a number of unique properties: being the smallest known Galactic SNR with a diameter of $\approx$ 92 arcsec (3.8 pc), having the fastest shock velocity ever reported in a SNR (14,000 km s^{-1}), being one of just four identified X-ray synchrotron dominated Galactic SNRs (including SN 1006, G347.3–0.5, and G266.2–1.2), and being the only known Galactic SNR to be *increasing* in radio brightness (Green et al. 2008; Reynolds et al. 2008).

Studies of G1.9+0.3 have focussed on radio and X-ray emission, as the SNR has not been detected at infrared or optical wavelengths due to extinction towards the Galactic centre (GC), and a high column density of $N_H \sim 6\times10^{22}$ cm^{-2} (Reynolds et al. 2009). Similarly, the remnant has not been detected in γ-rays (Ksenofontov et al. 2010). The high absorption column density, as inferred from the X-ray spectrum, places the shell type remnant at a distance of about 8.5 kpc, close to the GC.

Independent radio and X-ray observations show that the remnant expanded by $\approx$ 16 percent between 1985 and 2008, giving a large expansion rate of $\sim$ 0.65 percent yr^{-1} (Green et al. 2008). Analysis of archival radio observations indicate that G1.9+0.3 is increasing in brightness by a rate of $\sim$ 1.2 percent yr^{-1} (Murphy et al. 2008), suggesting the remnant is currently undergoing a period of magnetic field amplification or particle acceleration. This is not unexpected as young SNRs should brighten on time-scales of roughly a century when they have swept up sufficient interstellar medium (Carlton et al. 2011).

The X-ray structure shows the synchrotron emission to have strong bilateral symmetry, appearing morphologically similar to SN 1006. Faint thermal X-ray emission has also been detected in some regions. Strong Kα lines in the spectra indicate the presence of Si, S, Ar, Ca, and Fe. It is anticipated that O, Ne, and Mg may also be present at low energies but cannot be seen due to the high absorption. Remarkably, emission at 4.1 keV has been attributed to ^{44}Sc, produced by electron capture in radioactive ^{44}Ti. If confirmed, this could potentially allow a unique insight into nucleosynthesis in SNe (Borkowski et al. 2010).

The identification of these spectral lines, particularly the ^{44}Sc line, is consistent with the progenitor undergoing a Type Ia event. While a core-collapse origin cannot currently be ruled out, the bilaterally symmetric X-ray morphology, high shock velocities, and prominent Fe K emission all slightly favour a Type Ia scenario (Reynolds et al. 2009). Radio searches have not located a central source, again consistent with a Type Ia origin, although it is feasible that current observations may be insensitive to faint emission in the centre of the remnant.

Searches for spectral variations in X-ray emission show the hardest spectra to be in the bright SE and NW limbs of the shell, with steepening around the shell or into the interior. The projecting fainter 'ears' to the E and W have the flattest spectra of all and are not detected at radio wavelengths (Reynolds et al. 2009).

VLA observations between 1.45 GHz and 4.86 GHz show a strong brightness asymmetry in the shell, with the remnant being brighter to the N. This perhaps indicates an external density gradient (Green et al. 2008). If there is a significant density gradient, this may be expected to show up as changes in the spectral index across the remnant, as areas of increased density will exhibit higher Mach numbers and consequently lower spectral indices. Variations in the magnetic field will also show up as differences in polarisation, allowing both the *B* field and local density gradient to be explored.

In Section 8.2, the parameters of the observations and calibration process are detailed. Section 8.3 provides information on matching observations for spectral comparison and displays the final images of G1.9+0.3 used throughout the analysis. In Section 8.4 the integrated spectral index of the source is derived and final corrections for systematic offsets between the data are made. Section 8.5 details the identified spectral variations, while Section 8.6 contains analysis of the polarisation results. An in-depth discussion of the results is provided in Section 8.7.

8.2 Observational Details

The IF frequencies and derived flux for the phase calibrator are listed in Table 8.1.

Table 8.1: Frequency settings and bootstrapped flux density.

Instrument	Config.	IF	Frequency	J1751–253 derived flux[18] /Jy
GMRT	—	—	0.6120 GHz	0.739 ± 0.011
VLA	B	IF1	1.5159 GHz	1.057 ± 0.014
VLA	B	IF2	1.3651 GHz	1.158 ± 0.006
VLA	C	IF1	1.5159 GHz	1.072 ± 0.009
VLA	C	IF2	1.3651 GHz	1.133 ± 0.003
VLA	C	IF1	4.8851 GHz	0.56 ± 0.03
VLA	C	IF2	4.8351 GHz	0.57 ± 0.03

G1.9+0.3 is in close proximity to the GC, posing a problem for absolute flux calibration at low frequencies. The abundance of non-thermal emission emanating from near the GC results in a raised sky temperature, which in turn increases the system temperature of the antenna receivers. As the sky temperature is considerably lower for observations of the flux calibrators (which are typically far from the GC), the complex gains determined from the flux calibration do not apply when observing the target source. This results in significantly reduced flux measurements when the target source is near to the Galactic plane. This effect has a substantial effect on the GMRT data at 610 MHz, as unlike the VLA, the GMRT does not have an automatic gain control system that scales the signal with the system temperature. This can be corrected by multiplying the data by a correction equal to $T_{\rm tar}^{\rm sys}/T_{\rm cal}^{\rm sys}$, where $T_{\rm x}^{\rm sys}$ is the system temperature of the target/flux calibrator field (Bhatnagar 2001). The flux of the GMRT data was therefore corrected using the AIPS task VBCAL. It was assumed that the system temperature was a typical 102 K during observation of the flux calibrator. The system temperature during observation of G1.9+0.3 was estimated using the 408 MHz all-sky survey to be 600 ± 50 K, this value was scaled by a brightness temperature spectral index of 2.7 yielding a correction factor of 1.99 ± 0.17 (Haslam et al. 1982).

All of the observations were iteratively self-calibrated using three rounds of phase-only calibration, with the noise decreasing in each successive iteration, followed by a final iteration for both amplitude and phase. Following self-calibration, the 1.44 GHz B and C array data were combined into a single dataset using the AIPS task DBCON, before producing the final image. The GMRT data were processed using multi-facet imaging, breaking the sky up into 31 facets across the field of view in order to correct for non-coplanar effects across the large primary beam at 610 MHz (FWHM= 44.4′).

8.3 Matching Observations

The intent is to use the 610 MHz and 1.44 GHz data to search for spectral variations across the remnant. It is therefore crucial to correct for any systematic differences between observations, particularly as the data are obtained with different instruments.

The VLA and GMRT observations had different pointing centres, and this was corrected for during imaging of the VLA data in IMAGR. Checks on the positional offset of three nearby discrete sources show that the resulting images are aligned to within $\sim 0.5''$.

The 610 MHz and 1.44 GHz images were both restored to a common beam of $10.62'' \times 4.92''$ with a position angle of $-1.12°$, chosen in order to obtain the highest available resolution. Both images were corrected for the effects of primary beam attenuation.

The spectral index, α, defined such that $S \propto \nu^{-\alpha}$, is sensitive to missing short spacings and both images were therefore imaged using similar coverage of small baselines so that both images

[18] The noted formal errors are those output by AIPS task GETJY. The actual errors are dominated by flux calibration systematics, which are taken to be a nominal 5%.

contain similar amounts of missing flux. As the data are obtained with different telescopes, it is difficult to obtain exactly the same coverage – however, the technique I shall use to measure the spectral indices is designed to alleviate problems arising from differing *uv*-coverage. The *uv*-coverage at small baseline lengths is shown for both observations in Figure 8.1. The VLA data are more sparsely sampled at smaller baseline lengths than the GMRT data. Consequently, the absolute values of the spectral indices will tend to be overestimated (assuming accuracy of the correction due to the increased sky temperature). Nevertheless, this will not affect the identification of spatial spectral variations. The largest angular scale the images are sensitive to is $\sim 5'$.

As a further complication, these data are obtained at different epochs. Between 2009 May (the central time between the B and C configuration VLA observations) and 2010 January, the remnant is expected to have expanded by 0.44% based on an expansion of $\sim$ 0.65% per year (Carlton et al. 2011). The expansion of 0.44% was therefore adopted for the final analysis.

8.3.1 Contour maps

The final images of G1.9+0.3 are shown in Figures 8.2 and 8.3. Figure 8.2 shows the full resolution image of G1.9+0.3 at 610 MHz. Figure 8.3 shows the dual-frequency images used throughout the analysis, restored to a common synthesised beam. The 610 MHz images have an rms of 95 μJy beam^{-1}, while the 1.44 GHz image has an rms of 66 μJy beam^{-1}.

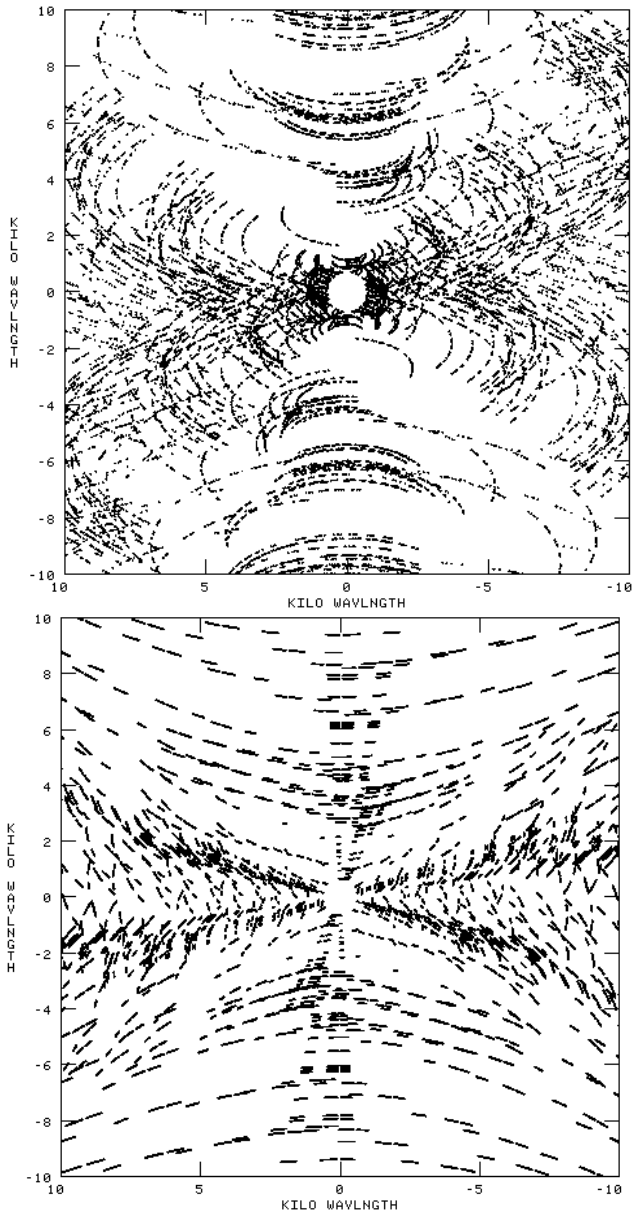

Figure 8.1: The *uv*-coverage of sampled small baseline lengths (less than 10 kλ) used during imaging. Displayed for both the GMRT (top) and VLA (bottom) observations at 610 MHz and 1.44 GHz respectively.

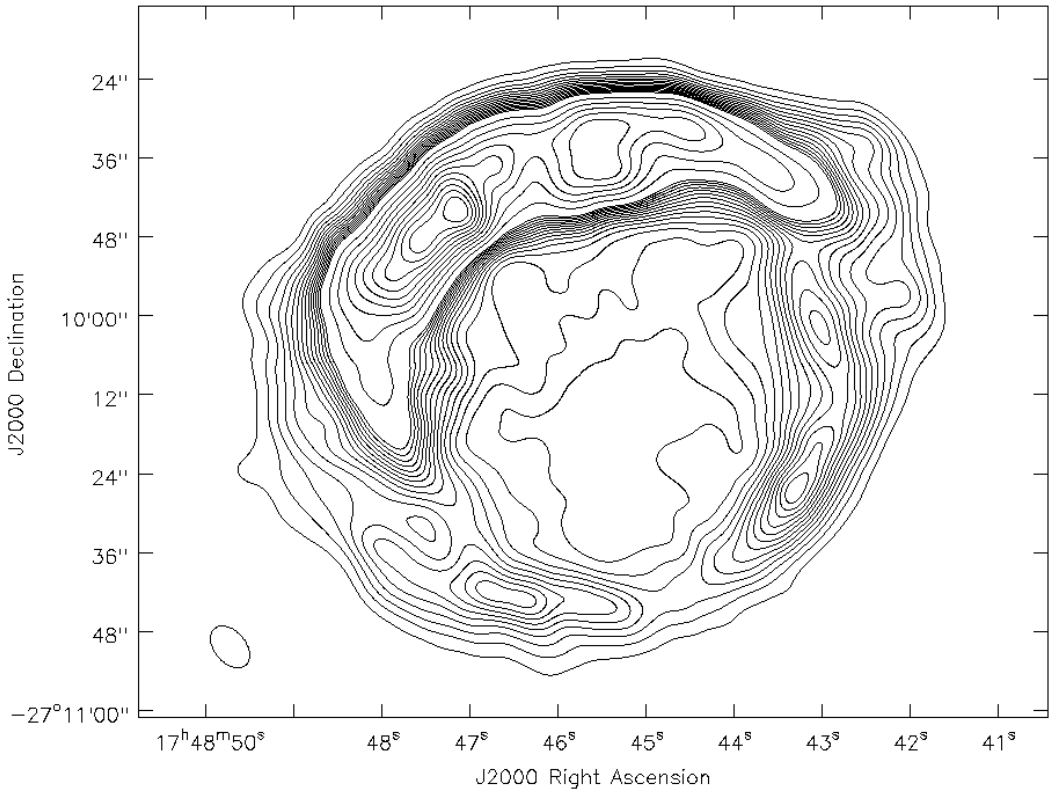

Figure 8.2: Observation of G1.9+0.3 at 610 MHz with contour levels at (−1, 1, 2, 3. . . 15, 20, 25. . . 65) × 0.475 mJy beam^{-1}. The image is at full resolution of 7.29″ × 4.74″ with a PA of 40.5°.

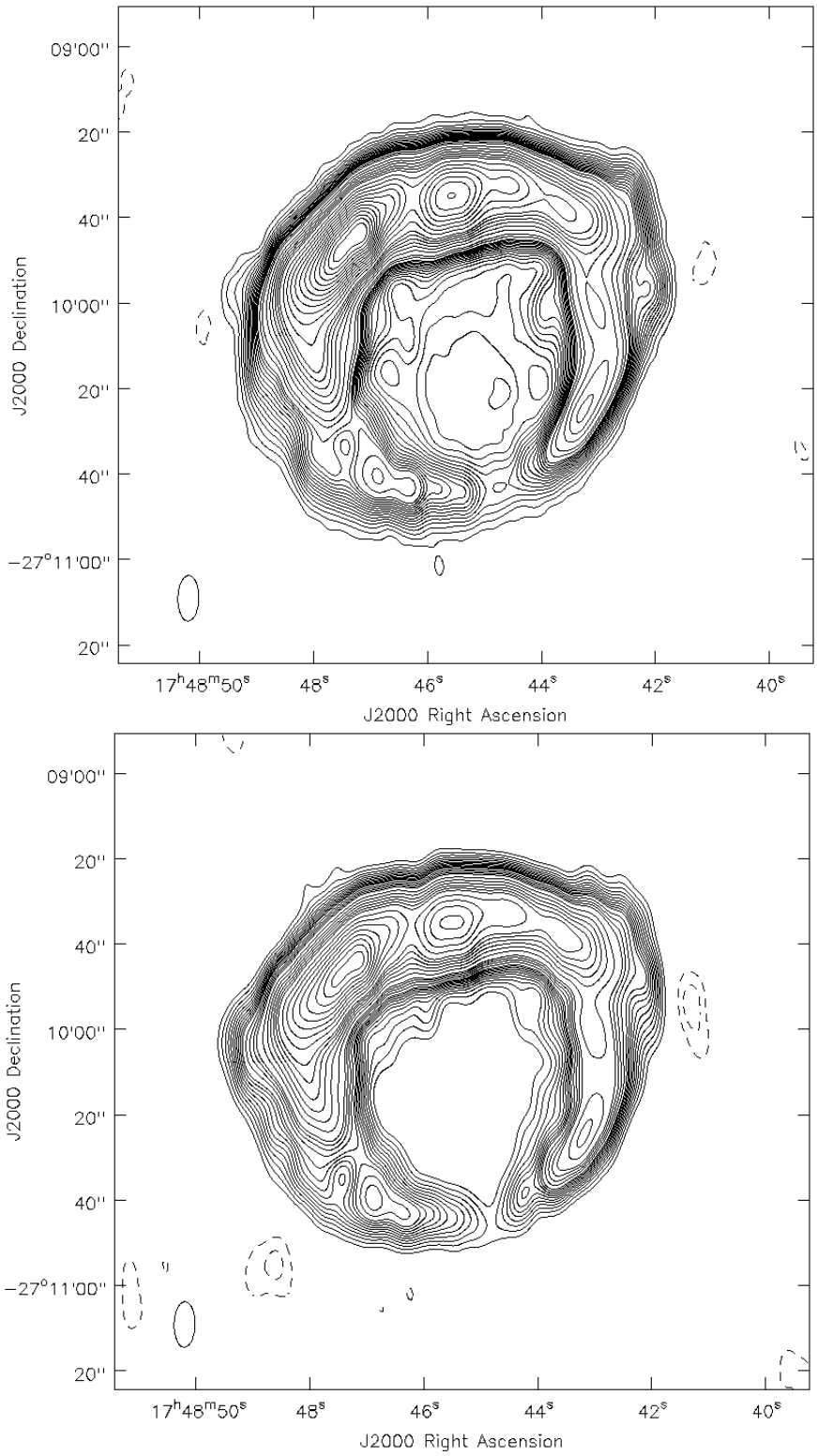

Figure 8.3: Observations of G1.9+0.3: at 610 MHz (top panel) with contour levels at $(-2, -1, 1, 2, 3, 4 \ldots 15, 17.5, 20, 25, 30 \ldots 50, 60 \ldots 170) \times 0.475$ mJy beam^{-1}, and at 1.44 GHz (bottom panel) with contour levels at $(-2, -1, 1, 2, 3, 4 \ldots 12, 14 \ldots 20, 25 \ldots 50, 60 \ldots 130) \times 0.330$ mJy beam^{-1}. Both images have a resolution of $10.62'' \times 4.92''$ with a position angle of $-1.12°$ from N. Negative contours are dashed.

8.4 Integrated Spectral Index and Errors

In order to quantify the quality of the flux correction applied due to the proximity to the Galactic centre (see Section 8.2), the integrated flux densities and the derived spectral index are a useful check.

Firstly, by integrating the flux within an irregular polygon placed around the emission and taking 5 measurements at each frequency yields an integrated flux density of 1.4171 ± 0.0012 Jy at 610 MHz, 0.852 ± 0.003 Jy at 1.44 GHz, and an integrated spectral index of 0.593 ± 0.005. Note that the formal error of 0.005 in the integrated spectral index is not representative of the true systematics affecting the data. *The true errors in all of the derived spectral indices are dominated by flux calibration errors, which are taken to be a nominal 5%.* This yields a value for $\alpha_{\rm int}$ of 0.59 ± 0.08. The data are additionally affected by the uncertainty in the correction factor for proximity to the Galactic plane.

Secondly, the integrated spectral index was determined by fitting a straight line to a plot of the 610 MHz against the 1.44 GHz surface brightness (a 'T-T plot') (see Section 8.5). As the pixel size in the final images is $1.0''$, which oversamples the beam considerably, only every 3rd pixel in the N-S direction and every 2nd pixel in the E-W direction was used. Plotting the 610 MHz against the 1.44 GHz flux density and performing a least squares fit on the brighter emission should yield the spectral index, as calculated using

$$S_{0.61\ \mathrm{GHz}} = S_{1.44\ \mathrm{GHz}} \left(\frac{\nu_{1.44\ \mathrm{GHz}}}{\nu_{0.61\ \mathrm{GHz}}} \right)^{\alpha} + \mathrm{constant}\,. \tag{8.1}$$

The determination of the spectral indices relies on the setting of 'gate values' or cutoff values below which data are not included in the regression. The gate values for all of the T-T plots were set at 20σ, so that the straight line fit was only to emission from the remnant and not to faint background emission. In addition, such a high cutoff eliminates low level artefacts from affecting the spectral indices – this may otherwise be a significant problem as the VLA data has reduced *uv*-coverage of smaller baseline lengths in comparison to the GMRT data. The high cutoff biases the T-T plots to determine the spectral indices of only the brightest emission.

A ordinary least squares (OLS) fit considers only errors in the dependent variable, whereas for these data it is not clear which of the variables could be treated as dependent. There are also additional errors in both variables originating from the off-source rms in each image. Further complicating the issue, the intrinsic scatter is substantially greater than that expected due to noise. An OLS regression of a dependent variable Y against an independent variable X is not applicable in this situation. Despite this, an OLS fit is frequently used in the literature for regression of T-T plots. It is statistically sound to use an OLS bisector fit, which splits the difference between the regression lines generated by alternately regressing OLS(Y|X) and OLS(X|Y). This technique has been shown to outperform other approaches (Isobe et al. 1990), and is used for all of the T-T plots in this chapter. While the difference in α derived using

the OLS bisector fit is small for these data, it is crucial to eliminate systematic offsets when searching for subtle spectral variations.

Fitting to the bright emission yields $\alpha_{\rm int} = 0.72$, with a formal error of 0.003. The actual error is again dominated by flux calibration systematics, so that $\Delta\alpha \sim 0.1$. The T-T plot is shown in Figure 8.4. Both of the derived values for the spectral index are in general agreement with previously published values of ~ 0.62 (Green et al. 2008).

The spectral indices throughout this chapter are all potentially systematically offset from their true value due to the correction factor for proximity to the GC, and the aforementioned flux calibration errors. These factors will not affect the identification of relative spectral variations across the remnant, but may accumulate so that the absolute values of spectral index reported here are offset from their true value by as much as 0.1.

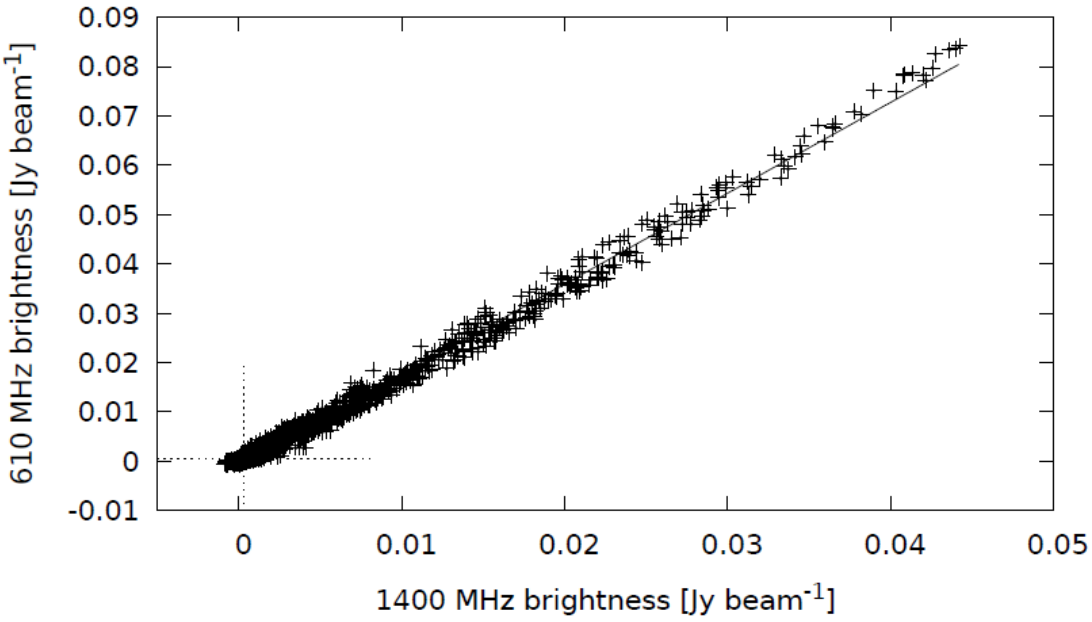

Figure 8.4: A T-T plot of the 610 MHz against 1.44 GHz brightness in units of Jy beam^{-1} for all of the remnant emission. The gate values at 20σ are indicated by dotted lines, and emission below these values were excluded from the OLS bisector regression.

The T-T plot can also be used to identify any large scale DC offset between the two images, whose base levels have been determined differently. Regressing to a surface brightness of zero on one scale, should yield zero on the other scale. This suggests the existence of the equivalent of a large scale offset of -0.874 mJy beam^{-1} affecting the 610 MHz data. It is not possible to determine whether this is originating from the 1.44 GHz or 610 MHz data, however the T-T plots are insensitive to DC offsets. This offset will be important when performing spectral tomography and will be discussed further in Section 8.5.2.

8.5 Spectral Variations

8.5.1 T-T plots

Directly produced spectral index images can be corrupted due to the differing large-scale base-levels in each image. Using plots of flux density at one frequency against that at another frequency, allows for the effect of the base-levels to be eliminated – a technique known as a T-T plot due to the historical use of brightness temperatures for these plots.

The same procedure used in Section 8.4 was used, with the same criteria used to avoid oversampling and the gate values again set to cut off all data below a 20σ threshold. The remnant was separated into twelve distinct annular sectors, with each sector subtending 30°. The centre of the annulus is located at 17h 48m 45.4s, $-27°\ 10'\ 06''$, which is close to the geometric centre of the remnant. The central axis of the annular sectors (i.e. the line separating sector 1 from 12) is displaced to 16.3° from N through E, which is approximately aligned with the remnant's axis of symmetry in Stokes *I* at radio frequencies. Pixels within the defined inner radius of the annulus were all excluded from the analysis, as these pixels are most strongly affected by the effects of the 'negative-bowl' originating from limited sampling of smaller baselines.

The position of each sector is shown in Figure 8.5, while a plot showing the physical location of data excluded by the 20σ gate values is shown in Figure 8.6. The obtained T-T plots and derived spectral indices are shown in Figures 8.7 and 8.8. A graphic showing the variation of spectral index across the remnant is shown in Figure 8.9. Note that some plots show evidence for either two or more distinct electron populations or for artefacts affecting the data – see, for example, sector 10. The fits in these sectors and the corresponding derived spectral index may therefore be adversely affected.

Note that the GMRT and VLA data were obtained at different epochs, and the VLA data has been corrected for an expansion of 0.44% to counter any expansion dependent effects. If incorrect the presumed expansion may systematically affect the derived spectral indices. To check this, varying trial expansions varying from 0% to 1% were tested and it was found that the derived spectral indices were affected by less than 0.008 in all cases.

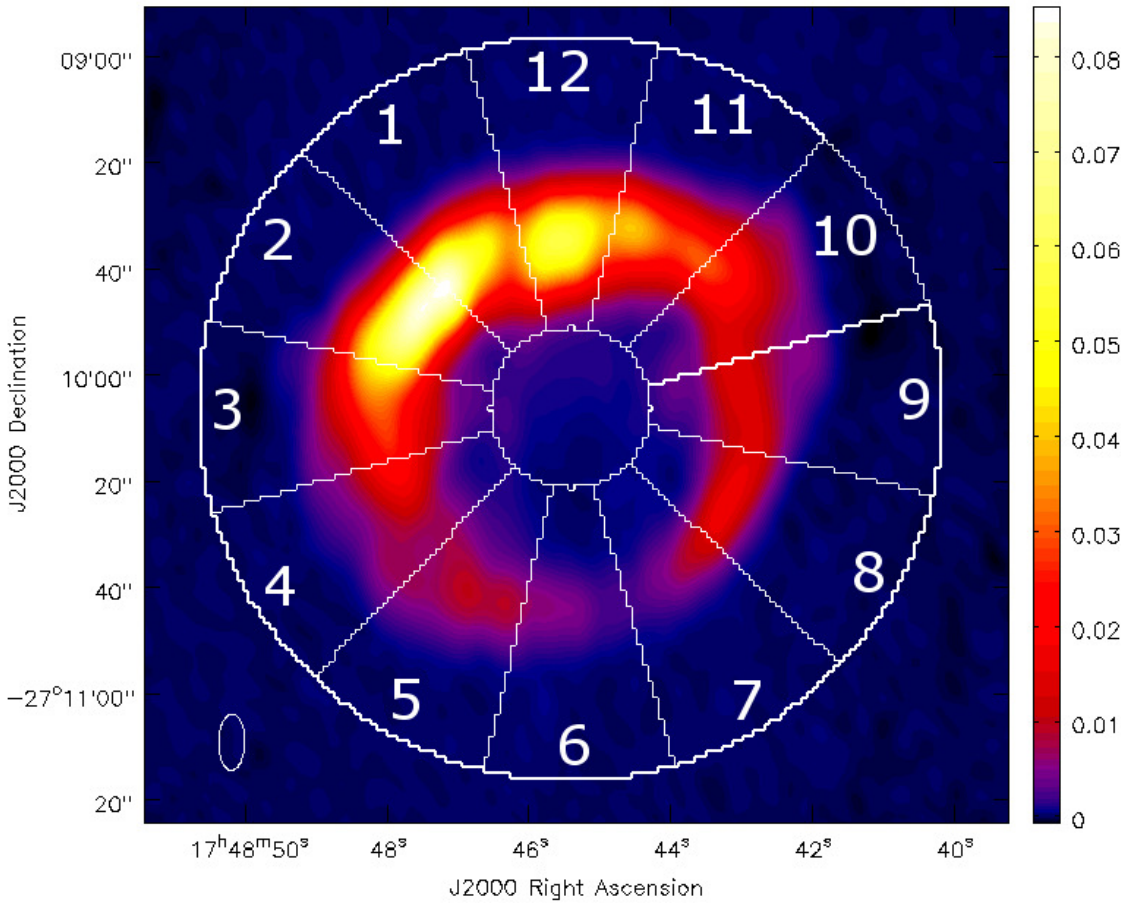

Figure 8.5: G1.9+0.3 at 610 MHz, at matched resolution of $10.62'' \times 4.92''$ with a PA of $-1.1°$. The pseudocolour scale is in units of Jy beam^{-1}. The twelve regions used for the T-T plots are enclosed within the annular sectors labelled 1 through 12.

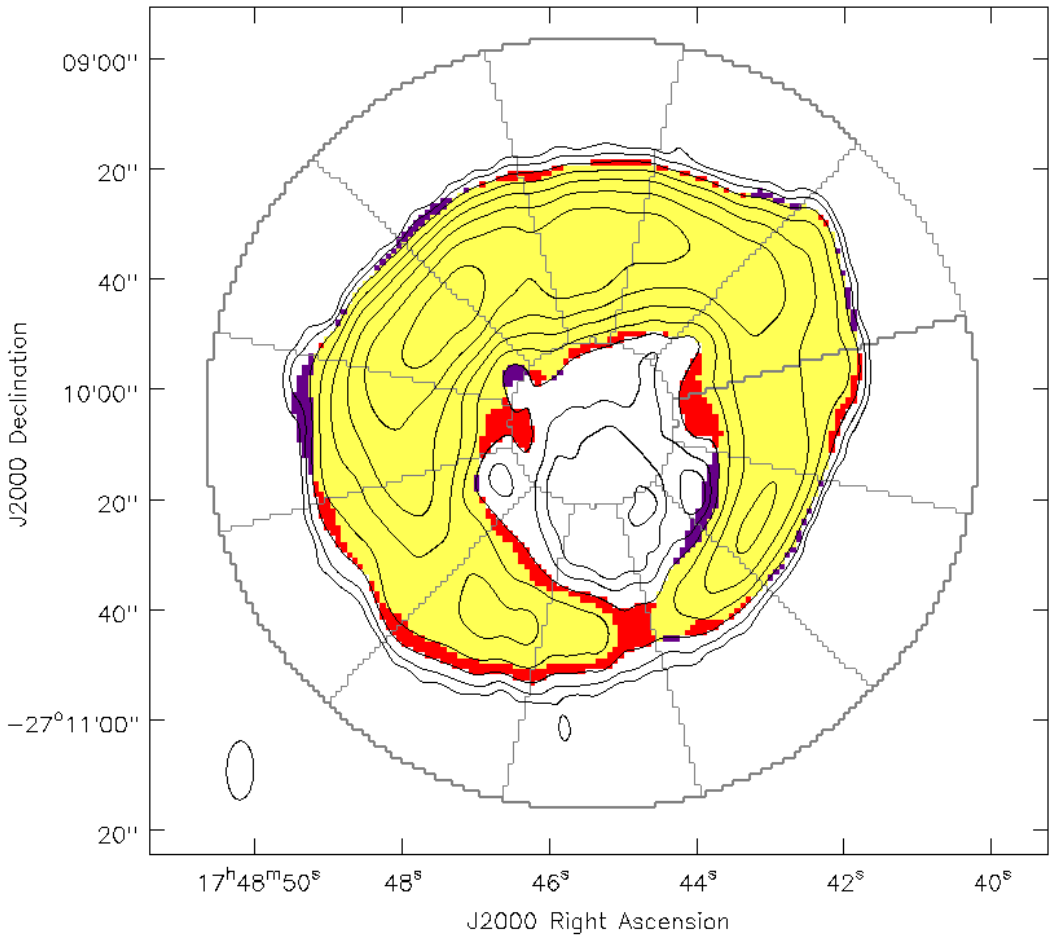

Figure 8.6: A plot showing the physical locations of pixels excluded from the analysis due to being below the 20σ gate values. White pixels are below the gate value in both the 610 MHz and 1.44 GHz data, purple pixels are below the gate value in the 610 MHz data, red pixels are below the gate value in the 1.44 GHz data, and yellow pixels are above the gate values. The black contours are of G1.9+0.3 at 610 MHz, at matched resolution of $10.62'' \times 4.92''$ with a PA of $-1.1°$. Contour levels are at $(1, 2, 4, 8 \ldots 128) \times 0.475$ mJy beam^{-1}. The grey contours show the location of the annular sectors used for the T-T plots. Note that pixels within the defined inner radius of the annulus were all excluded from the analysis.

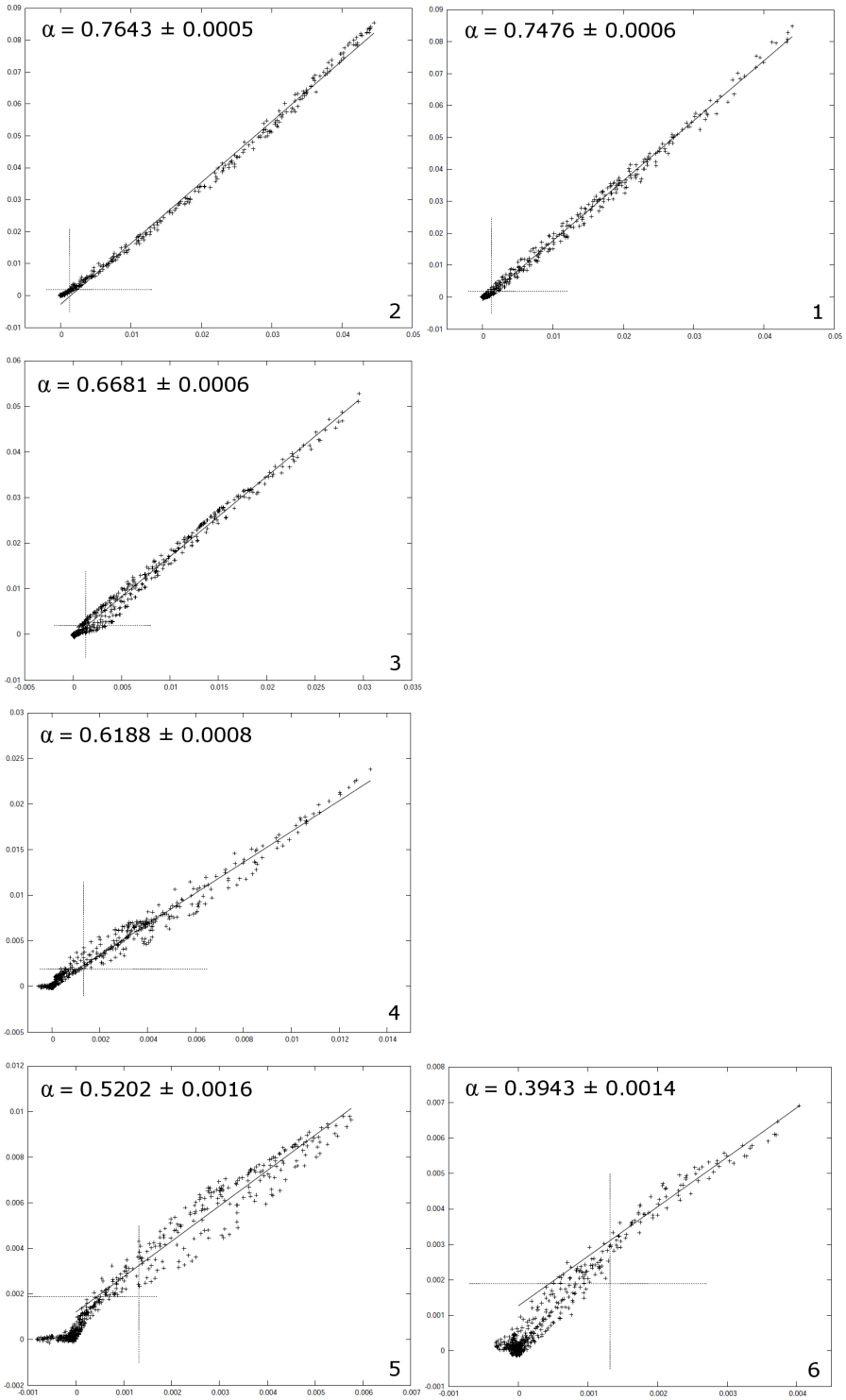

Figure 8.7: T-T plots of the 610 MHz against 1.44 GHz surface brightness in units of Jy beam^{-1} for sectors 1 through 6. The plots are arranged according to the approximate layout across the remnant, as indicated in Figure 8.5. Note the different scales used in each plot, as is necessary due to the varying emission across the remnant. The derived spectral index and sector number are displayed within each plot. Errors shown are the formal error from the OLS bisector fit. Gate values are indicated by the dotted lines. The physical location of data above the gate values is shown in Figure 8.6.

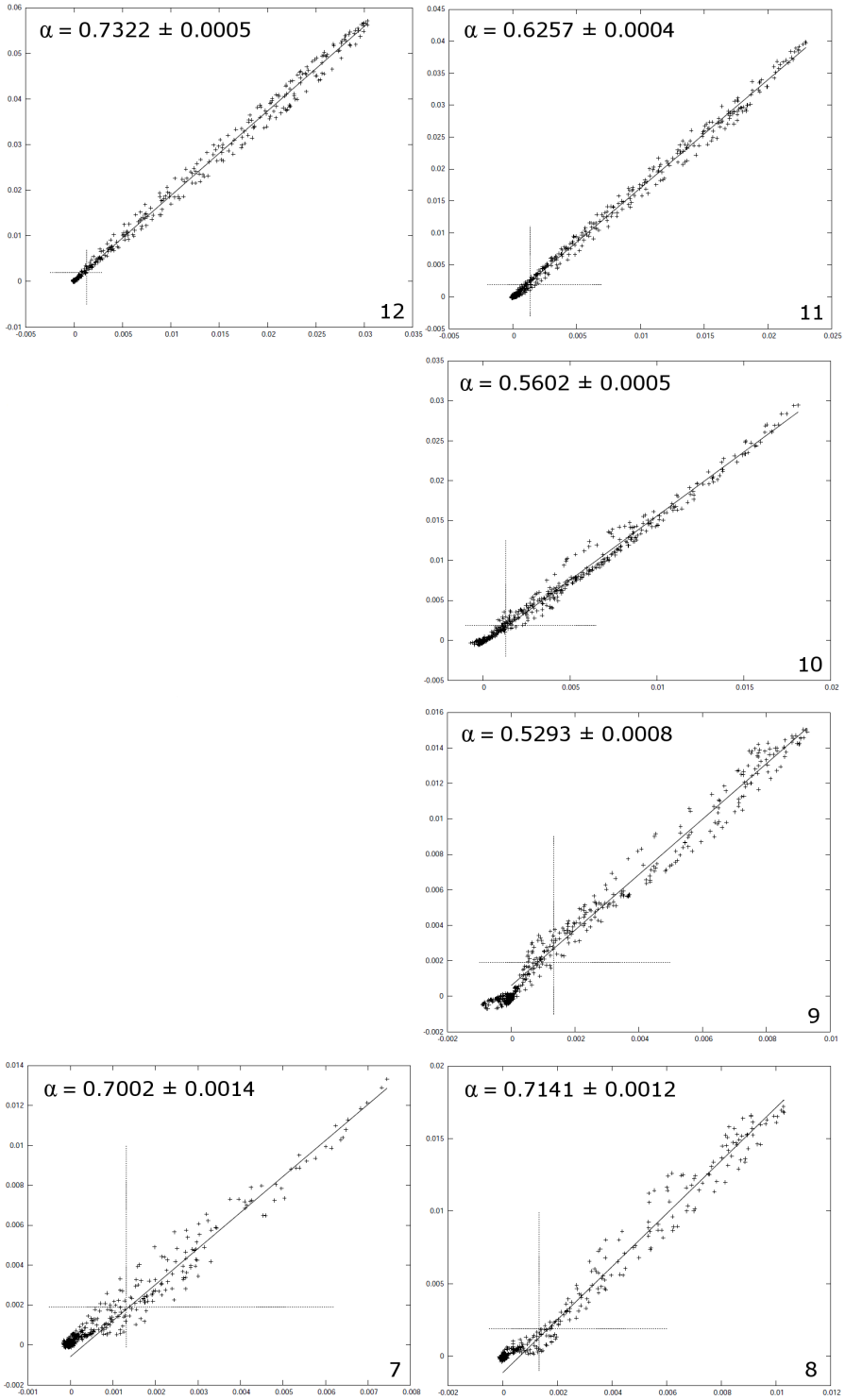

Figure 8.8: The same as Figure 8.7, for sectors 7 through 12.

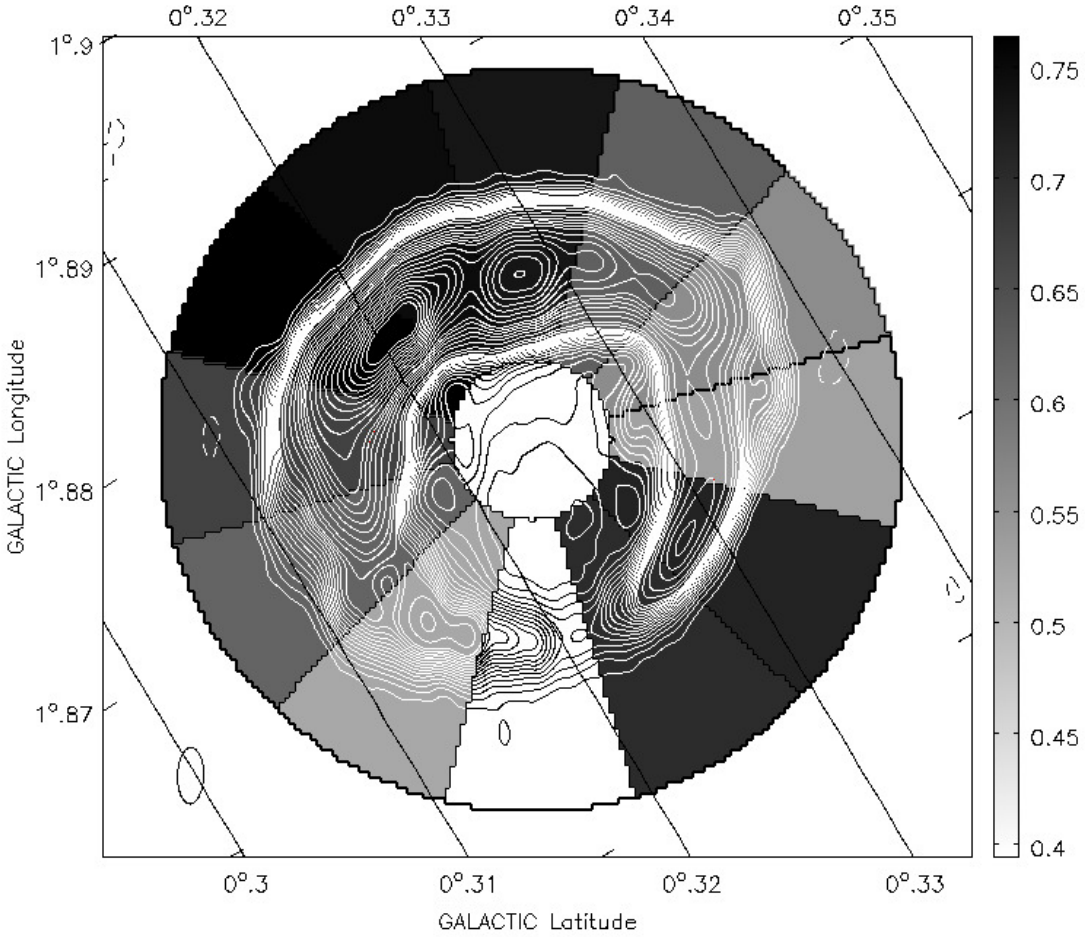

Figure 8.9: Contours of G1.9+0.3 at 610 MHz, at matched resolution of $10.62'' \times 4.92''$ with a PA of -1.1° overlaid upon a grayscale display of the spectral index in each annular sector. The contour levels are the same as in Figure 8.3. The grayscale shows the spectral index as determined from the T-T plots. Lines of constant Galactic latitude are shown overlaid across the remnant.

8.5.2 Spectral Tomography

It is possible that overlapping regions with differing spectral indices may confuse the identification of spectral variations across the remnant. In principle, the technique of Spectral Tomography can assist in separating out overlapping areas with differing spectral indices by producing a gallery of images in which components with a given trial spectral index are subtracted out (Katz-Stone et al. 2000), as calculated using

$$I(\alpha_t) = I_{0.61\ \mathrm{GHz}} - I_{1.44\ \mathrm{GHz}} \left(\frac{\nu_{1.44\ \mathrm{GHz}}}{\nu_{0.61\ \mathrm{GHz}}} \right)^{\alpha_t}, \tag{8.2}$$

where $I_{0.61\ \mathrm{GHz}}$ and $I_{1.44\ \mathrm{GHz}}$ are the images at 610 MHz and 1.44 GHz, α_t is a trial spectral index, and $I(\alpha_t)$ is the tomography image at a given α_t. Regions with $\alpha = \alpha_t$ will disappear with respect to its surroundings in the resulting tomography image. If $\alpha < \alpha_t$, the component will be oversubtracted and have negative brightness, similarly a component with $\alpha > \alpha_t$ will be undersubtracted and have positive brightness.

The technique is highly sensitive to the large scale base-levels which have been determined differently in each independent image. In Section 8.4, the data were found to have a large scale DC offset equivalent to -0.874 mJy beam^{-1} affecting the 610 MHz data. However, while it is possible to correct for a large scale DC component, a gradient across the images or small scale variations can still remain. There is evidence that the DC offset does indeed vary significantly across the source, as determined from the intercepts of the T-T plots and detailed in Table 8.2. Corrections were therefore made for the DC offset in each annular sector. While this allows for the spectral index in each individual sector to be determined far more reliably, contiguous sectors will consequently display artefacts along the sector boundary.

Due to the effects of the DC offsets, the gallery of tomography images need to be interpreted with particular care. The gallery images suffer from the same artefacts as other image-based spectral index comparisons due to differing *uv*-coverage and the differently determined base-levels of both images, but can be useful in deducing the physical location of areas which host varying spectral indices. This is particularly important as the T-T plots smear out the spectral index within each annular sector.

Using the tomography gallery, it is possible to identify a number of areas with flatter spectral index in comparison to a typically steeper large-scale component. The tomography derived variations in α across G1.9+0.3 are very similar to those obtained using T-T plots, with steeper components to the NE and SW and flatter components to the NW and SE.

Some regions show spectral indices which are discrepant with those derived from the T-T plots, as for example the 'knot' with very low spectral index on the Eastern periphery. If real, this would have been smeared out within the T-T plots, however the region's spectral index of $\alpha \sim 0$ means it is likely a consequence of the effects of differing *uv*-coverage and DC offset. Particularly as it only appears along the far edge of the remnants outer rim, where the Stokes *I* emission is fainter and the accuracy of the DC offset correction has a more significant impact.

Table 8.2: Estimated DC offset in T-T plot sectors

Sector No.	DC Offset /mJy beam^{-1}
1	−1.17375
2	−2.73120
3	−0.50632
4	+0.11275
5	+1.20910
6	+1.27134
7	−0.58573
8	−1.11883
9	+0.60971
10	−0.48323
11	+0.08310
12	+0.27517

Interestingly, the tomography gallery would appear to apply better constraints on the physical location of the flatter spectral regions to the NW and SE. With the region to NW located along the remnant's periphery, and the region to the SE located closer to the centre of the remnant. However, to what extent the data are limited by the accuracy of the DC offset corrections is unclear. Similarly to the 'knot', it should be noted that the steeper spectral index in the outer SE is located in a region with faint emission near the remnants outer rim.

The spectral indices inferred using T-T plots are deemed to be considerably more reliable, as that method is specifically applicable to data where the *uv*-coverage and DC component may result in low level artefacts. However, the tomography's general agreement with the T-T plots acts as confirmation of the previously determined results.

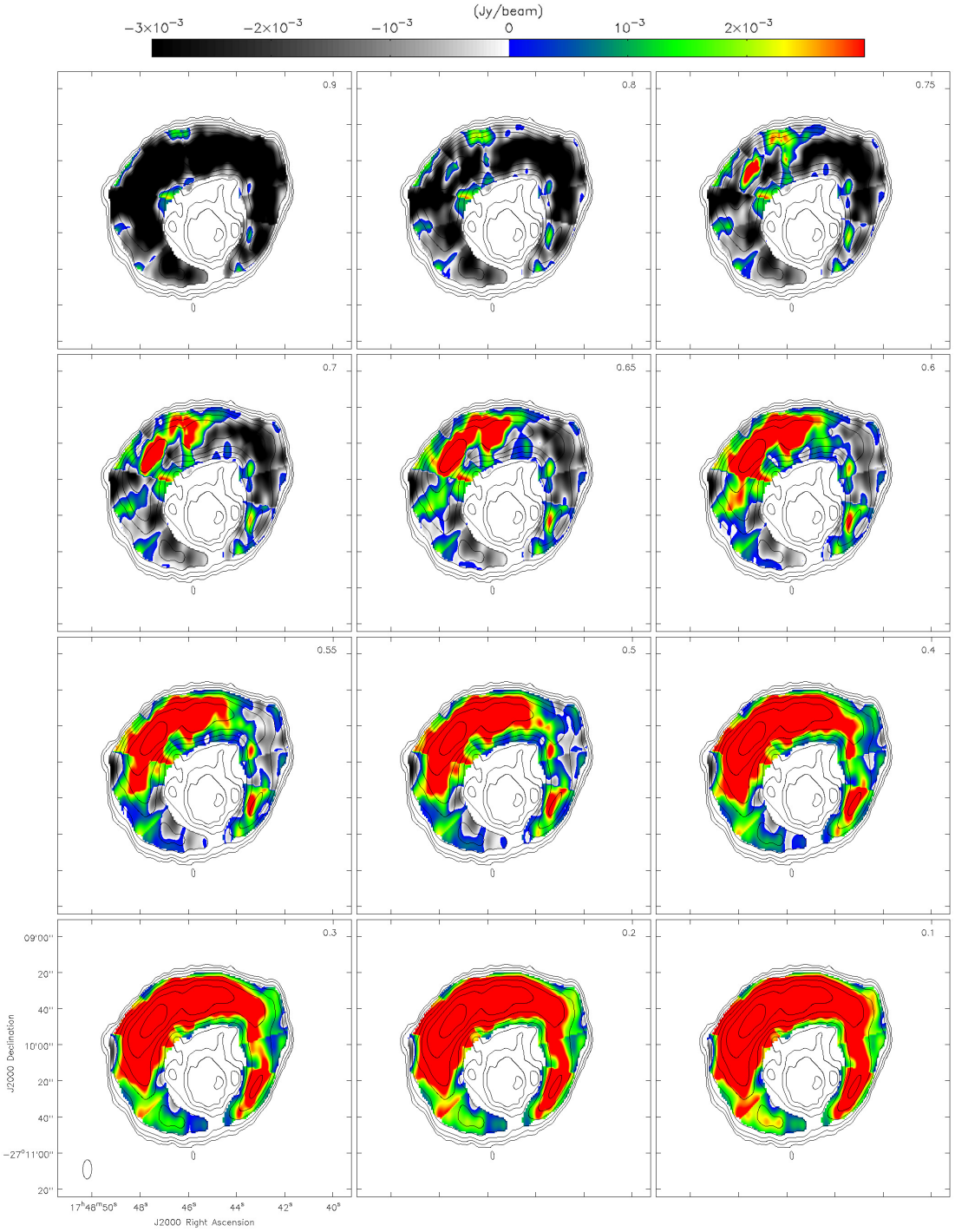

Figure 8.10: The spectral tomography gallery for varying trial spectral indices, decreasing from left to right. The shown images are for $\alpha_t = 0.9, 0.8, 0.75, 0.7, 0.65, 0.6, 0.55, 0.5, 0.4, 0.3, 0.2, 0.1$. The black contours indicate the 610 MHz Stokes I emission. Contour levels are at $(1, 2, 4, 8 \ldots 128) \times 0.475$ mJy beam^{-1}. Positive values (indicating that $\alpha_t < \alpha$) are shown in pseudocolour, while negative values (indicating that $\alpha_t > \alpha$) are shown in grayscale. The tomography output has been blanked below a 20σ threshold.

8.6 Polarisation

Following the polarisation calibration of the C-band data, images were made in Stokes I, Q, U, and V. Checks on the quality of polarisation calibration are discussed in Section 8.6.1. Deconvolution of the Q, U, and V images was carried out down to a 2σ limit, with σ determined to be 53 μJy beam^{-1} from the Stokes I image. All images were convolved to a resolution of $13.23'' \times 7.14''$ with a position angle of $-18.84°$.

The Stokes Q and U images were combined into an image of the linearly polarised intensity. The P image was corrected for the effects of Rician bias using a maximum likelihood estimator, which corrects for the effects of non-Gaussian noise statistics (Simmons & Stewart 1985). However, for this statistically significant detection, the magnitude of the correction is negligible.

For the first time, the presence of linear polarisation is detected in G1.9+0.3 at 4.86 GHz, as shown in Figure 8.11. The polarised emission is bipolar with two bright limbs opposite one another. Polarised intensity is predominantly located along the E and W edges of the shell, and is brighter in the limb to the E. There appears to be significant depolarisation to the N of the remnant, and no emission is detected towards the remnant's centre. Note that the polarisation structure is not correlated with total intensity. No emission was detected in Stokes V.

8.6.1 Instrumental Effects

The 4.86 GHz polarisation observations were short observations, which in accordance with conventional wisdom does not allow for the separation of instrumental and source polarisation using the phase calibrator. The reliability of polarisation calibration could be adversely affected, in some circumstances, for observations with low parallactic angle coverage.

However, this rule of thumb can be ungrounded as although full-track observations are generally an efficient way to get high parallactic angle coverage, the variation is dependent on source declination. The solutions for the instrumental polarisation are also not just dependent on the parallactic angle variation, but also on the s/n, the instrumental stability, and the magnitudes of both the source and instrumental polarisation – for further detail see Chapter 2. The quality of polarisation calibration is therefore not necessarily strongly dependent on the parallactic angle coverage. Crucially, checks on the data should be made to quantify any residual instrumental polarisation, something which is not always done throughout the literature. After instrumental polarisation calibration using the phase calibrator and a linear model, the maximum leakage of any antenna was calculated to be $6.7 \pm 0.8\%$, with the mean leakage of the array being $2.75 \pm 0.16\%$. After calibration, the standard deviation in the RL and LR phases of the EVPA calibrator were less than 1°. The EVPA was set using an observation of 3C286 and the residual polarisation was determined to be $< 0.2\%$ in polarised intensity.

To confirm that the parallactic angle variation of $\Delta\chi = 7.7°$ for the 4.86 GHz observation is not detrimental to the quality of calibration, the leakage terms for both R and L in each IF were perturbed incrementally by $\pm 1\%$ to test the impact on the measured polarised flux density.

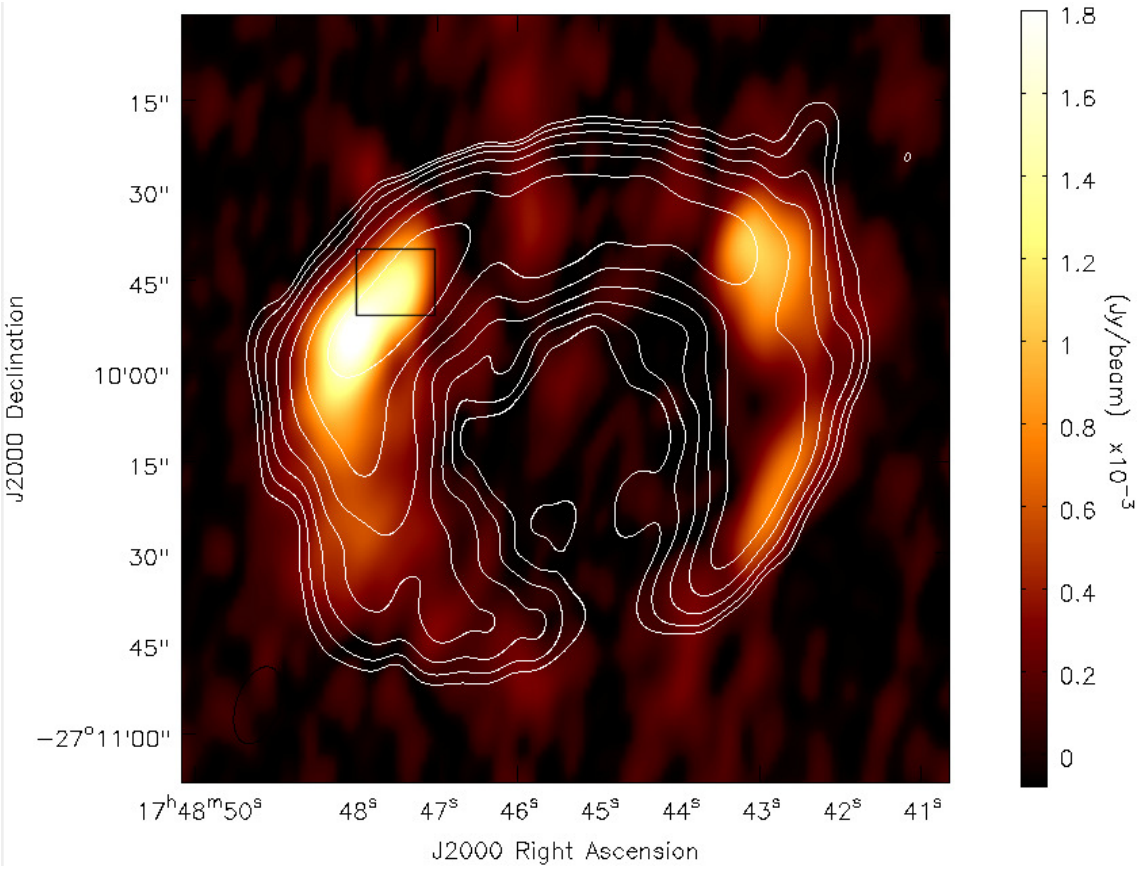

Figure 8.11: The Rician bias corrected polarised intensity, $P = \sqrt{Q^2 + U^2}$, of G1.9+0.3 at 4.86 GHz, overlaid with Stokes I contours. The pseudo-colour polarised intensity scale is in mJy beam^{-1}, and contour levels are at (1, 2, 4, 8...64) $\times$ 0.265 mJy beam^{-1}. The black box indicates the region used to check for variations in polarised brightness when the leakage terms were perturbed in Section 8.6.1.

As the amplitude of the leakage directly effects the amount of total intensity flux that 'leaks' into polarised intensity, it is expected that small perturbations in the leakages should result in a *decrease* in polarised flux density if the leakages are poorly estimated.

Images of linearly polarised intensity, $P = \sqrt{Q^2 + U^2}$, were created at fixed resolution for each permutation of the leakages. The integrated flux density was then measured in a small box region of 143 pixels centred on the brightest polarised emission in the Eastern limb. For antennas where the leakage had been determined to be less than 1%, the leakage was set to zero for the negative perturbation. Plots of the measured differences in polarised flux density are shown for both IFs in Figure 8.12. The location of the box is shown in Figure 8.11.

Some leakage perturbations show a distinct decrease in polarised flux density for small perturbations in the leakage amplitude. While this shows that the leakage amplitude has not been accurately determined for these antennas, some level of inaccuracy is expected due to the use of

a linearised model for the polarisation calibration. The general trend overwhelmingly shows an increase in the polarised flux density for perturbations of the leakage amplitude, suggesting that the leakages are typically accurate to better than ±1%. Note that the largest error in polarised flux density as a result of leakage perturbations is 18 μJy. The noise in Q/U is ∼ 35 μJy beam^{-1}, this suggests that the 4.86 GHz polarisation measurements are dominated by noise rather than by leakage errors.

As previously stated, after polarisation calibration the standard deviation in the *RL* and *LR* phases of the EVPA calibrator 3C286 were $< 1^{\circ}$, and the residual instrumental polarisation was measured to be less than 0.2% in polarised intensity. The discrete source $1.6'$ to the N of the remnant is also depolarised to a 2σ upper limit of $< 0.75\%$. All of this suggests that the leakage terms have been sufficiently well determined.

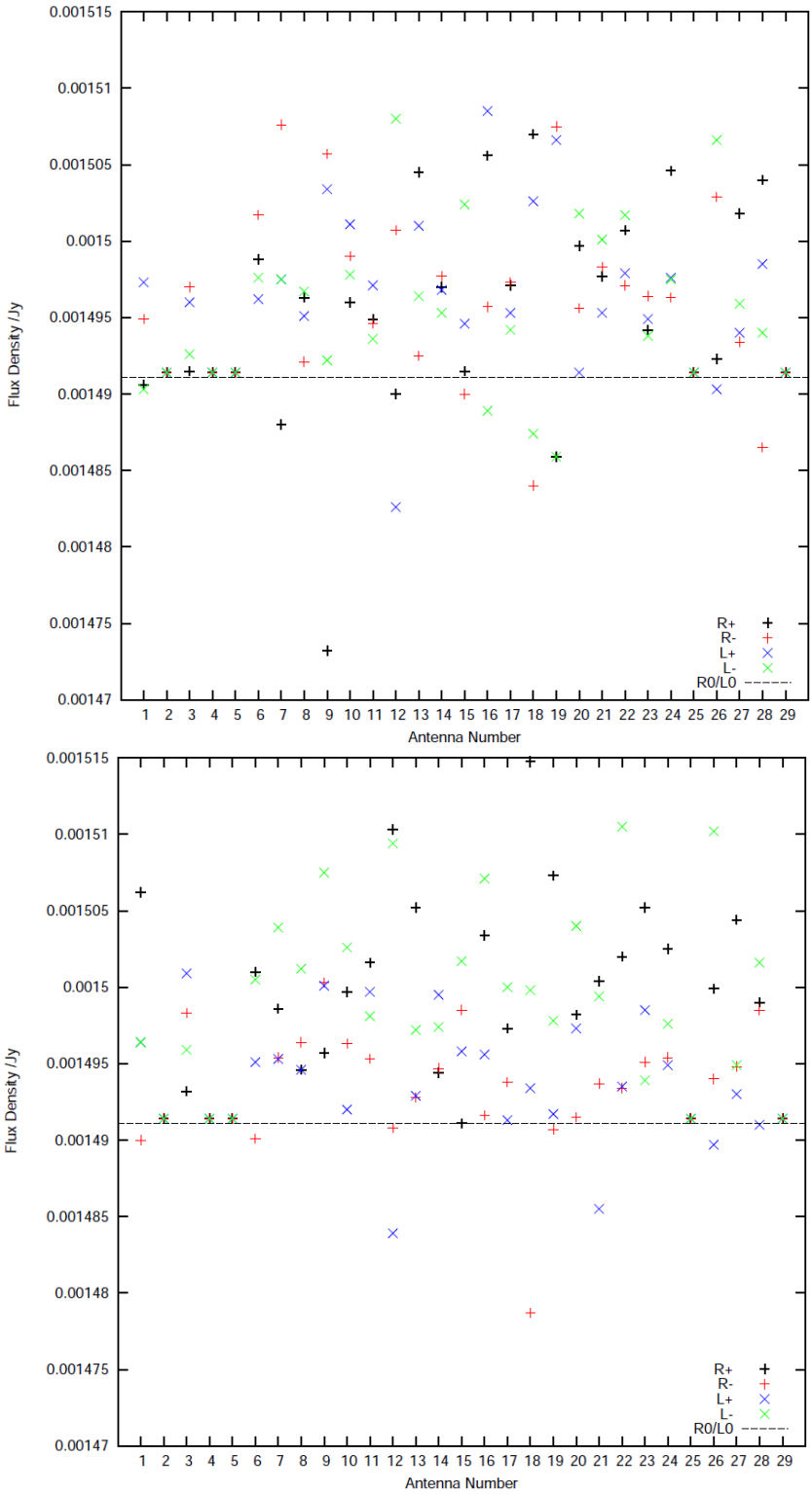

Figure 8.12: The polarised flux density response for variations of ±1% in the leakage amplitude for all antennas. Both IF1 (top) and IF2 (bottom) are shown, for positive and negative perturbations in R and L. The dotted line indicates the polarised flux density obtained when using the leakages determined via polarisation calibration. Antenna numbers 2, 4, 5, 25, and 29 are not used in this dataset. The reference antenna was number 15.

8.6.2 Fractional Polarisation

The fractional polarisation image and corresponding error image are shown in Figure 8.13. Due to missing short interferometer spacings, the fractional polarisation can appear higher than the true value, as such the fractional polarisation images represent upper limits.

The mean fractional polarisation is ~ 9% in the eastern limb with σ = 7%, and ~ 13% to the west with σ = 6% as determined from integration of the image values. There are peaks in polarisation of up to ~ 33% in the outer NW and up to 63% in the outer SE – although it should be noted that the peaks are occurring in regions with decreasing total intensity. The mean fractional polarisation of ~ 10% is typical of young SNRs. The mean fractional polarisation and localised peaks resemble the bipolar polarised emission in SN 1006, which has a mean fractional polarisation of ~ 13% and local ratios of up to 30% (Reynolds & Gilmore 1993). The polarisation structure is also reminiscent of the bilaterally symmetric X-ray synchrotron emission observed in G1.9+0.3 (Reynolds et al. 2009).

The fractional polarisation in G1.9+0.3 appears to increase towards the edges of the remnant. Despite the decreasing Stokes *I* emission towards the remnant periphery, the observed increase in fractional polarisation is greater than the also increasing error. Corrections have not been made for spurious off-axis instrumental polarisation, however for the VLA at 4.86 GHz, the off-axis leakage should be less than 0.5% at the remnant periphery. The convincing increase in Π towards the edge of the remnant is in the region towards the NW. Conversely, there is no discernible increase in the region to the NE. There is also the prospect of an increase towards the S periphery, although the increase to the SE in particular appears to correlate with the Stokes *I* emission and is plausibly the result of systematics.

Due to the decreasing s/n at the remnant periphery, the high values of peak polarisation are distinct upper limits. However, the regions of peak polarisation also appear to correlate with areas of flatter spectral index. This needs to be confirmed with higher sensitivity observations, but appears to indicate enhanced ordering of the magnetic field towards the remnant periphery.

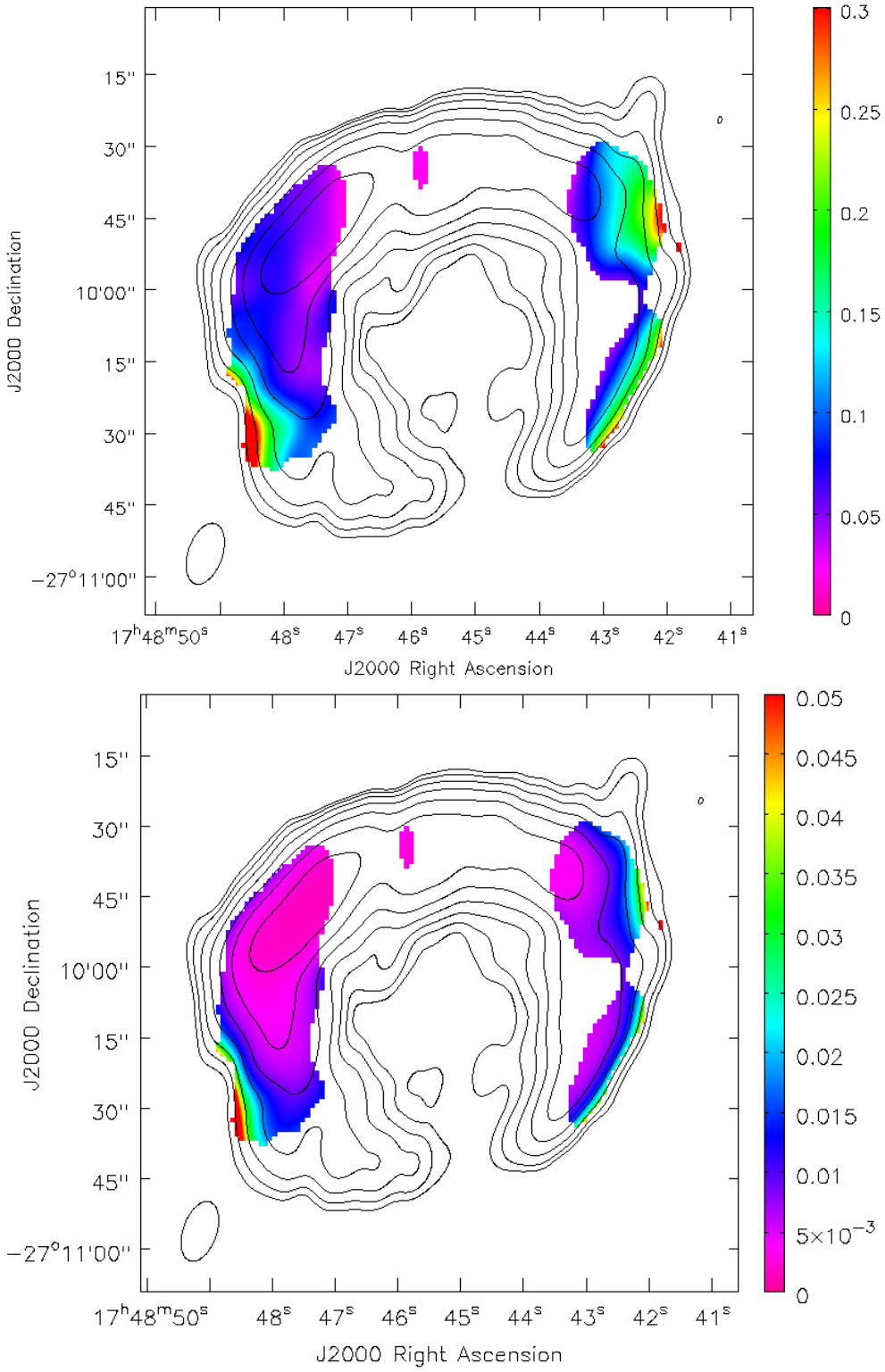

Figure 8.13: The fractional polarisation, $\Pi = \sqrt{Q^2 + U^2}/I$, of G1.9+0.3 at 4.86 GHz (top) and the corresponding error image (bottom), overlaid with Stokes I contours. The pseudocolour scale of fractional polarisation is from 0–30%, and the error image from 0–5%. The contour levels are as in Figure 8.11. The images were blanked where either polarised or total intensity fell below the 5σ level.

8.6.3 Depolarisation

Neglecting depolarisation effects, the polarisation degree for optically thin synchrotron radiation is directly related to the spectral index by

$$\Pi = \left(\frac{3+3\alpha}{5+3\alpha}\right)\frac{H_0^2}{H_0^2+H_r^2}\,, \tag{8.3}$$

where H_0 and H_r are the uniform and random field strengths respectively (e.g. Burn 1966). For an entirely uniform magnetic field ($H_r = 0$) with $\alpha \approx 0.62$, a maximum polarisation fraction of 71% is expected. As the fractional polarisation ($\sim 10\%$ at 4.86 GHz) is considerably lower than the theory suggests, this could indicate that the magnetic field is disordered on scales smaller than the beam size. In G1.9+0.3, the magnetic field would therefore have to be disordered on 0.4 pc scales. The measurements suggest that the ratio of random to uniform field strengths in G1.9+0.3, $H_r/H_0 = 2.5\pm^{1.2}_{0.9}$.

Nevertheless, the low observed fractional polarisation at 4.86 GHz could be a consequence of multiple depolarisation mechanisms, including bandwidth depolarisation, beam depolarisation, and Faraday dispersion (see Chapter 2). Bandwidth depolarisation would only affect these data for a RM$>$ 10000 rad m^{-2}. There is also no evidence to suggest that the spectral index in G1.9+0.3 is frequency-dependent.

The observations at 610 MHz and 1.44 GHz allowed for checks on the amount of depolarisation. The field of view surrounding G1.9+0.3 at 610 MHz is shown in Stokes I in Figure 8.14 and in P at a Faraday depth of 0 rad m^{-2} in Figure 8.15. G1.9+0.3 was found to be depolarised at 610 MHz with the brightest Stokes I emission (to the N of the remnant) having a polarisation fraction of $< 0.05 \pm 0.04\%$. Polarisation calibration was also enacted on the L-band data, and the remnant found to be depolarised to a 2σ limit of < 65 μJy beam^{-1} at 1.44 GHz – with the brightest I emission corresponding to $\Pi < 0.1 \pm 1.3\%$. The same bright emission in Stokes I has $\Pi = 4.13 \pm 0.14$ at 6 cm, with an elliptical synthesised beam of $13.23'' \times 7.14''$ with a position angle of $-18.84°$. The lack of detection at lower frequencies, combined with the increased sensitivity and steep spectral index of the remnant, shows that there must be strong Faraday depolarisation between 6 cm and 21 cm. The situation along the line of sight may therefore be Faraday-thick, and in such a case the EVPA is unlikely to follow a linear relationship with λ^2. Nevertheless, as the polarised emission has not been detected using spectropolarimetry, I will assume here that the data can be parameterised in terms of a single RM value. Additionally, I only consider the absolute value of the complex polarisation, as individual measurements of Q and U are only available at two frequencies.

The observed strong Faraday depolarisation could be occurring either internally or externally to the remnant due to a number of effects. I now examine the possible scenarios that may be responsible for the observed depolarisation. I take the depolarisation at λ to be equal to $p(\lambda^2)/p(6\text{cm})$, and for no depolarisation this is equal to 1.

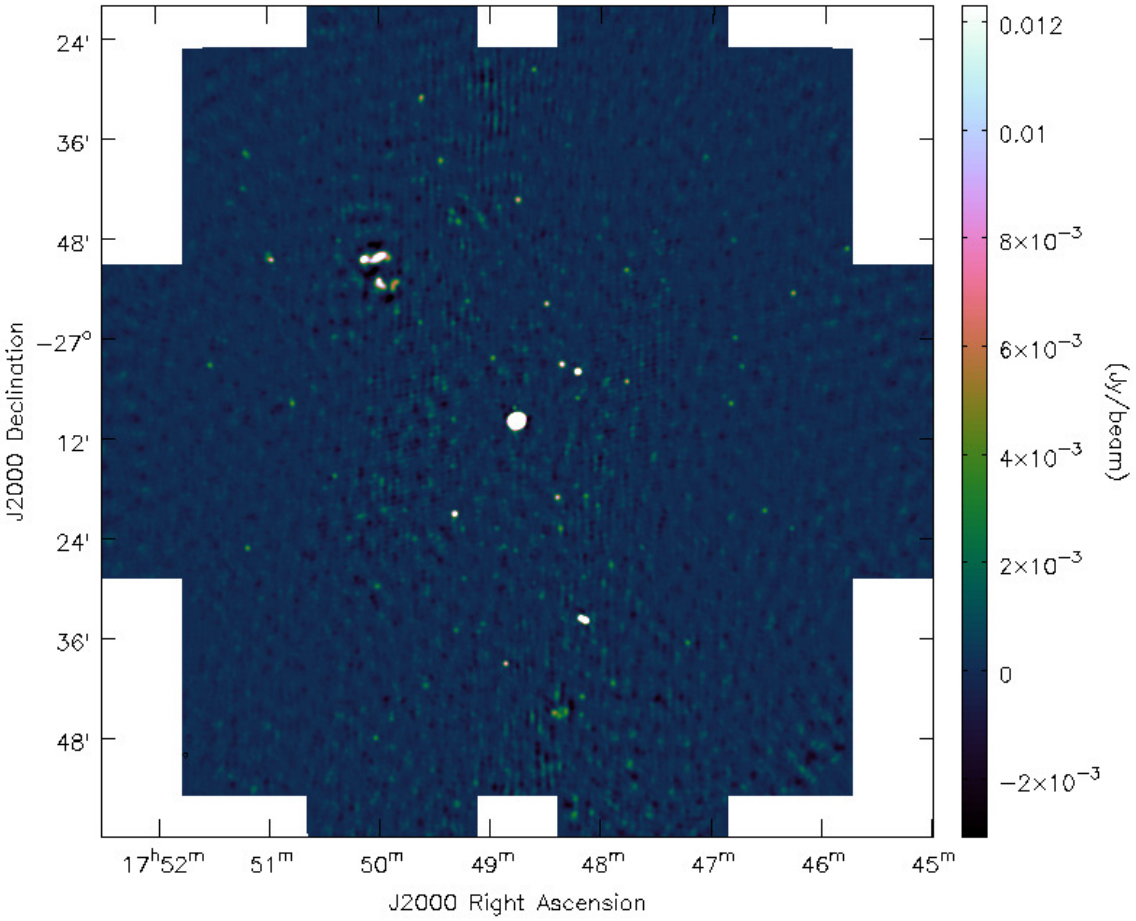

Figure 8.14: A Stokes *I* image of the field surrounding G1.9+0.3 at 610 MHz. The image has a resolution of 30″ × 30″, and has not been corrected for the effects of the primary beam. The remnant is at the phase-centre of the image. The pseudocolour scale is in units of Jy beam^{-1}.

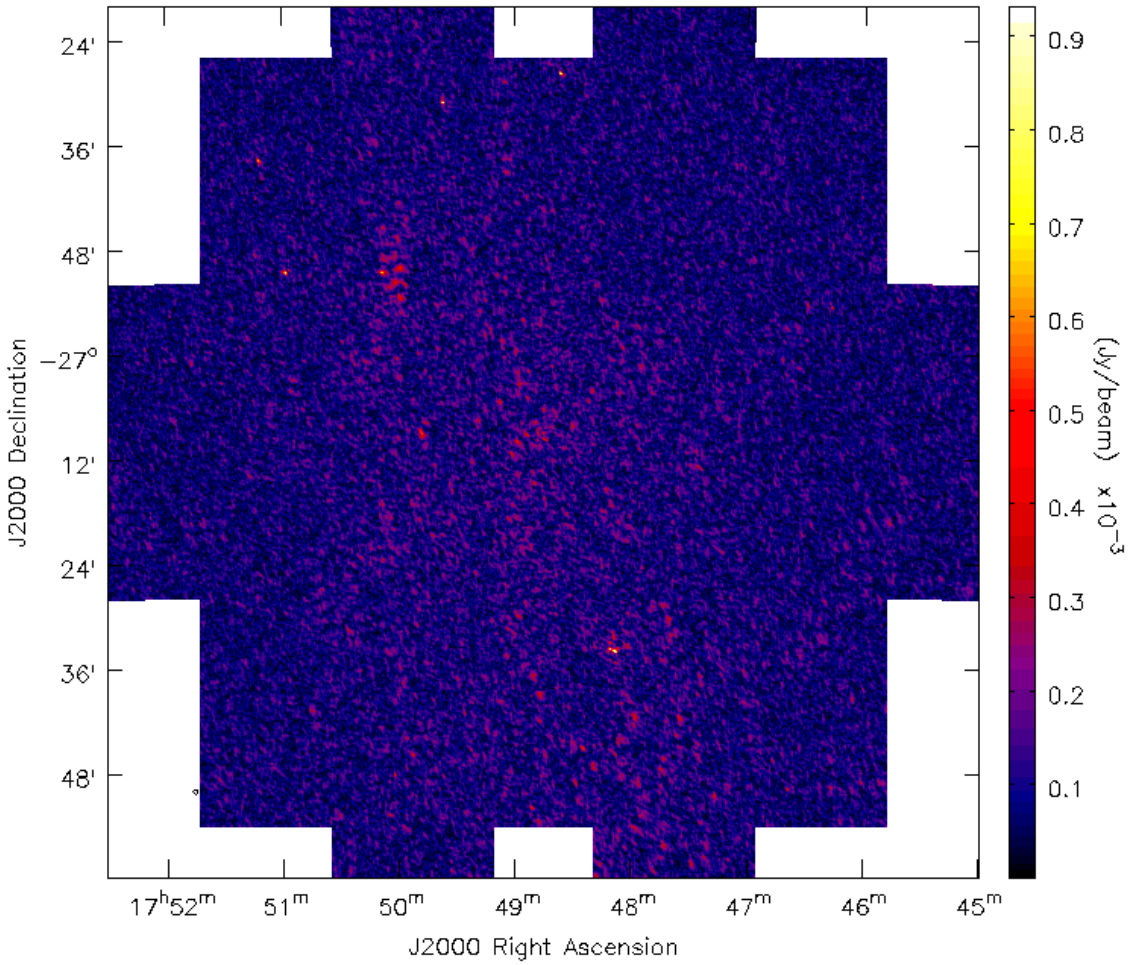

Figure 8.15: A polarised intensity, P, image of the field surrounding G1.9+0.3 at a Faraday depth of 0 rad m^{-2} following RM Synthesis at 610 MHz. Residual instrumental polarisation is present throughout the field, although several apparently polarised sources are also clearly visible. The image has a resolution of $30'' \times 30''$, and has not been corrected for the effects of the primary beam or Rician bias. The noise level of the ϕ-cube is 56 μJy beam^{-1} rmsf^{-1}. The remnant is at the phase-centre of the image. The pseudocolour scale is in units of mJy beam^{-1}.

8.6.3.1 Internal Faraday Depolarisation

Internal Faraday depolarisation takes places when the emitting and Faraday rotating regions within a source are intermixed. In the presence of a regular magnetic field, the plane of polarisation of emission from the far side of the region undergoes a different amount of Faraday rotation compared to emission from the near side. The process is known as 'differential Faraday rotation' (DFR) and the sum over the entire region results in depolarisation (e.g. Arshakian & Beck 2011). Furthermore, in the presence of a turbulent magnetic field, the plane of polarisation experiences random fluctuations as it propagates through the region. This process is known as 'internal Faraday dispersion' (IFD) and this addition of random anisotropic magnetic fields results in further depolarisation (e.g. O'Sullivan et al. 2012).

I first consider the effects of DFR. The depolarisation via this mechanism is given by

$$p(\lambda^2) = p(0)\left|\frac{\sin(2\mathrm{RM}\,\lambda^2)}{2\mathrm{RM}\,\lambda^2}\right| . \tag{8.4}$$

A plot of a model of the DFR as a function of λ^2 for G1.9+0.3 is shown in Figure 8.16. Due to the lack of data, it is not possible to confirm the presence or absence of DFR. The characteristic polarisation variations that result from DFR are not identifiable given the limited data. Nevertheless, if DFR is solely responsible for the depolarisation in G1.9+0.3, the observations provide a lower bound of a $|\mathrm{RM}| \geq 26$ rad m^{-2}.

I now consider the effects of IFD. Following Burn (1966), I assume a simple slab model for G1.9+0.3. Such a model is presumed as adequate as the SNR is well-resolved by the synthesised beam. Therefore, emission detected within each beam originates from an approximately cylindrical column along the line of sight. For such a slab, the complex polarisation is given by

$$p(\lambda^2) = p(0)\frac{1-e^{-s}}{s} , \tag{8.5}$$

such that

$$s = 2\mu q_0^2 L^2 \lambda^4 - 2iq_0 L\lambda^2 , \tag{8.6}$$

and

$$\mu = \left(\frac{q_r}{q_0}\right)^2 \left(\frac{d}{L}\right) . \tag{8.7}$$

Following Velusamy & Kundu (1975), the source is assumed to have a uniform RM, q_0. The extent of the emitting region along the line of sight, L, consists of irregular cells of size d randomly distributed within the source and separated by a distance $\approx d$. The cells are sufficiently small that $d \ll L$. The RM within the irregular cells is given by q_r, so that the cells have random RMs with an rms amplitude $q_r d$ and a mean value of zero. μ is an inhomogeneity parameter and denotes the irregularities within the source, with $\mu = 0$ indicating no irregularities. $q_0 L$ defines the internal RM due to the uniform density and field in the source. In cases where $p(\lambda^2)/p(0) > 0.5$ (i.e. the source is depolarised by no more than 50%) the relation between the

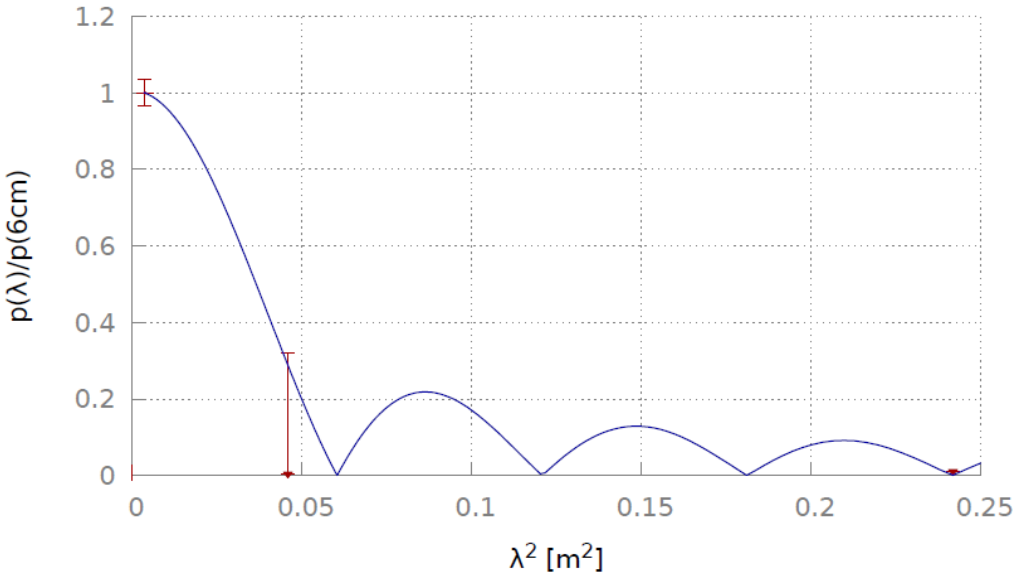

Figure 8.16: The depolarisation $p(\lambda^2)/p(6\text{cm})$ as a function of λ^2 for G1.9+0.3. The polarised detection at 4.86 GHz and the upper limits for non-detections at 1.44 GHz and 610 MHz are shown in red. A model of the effects of differential Faraday rotation is shown in blue for the lowest value of RM that fits the data. The observations suggest that if differential Faraday rotation is solely responsible for the depolarisation then $|\text{RM}| \geq 26$ rad m^{-2}.

EVPA and λ^2 follows a linear relationship with a RM corresponding to $q_0 L/2$ (the average RM within the source).

A plot of a model of the IFD as a function of λ^2 for G1.9+0.3 is shown in Figure 8.17, for various values of μ and $q_0 L$. Similarly to the constraints placed on DFR, the lack of data means it is not possible to confirm the presence or absence of IFD. In addition, it is not possible to easily distinguish between either a large number of irregularities or a larger RM. Nevertheless, if IFD is solely responsible for the depolarisation in G1.9+0.3, the observations provide a lower bound for the internal RM of $|q_0 L| \geq 30$ rad m^{-2} – irrespective of the value of μ.

8.6.3.2 External Faraday Dispersion/Beam Depolarisation

External Faraday dispersion occurs in resolved sources if the Faraday rotation in front of the emitting region varies significantly across the source over a solid angle smaller than the beam (e.g. Velusamy & Kundu 1975). Such a Faraday screen would consist of a magnetoionic region that is devoid of relativistic particles and that exists somewhere along the line of sight between the observer and the SNR (e.g. Sokoloff et al. 1998). If this Faraday screen contained a *constant* regular field then the region would cause Faraday rotation of the polarised emission from background sources, but would *not* cause any depolarisation. Nevertheless, any deviation from a constant field within the synthesised beam will create a RM gradient and subsequently

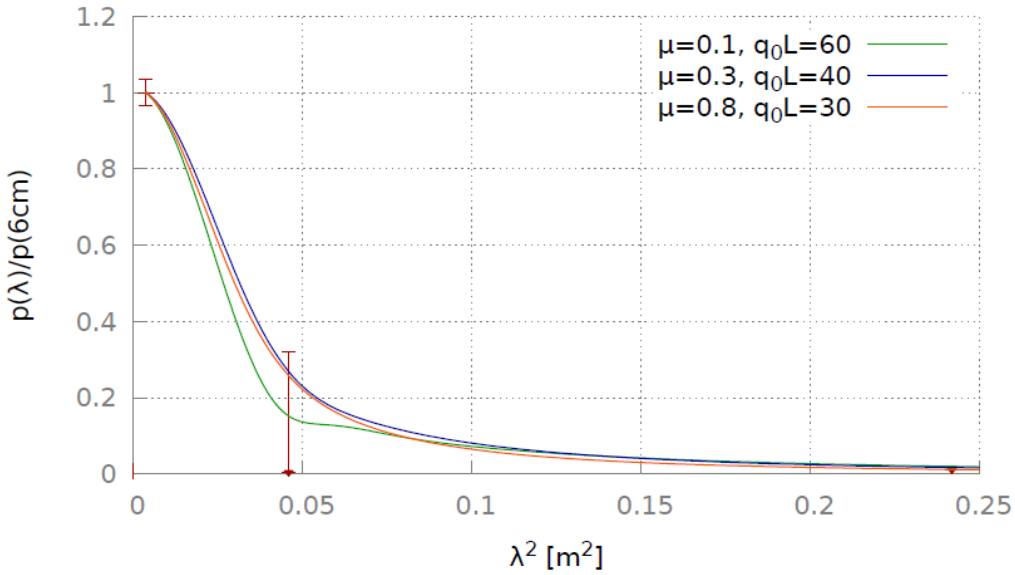

Figure 8.17: The depolarisation $p(\lambda^2)/p(6\text{cm})$ as a function of λ^2 for G1.9+0.3. The polarised detection at 4.86 GHz and the upper limits for non-detections at 1.44 GHz and 610 MHz are shown in red. Three models of the effects of internal Faraday dispersion are shown in green, blue, and orange respectively for low values of q_0L that provide reasonable fits to the data given various μ. Irrespective of μ, the observations suggest that if internal Faraday dispersion is solely responsible for the depolarisation then the internal RM, $|q_0L| \geq 30$ rad m^{-2}.

cause depolarisation. Such anisotropy of the B field would be caused by either turbulent, or systematically varying regular fields. For turbulent magnetic fields, depolarisation will occur when there are many turbulent regions within the synthesised beam. For regular magnetic fields, depolarisation will occur if there are any variations in the strength or orientation of the field within the synthesised beam (e.g. O'Sullivan et al. 2012).

I first consider the effect of turbulent fields. If the values of RM have a large spread over the beam, at longer λ the polarisation is rotated through different angles in each direction, resulting in a reduction in Π. Such depolarisation due to random fluctuations in the external RM can be calculated via

$$p(\lambda^2) \approx p(0) \exp\left[-2R_r^2 \frac{\Omega}{\delta^2}\lambda^4 + 2iR_0\lambda^2\right], \tag{8.8}$$

where R_0 is the mean RM over the beam, R_r is the rms fluctuation of the RM, δ is the angular size of the regions of random fluctuations, and Ω is the beam solid angle (Burn 1966; Velusamy & Kundu 1975). For an elliptical Gaussian beam with major and minor axes of FWHM θ_{maj} and θ_{min}, the beam solid angle is given by

$$\Omega = \frac{\pi\theta_{\text{max}}\theta_{\text{min}}}{4\ln 2}. \tag{8.9}$$

Explaining the depolarisation in G1.9+0.3 as being entirely the consequence of turbulent

fields within the synthesised beam would require implausibly large random fluctuations in the external RM of $R_r/\delta \geq 100$ rad m^{-2} arcsec^{-1}.

I now consider the effect of a systematically varying regular field. Such variation may occur within the remnant itself, or in a nearby Faraday screen. Following Velusamy & Kundu (1975), I consider the effect of such systematic variation in RM across G1.9+0.3. The distribution of the gradient in RM has been found to correlate with the distribution of depolarisation when derived assuming a λ^2-law (e.g. Kundu et al. 1973). Assuming a λ^2-law, then a gradient, g, in the external RM across the beam will result in depolarisation at λ given by

$$p(\lambda^2) = p(0) \exp\left(-\frac{g^2 \theta_{\rm max} \theta_{\rm min} \lambda^4}{2500}\right), \tag{8.10}$$

where $\theta_{\rm max}/\theta_{\rm min}$ is the FWHM of the synthesised beam in arcsec. A gradient of just 2 rad m^{-2} arcsec^{-1} is sufficient to explain the observed depolarisation. The depolarisation in G1.9+0.3 could therefore be caused by a systematic RM gradient across the source. Nevertheless, without confirming whether the observed RM follows a λ^2-law (which would require constraints on the complex polarisation at multiple wavelengths), it is difficult to confirm the nature of the depolarisation mechanism. It does however seem reasonable that such a systematic gradient in RM may be present in either the remnant itself, or an intervening Faraday screen. If a systematic gradient in RM is solely responsible for the depolarisation and this gradient is assumed to be constant across the near side of G1.9+0.3, then the observed values imply a lower bound for variation in RM across the $\approx 92''$ remnant to be ≥ 190 rad m^{-2}.

8.6.4 Rotation Measure

The magnetic field vectors ($B = E + 90°$) observed at the telescope are corrupted by Faraday rotation along the line of sight between the telescope and the source. However, in principle it is possible to create a RM image to correct for the effects of Faraday rotation. As the remnant is depolarised below the sensitivity limit at frequencies ≤ 1.44 GHz, the RM is determined from the two sidebands at 4.86 GHz, as shown in Figure 8.18. RMs determined using just two frequencies are notoriously unreliable due to the $n\pi$ ambiguity. In addition, the presence of strong Faraday depolarisation in G1.9+0.3 (see Section 8.6.3) is likely to provide substantial deviations from a λ^2-law. For the sake of completeness, and in order to attempt to place further constraints on the remnant's emission, I shall still attempt to calculate the RM.

An NVSS catalogue of source RMs within 3 degrees of G1.9+0.3 (Taylor et al. 2009) show that the SNR is located in an area with a mean RM of ~ 150 rad m^{-2}, with σ of ~ 275 rad m^{-2}. The large scale component of the RM image is consistent with this, with a RM of 335 rad m^{-2} and σ of 117 rad m^{-2} as calculated by integrating the pixel values. Although there is substantial noise, the positive RM found for both the extragalactic sources and G1.9+0.3 appears to indicate that the line of sight B field is oriented towards us. Nevertheless, the magnitude of G1.9+0.3's RM is not well-determined from these data. This magnitude would not necessarily be similar

to that of nearby extragalactic sources, as the remnant is inside of the Galactic magnetoionic layer. One may however still expect the RM to be of the same sign, as it is likely that significant Faraday rotation takes place within the ISM – particularly due to the remnant's proximity to the GC.

The substantial scatter across the source is clearly shown in the histogram of pixel values in Figure 8.19. To investigate the effect of noise on the RM image, equation 8.11 can be used

$$\delta\mathrm{RM} = \frac{1}{2\Sigma\delta\lambda^2} \approx \frac{6380}{\Sigma}\ \mathrm{rad\ m^{-2}}, \tag{8.11}$$

where δRM is the uncertainty in the RM, Σ is the s/n in polarised intensity and $\delta\lambda^2$ is the difference in the squares of the wavelengths (Fletcher et al. 2011). With a typical s/n of ~ 18, $\delta\mathrm{RM} \approx 350$ rad m^{-2}. The fluctuations can therefore be entirely explained as due to noise. Due to this noise, it has not been possible to correct for the effects of Faraday rotation and to retrieve the intrinsic B vectors.

The uncorrected B vectors are shown in Figure 8.20, but will be affected by the RM towards the remnant.

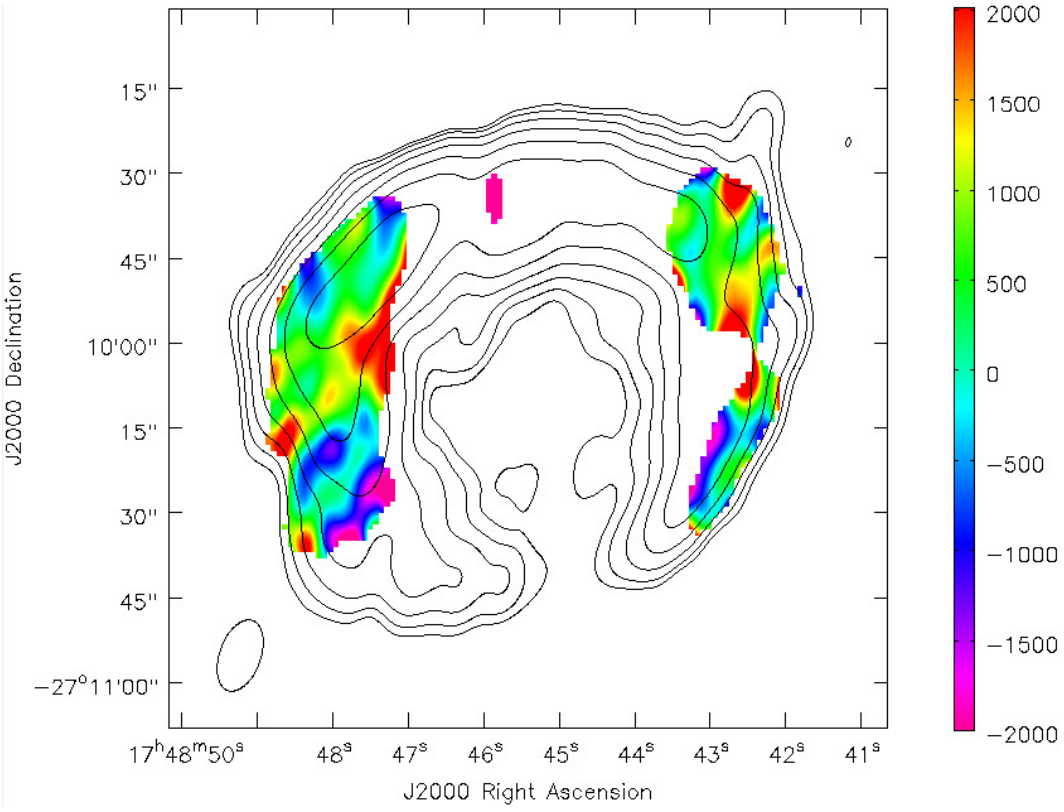

Figure 8.18: The two-point RM as determined from the 4.86 GHz sidebands. The image is dominated by noise fluctuations, as explained in the text. The contours are as in Figure 8.11.

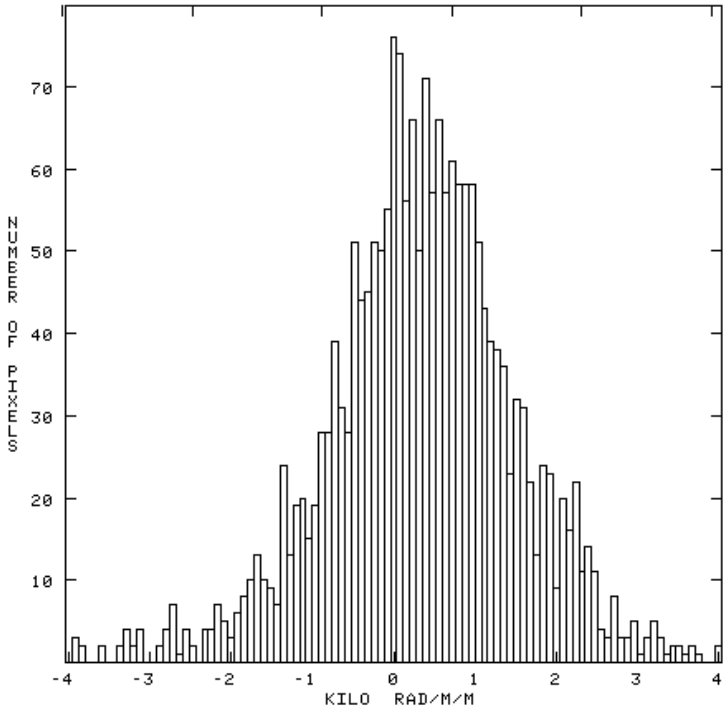

Figure 8.19: A histogram of the RM pixel values from Figure 8.18. The beam has been significantly over-sampled and consequently the data do not represent statistically independent data points.

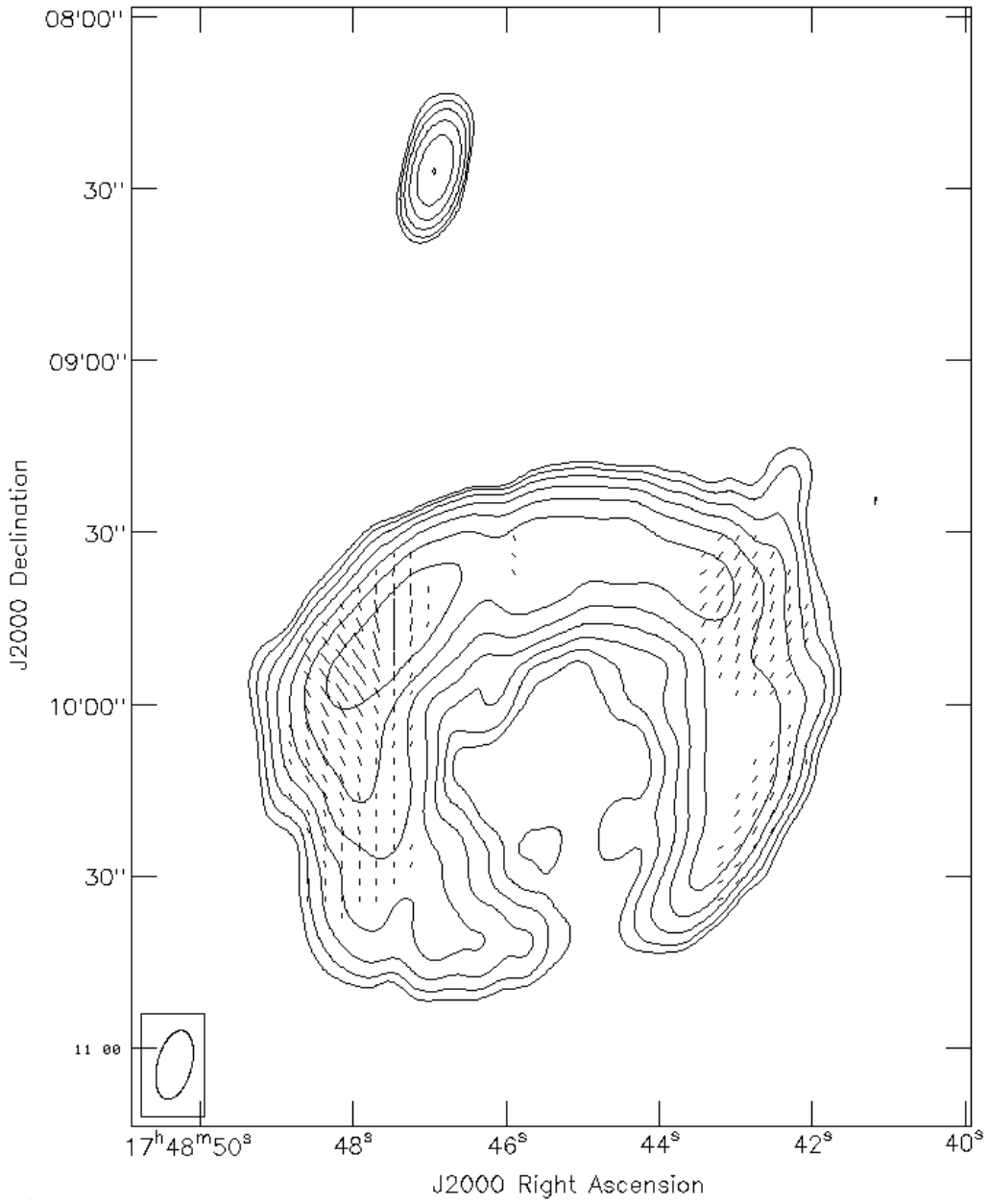

Figure 8.20: The magnetic field vectors ($E + 90°$) in G1.9+0.3 at 4.86 GHz. The vectors are proportional to polarised intensity, with $1'' = 0.5$ mJy beam^{-1}. The vectors have not been corrected for the effects of Faraday rotation, as explained in the text. The contours are as in Figure 8.11. Note the depolarised point source to the N, which serves as evidence of the polarisation calibration having been successful.

8.7 Discussion

A comprehensive understanding of the magnetic fields in G1.9+0.3 is likely to only be achieved via a concerted multi-wavelength campaign, a process that is complicated by the proximity to the Galactic centre. However, from these data it has been possible to investigate some details of the magnetic field structure and electron populations at play within the remnant.

For G1.9+0.3 to exhibit such distinct bilateral morphology suggests that the structure is dominated by variations in magnetic field rather than interactions with the ISM. This assertion is strengthened as the evolution of a remnant in the free-expansion phase should be dominated by the initial properties of the (presumed Type Ia) explosion, with the dynamical influence of the ISM remaining negligible (Bhatnagar 2001). However, this is not clear cut as measurements of the remnant's expansion indicate it is currently straddling the free-expansion and Sedov evolutionary phases (Murphy et al. 2008).

If the morphology of G1.9+0.3 is indeed dominated by magnetic field variations, then the direction of the ambient magnetic field is of particular interest. However, the direction of the ambient field can not always be easily inferred in bipolar remnants. In the case of SN 1006, various models have suggested the bright rims to be caused by quasi-perpendicular *or* quasi-parallel acceleration of electrons in the SN shock. The results of differing models tend to be mutually exclusive (Rothenflug et al. 2004; Amano & Hoshino 2007; Orlando et al. 2009; Schneiter et al. 2010; Bocchino et al. 2011). Nevertheless, it appears most likely that the shock velocity in the brightened limbs is aligned parallel to the ambient magnetic field (Rothenflug et al. 2004; Bocchino et al. 2011). This suggests that the brightened limbs are 'caps' on the magnetic field lines rather than 'poles'.

Bipolar remnants typically exhibit a tendency for the bilateral axes to be aligned with the Galactic plane. This suggests that the bipolar morphology is dominated by extrinsic effects, and appears to indicate that bipolar structure typically arises from magnetic field compression and quasi-perpendicular acceleration. SN 1006 (G327.6+14.6) is still compatible with this model, despite appearing well-described by quasi-parallel acceleration. The remnant is at a significant height above the Galactic plane, where the ISM is dominated by perpendicular structures (Gaensler 1998).

Spatial variations in the radio spectral index have been found across G1.9+0.3. The steepest radio spectral indices are found in the NE and SW quadrants of the remnant, with flatter spectral indices in the NW and SE quadrants. These spectral indices could be considered consistent with the ambient field running parallel to both the Galactic plane and the remnant's bilateral axis as shown by the lines of constant Galactic latitude in Figure 8.9. The steeper spectral indices towards the NE and SW (sectors 1, 2, 7, 8 and 12 in Figures 8.7 and 8.8) could be explained as shocks propagating quasi-parallel to the ambient magnetic field – thus compressing the ambient B field and producing steeper spectra than shocks propagating perpendicularly as

$$\alpha = -\frac{3}{2(1-r)}\,, \tag{8.12}$$

where r is a local compression ratio. At face value, this scenario also appears consistent with the flatter spectral indices found towards the NW and SE, where conversely quasi-perpendicular acceleration could be expected. In such a model, the B field would undergo compression in areas where the shock velocity is perpendicular to the ambient field. This would also lead to increased ordering of the frozen-in fields and an increase in polarised emission. This appears to be consistent with the observations presented here, and also with the X-ray spectra which have been found to be hardest in the bright NW & SE limbs, with steepening around the shell (Reynolds et al. 2009).

Nevertheless, this possibly naive interpretation neglects the fast shock velocities reported in G1.9+0.3. It is likely more realistic for a strong shock to be assumed everywhere. Assuming $r = 4$ across the remnant, newer theoretical models of cosmic ray acceleration at oblique shocks can be used to justify a scenario in which the ambient field is perpendicular to the axis of symmetry. In this case, shocks with velocities greater than 10,000 km s^{-1} show spectral flattening in areas with quasi-parallel propagation and steepening in quasi-perpendicular areas (Bell et al. 2011). Furthermore, such a model shows that cosmic rays are accelerated less efficiently in quasi-perpendicular shocks. This model can therefore explain both the observed spectral variations in G1.9+0.3 and the decreased brightness to the S. Further still, the electron spectrum should be flatter where the shock is quasi-parallel and this will increase the number of cosmic ray electrons accelerated to high energy. This will consequently produce stronger X-ray synchrotron emission at the poles – consistent with X-ray studies of G1.9+0.3 (Reynolds et al. 2009). Intriguingly, if the obliquity angle between the shock normal and the upstream B field does explain both the bright rims and the α-variations in G1.9+0.3, this would suggest that the ambient field was largely undisturbed prior to the explosion. This lends mild support to a Type Ia explosion.

The model of cosmic ray acceleration at oblique shocks does not explain G1.9+0.3's increased brightness to the N. This could be a consequence of a density gradient or localised variations in the magnetic field. If the effects of first order Fermi acceleration in the test particle limit are considered, the derived spectral indices can be related to the corresponding Mach numbers in each sector through the relation

$$\alpha = \frac{M^2 + 3}{2(M^2 - 1)} \,. \tag{8.13}$$

This allows the resulting density ratio across the remnant to be determined via

$$\frac{n_i}{n_k} = \left(\frac{M_i}{M_k}\right)^2 \,. \tag{8.14}$$

Consequently, the density ratio between the brightest regions to the N and the fainter regions to the S is $n_\mathrm{N}/n_\mathrm{S} = 0.83 \pm 0.16$ for both sectors 1 and 7, and sectors 2 and 8. While this is essentially consistent with there being no density gradient, the stated error originates from errors in α. These errors are actually expected to cause a systematic offset in the images – having an

equal effect on all annular sectors. This result therefore implies increased density towards the S. The remnants increased brightness to the N may therefore be caused by an increase in the localised magnetic field strength, as the synchrotron emissivity $J(\nu) \propto n_0 B^{1+\alpha} \nu^{-\alpha}$.

G1.9+0.3 possibly exhibits faster expansion in the E and W and slower expansion in the N (Carlton et al. 2011). If the asymmetric expansion is real, the faster expansion in the E & W is unlikely to be caused by lower densities. Pressure equilibrium in the presupernova ISM would lead to higher temperatures in lower density areas. If the shock velocity is independent of density, higher temperatures would result in lower Mach numbers, and lower Mach numbers indicate weaker shocks and steeper expected α (DeLaney et al. 2002). Conversely, the regions to the E & W have a flatter spectrum. It is therefore possible that these regions imply an asymmetric explosion by the SN progenitor, or even an axisymmetric stellar wind from a massive star, although neither can be concluded from these data. It should be noted that other evidence appears to favour a Type Ia origin.

The fractional polarisation at 4.86 GHz appears to increase towards the periphery of G1.9+0.3. Localised polarisation peaks located in the NW and SE appear correlated with regions with a flatter spectrum – with the caveat that there is a decrease in s/n in these regions. Nevertheless, the increase in the NW appears convincing. This appears to indicate enhanced ordering of the magnetic field towards the remnant periphery. Although not conclusive, the potential peak of $\sim 60\%$ to the SE is close to the theoretical limit, and if real would indicate a highly ordered B field. Nevertheless, the fractional polarisation is generally lower than that suggested through theory, and the remnant has a typical polarisation fraction of $\sim$ 10% at 4.86 GHz, with a slightly increased polarisation fraction in the western limb. This indicates that the magnetic field is likely disordered on scales less than the beam size. The levels of fractional polarisation are therefore consistent with the blast wave having reordered the external magnetic field, and indicates that turbulence of significant amplitude is likely present on scales less than 0.4 pc. This suggests that the ratio of random to uniform field strengths, $H_r/H_0 = 2.5\pm^{1.2}_{0.9}$.

The brightest emission in Stokes I has $\Pi = 4.13 \pm 0.14\%$ at 4.86 GHz and is depolarised to $< 0.1 \pm 1.3\%$ at 1.44 GHz and $< 0.05 \pm 0.04\%$ at 610 MHz. Strong Faraday depolarisation must be present. Differential Faraday rotation, internal Faraday dispersion, or external Faraday dispersion due to an anisotropic regular magnetic field could all feasibly explain the observations. It is likely that a mixture of all three mechanisms is somewhat responsible.

The magnetic field vectors have predominantly been shown to be radially oriented in young SNRs (Milne 1987). Although Rayleigh–Taylor instabilities are frequently employed to explain this phenomena, the mechanism that generates these radial fields is still poorly understood. The radial fields are proposed to be the consequence of an early Rayleigh–Taylor unstable evolutionary phase accompanying the onset of ejecta deceleration (Gull 1973a, 1975). It is not apparent if G1.9+0.3 – which appears to be straddling the free expansion and Sedov phases (Murphy et al. 2008) – would yet be Rayleigh–Taylor unstable. G1.9+0.3 is interesting in this regard due to its young age, and recovering the intrinsic B ($E + 90^\circ$) vectors may have helped in

understanding the process responsible for radially oriented fields.

In the final image of the uncorrected B vectors (see Figure 8.20), the effect of the RM is important. Nevertheless, the regions to the SE and SW of the remnant display B vectors that do not tend to point radially outwards. A RM consistent with the mean of surrounding sources, ~ 150 rad m^{-2}, would rotate the B vectors by $\sim 30°$ – assuming it is believed that the remnant (which is within the Galactic magnetoionic layer) is subject to the same external RM as the extragalactic sources. Alternatively, a RM consistent with the image value of 335 rad m^{-2} – supposing we believe that this value is unaffected by the $n\pi$ ambiguity and effects of Faraday depolarisation, would rotate the B vectors by $\sim 70°$. If we were to assume the lower RM, then the B vectors could be interpreted as displaying a transition between transverse and radial magnetic fields. While it is not possible to confirm the existence of a systematic RM gradient across the source using the data presented here, a gradient in RM of just ≈ 140 rad m^{-2} from N to S across the remnant is enough to yield a radial orientation of the B field. This is very reasonable, and could occur as a consequence of an anisotropic regular magnetic field that varies across the source – either within the remnant itself or in an intervening Faraday screen. Such a systematic variation in RM across G1.9+0.3 can also explain the observed depolarisation if a RM gradient from N to S exists across the remnant that has RM≥ 190 rad m^{-2}. If internal Faraday depolarisation is also assumed to be present, a RM gradient of ≈ 140 rad m^{-2} can both explain the depolarisation and provide a radially oriented magnetic field. Nevertheless, the present lack of strong constraints on the RM, in combination with the remnants current evolutionary stage, leaves open the possibility that Rayleigh–Taylor instability formation has not yet fully taken place. All that can be said with certainty is that this observation highlights the requirement for frequent monitoring of G1.9+0.3 as it continues to evolve; this object will doubtlessly continue to provide new insights into the evolutionary phases of young SNRs.

CHAPTER 9

FUTURE WORK

"Don't be sorry that it's over – be happy that it happened."

Anon

I have set out to calibrate the GMRT's full-polar mode for the use of wide-field spectropolarimetry, in order to investigate some aspects of cosmic magnetism. I have shown that such a calibration is not only possible at the GMRT, but that the instrument can also be used to provide excellent insights into the low frequency polarised sky. Nevertheless, there are a number of problems with GMRT polarisation data that limit the instrument's current use for high-dynamic range polarimetric observations.

The on-axis instrumental polarisation is both large and highly frequency-dependent at 610 MHz and 325 MHz. The rapid wrapping of phase with frequency limits the quality of polarisation calibration. Furthermore, the high leakages truly require the use of a non-linear model in order to separate the source and instrumental polarisation. Such non-linear models are currently unavailable. The non-linear model implemented in AIPS is currently broken. Meanwhile, 'polcal' in the Common Astronomy Software Applications (CASA) package simply states that "non-linearised options will be available soon", and has expressed this since 2008. If high-dynamic range polarimetry is truly to be performed with the GMRT, a non-linear model is essential. Nevertheless, attempts have been made to write code that solves for the leakages independently of any limiting approximations. However, the results of such code have so far only provided a scatter consistent with the results of linearised methods. The application of such non-linear solutions has to date provided disappointing results (Sam George: priv. comm.). Fortunately, it has been possible to make progress with GMRT polarimetry by removing antennas

with instrumental polarisation > 15%, thereby eliminating antennas for which a small-leakage approximation breaks down. Such methods are not without their limitations. Removing these antennas, and the associated decrease in sensitivity, contradicts the outstanding potential that the GMRT has for wide-field spectropolarimetric observations. In addition, the loss of antennas that are located in the outer arms of the array frequently leaves significant holes in the *uv*-coverage. This requires careful tapering of the data in the *uv*-plane in order to avoid artefacts when imaging extended emission, and at the same time reduces the highest resolution that is available. Although having excellent potential for wide-field spectropolarimetry, the current consequence is that the GMRT can not at present provide consistent results when attempting to image extended polarised emission. For now, it may be that the GMRT is ideally situated for the vast amount of polarimetric science that can be conducted using unresolved sources. Nevertheless, the continuing efforts at the observatory to improve the polarimetric purity of the GMRT's antennas will likely cause this to change rapidly. Indeed, the major upgrade that is currently underway will essentially revolutionise GMRT polarimetry, as the better quality receivers that are currently being installed will likely have completely different polarisation properties.

The lack of non-linearised instrumental polarisation solvers is not the only limitation of GMRT polarimetry. I have shown that time-variable instrumental polarisation is significant during certain observing epochs. Feedback of these results to the observatory, combined with the GMRT's polarisation isolation monitoring programme, appears to have reduced the number of antennas with time-variable leakage over the duration of an observation. Nevertheless, the rapidly varying long-term fluctuations demonstrate that this time-dependence is far from having been stabilised. The GMRT have now enhanced their monitoring of the polarisation isolation as a consequence of these long-term fluctuations. Previously, only a small number of channels were used for the monitoring process. The observatory have recently extended their procedures so that data across the entire band is now analysed (Nimisha Kantharia: priv. comm.). It is hopeful that these new procedures will allow for further understanding of the long-term stability, and it is apparent that the stability of the instrument has improved over recent observing cycles. Furthermore, such monitoring of the antenna isolation may also allow for the high leakage of several antennas to be consistently reduced – thereby alleviating the requirement for non-linear calibration options.

Following calibration with a large range in parallactic angle, it has been shown that excellent and uniquely sensitive polarimetry can be carried out with the GMRT. On-axis measurements of linear polarisation fractions are consistent with previous investigations, while on-axis circular polarisation measurements are reasonable for an interferometer with circular-basis feeds. Nevertheless, truly investigating cosmic magnetism with the GMRT requires careful calibration of the EVPA – an essential requirement given the interferometer's large instrumental rotation measure. As GMRT data at low frequency is intrinsically noisy, the best results for EVPA calibration have been obtained by using corrections determined in the image-plane,

rather than via the conventional method of the matrix of the *RL*/*LR* phase. While the image-plane technique appears to improve the calibration, the fact that the *RL*/*LR* phases appear discordant with the image values could well be considered a symptom of underlying systematics. Again, the implementation of non-linear algorithms and continued attempts to monitor and reduce time-variable leakage will improve the obtainable calibration substantially. Nevertheless, preliminary observations of M51 show that despite these issues, the GMRT can still be used for unique polarimetric imaging. Instrumental polarisation effects can indeed be minimised and the peak Faraday depth of sources can be retrieved, providing results consistent with previous measurements.

For full wide-field spectropolarimetry to be achieved, the effects of direction-dependent instrumental polarisation also need to be considered. My results show that the instantaneous off-axis response is large at both 610 MHz and 325 MHz, and that this scales with the FWHM of the Stokes *I* beam. Furthermore, this response appears to be oriented radially, allowing for the averaging down of wide-field polarisation with a large range in parallactic angle. Indeed, measurements across an observed field of view show that the direction-dependent response is significantly reduced far out into the beam. Nevertheless, there is still ambiguity in these results, which are derived from sources on the sky in a field with an extended galaxy present. They therefore only provide a crude indication of the off-axis response. Interpretation of the instantaneous measurement is complicated further by the unanticipated change of sign in one of the axes diagonal to both azimuth and elevation. Perhaps this flip truly indicates the beam shape, however the results of RM Synthesis and the attempts to correct for direction-dependent effects appear to suggest that the polarisation vectors within the beam are oriented radially with respect to the phase-centre. Further independent measurements are clearly required, and are already underway (Russ Taylor: priv. comm.). My measurements of the GMRT's beam have also shown that the Stokes *I* beam is stretched outwards along the axes that are diagonal to azimuth and elevation – coincident with the location of the feed support legs. Peeling is often required at the GMRT, and may therefore be a result of time-variable direction-dependent gains that are caused by the non-circular symmetry of the Stokes *I* beam as it rotates on the sky with parallactic angle. Further follow-up observations could likely lead to improvements in the pointing model and dynamic range at all frequencies, allowing for the reduction of low-level artefacts in GMRT surveys. Furthermore, such observations provide the possibility of describing the GMRT beam with a unified model which is a function of frequency. Such knowledge of a telescope's beam is extremely important, as demonstrated by the ability to calibrate the EVPA using the direction-dependent instrumental polarisation – allowing for corrections that are independent of ionospheric effects and do not require known polarised sources on the sky. It would be an interesting experiment to extend this concept to other interferometers, and to see if such a technique can be used for the next generation of low-frequency aperture-array based facilities – for which the sparsity of polarised sources and ionospheric Faraday rotation is a significant issue. Nevertheless, the lack of a curved surface in such arrays limits the magnitude

of direction-dependent effects.

Applying my findings on the GMRT's full-polar mode has allowed for two southern compact groups to be investigated. The initial concept for these observations was to provide a foundation upon which to build a catalogue of these groups – allowing for evidence of galaxy interactions and the effect on ordered magnetic fields to be explored in detail. Depolarisation at low frequencies is substantial. Although the dominating mechanisms are not fully understood, the data presented here suggest that an improvement in sensitivity may be required before such a catalogue is capable of being produced. Nevertheless, a multi-wavelength investigation of large numbers of galaxies will allow for more detailed studies. Unfortunately, complementary data is not commonplace for these southern sources – the inclusion of X-ray data could allow for a thorough analysis into the nature of AGN feedback in galaxy groups (e.g. Giacintucci et al. 2011; O'Sullivan et al. 2011). Multi-wavelength radio observations would also allow for much stronger constraints to be placed on the depolarisation mechanisms in late-types at low frequencies. This will allow for improved estimates of polarised source counts at low frequencies, and increase confidence in the feasibility of using next-generation facilities, such as the SKA, for observing the RM-grids that will be essential for understanding cosmic magnetism at low frequencies. In terms of GMRT observations, the use of TIFR GMRT Sky Survey (TGSS) data in conjunction with 610 MHz data will provide much better estimates of the spectral index in galaxy groups. Severe limitations are currently provided by the lack of data available for the southern sky. In combination with the aforementioned upgrades that are underway at the GMRT, these galaxy groups will soon be accessible for enhanced polarimetry with the GMRT. The large increase in bandwidth will provide excellent opportunities for observing a full catalogue of compact groups and additionally for measuring large unbiased samples of polarised point sources.

Understanding of the young supernova remnant, G1.9+0.3, could be substantially improved through further deep observations. The EVLA at L-band and C-band provide excellent opportunities to detect polarisation in the shell remnant. The combination of X-band data, although limited by the remnant's steep spectral index, would allow for strong constraints to be placed on the depolarisation that is taking place and would further our knowledge of magnetism in young supernova remnants. Such observations can provide valuable information on the magnetic field strength along the line of sight, and could definitively answer whether there is an anisotropic regular magnetic field across the remnant or whether the depolarisation is predominantly internal and G1.9+0.3 is not yet Rayleigh-Taylor unstable. In the long term, frequent monitoring in polarisation would allow for magnetic amplification mechanisms to be investigated in unprecedented detail. Importantly, the technique of chopping up the remnant into a 'clock-dial' for analysis of spatially varying properties is directly applicable to other similar objects. Shock physics in young remnants is still poorly understood, as is the relative influence of intrinsic and extrinsic factors on remnant evolution. These situations would be well investigated through statistical studies of spatially varying properties. Nevertheless, to

date such studies are rare. The advent of new facilities provides an opportunity to not only observe remnants 'here and there', but to create a comprehensive atlas of all known Galactic supernova remnants. Such an atlas could be used to analyse how spatial variations arise due to differing electron populations, varying magnetic fields, and the environment that surrounds such remnants. Such a large-scale study could further our understanding of high-velocity shock physics, and finally assist in separating out the dominating influences on supernova remnant evolution.

Finally, the GMRT was originally conceived for the purpose of large-scale surveys. One such survey is currently underway and the TGSS will detect a vast number of sources in Stokes I. However, now that the GMRT is calibrated for polarimetry, it is important to explore the idea of full-polarisation surveys. New facilities are about to observe the magnetic Universe at a range of frequencies. LOFAR will observe at frequencies < 230 MHz, the EVLA at > 1.2 GHz, and ASKAP between 700 MHz–1.8 GHz. When the GMRT's upgrade is complete, the nearly seamless coverage from 50 MHz to 1.5 GHz, with instantaneous bandwidths of 400 MHz, is centred within an important observational void. Such wide-field polarimetric surveys with the GMRT therefore have the potential to fill a crucial gap in our understanding of cosmic magnetism.

APPENDIX A

IMAGES OF THE SOUTHERN COMPACT GROUP FIELDS

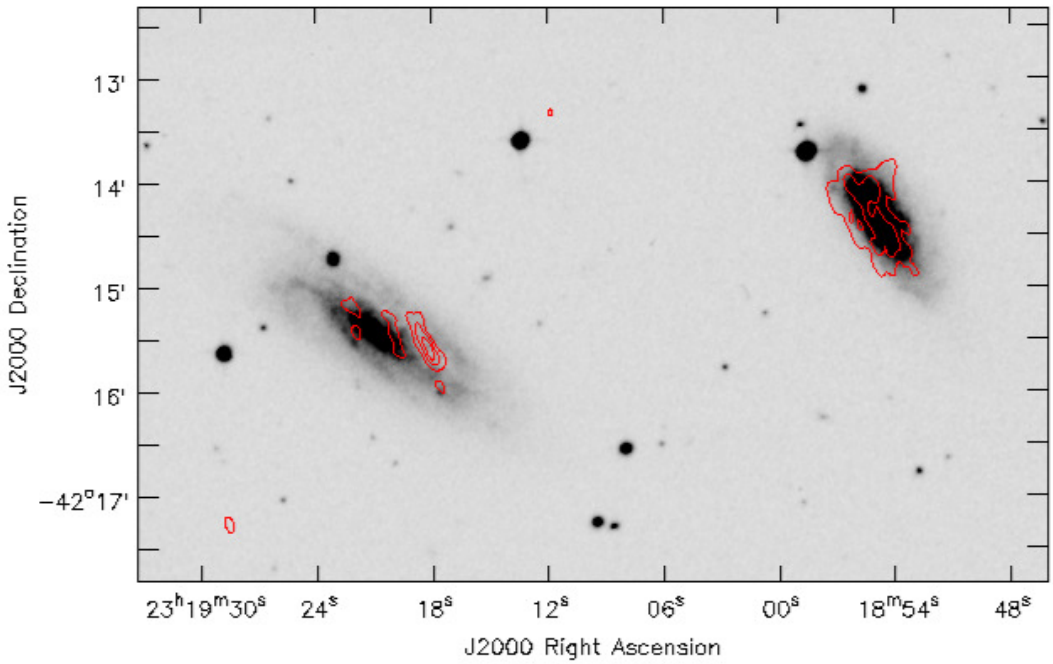

Figure A.1: Stokes I contours at 610 MHz overlaid on the near-IR DSS-2 image of NGC 7590 and NGC 7599 in the field of the Grus Quartet. NGC 7590 is further to the W. The contours are at $(-2, -1, 1, 2, 3) \times$ the off-source 4σ level, where σ is 205 μJy beam^{-1}. The 610 MHz image is at full resolution of $9.5'' \times 4.6''$ with a PA of 16°.

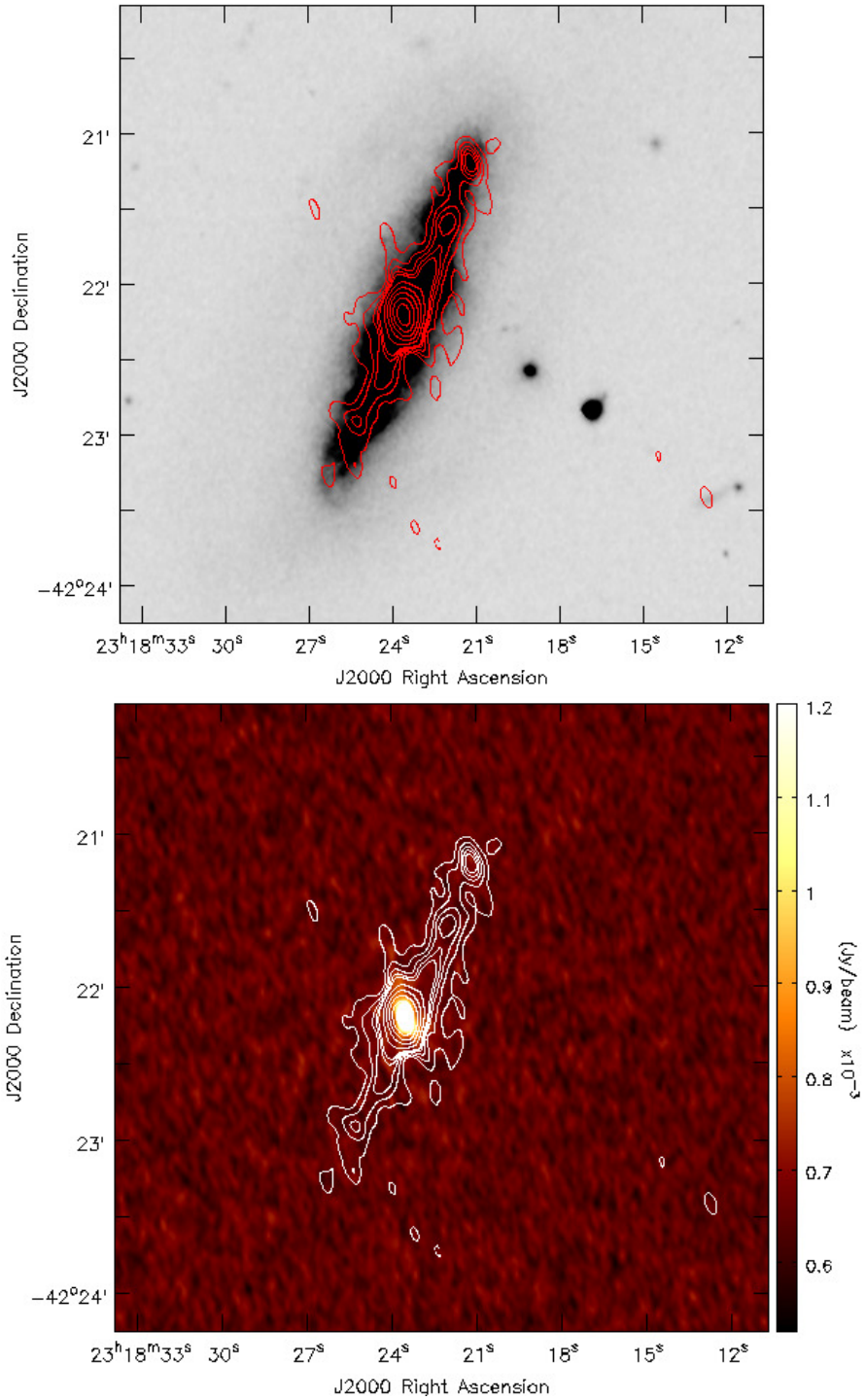

Figure A.2: Top: Stokes I contours at 610 MHz overlaid on the near-IR DSS-2 image of NGC 7582 in the field of the Grus Quartet. The contours are at (−2, −1, 1, 2, 3, 4, 5, 10, 20, 40, 80, 160) × the off-source 4σ level, where σ is 185 μJy beam^{-1}. The 610 MHz image is at full resolution of 9.5″ × 4.6″ with a PA of 16°. Bottom: Stokes I contours at 610 MHz overlaid on the image of the band-averaged P of NGC 7582. The pseudo-colour scale is in units of mJy beam^{-1}. The P image has a resolution of 24″ × 24″, and has not been corrected for the effects of the primary beam or for Rician bias.

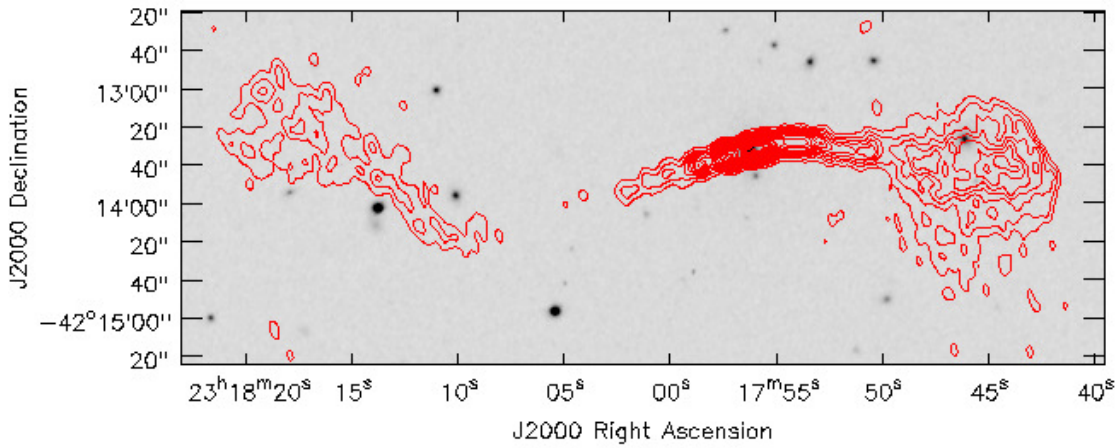

Figure A.3: Stokes I contours at 610 MHz overlaid on the near-IR DSS-2 image of J2317.9–4213 in the field of the Grus Quartet. The contours are at $(-2, -1, 1, 2, 3 \ldots 8, 10, 12 \ldots 28) \times$ the off-source 3σ level, where σ is 185 μJy beam^{-1}. The 610 MHz image is at full resolution of $9.5'' \times 4.6''$ with a PA of 16°.

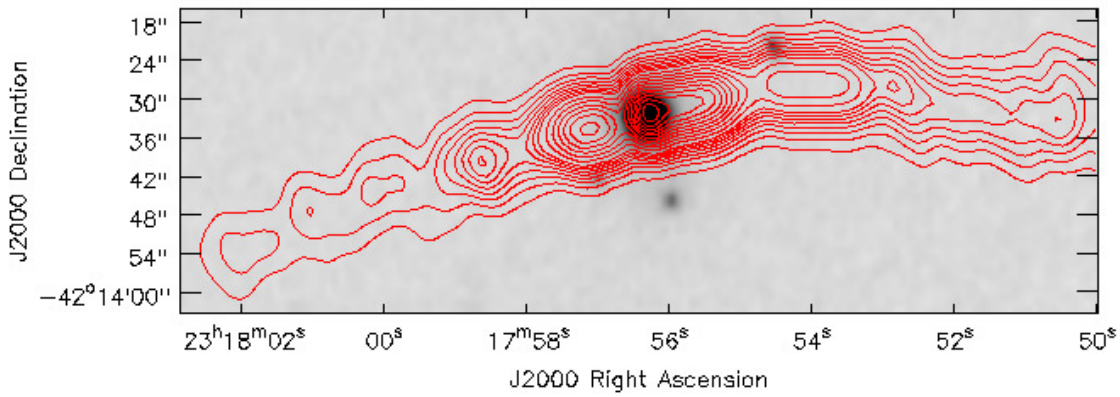

Figure A.4: As in Figure A.3, but zoomed in towards the centre of J2317.9–4213 in the field of the Grus Quartet.

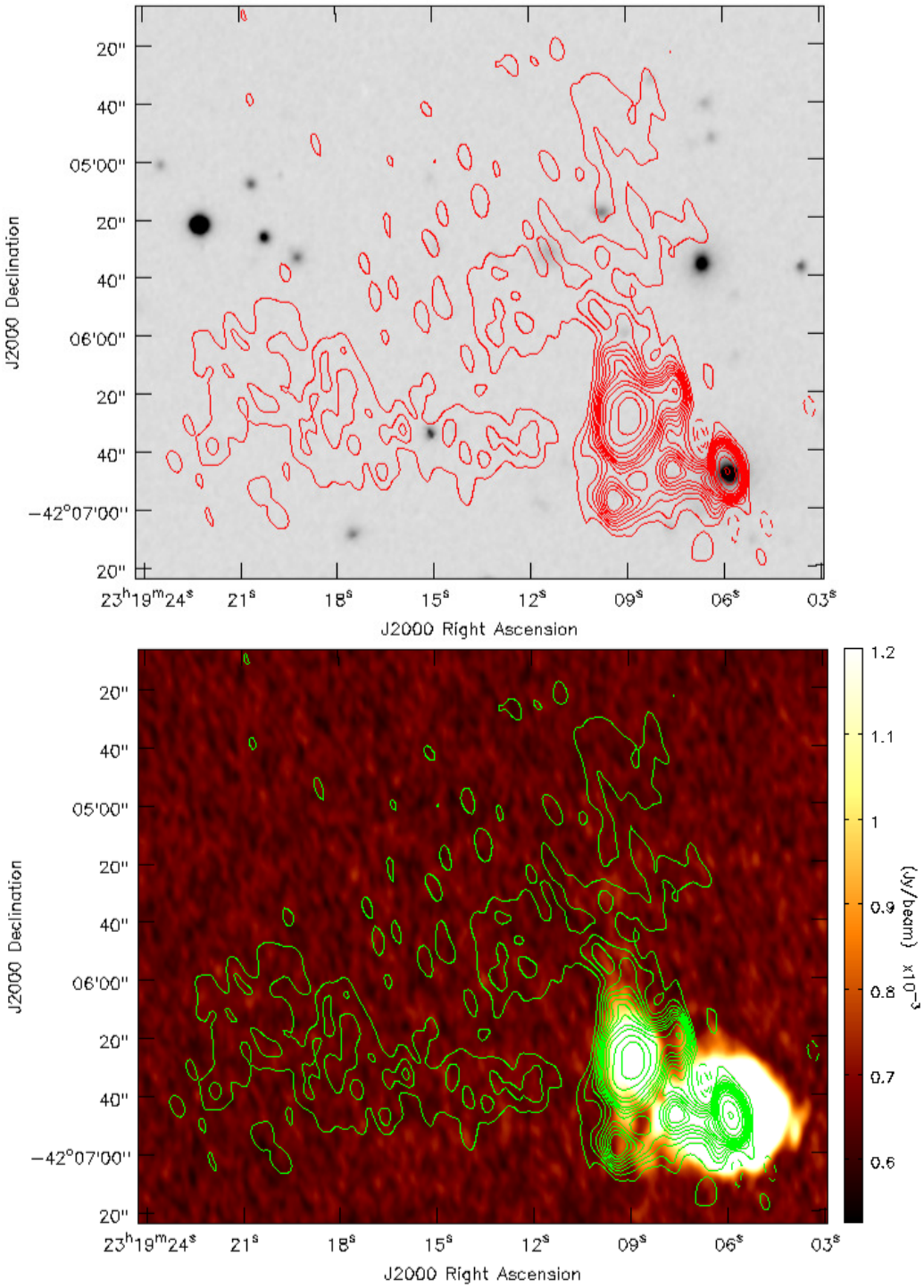

Figure A.5: Top: Stokes I contours at 610 MHz overlaid on the near-IR DSS-2 image of MCG–07–47–031 in the field of the Grus Quartet. The contours are at (−2, −1, 1, 2, 3. . . 8, 10, 12, 16, 20, 32, 64, 128) × the off-source 3σ level, where σ is 555 μJy beam^{-1}. The 610 MHz image is at full resolution of $9.5'' \times 4.6''$ with a PA of 16°. Bottom: Stokes I contours at 610 MHz overlaid on the image of the band-averaged P of MCG–07–47–031. The pseudo-colour scale is in units of mJy beam^{-1}. The P image has a resolution of $24'' \times 24''$, and has not been corrected for the effects of the primary beam or for Rician bias.

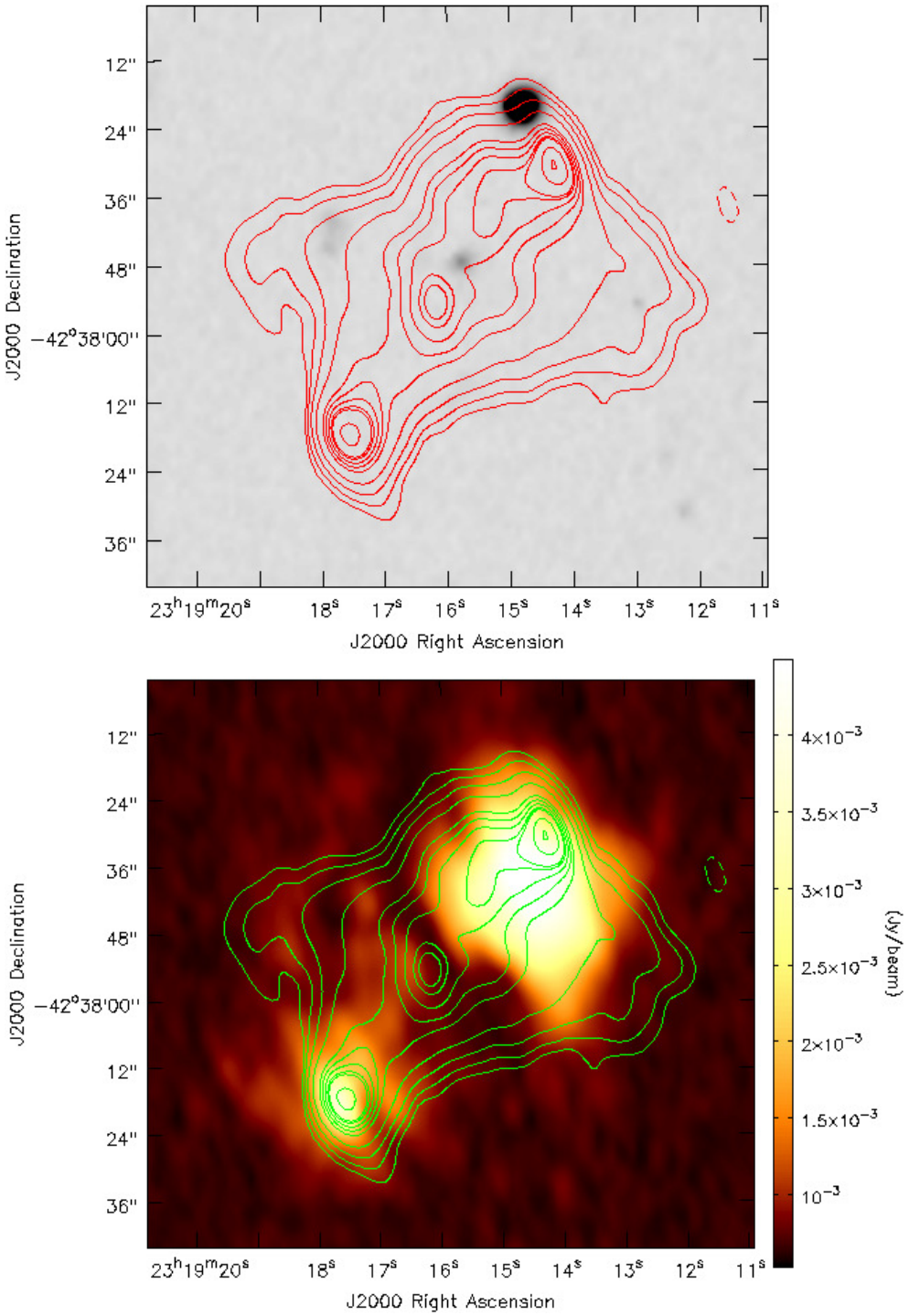

Figure A.6: Top: Stokes I contours at 610 MHz overlaid on the near-IR DSS-2 image of PKS 2316–429 in the field of the Grus Quartet. The contours are at (−2, −1, 1, 2, 4, 8, 16, 20, 24, 28, 30, 40, 50) × the off-source 4σ level, where σ is 225 μJy beam^{-1}. The 610 MHz image is at full resolution of 9.5″ × 4.6″ with a PA of 16°. Bottom: Stokes I contours at 610 MHz overlaid on the image of the band-averaged P of PKS 2316–429. The pseudo-colour scale is in units of Jy beam^{-1}. The P image has a resolution of 24″ × 24″, and has not been corrected for the effects of the primary beam or for Rician bias.

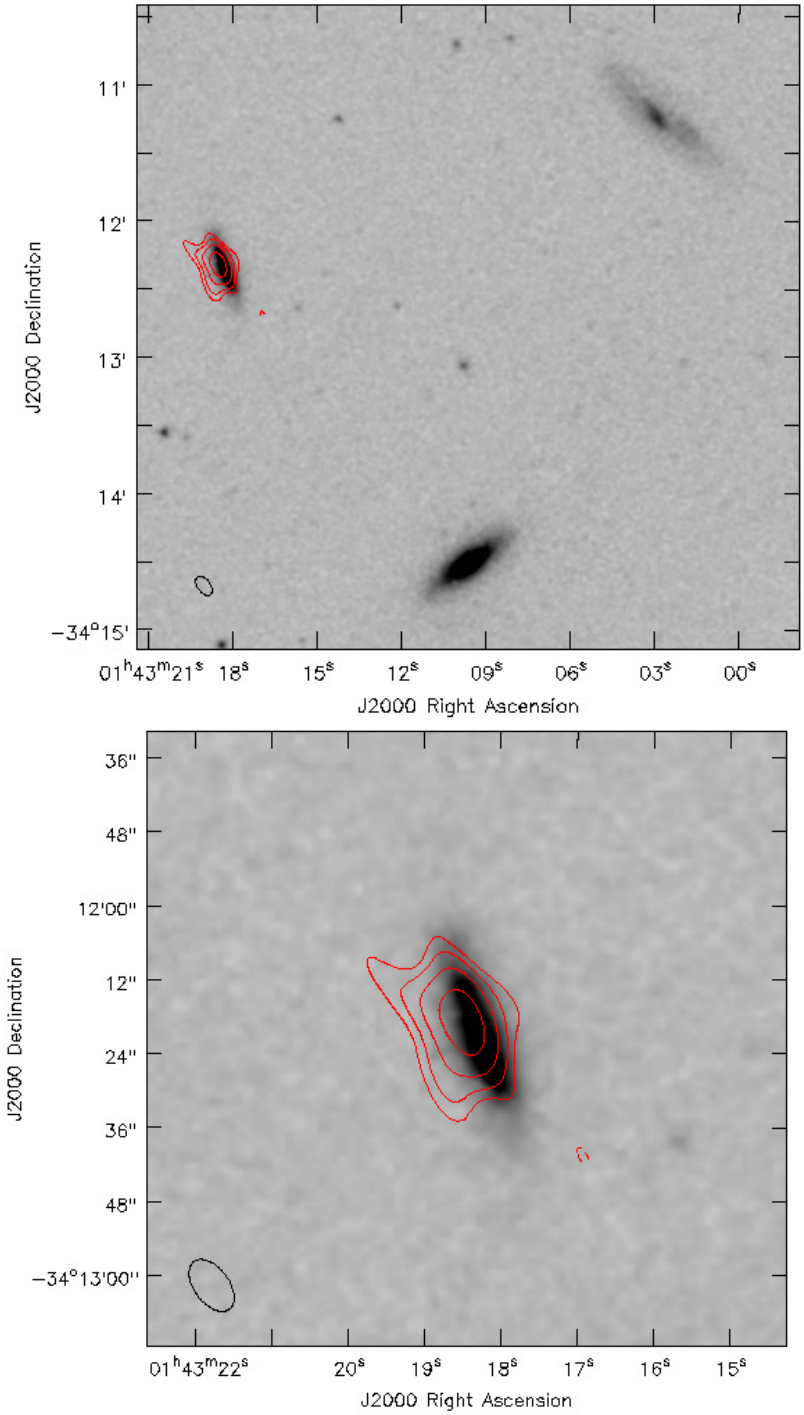

Figure A.7: Top: Stokes I contours at 610 MHz overlaid on the near-IR DSS-2 image of the region surrounding ESO 0353–G036 in the field of USCG S063. The galaxies IC 1722 and IC 1724 are visible to the NW and S respectively. The contours are at (−2, −1, 1, 2, 4, 8, 16) × the off-source 4σ level, where σ is 270 μJy beam^{-1}. The 610 MHz image is at full resolution of $9.7'' \times 5.6''$ with a PA of 37°. Bottom: The image is the same as above, but zoomed in towards ESO 0353–G036.

APPENDIX B

Treatment of Errors

Unless directly otherwise specified, all noted errors throughout this thesis are the 1σ uncertainties associated with a given measurement. The errors have been derived using standard error propagation.

For measurements of the EVPA, this provides

$$\sigma^2_{\Phi_{\rm EVPA}} = \left(\frac{\delta\Phi_{\rm EVPA}}{\delta Q}\right)^2 \sigma^2_Q + \left(\frac{\delta\Phi_{\rm EVPA}}{\delta U}\right)^2 \sigma^2_U \,, \tag{B.1}$$

which can be shown equivalent to

$$\sigma^2_{\Phi_{\rm EVPA}} = \frac{U^2\sigma^2_Q + Q^2\sigma^2_U}{4(Q^2+U^2)^2} \,. \tag{B.2}$$

For GMRT data, $\sigma_Q \approx \sigma_U = \sigma_{QU}$. Therefore

$$\sigma^2_{\Phi_{\rm EVPA}} = \frac{\sigma^2_{QU}}{4(Q^2+U^2)} \tag{B.3}$$

has been used to estimate the errors in the EVPA. Using a similar method, the noise in P for a single channel has been taken to be

$$\sigma_P \approx \sigma_{QU} \,. \tag{B.4}$$

Additionally, the 1σ uncertainty in the fractional polarisation, σ_Π, has been taken to be

$$\left(\frac{\sigma_\Pi}{\Pi}\right)^2 = \left(\frac{\sigma_I}{I}\right)^2 + \left(\frac{\sigma_P}{P}\right)^2 \,. \tag{B.5}$$

The 1σ uncertainty in the Faraday depth, σ_ϕ, was calculated using

$$\sigma^2_\phi = \frac{\sigma^2_{QU}}{4(N-2)P^2\sigma^2_\lambda} \,, \tag{B.6}$$

where σ_λ^2 is the variance in the λ^2-coverage, and all other symbols have their usual meanings. See Brentjens & de Bruyn (2005) for the derivation.

The 1σ uncertainty in the spectral index is calculated using

$$\sigma_\alpha = \frac{1}{\log\left(\frac{\nu_{\mathrm{HI}}}{\nu_{\mathrm{LO}}}\right)} \sqrt{\left(\frac{\sigma_{\nu_{\mathrm{LO}}}}{S_{\nu_{\mathrm{LO}}}}\right)^2 + \left(\frac{\sigma_{\nu_{\mathrm{HI}}}}{S_{\nu_{\mathrm{HI}}}}\right)^2}\,. \tag{B.7}$$

The error is dependent not just on the s/n of the images, but also on the relative separation between the observing frequencies used.

References

Amano T., Hoshino M., 2007, ApJ, 661, 190.

Anderson M. C., Rudnick L., 1993, ApJ, 408, 514.

Appleton P. N., et al., 2004, ApJS, 154, 147.

Arshakian T. G., Beck R., Krause M., Sokoloff D., 2009, A&A, 494, 21.

Arshakian T. G., Beck R., 2011, MNRAS, 418, 4.

Beck R., 1999, "Depolarization effects in galaxies", Galactic Foreground Polarization: Proceedings of a Workshop held in Bonn, 7–9 September 1998. Published by the Max-Planck-Institut fur Radioastronomie.

Beck R., Fletcher A., Shukurov A., Snodin A., Sokoloff D. D., Ehle M., Moss D., Shoutenkov V., 2005, A&A, 444, 739.

Beck R., 2006, "Magnetic fields in star-forming galaxies at low and high redshifts", Cosmology, Galaxy Formation and Astroparticle Physics on the Pathway to the SKA: Proceedings of the conference, held in Oxford, April 10–12, 2006. Published by ASTRON.

Bell A. R., Schure K. M., Reville B., 2011, MNRAS, 418, 1208.

Bell M. R., Enßlin T. A., 2012, A&A, 540, 80.

Bhatnagar S., 2001, "Radio Study of Galactic Supernova Remnants and the Interstellar Medium", PhD thesis, University of Pune.

Bhatnagar S., Cornwell T. J., Golap K., Uson J. M., 2008, A&A, 487, 419.

Bicay M. D., Helou G., 1990, ApJ, 362, 59.

Bisnovatyi-Kogan G. S., Lozinskaia T. A., Silich S. A., 1990, Ap&SS, 166, 277.

Bocchino F., Orlando S., Miceli M., Petruk O., 2011, A&A, 531, A129.

Bock D. C.-J., Large M. I., Sadler E. M., 1999, AJ, 117, 1578.

Borkowski K. J., Reynolds S. P., Green D. A., Hwang U., Petre R., Krishnamurthy K., Willett R., 2010, ApJ, 724, L161.

Bower G. C., Falcke H., Backer D. C., 1999, ApJ, 523, L29.

Brentjens M. A., 2008, A&A, 489, 69.

Brentjens M. A., de Bruyn A. G., 2005, A&A, 441, 1217.

Broten N. W., MacLeod J. M., Vallée J. P., 1988, Ap&SS, 141, 303.

Burn B. J., 1966, MNRAS, 133, 67.

Carilli C. L., Taylor G. B., 2002, ARA&A, 40, 319.

Carlton A., Borkowski K. J., Reynolds S. P., Willett R., Krishnamurthy K., Green D. A., Petre R., 2011, AAS, 43, #256.12.

Cayatte V., Kotanyi C., Balkowski C., van Gorkom J. H., 1994, AJ, 107, 1003.

Cenacchi E., Kraus A., Beckert T., Mack K. H., 2009, "Circular Polarimetry of Extragalactic Radio Sources", in ASP Conference Series, Astronomical Polarimetry 2008: Science from Small to Large Telescopes. Published by the Astronomical Society of the Pacific, San Francisco, in press, arXiv 0901.4678.

Chengalur J., Gupta, Y., Dwarakanath, K., 1999, "Low Frequency Radio Astronomy", Notes from an NCRA school, held in Pune, India, 21 June–17 July 1999. Published by the National Centre for Radio Astrophysics, Pune.

Condon J. J., 1992, ARA&A, 30, 575.

Cordes J. M., Lazio T. J. W., 1997, ApJ, 475, 557.

Cotton W. D., 1993, AJ, 106, 1241.

Cotton W. D., 1994, AIPS Memo #86, "Widefield Polarisation Correction of VLA Snapshot Images at 1.4 GHz".

Cotton W. D., 1999, "Polarization in Interferometry", Synthesis Imaging in Radio Astronomy II, A Collection of Lectures from the Sixth NRAO/NMIMT Synthesis Imaging Summer School. ASP Conference Series, 180, 111.

Cotton W. D., Dallacasa D., Fanti C., Fanti R., Foley A. R., Schilizzi R. T., Spencer R. E., 1997, A&A, 325, 493.

Cotton W. D., et al., 2003, PASA, 20, 12.

Coziol R., Brinks E., Bravo-Alfaro H., 2004, AJ, 128, 68.

Coziol R., Ribeiro A. L. B., de Carvalho R. R., Capelato H. V., 1998, ApJ, 493, 563.

Dahlem M., 2005, A&A, 429, L5.

Dallacasa D., Cotton W. D., Fanti C., Fanti R., Foley A. R., Schilizzi R. T., Spencer R. E., 1995, A&A, 299, 671.

Dallacasa D., Schilizzi R. T., Sanghera H. S., Jiang D. R., Lüdke E., Cotton W. D., 1996, "5 GHz EVN Polarization of 3C286", Extragalactic radio sources, Proceedings of the 175th Symposium of the International Astronomical Union, held in Bologna, Italy, October 10–14, 1995. Published by Kluwer Academic Publishers.

DeLaney T., Koralesky B., Rudnick L., Dickel J. R., 2002, ApJ, 580, 914.

Deneva J. S., Cordes J. M., Lazio T. J. W., 2009, ApJ, 702, L177.

Diehl R., et al., 2006, Natur, 439, 45.

Ewald S. P., Hjellming R. M., 1980, BAAS, 12, 804.

Farnsworth D., Rudnick L., Brown S., 2011, AJ, 141, 191.

Feretti L., Johnston-Hollitt M., 2004, NewAR, 48, 1145.

Fernandez Guasti M., Melendez Cobarrubias A., Renero Carrillo F. J., Cornejo Rodriguez A., 2005, Optik, 116, 265.

Fitt A. J., Howarth N. A., Alexander P., Lasenby A. N., 1992, MNRAS, 255, 146.

Fletcher A., Beck R., Shukurov A., Berkhuijsen E. M., Horellou C., 2011, MNRAS, 412, 2396.
Frick P., Sokoloff D., Stepanov R., Beck R., 2010, MNRAS, 401, L24.
Forbes, D. A., Kotilainen, J. K., Moorwood, A. F. M., 1994, ApJ, 433, L13.
Forbes, D. A., Norris, R. P., 1998, MNRAS, 300, 757.
Gaensler B. M., 1998, ApJ, 493, 781.
Gaensler B. M., Beck R., Feretti L., 2004, NewAR, 48, 1003.
Gardner F. F., Whiteoak J. B., 1966, ARA&A, 4, 245.
Garn T. S., 2009, "610 MHz observations of galaxy evolution", PhD thesis, University of Cambridge.
Garn T., Ford D., Alexander P., Green D. A., Riley J. M., 2007, "Magnetic fields in star-forming galaxies at high and low redshift", The Modern Radio Universe: From Planets to Dark Energy, Proceedings of the conference, held in Manchester, October 1–5, 2007. Published by University of Manchester.
Garrington S. T., Leahy J. P., Conway R. G., Laing R. A., 1988, Natur, 331, 147.
George S. J., Stil J. M., Keller B. W., 2011, PASA, in press, arXiv 1106.5362.
Giacintucci S., et al., 2011, ApJ, 732, 95.
Gould D. M., Lyne A. G., 1998, MNRAS, 301, 235.
Govoni F., Feretti L., 2004, IJMPD, 13, 1549.
Green D. A., 1990, AJ, 100, 1927.
Green D. A., 2004, BASI, 32, 335.
Green D. A., 2011, BASI, 39, 289.
Green D. A., Reynolds S. P., Borkowski K. J., Hwang U., Harrus I., Petre R., 2008, MNRAS, 387, L54.
Gull S. F., 1973a, MNRAS, 161, 47.
Gull S. F., 1973b, MNRAS, 162, 135.
Gull S. F., 1975, MNRAS, 171, 263.
Hamaker J. P., Bregman J. D., Sault R. J., 1996, A&AS, 117, 137.
Hao J., et al., 2010, ApJS, 191, 254.
Hardcastle M. J., Alexander P., Pooley G. G., Riley J. M., 1996, MNRAS, 278, 273.
Haslam C. G. T., Salter C. J., Stoffel H., Wilson W. E., 1982, A&AS, 47, 1.
Heald G., 2009, "The Faraday rotation measure synthesis technique", Cosmic Magnetic Fields: From Planets, to Stars, and Galaxies, Proceedings of the International Astronomical Union, IAU Symposium, 259, 591.
Heald G., Braun R., Edmonds R., 2009, A&A, 503, 409.
Heiles C., 1999, Arecibo Observatory Technical Memo AOTM 99-02, "The LBW Feed: Pointing Accuracy, Beamwidth, Beam Squint, Beam Squash'.
Heiles C., 2002, "A Heuristic Introduction to Radioastronomical Polarization", in ASP Conference Series, Single-Dish Radio Astronomy: Techniques and Applications. Published by the Astronomical Society of the Pacific, San Francisco.

Heiles C., Robishaw T., Troland T., Anish Roshi D., 2003, "GBT Commissioning Memo #23".
Hickson P., 1982, ApJ, 255, 382.
Horellou C., Beck R., Berkhuijsen E. M., Krause M., Klein U., 1992, A&A, 265, 417.
Hubble E. P., 1926, ApJ, 64, 321.
Iovino A., 2002, AJ, 124, 2471.
Isobe T., Feigelson E. D., Akritas M. G., Babu G. J., 1990, ApJ, 364, 104.
Johnston S., Kramer M., Lorimer D. R., Lyne A. G., McLaughlin M., Klein B., Manchester R. N., 2006, MNRAS, 373, L6.
Katz-Stone D. M., Kassim N. E., Lazio T. J. W., O'Donnell R., 2000, ApJ, 529, 453.
Kitchin C. R., 2003, "Astrophysical Techniques", 4th ed. Bristol; Philadelphia: Institute of Physics Publishing.
Krause M., 2003, AcASn, 44, 123.
Ksenofontov L. T., Völk H. J., Berezhko E. G., 2010, ApJ, 714, 1187.
Kulsrud R. M., Zweibel E. G., 2008, RPPh, 71, 046901.
Kundu M. R., Becker R. H., Velusarny T., 1973, AJ, 78, 170.
Lang C. C., Morris M., Echevarria L., 1999, ApJ, 526, 727.
Large M. I., Mills B. Y., Little A. G., Crawford D. F., Sutton J. M., 1981, MNRAS, 194, 693.
Law C. J., Yusef-Zadeh F., Cotton W. D., 2008, ApJS, 177, 515.
Leahy J. P., Pooley G. G., Jagers W. J., 1986, A&A, 156, 234.
Macquart J.-P., Bower G. C., Wright M. C. H., Backer D. C., Falcke H., 2006, ApJ, 646, L111.
Marsh K. A., Helou G., 1995, ApJ, 445, 599.
Massaro E., Giommi P., Leto C., Marchegiani P., Maselli A., Perri M., Piranomonte S., Sclavi S., 2009, A&A, 495, 691.
Mauch T., Murphy T., Buttery H. J., Curran J., Hunstead R. W., Piestrzynski B., Robertson J. G., Sadler E. M., 2003, MNRAS, 342, 1117.
Mellon R. R., Li Z., 2009, AAS, 41, #347.02.
Milne D. K., 1987, AuJPh, 40, 771.
Moss D., Shukurov A., 1996, MNRAS, 279, 229.
Murgia M., Helfer T. T., Ekers R., Blitz L., Moscadelli L., Wong T., Paladino R., 2005, A&A, 437, 389.
Murphy E. J., Kenney J. D. P., Helou G., Chung A., Howell J. H., 2009, ApJ, 694, 1435.
Murphy T., Gaensler B. M., Chatterjee S., 2008, MNRAS, 389, L23.
Nord M. E., Lazio T. J. W., Kassim N. E., Hyman S. D., LaRosa T. N., Brogan C. L., Duric N., 2004, AJ, 128, 1646.
O'Sullivan E., Giacintucci S., David L., Vrtilek J., Gitti M., Raychaudhury S., Ponman T., 2011, "AGN feedback in galaxy groups: a combined X-ray/low-frequency radio view", The X-ray Universe 2011, Presentations of the conference, held in Berlin, June 27–30, 2011.
O'Sullivan S. P., et al., 2012, MNRAS, 2504.
Oppermann N., et al., 2011, arXiv 1111.6186.

Orlando S., Bocchino F., Miceli M., Reale F., Peres G., 2009, MSAIS, 13, 97.

Palmer D. M., et al., 2005, Natur, 434, 1107.

Pen U.-L., Chang T.-C., Hirata C. M., Peterson J. B., Roy J., Gupta Y., Odegova J., Sigurdson K., 2009, MNRAS, 399, 181.

Perley R. A., Schwab F. R., Bridle A. H., Ekers R. D., 1986, Synthesis imaging. Course notes from an NRAO summer school, held at Socorro, New Mexico, USA, 5–9 August 1985. Published by the National Radio Astronomy Observatory.

Perlman E. S., Padovani P., Giommi P., Sambruna R., Jones L. R., Tzioumis A., Reynolds J., 1998, AJ, 115, 1253.

Pompei E., Dahlem M., Iovino A., 2007, A&A, 473, 399.

Ponman T. J., Bourner P. D. J., Ebeling H., Böhringer H., 1996, MNRAS, 283, 690.

Popping A., Braun R., 2008, A&A, 479, 903.

Prandoni I., Iovino A., MacGillivray H. T., 1994, AJ, 107, 1235.

Rees M. J., 2006, AN, 327, 395.

Reynolds S. P., Gilmore D. M., 1993, AJ, 106, 272.

Reynolds S. P., Borkowski K. J., Green D. A., Hwang U., Harrus I., Petre R., 2008, ApJ, 680, L41.

Reynolds S. P., Borkowski K. J., Green D. A., Hwang U., Harrus I., Petre R., 2009, ApJ, 695, L149.

Ribeiro A. L. B., de Carvalho R. R., Capelato H. V., Zepf S. E., 1998, ApJ, 497, 72.

Ricci, T. V., Steiner, J. E., Menezes, R. B., Garcia-Rissmann, A., Cid-Fernandes, R., 2010, IAUS, 267, 134.

Roberts D. H., Wardle J. F. C., Brown L. F., 1994, ApJ, 427, 718.

Rothenflug R., Ballet J., Dubner G., Giacani E., Decourchelle A., Ferrando P., 2004, A&A, 425, 121.

Roy J., Gupta Y., Pen U.-L., Peterson J. B., Kudale S., Kodilkar J., 2010, ExA, 28, 25.

Sault R., Perley R., 2009, EVLA Memo #135, "Further EVLA Polarizer Stability Measurements".

Schneider D. P., et al., 2005, AJ, 130, 367.

Schneiter E. M., Velázquez P. F., Reynoso E. M., de Colle F., 2010, MNRAS, 408, 430.

Simard-Normandin M., Kronberg P. P., Button S., 1981, ApJS, 45, 97.

Simmons J. F. L., Stewart B. G., 1985, A&A, 142, 100.

Sokoloff D. D., Bykov A. A., Shukurov A., Berkhuijsen E. M., Beck R., Poezd A. D., 1998, MNRAS, 299, 189.

Spoelstra T. A. T., 1997, AGP, 40, 865.

Spoelstra T. A. T., Yang Y.-P., 1990, URSI/IAU Symposium on Radio Astronomical Seeing, Beijing, People's Republic of China, May 15–19, 1989. Published by International Academic Publishers/Pergamon Press.

Stepanov R., Arshakian T. G., Beck R., Frick P., Krause M., 2008, A&A, 480, 45.

Stil J., 2007, “Polarisation of mJy radio sources”, The Modern Radio Universe: From Planets to Dark Energy, Proceedings of the conference, held in Manchester, October 1–5, 2007. Published by University of Manchester.

Tabara H., Inoue M., 1980, A&AS, 39, 379.

Taylor A. R., 2009, “High-Resolution Spectro-Polarimetric Radio Surveys”, in ASP Conference Series, The Low-Frequency Radio Universe. Proceedings of the conference, held at NCRA, Pune, India, December 8–12, 2008. Published by the Astronomical Society of the Pacific, San Francisco.

Taylor A. R., et al., 2007, ApJ, 666, 201.

Taylor A. R., Stil J. M., Sunstrum C., 2009, ApJ, 702, 1230.

Testori J. C., Reich P., Reich W., 2004, The Magnetized Interstellar Medium, Proceedings of the conference, held in Antalya, Turkey, September 8–12, 2003. Published by Copernicus GmbH, Katlenburg-Lindau.

Tinbergen J., 1996, “Astronomical Polarimetry”, Cambridge University Press.

Tully R. B., 1988, “Nearby galaxies catalog”, Cambridge University Press.

Turtle A. J., Pugh J. F., Kenderdine S., Pauliny-Toth I. I. K., 1962, MNRAS, 124, 297.

Vallée J. P., 1998, FCPh, 19, 319.

van den Bergh S., 1988, PASP, 100, 344.

Velusamy T., Kundu M. R., 1975, A&A, 41, 307.

Verdes-Montenegro L., Yun M. S., Williams B. A., Huchtmeier W. K., Del Olmo A., Perea J., 2001, A&A, 377, 812.

Vogt C., Enßlin T. A., 2005, A&A, 434, 67.

Wardle J. F. C., Kronberg P. P., 1974, ApJ, 194, 249.

Wielebinski R., Beck R., 2005, “Cosmic Magnetic Fields”, Lecture Notes in Physics, 664.

Wolfe A. M., Jorgenson R. A., Robishaw T., Heiles C., Prochaska J. X., 2008, Natur, 455, 638.

Wolleben M., Landecker T. L., Reich W., Wielebinski R., 2006, A&A, 448, 411.

Yun M. S., Reddy N. A., Condon J. J., 2001, ApJ, 554, 803.